TECHNISCHE UNIVERSITÄT
BERGAKADEMIE FREIBERG
Die Ressourcenuniversität. Seit 1765.

Determination of elastic (TI) anisotropy parameters from Logging-While-Drilling acoustic measurements - A feasibility study

Von der Fakultät für Geowissenschaften, Geotechnik und Bergbau
der Technischen Universität Bergakademie Freiberg

genehmigte

DISSERTATION

zur Erlangung des akademischen Grades

doctor rerum naturalium
(Dr. rer. nat.)

vorgelegt

von **M. Sc., Christoph, Demmler**

geboren am 30. Mai 1992 in Erlabrunn

Gutachter: Prof. Dr. Stefan Buske, TU Bergakademie Freiberg
Prof. Dr. Tim W. Geerits, Baker Hughes, Celle
Prof. Dr. Xiaoming Tang, China University of Petroleum

Tag der Verleihung: Freiberg, den 25. Oktober 2021

Abstract

The continuous growth of the world population causes an increasing energy demand. Despite the expansion of renewable energies, they cannot satisfy this demand alone. Thus, fossil energy sources, such as oil and gas, are still essential to supply the required amount of energy nowadays and in the future. Since the most conventional oil and gas deposits are already exploited, the importance of unconventional reservoirs, e.g., shale oil and shale gas, has grown. The unconventional shale gas production constitutes a large part of the total gas production in the United States and makes it an important hydrocarbon resource in North America. The exploitation of shale gas is challenging and requires horizontal wells as well as hydraulic fracturing. Therefore, it is crucial to derive precise seismic images of the subsurface formations from seismic migration or other algorithms. These methods need a velocity model of the subsurface as an input parameter. While the velocity model can be described by two bulk wave velocities for isotropic formations, this is not possible for anisotropic formations since the wave velocities depend on their propagation direction. Hence, anisotropic parameters are needed to obtain a correct velocity model. The number of parameters depends on the type of anisotropy. The simplest type is transverse isotropic (TI) symmetry possessing one isotropic plane. This TI symmetry is common in many rocks, such as in shales, which are the host rocks for shale oil and shale gas. Consequently, in the exploration of such resources, the quantification of the anisotropy is essential for the velocity model, which is input in seismic migration to obtain the correct depths of the imaged seismic structures. Otherwise, uncertainties in the depths can cause problems, e.g., unexpected drilling in overpressure zones resulting in a kick or even, in the worst case, in a blowout. Moreover, precise depths are important for reservoir navigation to attain optimal reservoir entry points for maximum oil or gas production.

Chapter 1 of this thesis gives an introduction to the field of borehole acoustics, which provides a method to quantify the anisotropic parameters of a formation. The advantage of borehole acoustics is that the logging is performed in the borehole very close to the rocks yielding in-situ information at various depths with a high resolution. In the past, the standard techniques to obtain anisotropic parameters were wireline (WL) cross-dipole (Esmersoy et al., 1994) and monopole measurements (Norris and Sinha, 1993; Tang, 2003). The disadvantage of the WL methods is that the tool string has to be removed entirely before the WL tool can be lowered into the borehole to perform the logging. Consequently, the drilling process must be interrupted for the logging, which increases the drill costs. Nowadays, WL logging is replaced by logging-while-drilling (LWD) measurements whenever possible. The advantage of LWD is that the logging is accomplished while the borehole is drilled, and the drilling process has not to be interrupted. Moreover, LWD measurements can provide information in

real-time, which can be used to navigate the drill path. On the other hand, the presence of the logging tool, which has a larger diameter and a higher rigidity than a WL tool, causes some challenges in determining anisotropic parameters. The aim of this thesis is to understand the relationship between the formation's anisotropic parameters and the LWD borehole waves, including not only monopole and dipole but also quadrupole waves. For this purpose, different modeling tools are used to forward model the borehole wavefield for given parameters.

Chapter 2 presents the theory of plane waves propagating in anisotropic media. The governing partial differential equations are transformed from Cartesian into cylindrical coordinates to obtain a solution in the borehole acoustic geometry for the most straightforward vertical transverse isotropic (VTI) symmetry. In this case, the formation's TI symmetry axis, which is perpendicular to the isotropic plane, lies parallel to the vertical borehole axis. On the other hand, it is outlined why a similar solution of the partial differential equations in cylindrical coordinates cannot be derived for generally anisotropic media, e.g., for the horizontal transverse isotropic (HTI) symmetry, where the TI symmetry axis is orthogonal to the borehole axis or for the tilted transverse isotropic (TTI) symmetry, where the symmetry axis is arbitrarily inclined to the borehole axis. Because of the lack of a general analytical solution, finite-difference (FD) modeling is used to simulate the waveforms in anisotropic formations with symmetries lower than VTI. Chapter 3 briefly explains the used FD method and discusses various spatial FD grids in more detail, which usage depends on the anisotropic symmetry.

Chapter 4 summarizes the results of the systematic investigation of the forward modeled borehole and refracted waves in TI formations in both the absence and the presence of an LWD tool. A monopole source emits refracted head waves and the borehole-guided *Stoneley* wave of order zero, which is helpful to determine anisotropic parameters for the VTI symmetry. Furthermore, the behavior of the flexural waves excited by a dipole source of order one is already well-understood in azimuthal anisotropic formations (HTI or TTI), which is not the case for quadrupole waves having the order two. One of the main discoveries of this thesis is that not only the flexural waves split into the fast principal flexural and slow principal flexural waves, but similarly all higher-order cylindrical waves, such as quadrupole waves. The concept of dipole shear wave splitting is generalized to all higher-order modes in a mathematical fashion and results in a generalized formula for the well-known *Alford* rotation (Alford, 1986). The derived formula is verified by applying it to the FD modeled quadrupole and hexapole waveforms. Furthermore, anisotropy-induced mode contaminants are investigated in detail for all three types of TI symmetries. While the VTI symmetry does not induce mode contaminants, it is shown that the HTI symmetry causes coupling between all borehole waves having odd orders and coupling between all borehole waves having even orders, including the *Stoneley* wave. Moreover, the TTI symmetry induces coupling between all borehole modes following a particular pattern. The investigation of the mode contaminants using FD modeling is consistent with the partial differential equations in cylindrical coordinates describing the wave motion in generally anisotropic media.

Based on the investigation of the forward modeled borehole waves, various inversion methods are proposed in chapter 5. While one inversion method introduced by Wang et al. (2016) uses non-orthogonal cross-dipole excitations, a similar inversion method has been developed in this thesis using non-orthogonal cross-quadrupole measurements. However, this proposed inversion method cannot be applied to current LWD tools since the double amount of azimuthal receivers is needed. Therefore, an alternative inversion method has been developed utilizing the anisotropy-induced mode coupling, particularly the *Stoneley* wave excited by a quadrupole source. However, all proposed inversion methods have limitations and might be difficult to apply in real measurements, which is discussed in the last section of chapter 5.

Contents

1. Introduction

1.1. Borehole acoustic configurations

Borehole acoustics is one method of the well logging disciplines with the purpose to excite acoustic waves in a wellbore that are sensitive to the surrounding rocks. Measuring and processing these waves yield valuable information for formation evaluation, including the velocities or slowness values (reciprocal velocity) of the compressional and shear waves propagating in the formation. The standard logging configuration of borehole acoustics consists of a circular, fluid-filled borehole surrounded by a formation and contains a logging tool, as displayed in figure 1.1. It can be distinguished into two different configurations, wireline (WL) logging and logging-while-drilling (LWD).

A WL tool is attached to a cable and lowered into the fluid-filled borehole after the drill string is removed (Fig. 1.1a). The logging is performed while the tool is pulled upwards by a winch. WL tools are slim and have a small diameter relative to the borehole diameter. In the lower part, the WL logging tool contains a transmitter consisting of four piezoelectric segments azimuthally separated by ninety degrees from each other to perform an omnidirectional monopole excitation. Additionally, a bender bar with two piezoelectric plates is mounted for uni-directional dipole excitation. A piezoelectric crystal has the property to change volume when a voltage is applied. Hence, applying an alternating voltage yields a periodic expansion and contraction of the crystal. The receiver array is located above the transmitter unit and consists of eight to twelve uniform-spaced receivers. Each receiver consists of four piezoelectric

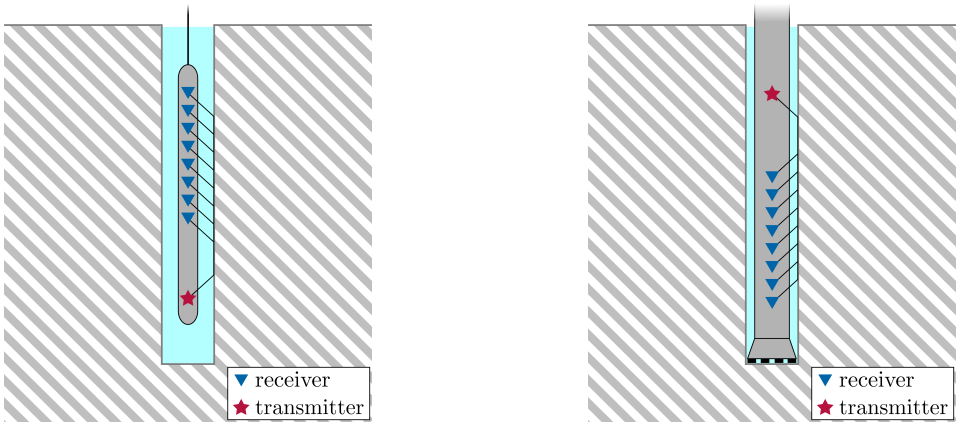

(a) WL configuration **(b)** LWD configuration

Fig. 1.1: Schematic view of a wireline (WL) (a) and logging-while-drilling (LWD) (b) configuration. The gray stripes indicate the formation, whereas the cyan color illustrates the borehole fluid. The different logging tools are displayed by the gray areas containing a transmitter unit (red star) and a receiver array (blue triangles).

sensors separated azimuthally by ninety degrees from each other and azimuthally aligned with the source. The signals received from each sensor are stacked with a particular polarity to improve the signal-to-noise ratio and suppress possible mode contaminants induced through source imbalances, borehole ellipticity, or tool eccentricity. The transmitter and the receiver array are separated by an acoustic isolator that has the purpose of isolating or attenuating acoustic waves traveling from the transmitter to the receivers along the tool. The receiver array location above the transmitter has the advantage that noise generated at the surface from the rig or roads has an opposite propagation direction to the acoustic waves generated by the transmitter. Therefore, the received coherent signal in the receiver array data has an opposite moveout to the noise, which is advantageous for processing.

On the other hand, LWD tools (Fig. 1.1b) are part of the bottom-hole-assembly (BHA) that denotes the lower part of the drill string containing the drill bit, the mud motor, heavy steel pipes, stabilizers, logging devices and other parts. Because of the large diameter of the BHA relative to the borehole diameter, the fluid annulus between the acoustic logging tool and the formation is very small. Furthermore, the LWD tool contains a fluid core in which the fluid is pumped downwards to the drill bit. The transmitter unit is located above the receiver array. This geometry is reverse to that in WL tools because the noise is primarily induced by the drill bit in LWD, which is much larger than the noise in WL measurements. The transmitter consists of four piezoelectric segments, which can be excited with equal or alternating polarities. The excitation of all four segments with equal polarity is referred to as monopole excitation (Fig. 1.2a). In contrast, if two opposite segments are excited with alternating (opposite) polarity, the excitation is referred to as dipole excitation (Fig. 1.2b), whereas the excitation of all four segments with alternating polarity yields the quadrupole excitation (Fig. 1.2c). The

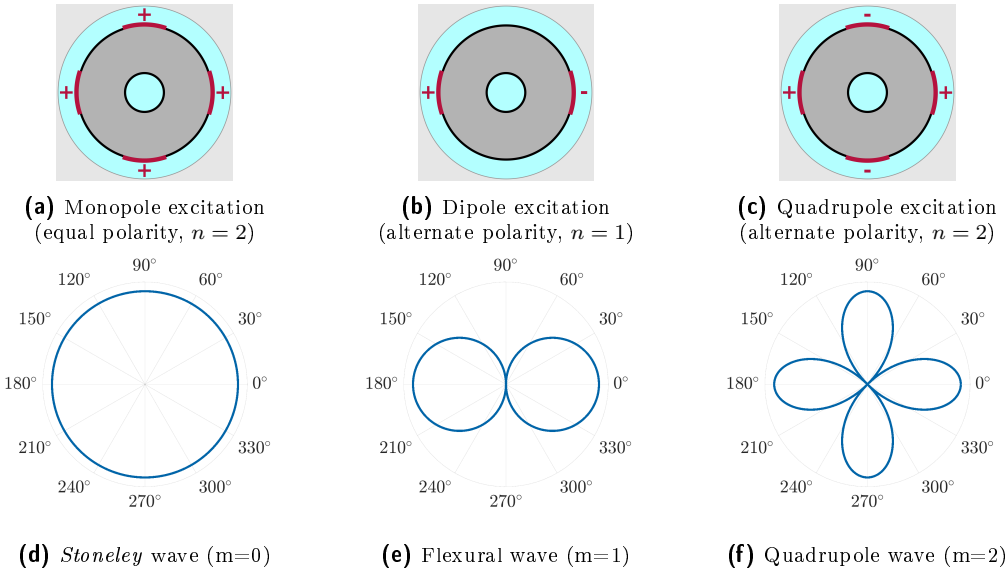

(a) Monopole excitation (equal polarity, $n = 2$)

(b) Dipole excitation (alternate polarity, $n = 1$)

(c) Quadrupole excitation (alternate polarity, $n = 2$)

(d) *Stoneley* wave (m=0)

(e) Flexural wave (m=1)

(f) Quadrupole wave (m=2)

Fig. 1.2: Equal and alternate polarity multipole sources of different excitation orders and the corresponding directivities of the emitted borehole-guided waves. The equal polarity monopole source (a) excites as the leading term the omnidirectional *Stoneley* wave ($m = 0$) (d). The alternate polarity dipole source of order one (b) excites the leading flexural wave ($m = 1$) (e), whereas an alternate polarity quadrupole source of order two (c) excites the leading quadrupole wave ($m = 2$) (f).

receiver array has the same structure as in WL tools and is separated from the transmitter by an acoustic isolator. Since LWD tools have a higher rigidity to be competent for drilling, the isolator cannot be made of soft materials like rubber to suppress tool modes traveling along the LWD tool. Therefore, the isolator is designed in a particular way to keep the tool modes and formation modes separate. The logging is directly performed while drilling, which has the advantage that the drilling has not to be interrupted, saving a significant amount of expensive rig time. Additionally, LWD enables real-time information and helps to drill more efficiently and safer because the obtained information can be used to navigate the drill path. Consequently, the emphasis in borehole acoustics has been shifted from WL to LWD.

The borehole fluid is drilling mud consisting of different components to satisfy specific properties such as carrying cuttings, providing hydrostatic pressure, or cooling the drill bit. However, for simplification, the borehole fluid is approximated by water in this thesis. The formation surrounding the borehole can be classified into slow and fast formations. In slow formations, the formation shear wave (S-wave) velocity is smaller than the velocity of the compressional wave (P-wave) in the borehole fluid. On the other hand, the velocity of the formation shear wave is higher than the compressional wave velocity of the borehole fluid in fast formations. In the latter, excited P-waves can convert to refracted shear waves at the borehole wall. These refracted shear waves propagate along the borehole wall and radiate P-waves into the fluid (*Huygens–Fresnel* principle). In this way, the shear wave slowness of the formation can be determined from the moveout of these radiated P-waves because their travel path in the borehole fluid is for all transmitter-receiver combinations identical (Fig. 1.1) and the moveout results only from traveling along the borehole wall at shear wave velocity. In contrast, in slow formations, compressional waves cannot convert to refracted shear waves at the borehole wall because of *Snell*'s law. Therefore, only refracted P-waves exist, and the shear wave slowness cannot be determined from head waves.

1.2. Wave propagation in a fluid-filled borehole in the absence of a logging tool

A transmitter in a fluid-filled borehole excites not only head waves but also borehole-guided wave modes because the borehole is an acoustic waveguide that supports an infinite number of propagating and non-propagating dispersive wave modes (Sinha and Asvadurov, 1998). Imaginably, elementary waves bouncing between the borehole wall and interfere constructively only for specific wave vector directions yielding particular azimuthal mode symmetries (Braunisch et al., 2004). Some modes radiate energy into the surrounding formations and are referred to as leaky modes because they are highly attenuative and do not contribute to the far field (Hellwig, 2017). Moreover, all borehole-guided wave modes exhibit geometrical dispersion effects and their dispersion and propagation characteristics depend on the properties of the formation, the borehole fluid, and the geometric dimensions. Furthermore, a real transmitter only excites a limited number of modes depending on its bandwidth and radiation characteristics (Sinha and Asvadurov, 1998).

First theoretical work on elastic wave propagation in a fluid-filled borehole of an infinite extent and in the absence of a logging tool was done by Biot (1952). He calculated the phase and group velocity dispersion curves of axial symmetric *Stoneley* waves ($m = 0$). Synthetic full-waveform logs of these axial symmetric waves were analytically modeled, for example, by Peterson (1974), Roever et al. (1974), or Paillet and White (1982) applying branch-cut integration (BCI). In contrast, Rosenbaum (1974), Tsang and Rader (1979) and Cheng and Toksöz (1981) used real-axis integration (RAI) to model the synthetic waveforms. Kurkjian and Chang (1986) presented a mathematical description of borehole-guided modes with higher azimuthal wavenumbers, such as flexural ($m = 1$) or quadrupole ($m = 2$) waves excited by an acoustic multipole source. Sinha and Asvadurov (2004), as well as Tang and Cheng (2004) have given an overview of the dispersion characteristics of borehole-guided modes in a fluid-filled borehole surrounded by slow and fast formations. They considered the axisymmetric monopole, dipole and quadrupole excitations. The dispersion curves are defined by the roots of the determinant of the boundary condition matrix. This matrix can be constructed by applying appropriate boundary conditions at the borehole wall to combine the wavefield in the borehole fluid and in the formation (Sinha and Asvadurov, 2004).

Figure 1.3 displays the phase slowness dispersion curves of various borehole-guided waves in slow and fast formations. For an axisymmetric monopole excitation, the excited dominant lowest-order mode is the *Stoneley* wave. The *Stoneley* wave originally denotes the interface wave traveling along a planar interface between two solids. In borehole acoustics, the *Stoneley* wave is referred to as the wave propagating along the borehole wall, which is excited at all frequencies. Depending on the formation (slow or fast), its phase slowness dispersion

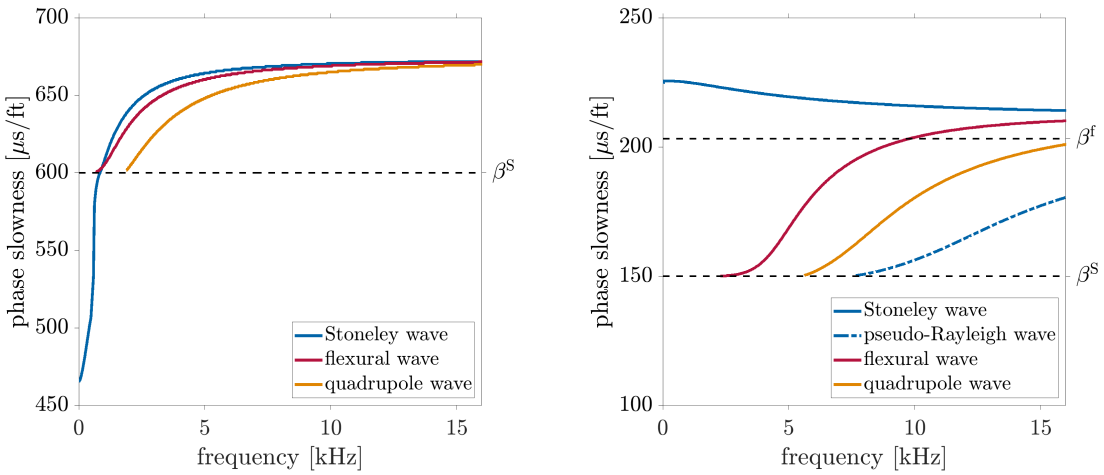

(a) Slow formation **(b)** Fast formation

Fig. 1.3: Phase slowness dispersion curves of the *Stoneley* ($m = 0$), flexural ($m = 1$), and quadrupole ($m = 2$) waves excited in a fluid-filled borehole surrounded by a slow (a) and fast (b) formation in the absence of a logging tool. The dashed blue line shows the pseudo-*Rayleigh* wave excited by a monopole source in fast formations. The dashed black lines illustrate the compressional wave slowness in the borehole fluid (β^{f}) and the shear wave slowness in the formation (β^{S}), respectively.

curve increases or decreases from the tube wave slowness at low frequencies to asymptote the *Scholte* wave slowness at high frequencies. In slow formations, the tube wave slowness can be significantly lower than the formation shear wave slowness. The *Scholte* wave denotes the wave traveling along a planar interface between a solid and a fluid. At higher frequencies, the wavelength of the *Stoneley* wave becomes shorter and the cylindrical borehole wall appears to be flat, which yields the asymptote to the *Scholte* wave slowness. Additionally to the *Stoneley* wave, pseudo-*Rayleigh* waves are excited in fast formations and have the combined effects of reflected waves in the fluid and refraction along the borehole wall (Tang and Cheng, 2004). There exists an infinite number of such modes along the frequency axis. In the frequency range displayed in figure 1.3b, only one pseudo-*Rayleigh* wave is visible. Its phase slowness dispersion curve increases from the formation shear wave slowness at the cutoff frequency and asymptotes the borehole fluid slowness at high frequencies. The borehole only guides the wave modes if their phase slowness is higher than the formation shear wave slowness. Below this slowness, the wave modes become leaky modes because they radiate energy into the formation. One of these modes is referred to as leaky P-wave, which is dominated by the refraction of compressional waves but loses energy by converting to shear waves that radiate energy into the formation (Tang and Cheng, 2004). Its phase slowness dispersion curve asymptotes at high frequencies the slowness in the borehole fluid.

Second, the dipole excitation is considered, which excites flexural waves ($m = 1$). Similar to the pseudo-*Rayleigh* wave, there exists an infinite number of flexural waves along the frequency axis. The lowest-order flexural wave is displayed in figure 1.3 in red for slow and fast formations. The flexural wave travels with the formation shear wave slowness at the cutoff frequency and increases to the *Scholte* wave slowness asymptote at high frequencies. Therefore, the flexural wave can be used to determine the formation shear wave slowness in slow formations where refracted shear waves do not exist. Consequently, the standard technique to obtain the formation shear wave slowness from WL measurements is to use dipole excitations proposed by Zemanek et al. (1984) first.

Finally, the quadrupole excitation is considered, which excites quadrupole modes ($m = 2$). Their phase slowness dispersion characteristics are similar to that of flexural waves. Figure 1.3 shows that the quadrupole mode travels with formation shear wave slowness at the cutoff frequency and asymptotes to the *Scholte* wave slowness at high frequencies. Moreover, the cutoff frequency of the quadrupole modes is higher than that of the flexural waves.

1.3. Wave propagation in a fluid-filled borehole in the presence of a logging tool

The presence of a logging tool in the center of a fluid-filled borehole provides an additional path for wave propagation along the tool wall, introducing an additional set of tool modes. Some formation borehole modes significantly interact with these tool modes and some are unaffected by them (Sinha and Asvadurov, 2004). The borehole waves are guided by the

fluid-filled annular space between the logging tool and the borehole wall. Since a WL tool has only a small diameter, it affects the wave propagation not as much as an LWD tool. The latter occupies a large portion of the borehole and can strongly affect the acoustic wave propagation. Cheng and Toksöz (1981) modeled the influence of a logging tool on *Stoneley* and pseudo-*Rayleigh* waves. They showed that the determinant of the boundary condition matrix has some additional roots that correspond to the excited tool modes. Hsu and Sinha (1998) investigated the effects of a WL logging tool on the phase slowness of the formation flexural wave. Therefore, they considered three different configurations: a tool modeled by a steel rod or steel pipe in an infinite fluid and a fluid-filled borehole of infinite extent in the absence and in the presence of a tool. Sinha et al. (2009) and Geerits et al. (2010) compared the phase slowness dispersion curves of the *Stoneley*, flexural, and quadrupole waves in the presence of an LWD tool. The phase slowness dispersion curves of these modes are plotted in figures 1.4–1.6 for a slow and a fast formation.

Figure 1.4 displays the phase slowness dispersion curves of the dominant modes excited by a monopole source in different configurations. The dashed blue line shows the dispersion curve of the *Stoneley* waves excited in an open fluid-filled borehole in the absence of a tool, which was already displayed in figure 1.3. The dashed red line denotes the tool mode excited in a configuration consisting of an LWD tool modeled by a steel pipe in an infinite fluid. Correspondingly, the solid lines are the dispersion curves of the formation and tool *Stoneley* wave excited in the combined configuration, i.e., an LWD tool centered in a fluid-filled borehole surrounded by a slow (Fig. 1.4a) or fast (Fig. 1.4b) formation. In the slow formation, the presence of the LWD tool perturbs the general dispersion characteristics of the

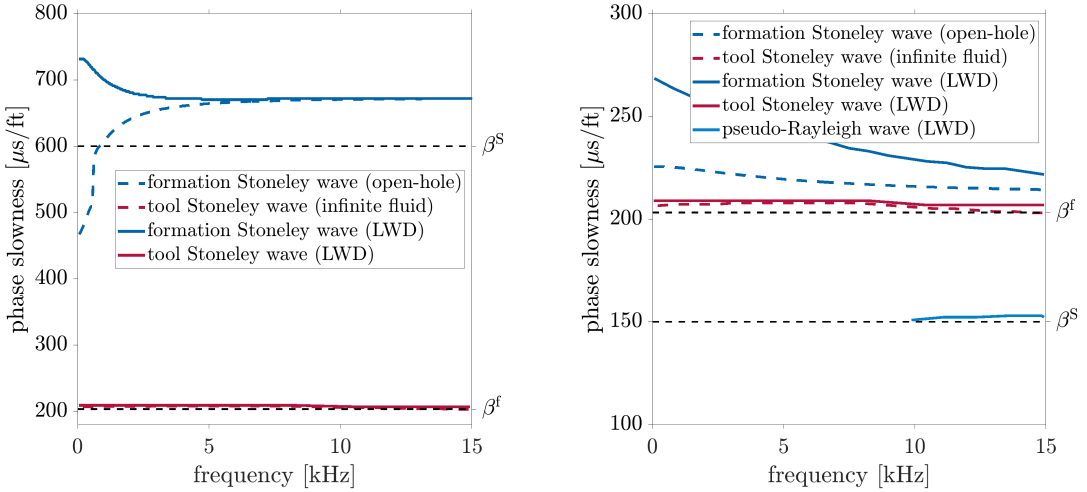

(a) Slow formation **(b)** Fast formation

Fig. 1.4: Phase slowness dispersion curves of the leading borehole- and tool-guided waves excited by a monopole source in various configurations. The dashed blue line illustrates the phase slowness dispersion curve of the formation *Stoneley* wave excited in a fluid-filled borehole in the absence of a logging tool (Fig. 1.3). The tool *Stoneley* wave excited in the presence of an LWD tool modeled by a steel pipe in an infinite fluid is displayed by the dashed red line. The solid lines represent the dispersion curves of the tool and formation *Stoneley* waves in a combined configuration, i.e., an LWD tool in a fluid-filled borehole surrounded by a slow (a) and fast (b) formation. The data is based on Sinha et al. (2009).

formation *Stoneley* wave. Its slowness values decrease with increasing frequencies and do not intersect with the true formation shear wave slowness. Hence, the low-frequency limit (tube wave slowness) is strongly altered, but the high-frequency limit still coincides with the *Scholte* wave slowness. In fast formations (Fig. 1.4b), the tool mode repels the dispersion curve of the *Stoneley* wave to higher frequencies, but the decreasing behavior is preserved. In contrast, the pseudo-*Rayleigh* wave, which is excited only in fast formations, is repelled to lower slowness values but still attains the true formation shear wave slowness at the cutoff frequency.

Figure 1.5 provides an overview of the influence of an LWD tool on the flexural wave excited by a dipole source. In the fast formation, figure 1.5b shows that the dispersion curves of the formation flexural wave in the absence of a tool (dashed blue line) and the tool flexural wave in the absence of a formation (dashed red line) intersect at about 5 kHz. However, if both configurations are combined, the formation and tool flexural waves couple and do not intersect but repel one from the other. At low frequencies, the dispersion curve of the tool flexural wave follows the dispersion curve of the tool mode in an infinite fluid. Analogously, the formation flexural wave shows a similar dispersion characteristic as the flexural wave in the absence of a tool. However, at higher frequencies, they switch identities and the tool flexural wave dispersion curve follows that of the formation flexural wave excited in an open fluid-filled borehole, whereas the formation flexural wave dispersion curve coincides with that of the tool flexural wave in an infinite fluid. Since the formation flexural wave attains the true formation shear wave slowness at low frequencies, it is still possible to obtain the formation shear wave slowness from dipole measurements. In contrast, this is not possible in slow formations (Fig. 1.5a). The formation flexural and tool flexural waves also couple and repel one

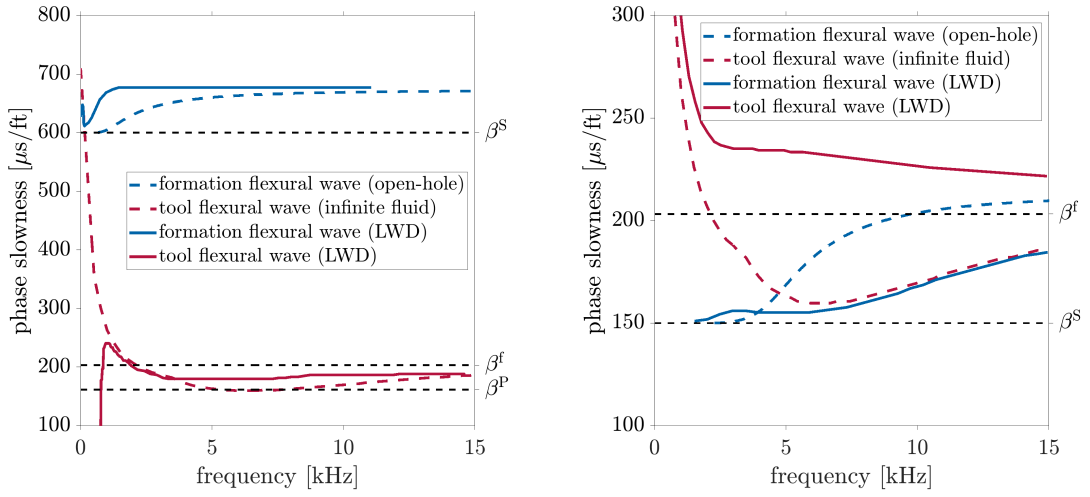

(a) Slow formation **(b)** Fast formation

Fig. 1.5: Phase slowness dispersion curves of the leading borehole- and tool-guided flexural waves excited by a dipole source ($n = 1$) in various configurations. The dashed blue line illustrates the phase slowness dispersion curve of the formation flexural wave excited in a fluid-filled borehole in the absence of a logging tool (Fig. 1.3). The tool flexural wave excited in the presence of an LWD tool modeled by a steel pipe in an infinite fluid is displayed by the dashed red line. The solid lines represent the dispersion curves of the tool and formation flexural waves in a combined configuration, i.e., an LWD tool in a fluid-filled borehole surrounded by a slow (a) and fast (b) formation. The data is based on Sinha et al. (2009).

from the other, but the low-frequency portion of the formation flexural wave does not attain the true formation shear wave slowness (Sinha et al., 2009). Instead, the dispersion curve follows the one of the tool flexural wave in an infinite fluid. Moreover, Geerits et al. (2010) have demonstrated that the formation flexural wave can even be absent in slow formation, and only the tool flexural wave exists. Consequently, LWD dipole measurements are not appropriate to obtain the formation shear wave slowness in slow formations. Geerits et al. (2010) have shown that a WL tool also causes coupling between the formation and tool flexural wave and also switches identities at higher frequencies. However, the dispersion characteristic of the formation flexural wave at low frequencies is only slightly perturbed and still attains the true formation shear wave slowness even in slow formations. Thus, it is possible to use WL dipole measurements to obtain the formation shear wave slowness in all formations, which is not possible in an LWD configuration for slow formations.

Finally, the effects of an LWD tool on the waves excited by a quadrupole source are discussed. In both slow (Fig. 1.6a) and fast (Fig. 1.6b) formations, the general characteristic of the formation quadrupole mode is only slightly affected by the LWD tool. The cutoff frequency is decreased and the dispersion curves increase steeper starting from the cutoff frequency than in the absence of a tool, but the formation quadrupole mode still attains the true formation shear wave slowness at low frequencies. Thus, the quadrupole mode is convenient to obtain the formation shear wave slowness from LWD measurements in slow formations, which was first demonstrated by Tang et al. (2003).

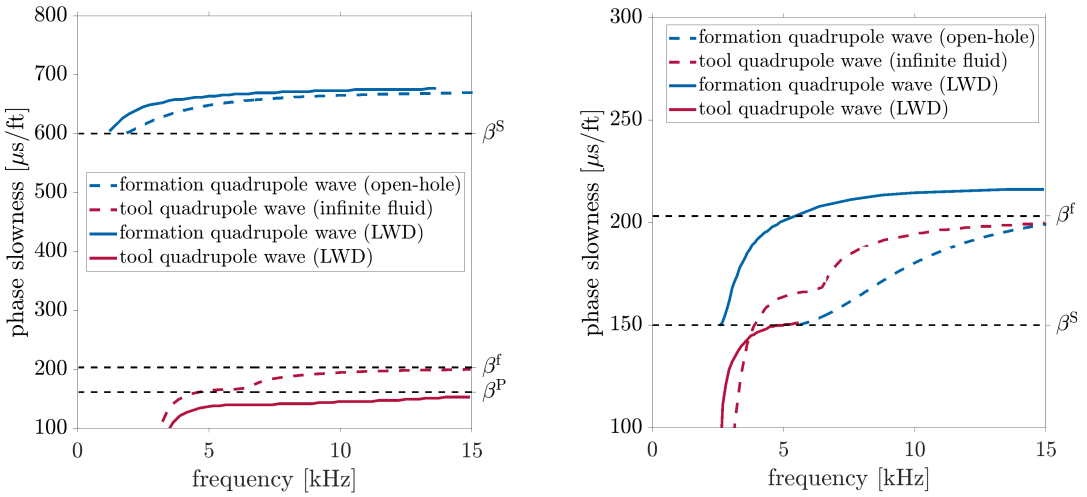

(a) Slow formation **(b)** Fast formation

Fig. 1.6: Phase slowness dispersion curves of the leading borehole- and tool-guided quadrupole waves excited by a quadrupole source ($n = 2$) in various configurations. The dashed blue line illustrates the phase slowness dispersion curve of the formation quadrupole wave excited in a fluid-filled borehole in the absence of a logging tool (Fig. 1.3). The tool quadrupole wave excited in the presence of an LWD tool modeled by a steel pipe in an infinite fluid is displayed by the dashed red line. The solid lines represent the dispersion curves of the tool and formation quadrupole waves in a combined configuration, i.e., an LWD tool in a fluid-filled borehole surrounded by a slow (a) and fast (b) formation. The data is based on Sinha et al. (2009).

1.4. Anisotropy

The most theoretical formulations of wave propagation in a fluid-filled borehole in the presence or absence of a logging tool assume a surrounding isotropic formation. However, in oil and gas exploration, many common formations are anisotropic, such as shales. A medium is called anisotropic with respect to a parameter if this parameter is direction-dependent. For an anisotropic elastic medium, the seismic wave velocities depend on the direction of their particle motion. Consequently, two shear waves having the same propagation direction may travel with different velocities in an anisotropic formation if their polarization directions are distinct. Formation anisotropy can be caused by various mechanisms. Intrinsic anisotropy is caused by a preferred orientation of mineral grains or the particular shape of isotropic minerals, e.g., flat-lying platelets (Thomsen, 1986). Additionally, thin bedding of isotropic layers can cause anisotropy. These layers are heterogeneous and isotropic on a small scale but homogeneous and anisotropic on a large scale if the wavelength is large compared to the thickness of the layers (Backus, 1962). Furthermore, a system of aligned vertical or dipping fractures or microcracks causes anisotropy (Crampin, 1985), and anisotropy can be induced by tectonic stresses or by altering the local stress field distribution through drilling a borehole (Sinha and Kostek, 1996).

Anisotropic media exhibit various symmetries and can be classified into different symmetry classes (Auld, 1973; Musgrave, 1970; Nayfeh, 1995). In most cases, anisotropy is modeled by the most straightforward symmetry denoted as transverse isotropy (TI). Such media possess one isotropic plane in which the wave velocities are direction invariant. The symmetry axis is defined to be perpendicular to that isotropic plane. Outside the isotropic plane, the wave velocities change with direction. There exists two exceptional cases of TI symmetry in borehole acoustics. If the symmetry axis of a TI formation is aligned with the borehole axis, the symmetry is referred to as vertical transverse isotropy (VTI). This symmetry class often occurs, e.g., for a vertical borehole in thin bedding of horizontal layers. Analogously, if the symmetry axis is perpendicular to the borehole axis, the symmetry is referred to as horizontal transverse isotropy (HTI). This type of symmetry can occur for a horizontal borehole in thin bedding of horizontal layers or a vertical borehole surrounded by a formation containing a system of aligned vertical fractures. If the borehole axis is arbitrarily aligned to the formation symmetry axis, the symmetry is called only TI or tilted transverse isotropy (TTI), which occurs for deviated boreholes.

In borehole acoustics, the correct quantification of anisotropy is essential for prestack depth migrations, amplitude-versus-offset (AVO) analysis, wellbore stability, optimization of completion design, hydraulic fracturing monitoring, or production management. Analytical solutions of wave propagation in a fluid-filled borehole surrounded by an intrinsically anisotropic formation can only be obtained if the formation exhibits VTI symmetry. The first researchers who modeled axisymmetric waves in a fluid-filled borehole surrounded by an anisotropic VTI formation were White and Tongtaow (1981) using branch-cut integration (BCI) and Chan and

Tsang (1983) using real-axis integration (RAI). Additionally, Ellefsen et al. (1990) modeled higher-order borehole waves, such as the flexural or quadrupole wave, and Schmitt (1989) extended the work to model wave propagation in poroelastic formations. If the formation exhibits HTI or TTI symmetry, analytical solutions are not available, but perturbation methods were developed by Ellefsen et al. (1991), Norris and Sinha (1993), Sinha et al. (1994), and Zhang and Wang (1996) to model the borehole waves. Sinha et al. (1994) used a perturbation method to calculate the dispersion curves of borehole modes in TI formations, but their waveforms result from an isotropic reference state. For the modeling of full elastic anisotropic waveforms in fluid-filled boreholes surrounded by a formation exhibiting general anisotropy, finite-difference (FD) modeling is used. Leslie and Randall (1992) developed a 2.5-dimensional time-domain FD method to model such borehole waves, whereas Cheng et al. (1995) used a three-dimensional FD code in Cartesian coordinates.

The sensitivity of borehole modes to anisotropy parameters depends on their order and radiation pattern. The *Stoneley* wave is the only borehole mode sensitive to formation properties transverse to the borehole axis since this mode radially deforms the borehole at low frequencies. Norris and Sinha (1993) used a perturbation method to model the low-frequency velocity of the *Stoneley* wave (tube wave velocity) for deviated boreholes that penetrates a weak anisotropic formation exhibiting TI symmetry. Additionally, they proposed an inversion procedure to output formation anisotropy parameters in fast formations, assuming a known deviation angle and some correlations between the anisotropy parameters that may be violated for strong anisotropic formations. In contrast, Nicoletis et al. (1990) used a combination of analytical solutions and numerical methods to calculate the velocity of the *Stoneley* wave in the low-frequency limit. Tang (2003) investigated the effect of the presence of a logging tool on the tube wave speed in VTI formations. He modeled the tool by an effective tool modulus and proposed an inversion algorithm to output the horizontal shear velocity assuming that all other parameters are known. Chi and Tang (2006) compared two and three-dimensional solutions to model the tube wave velocity in arbitrary anisotropic formations. Moreover, finite-difference modeling of the *Stoneley* wave in anisotropic formations was performed by Leslie and Randall (1992) and Sinha et al. (2006).

Since the flexural wave is only sensitive to the vertical shear wave velocity, it is not helpful to determine differences in the shear wave velocities if the symmetry axis is parallel to the borehole axis (VTI). However, if the symmetry axis is inclined, the sensitivity of the flexural wave to anisotropic parameters increases with an increasing inclination and is at a maximum if the symmetry axis is perpendicular to the borehole axis (HTI). Esmersoy et al. (1994) and Mueller et al. (1994) have shown that WL cross-dipole measurements provide an opportunity to obtain formation anisotropy parameters. An HTI formation can be characterized by two distinct mutually perpendicular directions associated with a slow and a fast principal shear wave velocity. Analogously, in HTI media, there exists one slow and one fast principal flexural wave, whose directivities are azimuthally rotated by ninety degrees. In general, a dipole source excites a weighted superposition of both principal flexural waves, which are recorded at the

receivers. The measured wave signal is rotated using the *Alford* rotation introduced by Alford (1986) to obtain the slow and fast principal waves. Since both principal waves travel with the true formation shear wave slowness at low frequencies, the principal shear wave velocities can be determined. Furthermore, Tang and Chunduru (1999) proposed a more robust inversion method to simultaneously invert the orientation and associated slowness values of the principal directions by minimizing an error function. In consequence, cross-dipole measurements are the standard technique in WL logging to obtain HTI parameters.

However, this method fails in an LWD configuration, especially in slow formations, since the formation dipole or flexural wave cannot be used to determine the true formation shear wave slowness. Section 1.3 explains that the quadrupole mode is more convenient to obtain the true formation shear wave slowness in isotropic formations. This poses the question if LWD quadrupole modes can also be used to determine TI parameters. The main disadvantage of the quadrupole mode is the non-unique directivity (Fig. 1.2). Nevertheless, Wang and Tang (2003) investigated LWD quadrupole modes in anisotropic TI formations and showed that the quadrupole mode also splits into earlier and later arrivals. Additionally, Blyth et al. (2016) demonstrated that there exists a symmetric and an antisymmetric principal quadrupole mode. While the symmetric quadrupole tends to travel at low frequencies with the fast shear wave slowness, the low-frequency limit of the antisymmetric quadrupole mode is closer to the slow shear wave slowness. However, it is not possible to directly read the true fast and slow shear wave slowness values from the dispersion curves.

Moreover, Mickael et al. (2012a,b), Nestyagin et al. (2017), Nwosu et al. (2015), Sakiyama et al. (2016), and Syresin et al. (2016) proposed LWD unipole sources to determine anisotropic parameters. A unipole source consists of one single source mounted at one side of the LWD tool and excites a superposition of an infinite number of borehole modes having azimuthal wavenumbers from zero to infinity. In the frequency range of interest, a superposition of the monopole, dipole, and quadrupole mode is dominant (Wang et al., 2011). The emitted total wavefield is focused and can be used to obtain the slowness of the non-dispersive refracted compressional and shear waves for a particular azimuth. By taking advantage of the tool rotation, it is possible to provide slowness information at all azimuths. Hence, in HTI formations, the azimuth having the lowest slowness value corresponds to the fast principal direction, whereas the azimuth with the highest slowness value belongs to the slow principal direction. However, unipole measurements are only helpful in fast formations because refracted shear waves do not exist in slow formations (Sec. 1.1).

Furthermore, Hornby et al. (2003) presented an inversion method to obtain TI parameters using data from multiple wells with different deviation angles relative to the formation TI symmetry axis. Moreover, Horne et al. (2012) discussed an analogous inversion method, using only one well having vertical, horizontal, and tilted parts relative to the TI symmetry axis. Additionally, a similar inversion method was discussed by Walsh et al. (2006), but all of them are very specific and cannot be generalized. Consequently, they did not become mainstream

techniques in borehole acoustics.

Although most research was focused on intrinsic anisotropy, Sinha and Kostek (1996) investigated the effect of stress-induced anisotropy on borehole flexural waves. They showed that drilling a borehole significantly alters the existing stress state in the near field. However, at low frequencies, the borehole flexural wave has a larger radial depth of investigation and is unaffected by the stress-induced altered zone. In contrast, at higher frequencies, the flexural wave becomes sensitive to the stress-induced altered zone close to the borehole. Consequently, horizontal uniaxial stress in the formation causes a crossover in the dispersion curves of the flexural waves aligned parallel and perpendicular to the stress direction, respectively. Since this flexural dispersion crossover is not observed in intrinsically anisotropic formation, it is an indicator of stress-induced anisotropy. Besides, Liu and Sinha (2000, 2003) used FD modeling to study the influence of borehole stress on monopole and dipole dispersion curves. Fang et al. (2014) discussed the effect of stress-induced anisotropy on borehole compressional wave propagation, whereas Zheng et al. (2009) investigated cross-dipole modes.

2. Theory

In the scope of this thesis only intrinsic anisotropy is considered, which can be mathematically described by the stiffness or compliance tensor. The first part of this chapter presents the properties and various symmetries of these tensors. The next part deals with the theory of seismic wave propagation in linear elastic anisotropic media. The solutions of the governing equations given in Cartesian coordinates are harmonic plane waves. However, cylindrical coordinates are more convenient for the borehole acoustic problem. Thus, the governing differential equations are transformed from Cartesian to cylindrical coordinates and solved for the most straightforward VTI symmetry, yielding the modified *Bessel* functions as elementary solutions. The solutions valid in VTI media are connected to the solutions valid in the borehole fluid by applying boundary conditions at the borehole wall. In this way, an analytical solution for the borehole acoustic configuration is obtained, which was presented by Schmitt (1989) for poro-elastic VTI media. In contrast, an analogous solution of the partial differential equations in cylindrical coordinates could not be found if the anisotropic formation exhibits symmetries lower than VTI. These symmetries require a different ansatz. Although the ansatz was already developed, there was no time to implement and test the underlying ideas in the scope of this thesis. The new ansatz will be the content of another work and is thus omitted here.

2.1. Stiffness and compliance tensor

A linear elastic, intrinsic anisotropic medium can be fully described by the volumetric mass density ρ^{s} and the stiffness tensor $C''_{i,j,k,l}$ or the compliance tensor $S''_{i,j,k,l}$. Both tensors of rank four define the coefficients of the linear relation between the stress tensor τ'' and the strain tensor ϵ'' (*Hooke*'s law)

$$\tau''_{i,j} = C''_{i,j,k,l}\epsilon''_{k,l}, \tag{2.1a}$$

or

$$\epsilon''_{i,j} = S''_{i,j,k,l}\tau''_{k,l}. \tag{2.1b}$$

From equations 2.1a and 2.1b is deduced that the compliance tensor is the inverse of the stiffness tensor, and vice versa

$$S''_{i,j,k,l}C''_{k,l,p,q} = C''_{i,j,k,l}S''_{k,l,p,q} = \delta_{i,p}\delta_{j,q}, \tag{2.2}$$

where $\delta_{i,j}$ denotes the unit tensor of rank two

$$\delta_{i,j} = \begin{cases} 1 & i = j \\ 0 & i \neq j \end{cases}. \tag{2.3}$$

In the following of this section, the properties and symmetries are presented only for the stiffness tensor applying also to the compliance tensor.

The stiffness tensor possesses eighty-one (3^4) components in the three-dimensional space. Since the stress and strain tensors are symmetric ($\tau''_{i,j} = \tau''_{j,i}$ and $\epsilon''_{i,j} = \epsilon''_{j,i}$), the first and the second index of the stiffness tensor can be interchanged, as well as the third and the fourth index. This symmetry property of the stiffness tensor

$$C''_{i,j,k,l} = C''_{j,i,k,l} = C''_{i,j,l,k} = C''_{j,i,l,k}, \tag{2.4}$$

reduces the number of independent components to thirty-six. Further symmetries can be shown by considering the strain energy density defined as (e.g., Nayfeh, 1995)

$$U = \frac{1}{2}\tau''_{i,j}\epsilon''_{i,j} = \frac{1}{2}C''_{i,j,k,l}\epsilon''_{k,l}\epsilon''_{i,j}. \tag{2.5}$$

Straightforward differentiation of equation 2.5 yields

$$C''_{i,j,k,l} = \frac{\partial^2 U}{\partial\epsilon''_{i,j}\partial\epsilon''_{k,l}}, \tag{2.6}$$

and it can be shown that interchanging the order of differentiation does not change the relation (Nayfeh, 1995). Hence, the first two indices of the stiffness tensor can be interchanged with the last two indices. This additional symmetry property

$$C''_{i,j,k,l} = C''_{k,l,i,j} \tag{2.7}$$

reduces the number of independent components to twenty-one. The stiffness tensor of rank four can be rewritten into a matrix with six rows and six columns utilizing the symmetries. Therefore, a pair of indices is contracted to one single index according to the *Voigt*'s notation (Voigt, 1910)

$$1,1 \to 1 \qquad 2,2 \to 2 \qquad 3,3 \to 3 \qquad 2,3 \to 4 \qquad 1,3 \to 5 \qquad 1,2 \to 6. \tag{2.8}$$

2.1.1. Triclinic symmetry

Applying the *Voigt*'s notation to equation 2.1a, *Hooke*'s law can be written in a matrix-vector form (e.g., Nayfeh, 1995)

$$\begin{pmatrix} \tau''_{1,1} \\ \tau''_{2,2} \\ \tau''_{3,3} \\ \tau''_{2,3} \\ \tau''_{1,3} \\ \tau''_{1,2} \end{pmatrix} = \begin{pmatrix} C''_{1,1} & C''_{1,2} & C''_{1,3} & C''_{1,4} & C''_{1,5} & C''_{1,6} \\ & C''_{2,2} & C''_{2,3} & C''_{2,4} & C''_{2,5} & C''_{2,6} \\ & & C''_{3,3} & C''_{3,4} & C''_{3,5} & C''_{3,6} \\ & & & C''_{4,4} & C''_{4,5} & C''_{4,6} \\ & \text{sym} & & & C''_{5,5} & C''_{5,6} \\ & & & & & C''_{6,6} \end{pmatrix} \begin{pmatrix} \epsilon''_{1,1} \\ \epsilon''_{2,2} \\ \epsilon''_{3,3} \\ 2\epsilon''_{2,3} \\ 2\epsilon''_{1,3} \\ 2\epsilon''_{1,2} \end{pmatrix}. \tag{2.9}$$

The stiffness matrix in equation 2.9 is symmetric and contains twenty-one independent components describing a triclinic medium, which is the most general case of anisotropy.

2.1.2. Monoclinic symmetry

Most materials exhibit material symmetries leading to simplifications of the stiffness tensor. An anisotropic medium possessing one plane of symmetry is referred to as monoclinic. For instance, if the symmetry plane coincides with the x''_1–x''_3 plane, the material that occupies the semi-space $x''_2 \geq 0$ has the same properties as the material in the semi-space $x''_2 \leq 0$ (Nayfeh, 1995). Consequently, the medium is invariant to mirroring at the symmetry plane. This invariance requires that several elements of the stiffness tensor vanish, and the number of independent elements reduces to thirteen. The vanishing elements depend on which plane is the symmetry plane. The stiffness tensor characterizing a monoclinic medium with the x''_1–x''_3 plane as the symmetry plane has the structure (e.g., Nayfeh, 1995)

$$C''_{i,j} = \begin{pmatrix} C''_{1,1} & C''_{1,2} & C''_{1,3} & 0 & C''_{1,5} & 0 \\ & C''_{2,2} & C''_{2,3} & 0 & C''_{2,5} & 0 \\ & & C''_{3,3} & 0 & C''_{3,5} & 0 \\ & & & C''_{4,4} & 0 & C''_{4,6} \\ & \text{sym} & & & C''_{5,5} & 0 \\ & & & & & C''_{6,6} \end{pmatrix}. \tag{2.10}$$

If the symmetry plane changes, the non-zero elements of the stiffness tensor also change. Additional symmetry planes cause more zero elements and further reduce the number of independent stiffness tensor elements.

2.1.3. Orthotropic symmetry

Media possessing three mutually orthogonal planes are referred to as orthorhombic or orthotropic media. Their stiffness tensor contains only nine independent elements and is defined

as (e.g., Nayfeh, 1995)

$$C''_{i,j} = \begin{pmatrix} C''_{1,1} & C''_{1,2} & C''_{1,3} & 0 & 0 & 0 \\ & C''_{2,2} & C''_{2,3} & 0 & 0 & 0 \\ & & C''_{3,3} & 0 & 0 & 0 \\ & & & C''_{4,4} & 0 & 0 \\ & \text{sym} & & & C''_{5,5} & 0 \\ & & & & & C''_{6,6} \end{pmatrix}. \tag{2.11}$$

2.1.4. Transverse isotropic (TI) symmetry

An essential type of anisotropy in borehole acoustics and this thesis is the transverse isotropic (TI) symmetry. Media exhibiting such a symmetry possess one isotropic plane. Within this plane, the wave velocities are direction invariant, and the axis perpendicular to that isotropic plane is referred to as the symmetry axis. All planes containing the symmetry axis are planes of mirror symmetry. A TI medium with a vertical symmetry axis (x''_3–axis) is referred to as vertical transverse isotropy (VTI) medium. The corresponding stiffness tensor contains five independent components, and *Hooke*'s law can be expressed as (e.g., Nayfeh, 1995)

$$\begin{pmatrix} \tau''_{1,1} \\ \tau''_{2,2} \\ \tau''_{3,3} \\ \tau''_{2,3} \\ \tau''_{1,3} \\ \tau''_{1,2} \end{pmatrix} = \begin{pmatrix} C''_{1,1} & C''_{1,1} - 2C''_{6,6} & C''_{1,3} & 0 & 0 & 0 \\ & C''_{1,1} & C''_{1,3} & 0 & 0 & 0 \\ & & C''_{3,3} & 0 & 0 & 0 \\ & & & C''_{4,4} & 0 & 0 \\ & \text{sym} & & & C''_{4,4} & 0 \\ & & & & & C''_{6,6} \end{pmatrix} \begin{pmatrix} \epsilon''_{1,1} \\ \epsilon''_{2,2} \\ \epsilon''_{3,3} \\ 2\epsilon''_{2,3} \\ 2\epsilon''_{1,3} \\ 2\epsilon''_{1,2} \end{pmatrix}. \tag{2.12}$$

In VTI media, the compressional and shear wave velocities of vertically or horizontally propagating plane waves can be derived directly from the stiffness tensor. Figure 2.1 illustrates

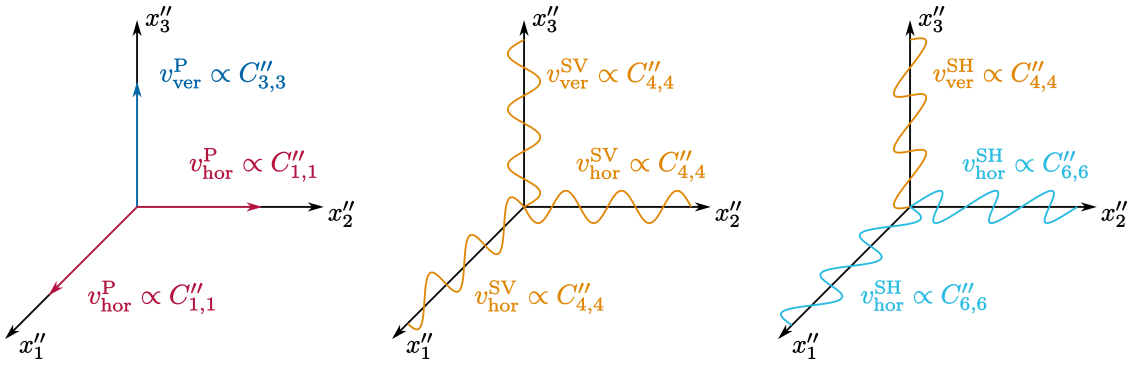

(a) P-waves **(b)** SV-waves **(c)** SH-waves

Fig. 2.1: The figures illustrate the relationship between vertically/horizontally propagating plane waves and the stiffness tensor elements characterizing the TI symmetry. The x''_3–axis is the TI symmetry axis.

the relationship between the wave velocities and the stiffness tensor elements. The P-wave propagating vertically in the VTI formation involves only the stress tensor component $\tau''_{3,3}$, which depends on the strain tensor elements $\epsilon''_{1,1}$, $\epsilon''_{2,2}$ and $\epsilon''_{3,3}$ (Eq. 2.12). Since the vertical P-wave is a pure mode, it exhibits only particle motion parallel to the vertical propagation direction and only the strain tensor element $\epsilon''_{3,3}$ is non-zero. Thus, the stress component $\tau''_{3,3}$ is proportional to $\epsilon''_{3,3}$ via the stiffness tensor element $C''_{3,3}$, defining the vertical P-wave velocity. Analogously, horizontally propagating P-waves in the x''_1 and x''_2 directions depend only on the stress tensor components $\tau''_{1,1}$ and $\tau''_{2,2}$, respectively. Both components are related to the corresponding strain tensor components via the stiffness tensor element $C''_{1,1}$. As a result, the velocities of vertically and horizontally propagating P-waves can be expressed as

$$v^{\mathrm{P}}_{\mathrm{ver}} = \sqrt{\frac{C''_{3,3}}{\rho^{\mathrm{s}}}}, \tag{2.13a}$$

$$v^{\mathrm{P}}_{\mathrm{hor}} = \sqrt{\frac{C''_{1,1}}{\rho^{\mathrm{s}}}}. \tag{2.13b}$$

The vertically and horizontally propagating shear waves can be considered in a similar way (Fig. 2.1b–2.1c). The shear waves propagating in the vertical x''_3–direction are polarized in the x''_1– and x''_2–directions corresponding to the stress tensor components $\tau''_{1,3}$ and $\tau''_{2,3}$, respectively. Both components are related to the corresponding strain tensor components by the stiffness tensor element $C''_{4,4}$ (Eq. 2.12). The same is true for horizontally propagating shear waves polarized in vertical x''_3–direction (SV-waves). Figure 2.1b shows that the same stress tensor components ($\tau''_{1,3}$ and $\tau''_{2,3}$) are involved as for vertically propagating shear waves. In contrast, a horizontally propagating shear wave polarized in the horizontal direction (SH-waves) involves the stress tensor component $\tau''_{1,2}$ (Fig. 2.1c), which is related to the strain tensor component $\epsilon''_{1,2}$ by the stiffness tensor element $C''_{6,6}$. In summary, the velocities of vertically and horizontally propagating SV- and SH-waves can be expressed as

$$v^{\mathrm{S}}_{\mathrm{ver}} = v^{\mathrm{SH}}_{\mathrm{ver}} = v^{\mathrm{SV}}_{\mathrm{ver}} = \sqrt{\frac{C''_{4,4}}{\rho^{\mathrm{s}}}}, \tag{2.13c}$$

$$v^{\mathrm{SH}}_{\mathrm{hor}} = \sqrt{\frac{C''_{6,6}}{\rho^{\mathrm{s}}}}, \qquad v^{\mathrm{SV}}_{\mathrm{hor}} = \sqrt{\frac{C''_{4,4}}{\rho^{\mathrm{s}}}}. \tag{2.13d}$$

The velocity of a vertically propagating shear wave is independent of its polarization direction since it is always polarized into the isotropic plane, and thus the polarization directions of the SV- and SH-wave are arbitrary.

Besides the stiffness tensor, a VTI medium can be characterized by an alternative representation. Thomsen (1986) introduced three dimensionless parameters defined as

$$\epsilon \equiv \frac{C''_{1,1} - C''_{3,3}}{2C''_{3,3}}, \tag{2.14a}$$

$$\gamma \equiv \frac{C''_{6,6} - C''_{4,4}}{2C''_{4,4}}, \tag{2.14b}$$

$$\delta \equiv \frac{\left(C''_{1,3} + C''_{4,4}\right)^2 - \left(C''_{3,3} - C''_{4,4}\right)^2}{2C''_{3,3}\left(C''_{3,3} - C''_{4,4}\right)}. \tag{2.14c}$$

The parameter ϵ describes the difference between the velocities of the horizontally and vertically propagating compressional waves, whereas the parameter γ is defined by the difference of the horizontal and vertical SH-wave velocities. In contrast, the parameter δ is less transparent but controls most anisotropic phenomena of importance in exploration geophysics (Thomsen, 1986). The three parameters, the vertical compressional (Eq. 2.13a), and the vertical shear wave velocities (Eq. 2.13c) describe a VTI medium, such as the stiffness tensor containing five independent elements. The inverse formulas to construct the stiffness tensor from the *Thomsen* notation are defined by

$$C''_{1,1} = \rho^{\mathrm{s}} \left(v^{\mathrm{P}}_{\mathrm{ver}}\right)^2 (2\epsilon + 1), \tag{2.15a}$$

$$C''_{1,3} = \rho^{\mathrm{s}} \left(\sqrt{\left(v^{\mathrm{P}}_{\mathrm{ver}}\right)^4 (2\delta + 1) - 2\left(v^{\mathrm{P}}_{\mathrm{ver}}\right)^2 \left(v^{\mathrm{S}}_{\mathrm{ver}}\right)^2 (\delta + 1) + \left(v^{\mathrm{S}}_{\mathrm{ver}}\right)^4} - \left(v^{\mathrm{S}}_{\mathrm{ver}}\right)^2 \right), \tag{2.15b}$$

$$C''_{3,3} = \rho^{\mathrm{s}} \left(v^{\mathrm{P}}_{\mathrm{ver}}\right)^2, \tag{2.15c}$$

$$C''_{4,4} = \rho^{\mathrm{s}} \left(v^{\mathrm{S}}_{\mathrm{ver}}\right)^2, \tag{2.15d}$$

$$C''_{6,6} = \rho^{\mathrm{s}} \left(v^{\mathrm{S}}_{\mathrm{ver}}\right)^2 (2\gamma + 1). \tag{2.15e}$$

2.1.5. Isotropy

For isotropic media, the three *Thomsen* parameters ϵ, γ, and δ vanish, and the media can be described by only two parameters, the vertical compressional and shear wave velocities. Using *Lamé*'s constants λ and μ, the stiffness tensor can be expressed as (e.g., Nayfeh, 1995)

$$C''_{i,j} = \begin{pmatrix} \lambda + 2\mu & \lambda & \lambda & 0 & 0 & 0 \\ & \lambda + 2\mu & \lambda & 0 & 0 & 0 \\ & & \lambda + 2\mu & 0 & 0 & 0 \\ & & & \mu & 0 & 0 \\ & \mathrm{sym} & & & \mu & 0 \\ & & & & & \mu \end{pmatrix}. \tag{2.16}$$

2.2. Reference frames

In the following of this work, three different reference frames are used, as displayed in figure 2.2. The red reference frame is referred to as the crystallographic reference frame ($\boldsymbol{x}''$), which is defined by the symmetries of the anisotropic medium. The blue reference frame is the borehole reference frame ($\boldsymbol{x}'$), where the x'_3–axis is defined to coincide with the vertical

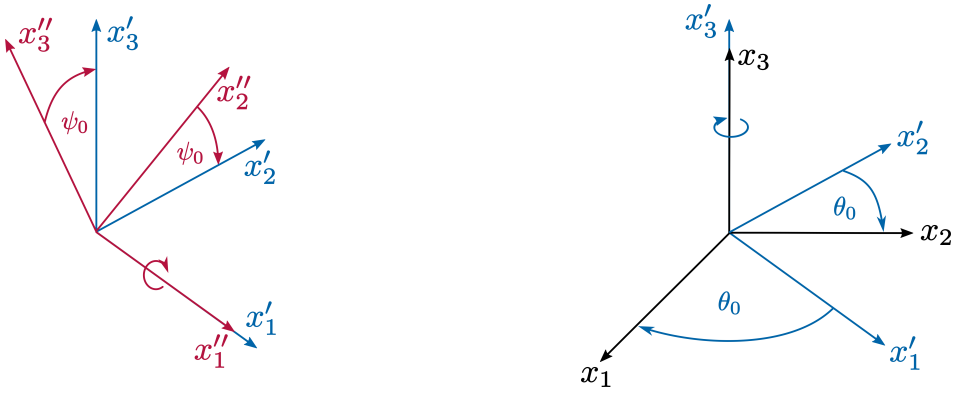

(a) Crystallographic to borehole reference frame

(b) Borehole to tool reference frame

Fig. 2.2: Illustration of the transformations from the crystallographic reference frame $\boldsymbol{x}''$ (red) to the borehole reference frame $\boldsymbol{x}'$ (blue) and the tool reference frame $\boldsymbol{x}$ (black).

borehole axis. Different quantities, e.g., the stiffness tensor elements, can be transformed from the crystallographic reference frame to the borehole reference frame by a rotation around the x_1''–axis over the angle ψ_0. The third reference frame is the tool reference frame ($\boldsymbol{x}$) displayed in figure 2.2b in black. While the vertical axes of the borehole and tool reference frames coincide, they are azimuthally separated from each other by the angle θ_0. Since all equations in the following sections of this chapter are expressed in the tool reference frame, the stiffness tensor must be transformed from the crystallographic reference to the tool reference frame by applying two rotations

$$C_{i,j,k,l} = \mathcal{R}_{i,i'}\mathcal{R}_{j,j'}\mathcal{R}_{k,k'}\mathcal{R}_{l,l'}C''_{i',j',k',l'}. \tag{2.17}$$

The two rotations are mathematically described by one rotation tensor $\mathcal{R}$ given in equation B.9 (App. B.1). Alternatively, the stiffness tensor expressed in *Voigt*'s notation can be directly transformed by the matrix-matrix-multiplications

$$C = RC''R^{\mathrm{T}}, \tag{2.18}$$

where the rotation matrix R is defined in Eq. B.15 (App. B.1), and R^{T} is the transpose of R.

2.3. Seismic wave equations for a linear elastic, anisotropic medium

2.3.1. Basic equations

The dynamic behavior of an anisotropic, heterogeneous, time-invariant, and locally reacting solid can be described in a Cartesian coordinate system by the equation of motion (de Hoop, 1995)

$$\Delta^{+}_{k,m,p,q}\partial_m\tau_{p,q}(\mathbf{x},t) - \rho^{\mathrm{s}}_{k,r}(\mathbf{x})\partial_t v_r(\mathbf{x},t) = 0, \tag{2.19}$$

given in tensor form using subscript notation. The summation is applied over all repeated indices, and k is a free index. The bold variables (e.g., $\boldsymbol{x}$) are vectors. Since the equation of motion is valid in the three-dimensional space, all indices take the values $1, 2$, and 3. Furthermore, ∂_t denotes differentiation with respect to the time coordinate, whereas all other derivatives (e.g., ∂_m) denote differentiation with respect to a spatial coordinate (e.g., x_m). The stress τ and the volumetric mass density of the solid ρ^{s} are tensors of rank two, whereas the particle velocity $\boldsymbol{v}$ is a tensor of rank one equivalent to a vector. The symmetrical unit tensor of rank four is defined as

$$\Delta^{+}_{i,j,p,q} = \frac{1}{2}\left(\delta_{i,p}\delta_{j,q} + \delta_{i,q}\delta_{j,p}\right), \tag{2.20}$$

where the unit tensor $\delta_{i,j}$ of rank two is defined in equation 2.3. The equation of motion given in equation 2.19 is a homogeneous partial differential equation since the right-hand side is zero. Physically, this equation describes a medium without any sources inside. Assuming a given density, the equation of motion contains two unknowns, the stress tensor and the particle velocity. Consequently, this partial differential equation cannot be solved without any relation between both quantities. Such a connection is defined by the constitutive relation (*Hooke*'s law) given by

$$\tau_{p,q}(\mathbf{x}, t) = C_{p,q,i,j}(\mathbf{x})\epsilon_{i,j}(\mathbf{x}, t), \tag{2.21a}$$

or by its inverse form

$$\epsilon_{i,j}(\mathbf{x}, t) = S_{i,j,p,q}(\mathbf{x})\tau_{p,q}(\mathbf{x}, t), \tag{2.21b}$$

describing a linear elastic relation between the stress τ and the strain ϵ. This linear relation is an approximation but reasonable for describing the wave propagation in anisotropic media since deformations are very small. When using a non-linear relation, the partial differential equation becomes non-linear and very complicated to solve. The proportionality factors are the stiffness tensor C and the compliance tensor S, as presented in section 2.1. The strain tensor ϵ of rank two is defined by

$$\epsilon_{i,j}(\mathbf{x}, t) = \frac{1}{2}\left(\partial_i u_j(\mathbf{x}, t) + \partial_j u_i(\mathbf{x}, t)\right), \tag{2.22}$$

where u denotes the particle displacement vector. Differentiation with respect to time yields

$$\partial_t \epsilon_{i,j}(\mathbf{x}, t) = \frac{1}{2}\left(\partial_i v_j(\mathbf{x}, t) + \partial_j v_i(\mathbf{x}, t)\right) = \Delta^{+}_{i,j,n,r}\partial_n v_r(\mathbf{x}, t), \tag{2.23}$$

because the particle velocity vector is defined as the temporal derivative of the particle displacement vector ($v_i = \partial_t u_i$). Substitution of equation 2.23 into the elastic constitutive relations (Eq. 2.21b) after temporal differentiation yields

$$\Delta^{+}_{i,j,n,r}\partial_n v_r(\mathbf{x}, t) - S_{i,j,p,q}(\mathbf{x})\partial_t \tau_{p,q}(\mathbf{x}, t) = 0. \tag{2.24}$$

The equation of motion (Eq. 2.19) and equation 2.24 fully describe the homogeneous first-order differential equations for the dynamic stress τ and the particle velocity v, which can be

written in matrix form as

$$\begin{pmatrix} -\Delta^{+}_{k,m,p,q}\partial_m & \rho^{\mathrm{s}}_{k,r}(\mathbf{x})\partial_t \\ -S_{i,j,p,q}(\mathbf{x})\partial_t & \Delta^{+}_{i,j,n,r}\partial_n \end{pmatrix} \begin{pmatrix} \tau_{p,q} \\ v_r \end{pmatrix} (\mathbf{x}, t) = \mathbf{0}, \tag{2.25}$$

defining a linear equation system of two linear differential equations and two unknowns. This equation system can be solved by applying appropriate integral transforms (van der Hijden, 1987).

2.3.2. Integral transforms

In the first step, an integral transform concerning the time coordinate is applied to equation 2.25. For causality reasons, the one-sided *Laplace* transform is used as defined in Appendix A.1. Accordingly, the time derivatives ∂_t are replaced by multiplication with the possibly complex parameter s representing a temporal frequency

$$\begin{pmatrix} -\Delta^{+}_{k,m,p,q}\partial_m & s\rho^{\mathrm{s}}_{k,r}(\mathbf{x}) \\ -sS_{i,j,p,q}(\mathbf{x}) & \Delta^{+}_{i,j,n,r}\partial_n \end{pmatrix} \begin{pmatrix} \check{\tau}_{p,q} \\ \check{v}_r \end{pmatrix} (\mathbf{x}, s) = \mathbf{0}. \tag{2.26}$$

In the following, it is assumed that the solid is homogeneous, i.e., the compliance tensor S and the volumetric mass density ρ^{s} are invariant in space. Hence, spatial *Fourier* transforms can be applied to equation 2.26. Appendix A.2 explains that the differentiation with respect to a spatial coordinate ∂_p is equivalent to the multiplication with the factor $s\beta_p$ if the radiation condition is fulfilled. The factor is the product of the *Laplace* transform parameter s and the phase slowness vector $\boldsymbol{\beta}$. The resulting linear equation system after applying the *Laplace* transform and spatial *Fourier* transforms is given by

$$\begin{pmatrix} -s\Delta^{+}_{k,m,p,q}\beta_m & s\delta_{k,r}\rho^{\mathrm{s}} \\ -sS_{i,j,p,q} & s\Delta^{+}_{i,j,n,r}\beta_n \end{pmatrix} \begin{pmatrix} \hat{\tau}_{p,q}(\boldsymbol{\beta}, s) \\ \hat{v}_r(\boldsymbol{\beta}, s) \end{pmatrix} = \mathbf{0}. \tag{2.27}$$

Because $s \neq 0$ (App. A.1), equation 2.27 can be divided by s,

$$\begin{pmatrix} -\Delta^{+}_{k,m,p,q}\beta_m & \delta_{k,r}\rho^{\mathrm{s}} \\ -S_{i,j,p,q} & \Delta^{+}_{i,j,n,r}\beta_n \end{pmatrix} \begin{pmatrix} \hat{\tau}_{p,q}(\boldsymbol{\beta}, s) \\ \hat{v}_r(\boldsymbol{\beta}, s) \end{pmatrix} = \mathbf{0}. \tag{2.28}$$

2.3.3. Christoffel equation

After applying the integral transforms, the linear equation system (Eq. 2.28) contains only algebraic expressions (no derivatives) and can be solved by standard algebra methods. A detailed derivation of the solution can be found in Appendix C.1, whereas this section only explains fundamental steps. The second equation (second row of the matrix) of equation 2.28 is rewritten to make it explicit for $\hat{\tau}_{p,q}$.

$$\hat{\tau}_{p,q}(\boldsymbol{\beta}, s) = C_{p,q,n,r}\beta_n\hat{v}_r(\boldsymbol{\beta}, s) \tag{2.29}$$

Substitution of equation 2.29 into the first equation (first row of the matrix) of equation 2.28 yields the so-called *Christoffel* equation

$$\left(\beta_m \bar{C}_{k,m,n,r} \beta_n - \delta_{k,r}\right) \hat{v}_r(\boldsymbol{\beta}, s) = 0, \tag{2.30}$$

where

$$\bar{C}_{k,m,n,r} = \frac{1}{\rho^s} C_{k,m,n,r}. \tag{2.31}$$

The *Christoffel* equation has only trivial solutions, i.e., the particle velocity vector is zero, except for the phase slowness vectors $\boldsymbol{\beta}$, that makes the term $(\beta_m \bar{C}_{k,m,n,r} \beta_n + \delta_{k,r})$ singular. To find these vectors, the phase slowness vector β is first decomposed in its length and direction

$$\beta_m = |\boldsymbol{\beta}|(\boldsymbol{\zeta})\zeta_m. \tag{2.32}$$

Now, the length of the phase slowness vector $|\boldsymbol{\beta}|$ is sought dependent on the unitary propagation vector $\boldsymbol{\zeta}$ defining the propagation direction. Substitution of equation 2.32 into the *Christoffel* equation (Eq. 2.30) yields

$$\left(|\boldsymbol{\beta}|^2 \Lambda_{k,r} - \delta_{k,r}\right) \hat{v}_r(\boldsymbol{\beta}, s) = 0, \tag{2.33}$$

with

$$\Lambda_{k,r} = \zeta_m \bar{C}_{k,m,n,r} \zeta_n. \tag{2.34}$$

The symmetry of the stiffness tensor ($C_{i,j,k,l} = C_{k,l,i,j}$) causes Λ to be symmetric ($\Lambda_{k,r} = \Lambda_{r,k}$). Because all tensors have a maximum rank of two, equation 2.33 can be written in a matrix-vector form

$$\left(|\boldsymbol{\beta}|^2 \Lambda - I\right) \hat{\boldsymbol{v}} = \mathbf{0}, \tag{2.35}$$

equivalent to

$$\left(\Lambda - \kappa I\right) \hat{\boldsymbol{v}} = \mathbf{0}, \tag{2.36}$$

where I denotes the unity matrix and

$$\kappa = \frac{1}{|\boldsymbol{\beta}|^2}. \tag{2.37}$$

Seeking the lengths of the phase slowness vector $|\boldsymbol{\beta}|(\boldsymbol{\zeta})$ is now equivalent to seeking the values $\kappa(\boldsymbol{\zeta})$ that make $\Lambda - \kappa I$ singular dependent on the unitary propagation vector $\boldsymbol{\zeta}$. Equation 2.36 is, by definition, a classical eigenvalue problem, where the eigenvalues are the unknown values κ and the eigenvectors define the direction of the particle velocity vectors $\hat{\boldsymbol{v}}$. Since the matrix Λ is real and symmetric, all eigenvalues are real, and the associated eigenvectors are orthogonal (Nayfeh, 1995). The eigenvalues can be computed analytically by finding the roots of the characteristic polynomial (App. C.1). Because this polynomial is of degree three, there exists three eigenvalues $\kappa^{[l]}$ and three corresponding orthogonal eigenvectors $V^{[l]}$ (l=1,2,3). These eigenvectors are non-trivial solutions of the *Christoffel* equation (Eq. 2.36). Since only their direction is uniquely defined but not their length, they can be multiplied by an arbitrary

coefficient, and therefore an infinite number of non-trivial solutions exist

$$\hat{v}_r^{[l]}(\boldsymbol{\beta}, s) = \begin{cases} \mathcal{T}^{[l]}(\boldsymbol{\beta}, s) V_r^{[l]}(\boldsymbol{\beta}) & \text{for} \quad \boldsymbol{\beta} = |\boldsymbol{\beta}|^{[l]}(\boldsymbol{\zeta})\boldsymbol{\zeta} \\ \mathbf{0} & \text{otherwise} \end{cases}, \qquad l = 1, 2, 3, \tag{2.38}$$

where $|\boldsymbol{\beta}|^{[l]}$ is defined by the inverse of equation 2.37

$$|\boldsymbol{\beta}|^{[l]}(\boldsymbol{\zeta}) = \frac{1}{\pm\sqrt{\kappa^{[l]}(\boldsymbol{\zeta})}}, \qquad l = 1, 2, 3. \tag{2.39}$$

The number of solutions can be reduced by determining the coefficients $\mathcal{T}^{[l]}$ by applying boundary conditions. Since the superposition of the solutions of a linear partial differential equation is another solution, one solution of the *Christoffel* equation for the particle velocity vector can be defined by

$$\hat{v}_r(\boldsymbol{\beta}, s) = \sum_{l=1}^{3} \hat{v}_r^{[l]}(\boldsymbol{\beta}, s). \tag{2.40}$$

The solutions for the particle velocity vector $\hat{v}_r$ can be substituted into equation 2.29 to obtain the solutions for the stress tensor $\hat{\tau}_{p,q}$.

Subsequently, the solutions can be transformed from the spectral and s-domain $(\boldsymbol{\beta}, s)$ back to the spatial and time domain $(\boldsymbol{x}, t)$ by applying inverse integral transforms. The inverse spatial *Fourier* transform converts the solutions from the spectral to the spatial domain. For transforming the solutions from the complex frequency or s-domain back to the time domain, the inverse *Laplace* transform is used. The application of these inverse integral transforms yields harmonic plane waves described by

$$v_r^{[l]}(\boldsymbol{x}, t) = \mathcal{V}_r^{[l]} \exp\left(s|\boldsymbol{\beta}|^{[l]}\zeta_q x_q + st\right). \tag{2.41}$$

Hence, the eigenvalues $\kappa^{[l]}$ of the *Christoffel* equation (Eq. 2.36) correspond to three plane wave solutions. For each plane wave, equation 2.39 yields two phase slowness values with identical absolute values but opposite signs. Hence, two solutions per wavetype are obtained, which propagate in opposite directions. The propagation direction is defined by the unitary propagation vector $\boldsymbol{\zeta}$ that is orthogonal to the plane wavefront. The vector $\boldsymbol{\mathcal{V}}^{[l]}$ contains the polarization direction and the amplitude of the plane waves. While the polarization direction is defined by the eigenvector belonging to the respective eigenvalue, the amplitude can be determined by applying boundary conditions.

In isotropic media, the largest eigenvalue corresponds to the compressional or P-wave. The two remaining eigenvalues, which are equal, correspond to the SV-wave (vertically polarized shear wave) and the SH-wave (horizontally polarized shear wave). The eigenvector corresponding to the P-wave is parallel to the unitary propagation vector $\boldsymbol{\zeta} \times \boldsymbol{v} = \mathbf{0}$, whereas

the other two eigenvectors are perpendicular to the unitary propagation vector $\boldsymbol{\zeta} \cdot \boldsymbol{v} = \mathbf{0}$ (Fig. 2.3a). This is, in general, violated in anisotropic solids. Since all three eigenvalues can be different in anisotropic media, the shear waves can split into two waves propagating with different phase slowness. Moreover, the three eigenvectors defining the three plane wave polarization directions are still mutually orthogonal but are not necessarily parallel or perpendicular to the unitary propagation vector. Consequently, the largest eigenvalue corresponds to the quasi-P-wave (qP-wave), and the two remaining eigenvalues correspond to the quasi-SH-wave (qSH-wave) and the quasi-SV-wave (qSV-wave). The prefix quasi means that the qP-wave is, in general, not a pure compressional wave because there is some particle motion transverse to the propagation direction. Vice versa, the qSV-wave contains particle motion parallel to the propagation direction. In transverse isotropic (TI) solids, the SH-wave is always a pure shear wave with particle motion perpendicular to the propagation direction and orthogonal to the qP- and qSV-wave (Fig. 2.3b). In triclinic media, the SH-wave is not necessarily perpendicular to the propagation direction (Fig. 2.3c) and thus becomes a quasi-SH-wave exhibiting particle motion parallel to the propagation direction.

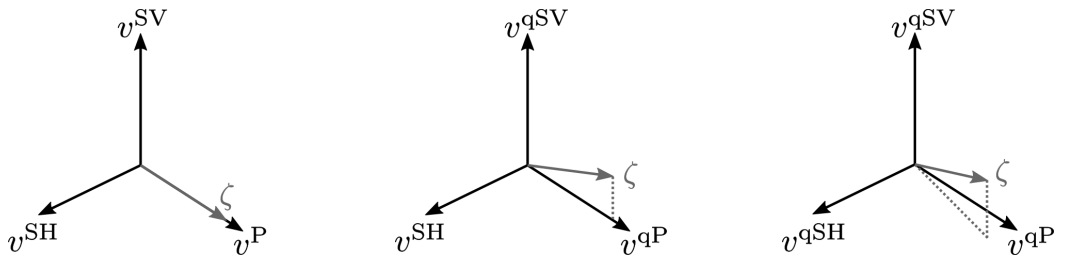

(a) Isotropic **(b)** Transverse isotropic **(c)** Triclinic

Fig. 2.3: Polarization vectors of the three plane wave modes propagating in the direction defined by $\boldsymbol{\zeta}$ in isotropic (a), TI (b), or triclinic (c) media.

There may exist directions for which the waves are pure modes, but these directions depend on the elastic properties of the anisotropic solid and the type of symmetry. If the qP-wave polarization vector is parallel to the unitary propagation vector ($\boldsymbol{\zeta} \times \boldsymbol{v} = \mathbf{0}$), both remaining polarization vectors necessarily satisfy $\boldsymbol{\zeta} \cdot \boldsymbol{v} = \mathbf{0}$ (Nayfeh, 1995). Consequently, all three waves are pure waves. On the other hand, if one polarization vector is perpendicular to the unitary propagation vector ($\boldsymbol{\zeta} \cdot \boldsymbol{v} = \mathbf{0}$), the other polarization vectors do not necessarily satisfy any condition. Therefore, only one wave may be pure, e.g., the SH-wave in TI solids.

2.3.4. Phase slowness surfaces

Once the eigenvalues are computed, the phase slowness values can be calculated in dependence with the propagation direction via

$$|\boldsymbol{\beta}^{\odot}|(\boldsymbol{\zeta}) = \frac{1}{+\sqrt{\kappa^{\odot}(\boldsymbol{\zeta})}} \qquad \odot = \{\mathrm{qP}, \mathrm{qSV}, \mathrm{qSH}\}. \tag{2.42}$$

The phase slowness surfaces can be constructed for all three wave modes by plotting the computed positive slowness values of each mode for all possible propagation directions. For

isotropic media, these phase slowness surfaces are spheres. One sphere corresponds to the P-wave, and two identical spheres correspond to the SV- and SH-waves. In anisotropic solids, the three phase slowness surfaces are arbitrarily shaped and can strongly deviate from spheres (Fig. 2.4) depending on the type of anisotropy. One problem constructing such phase slowness surfaces is assigning the computed eigenvalues to the correct wave modes. While the lowest phase slowness value always corresponds to the qP-wave, it is not trivial to assign the remaining phase slowness values to the qSV- and qSH-wave consistently for all propagation directions. For transverse isotropic solids, the eigenvectors that correspond to the respective eigenvalues can be used for the assignment. Since the SH-wave polarization direction is always perpendicular to the unitary propagation vector $\boldsymbol{\zeta}$ in such solids, the following relation can be used

$$|\boldsymbol{\zeta} \cdot \boldsymbol{v}^{\mathrm{SH}}| \leq |\boldsymbol{\zeta} \cdot \boldsymbol{v}^{\mathrm{qSV}}|. \tag{2.43}$$

A problem occurs only if the dot product of the left- and the right-hand side is equal (both are zero). This is always the case if the eigenvalues corresponding to the shear waves coincide. In that case, the eigenvectors are not uniquely defined and can be aligned arbitrarily perpendicular to the qP-wave polarization vector, which is parallel to the propagation direction vector. Tsvankin (2012) called this phenomenon shear wave singularity. He distinguished between "kiss" singularities and "intersection" singularities. In figure 2.4c, a slice of the three phase slowness surfaces for the Austin Chalk TI formation is displayed, and it can be seen that both types of singularities occur for this type of formation. At the angles $\psi_0 = 0°$ or $\psi_0 = 180°$, there are "kiss" singularities, where the phase slowness surfaces of the shear waves touch each other tangentially. Additionally, the phase slowness surfaces of the SH- and qSV-waves intersect, e.g., at about $\psi_0 = 43.5°$, which creates an "intersection" singularity. While anisotropic solids with transverse isotropic symmetry always possess a "kiss" singularity when the propagation direction is parallel to the symmetry axis, an "intersection" singularity does not necessarily exist. One example of such a TI solid is the Cotton Valley Shale formation, for which the phase slowness surfaces are displayed in figure 2.5. It can be seen that the qSV-wave is slower than the SH-wave for all propagation directions except at $\psi_0 = 30°$, where

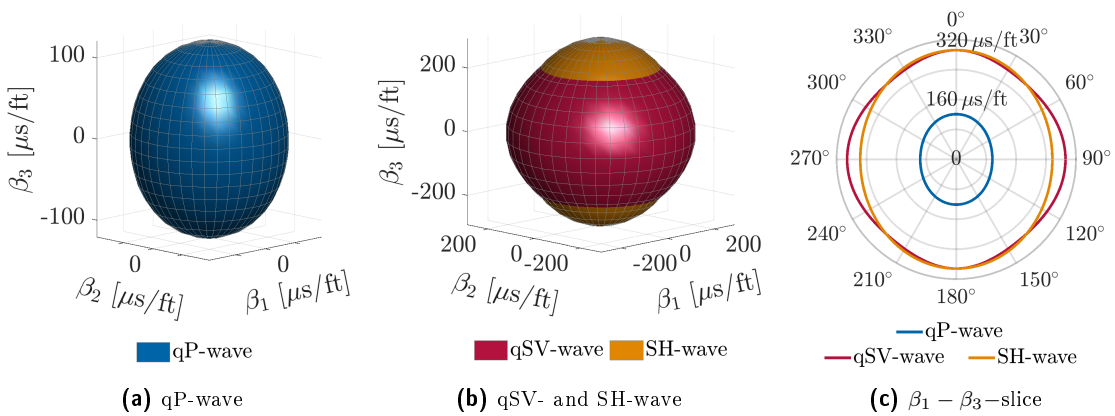

(a) qP-wave **(b)** qSV- and SH-wave **(c)** $\beta_1 - \beta_3$−slice

Fig. 2.4: Phase slowness surfaces of the plane wave modes in the slow Austin Chalk TI formation (Tab. 3.1) exhibiting a vertical symmetry axis (VTI).

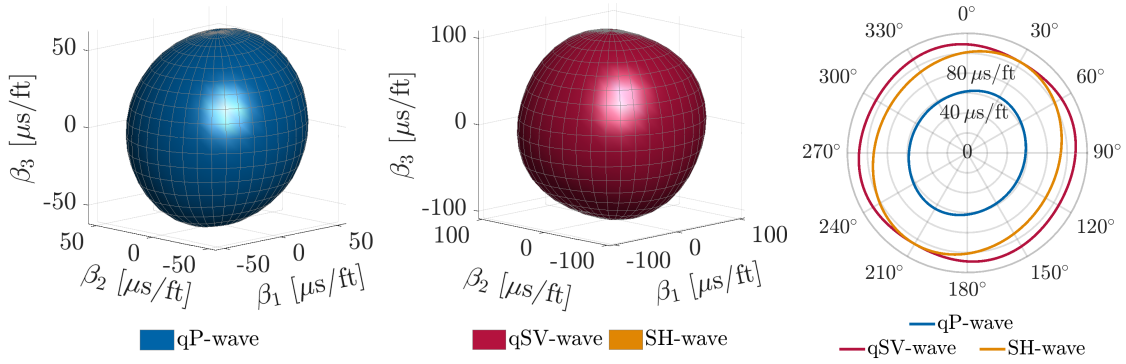

(a) qP-wave **(b)** qSV- and SH-wave **(c)** β_1–β_3–slice

Fig. 2.5: Phase slowness surfaces of the plane wave modes in the fast Cotton Valley Shale TI formation (Tab. 3.1), which symmetry axis is inclined by $\psi_0 = 30°$ to the vertical axis (TTI).

the phase slowness surfaces of both wave modes touch each other. This angle corresponds to the TI symmetry axis. In borehole acoustics, a "kiss" singularity always occurs if the TI symmetry axis is parallel to the borehole axis (VTI). On the other hand, if the TI symmetry axis is perpendicular to the borehole axis (HTI), no singularity exists. Besides, isotropic media possess "kiss" singularities for all propagation directions since both shear wave slowness values are identical.

2.3.5. Group velocity

While the phase slowness vector or its inverse, the phase velocity vector, defines the speed and the direction of a single plane wave harmonic at a given frequency, the group slowness vector or its inverse, the group velocity vector, determines the direction and the velocity of energy propagation and in fact the seismic ray. In anisotropic media, the phase slowness vector deviates from the group slowness vector, in general. Figure 2.6a shows that in a homogeneous, anisotropic medium, the group velocity vector $\boldsymbol{v}^{\mathrm{G}}$ is parallel to the vector between the source and an observation point (receiver). In contrast, the phase velocity vector or phase slowness vector $\boldsymbol{\beta}$ is normal to the wavefront. Consequently, the phase velocity vector, in general, deviates from the group velocity vector in anisotropic media since the wavefronts

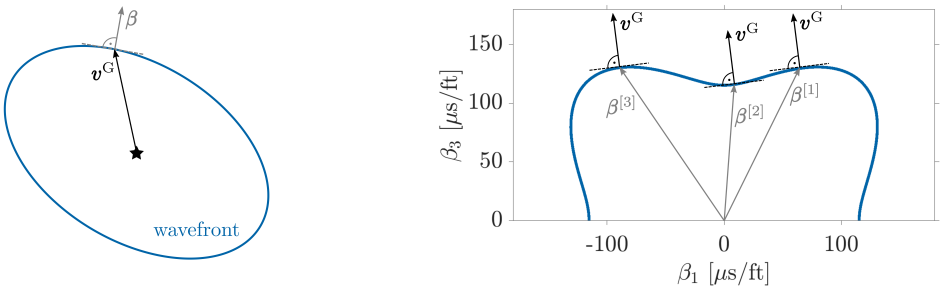

(a) Wavefront **(b)** Phase slowness surface (x–z–slice)

Fig. 2.6: Relationship between the phase slowness vector ($\boldsymbol{\beta}$) and group velocity vector ($\boldsymbol{v}_G$). While the phase slowness vector is normal to the wavefront (a), the group velocity vector is normal to the phase slowness surface (b) (the wavefront displayed in (a) does not correspond to the phase slowness surface in (b)).

are arbitrarily shaped. On the other hand, for homogeneous, non-dispersive isotropic media, both velocity vectors always coincide because the wavefronts are spheres. Besides anisotropy, velocity variations with frequency (velocity dispersion) can also cause deviations between the phase and the group velocity vector.

The group velocity vector depends on the function of the phase slowness ($\beta^{\odot} = |\boldsymbol{\beta}^{\odot}|$) in relation to the propagation direction and can be defined in the most general form by (e.g., Nayfeh, 1995)

$$v_n^{\mathrm{G};\odot} = \frac{\partial}{\partial \zeta_n}\left(\frac{1}{|\boldsymbol{\beta}^{\odot}|(\boldsymbol{\zeta})}\right), \qquad \odot = \{\mathrm{qP}, \mathrm{qSV}, \mathrm{qSH}\}. \tag{2.44}$$

An alternative expression can be found by substituting the solutions into the *Christoffel* equation (Eq. 2.30) and using $V_k^{\odot} V_k^{\odot} = 1$

$$-\bar{C}_{k,m,n,r}\zeta_m\zeta_n V_r^{\odot} V_k^{\odot} = \frac{1}{|\boldsymbol{\beta}^{\odot}|^2}. \tag{2.45}$$

Differentiation of equation 2.45 yields another expression for the group velocity (Nayfeh, 1995)

$$v_n^{\mathrm{G};\odot} = -|\boldsymbol{\beta}^{\odot}|\bar{C}_{k,m,n,r} V_r^{\odot} V_k^{\odot} \zeta_m. \tag{2.46}$$

Furthermore, Nayfeh (1995) has proven that the group velocity vector is always orthogonal to the phase slowness surfaces. Since these surfaces can become concave for anisotropic media, the direction of the group velocity vector may be identical for three different phase slowness directions, as displayed in figure 2.6b. Consequently, concave parts of the slowness surface generate triplications on the shear wavefronts referred to as cusps in some literature, e.g., Nayfeh (1995). Figure 2.7 presents an x–z–slice of the phase slowness surfaces (Fig. 2.7a) and the corresponding group velocity surfaces (Fig. 2.7b) of all three plane wave modes in a cubic

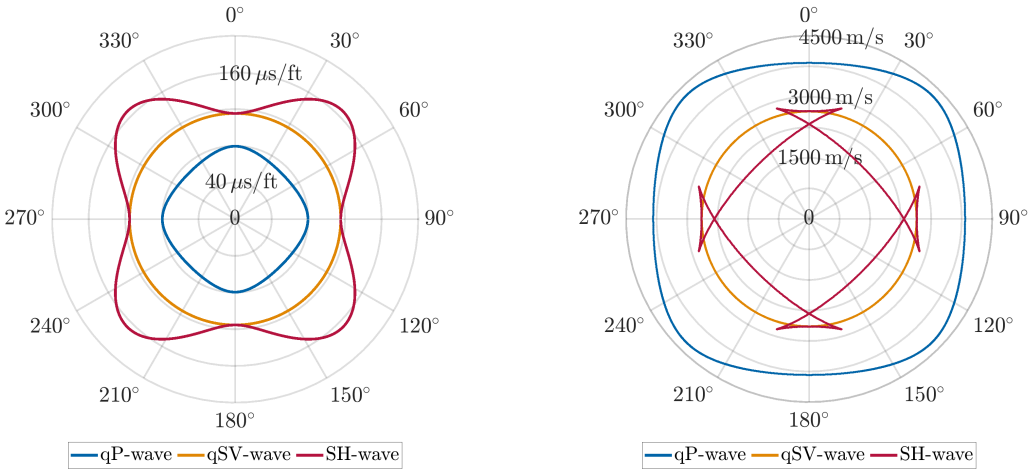

(a) Phase slowness surface **(b)** Group velocity surface

Fig. 2.7: Phase slowness (a) and group velocity (b) surfaces (x–y–slice) of the plane wave modes in a cubic indium arsenide crystal (InAs).

indium arsenide crystal (Nayfeh, 1995). The phase slowness surface of the qSV-wave possesses some concave parts corresponding to the triplications or cusps in the group velocity surface. Hence, for those phase slowness directions, three group velocities exist at which the energy can propagate, yielding self-intersecting wavefronts. In contrast, the qP- and SH-wave phase slowness surfaces have no concave parts, so there are no cusps. The qP-wave can never have cusps because its phase slowness surface is always convex (Tsvankin, 2012). Furthermore, the phase slowness surfaces corresponding to the anisotropic TI formations considered in this thesis are always convex, and thus, the cusps need no further investigation. Nevertheless, Brodov et al. (1993) have shown that cusps may occur for some clays exhibiting TI symmetry.

2.4. Solution in cylindrical coordinates for the borehole geometry

Since a borehole has cylindrical symmetry, it is advantageous to use cylindrical coordinates (r, θ, z) instead of Cartesian coordinates (x_1, x_2, x_3), defined by

$$x_1 = r\cos\theta, \tag{2.47a}$$

$$x_2 = r\sin\theta, \tag{2.47b}$$

$$x_3 = z. \tag{2.47c}$$

All quantities must be transformed from Cartesian to cylindrical coordinates using the transformation tensor $\mathcal{R}^{x_3}(\theta)$, describing a clockwise rotation over the angle θ around the x_3–axis

$$\mathcal{R}^{x_3}_{i,j}(\theta) = \begin{pmatrix} \cos\theta & \sin\theta & 0 \\ -\sin\theta & \cos\theta & 0 \\ 0 & 0 & 1 \end{pmatrix}. \tag{2.48}$$

While the particle velocity is transformed from Cartesian to cylindrical coordinates by

$$\check{v}_{r'}(r, \theta, z, s) = \mathcal{R}^{x_3}_{r',r}(\theta)\check{v}_r(x_1, x_2, x_3, s), \tag{2.49}$$

the second-order stress tensor is transformed via

$$\check{\tau}_{i',j'}(r, \theta, z, s) = \mathcal{R}^{x_3}_{i',i}(\theta)\mathcal{R}^{x_3}_{j',j}(\theta)\check{\tau}_{i,j}(x_1, x_2, x_3, s). \tag{2.50}$$

The constant density ρ^{s} of the formation is independent of the coordinate system because only homogeneous media are considered. In contrast, the stiffness tensor $C_{i,j,k,l}$ is constant in Cartesian coordinates but depends on the azimuth θ in cylindrical coordinates. Since *Hooke*'s law applies in all coordinate systems, it can be defined in cylindrical coordinates by

$$\check{\tau}_{i',j'}(r, \theta, z, s) = \tilde{C}_{i',j',k',l'}(\theta)\check{\epsilon}_{k',l'}(r, \theta, z, s), \tag{2.51}$$

where $\tilde{C}_{i',j',k',l'}$ designates the stiffness tensor in cylindrical coordinates defined by

$$\tilde{C}_{i',j',k',l'}(\theta) = \mathcal{R}^{x_3}_{i',i}(\theta)\mathcal{R}^{x_3}_{j',j}(\theta)\mathcal{R}^{x_3}_{k',k}(\theta)\mathcal{R}^{x_3}_{l',l}(\theta)C_{i,j,k,l}. \tag{2.52}$$

The expanded form of the stiffness tensor in cylindrical coordinates is given in Appendix B.2.

Furthermore, the *Laplace* transforms of the partial differential equations (Eq. 2.26) have to be transformed from Cartesian to cylindrical coordinates. The transformed first equation in the matrix-vector notation is defined by

$$-\begin{pmatrix} \partial_r + \frac{1}{r} & -\frac{1}{r} & 0 & 0 & \partial_z & \frac{1}{r}\partial_\theta \\ 0 & \frac{1}{r}\partial_\theta & 0 & \partial_z & 0 & \partial_r + \frac{2}{r} \\ 0 & 0 & \partial_z & \frac{1}{r}\partial_\theta & \partial_r + \frac{1}{r} & 0 \end{pmatrix} \begin{pmatrix} \check{\tau}_{r,r} \\ \check{\tau}_{\theta,\theta} \\ \check{\tau}_{z,z} \\ \check{\tau}_{\theta,z} \\ \check{\tau}_{r,z} \\ \check{\tau}_{r,\theta} \end{pmatrix} + \rho^{\mathrm{s}} s \begin{pmatrix} \check{v}_r \\ \check{v}_\theta \\ \check{v}_z \end{pmatrix} = \mathbf{0}, \tag{2.53}$$

and the second one by

$$s \begin{pmatrix} \check{\tau}_{r,r} \\ \check{\tau}_{\theta,\theta} \\ \check{\tau}_{z,z} \\ \check{\tau}_{\theta,z} \\ \check{\tau}_{r,z} \\ \check{\tau}_{r,\theta} \end{pmatrix} = \begin{pmatrix} \tilde{C}_{1,1} & \tilde{C}_{1,2} & \tilde{C}_{1,3} & \tilde{C}_{1,4} & \tilde{C}_{1,5} & \tilde{C}_{1,6} \\ \tilde{C}_{1,2} & \tilde{C}_{2,2} & \tilde{C}_{2,3} & \tilde{C}_{2,4} & \tilde{C}_{2,5} & \tilde{C}_{2,6} \\ \tilde{C}_{1,3} & \tilde{C}_{2,3} & \tilde{C}_{3,3} & \tilde{C}_{3,4} & \tilde{C}_{3,5} & \tilde{C}_{3,6} \\ \tilde{C}_{1,4} & \tilde{C}_{2,4} & \tilde{C}_{3,4} & \tilde{C}_{4,4} & \tilde{C}_{4,5} & \tilde{C}_{4,6} \\ \tilde{C}_{1,5} & \tilde{C}_{2,5} & \tilde{C}_{3,5} & \tilde{C}_{4,5} & \tilde{C}_{5,5} & \tilde{C}_{5,6} \\ \tilde{C}_{1,6} & \tilde{C}_{2,6} & \tilde{C}_{3,6} & \tilde{C}_{4,6} & \tilde{C}_{5,6} & \tilde{C}_{6,6} \end{pmatrix} \begin{pmatrix} \partial_r & 0 & 0 \\ \frac{1}{r} & \frac{1}{r}\partial_\theta & 0 \\ 0 & 0 & \partial_z \\ 0 & \partial_z & \frac{1}{r}\partial_\theta \\ \partial_z & 0 & \partial_r \\ \frac{1}{r}\partial_\theta & \partial_r - \frac{1}{r} & 0 \end{pmatrix} \begin{pmatrix} \check{v}_r \\ \check{v}_\theta \\ \check{v}_z \end{pmatrix}. \tag{2.54}$$

The subscripts r, θ, and z denote the components of the stress tensor and the particle velocity vector. The substitution of the second equation into the first one yields the *Christoffel* equation in cylindrical coordinates, expressed as

$$\left[\begin{pmatrix} \partial_r + \frac{1}{r} & -\frac{1}{r} & 0 & 0 & \partial_z & \frac{1}{r}\partial_\theta \\ 0 & \frac{1}{r}\partial_\theta & 0 & \partial_z & 0 & \partial_r + \frac{2}{r} \\ 0 & 0 & \partial_z & \frac{1}{r}\partial_\theta & \partial_r + \frac{1}{r} & 0 \end{pmatrix} \tilde{C} \begin{pmatrix} \partial_r & 0 & 0 \\ \frac{1}{r} & \frac{1}{r}\partial_\theta & 0 \\ 0 & 0 & \partial_z \\ 0 & \partial_z & \frac{1}{r}\partial_\theta \\ \partial_z & 0 & \partial_r \\ \frac{1}{r}\partial_\theta & \partial_r - \frac{1}{r} & 0 \end{pmatrix} - \rho^{\mathrm{s}} s^2 I \right] \begin{pmatrix} \check{v}_r \\ \check{v}_\theta \\ \check{v}_z \end{pmatrix} = \mathbf{0}, \tag{2.55}$$

where $\check{\boldsymbol{v}} = \check{\boldsymbol{v}}(r, \theta, z, s)$ denotes the *Laplace* transform of the particle velocity vector in cylin-

drical coordinates. The stiffness tensor $\tilde{C} = \tilde{C}(\theta)$ is still symmetric in cylindrical coordinates (App. B.2) but depends on the azimuth θ, which has to be noted for azimuthal differentiation. The expanded expressions of the *Christoffel* equation are given in Appendix C.2.

2.4.1. Special case: vertical transverse isotropy (VTI)

A VTI medium, where the symmetry axis is parallel to the vertical borehole axis (z-direction), can be described by only five independent components of the stiffness tensor (Sec. 2.1). Furthermore, the stiffness tensor is azimuthally invariant, and the *Christoffel* equation in cylindrical coordinates becomes simpler (App. C.2). The particle velocity can be expressed by three scalar potentials, given by (e.g., Tang and Cheng, 2004)

$$\check{\boldsymbol{v}}(r,\theta,z,s) = \nabla\check{\Phi} + \nabla\times\left(\check{\Psi}^{\mathrm{SH}}\boldsymbol{e}_z\right) + \nabla\times\nabla\times\left(\check{\Psi}^{\mathrm{qSV}}\boldsymbol{e}_z\right). \tag{2.56}$$

Applying the del operator ∇ in cylindrical coordinates yields

$$\nabla\check{\Phi} = \left(\partial_r\check{\Phi}, \frac{1}{r}\partial_\theta\check{\Phi}, \partial_z\check{\Phi}\right)^{\mathrm{T}}, \tag{2.57a}$$

$$\nabla\times\left(\check{\Psi}^{\mathrm{SH}}\boldsymbol{e}_z\right) = \left(\frac{1}{r}\partial_\theta\check{\Psi}^{\mathrm{SH}}, -\partial\check{\Psi}^{\mathrm{SH}}, 0\right)^{\mathrm{T}}, \tag{2.57b}$$

$$\nabla\times\nabla\times\left(\check{\Psi}^{\mathrm{qSV}}\boldsymbol{e}_z\right) = \left(\partial_r\partial_z\check{\Psi}^{\mathrm{qSV}}, \frac{1}{r}\partial_\theta\partial_z\check{\Psi}^{\mathrm{qSV}}, -\left(\nabla^2-\partial_z^2\right)\check{\Psi}^{\mathrm{qSV}}\right)^{\mathrm{T}}, \tag{2.57c}$$

while the *Laplace* operator in cylindrical coordinates is defined as

$$\nabla^2 = \partial_r^2 + \frac{1}{r}\partial_r + \frac{1}{r^2}\partial_\theta^2 + \partial_z^2. \tag{2.58}$$

Consequently, the particle velocity vector can be expressed as

$$\begin{pmatrix}\check{v}_r\\ \check{v}_\theta\\ \check{v}_z\end{pmatrix}(r,\theta,z,s) = \begin{pmatrix}\partial_r & \frac{1}{r}\partial_\theta & \partial_r\partial_z\\ \frac{1}{r}\partial_\theta & -\partial_r & \frac{1}{r}\partial_\theta\partial_z\\ \partial_z & 0 & -\left(\nabla^2-\partial_z^2\right)\end{pmatrix}\begin{pmatrix}\check{\Phi}\\ \check{\Psi}^{\mathrm{SH}}\\ \check{\Psi}^{\mathrm{qSV}}\end{pmatrix}(r,\theta,z,s). \tag{2.59}$$

Substituting equation 2.59 into the *Christoffel* equation (Eq. 2.55) yields three partial differential equations

$$\begin{aligned}&\partial_r\left[C_{1,1}\nabla^2 + \left(C_{1,3}+2C_{4,4}-C_{1,1}\right)\partial_z^2 - \rho^{\mathrm{s}}s^2\right]\check{\Phi}\\ &+\frac{1}{r}\partial_\theta\left[C_{6,6}\nabla^2 + \left(C_{4,4}-C_{6,6}\right)\partial_z^2 - \rho^{\mathrm{s}}s^2\right]\check{\Psi}^{\mathrm{SH}}\\ +\partial_r\partial_z&\left[\left(C_{1,1}-C_{1,3}-C_{4,4}\right)\nabla^2 + \left(C_{1,3}+2C_{4,4}-C_{1,1}\right)\partial_z^2 - \rho^{\mathrm{s}}s^2\right]\check{\Psi}^{\mathrm{qSV}} = 0,\end{aligned} \tag{2.60a}$$

$$\begin{aligned}
&\frac{1}{r}\partial_\theta \left[C_{1,1}\nabla^2 + (C_{1,3} + 2C_{4,4} - C_{1,1})\,\partial_z^2 - \rho^{\mathrm{s}} s^2\right]\check{\Phi} \\
&\qquad -\partial_r \left[C_{6,6}\nabla^2 + (C_{4,4} - C_{6,6})\,\partial_z^2 - \rho^{\mathrm{s}} s^2\right]\check{\Psi}^{\mathrm{SH}} \\
&+\frac{1}{r}\partial_\theta\partial_z \left[(C_{1,1} - C_{1,3} - C_{4,4})\,\nabla^2 + (C_{1,3} + 2C_{4,4} - C_{1,1})\,\partial_z^2 - \rho^{\mathrm{s}} s^2\right]\check{\Psi}^{\mathrm{qSV}} = 0, \qquad (2.60\mathrm{b})
\end{aligned}$$

$$\begin{aligned}
&\partial_z \left[(C_{1,3} + 2C_{4,4})\,\nabla^2 + (C_{3,3} - C_{1,3} - 2C_{4,4})\,\partial_z^2 - \rho^{\mathrm{s}} s^2\right]\check{\Phi} \\
&-\left(\nabla^2 - \partial_z^2\right)\left[C_{4,4}\nabla^2 + (C_{3,3} - 2C_{4,4} - C_{1,3})\,\partial_z^2 - \rho^{\mathrm{s}} s^2\right]\check{\Psi}^{\mathrm{qSV}} = 0. \qquad (2.60\mathrm{c})
\end{aligned}$$

These partial differential equations can be manipulated by computing the divergence of equations 2.60a–2.60c and subsequential subtraction of equation 2.60c to obtain equation 2.61a. Moreover, applying the curl operator to equations 2.60a–2.60c yields equation 2.61b. Both manipulated equations and equation 2.60c yield the following system of partial differential equations to be solved

$$\begin{aligned}
&\left[C_{1,1}\nabla^2 + (C_{1,3} + 2C_{4,4} - C_{1,1})\,\partial_z^2 - \rho^{\mathrm{s}} s^2\right]\check{\Phi} \\
&+\partial_z \left[(C_{1,1} - C_{1,3} - C_{4,4})\,\nabla^2 + (C_{1,3} + 2C_{4,4} - C_{1,1})\,\partial_z^2 - \rho^{\mathrm{s}} s^2\right]\check{\Psi}^{\mathrm{qSV}} = 0, \qquad (2.61\mathrm{a})
\end{aligned}$$

$$\begin{aligned}
&\partial_z \left[(C_{1,3} + 2C_{4,4})\,\nabla^2 + (C_{3,3} - 2C_{4,4} - C_{1,3})\,\partial_z^2 - \rho^{\mathrm{s}} s^2\right]\check{\Phi} \\
&-\left(\nabla^2 - \partial_z^2\right)\left[C_{4,4}\nabla^2 + (C_{3,3} - 2C_{4,4} - C_{1,3})\,\partial_z^2 - \rho^{\mathrm{s}} s^2\right]\check{\Psi}^{\mathrm{qSV}} = 0, \qquad (2.61\mathrm{b})
\end{aligned}$$

$$\left[C_{6,6}\nabla^2 + (C_{4,4} - C_{6,6})\,\partial_z^2 - \rho^{\mathrm{s}} s^2\right]\check{\Psi}^{\mathrm{SH}} = 0. \qquad (2.61\mathrm{c})$$

The first two equations are coupled partial differential equations, whereas the third equation is decoupled, describing the pure SH-wave.

The latter can be solved by applying a spatial *Fourier* transform concerning the vertical z–coordinate (App. A.2) and an azimuthal *Fourier* transform concerning the θ–coordinate (App. A.3). Hence, the partial derivatives ∂_z are replaced by the scalar factor $s\beta_z$ and the derivatives ∂_θ by the factor $\mathrm{i}m$. While β_z denotes the vertical phase slowness, m represents the azimuthal wavenumber. Accordingly, equation 2.61c can be transformed and rearranged to

$$\left[r^2\partial_r^2 + r\partial_r + r^2 s^2\beta_r^2 - m^2\right]\tilde{\Psi}^{\mathrm{SH}}(r, m, \beta_z, s) = 0, \qquad (2.62)$$

where the radial phase slowness is defined by

$$\beta_r = \beta_r^{\mathrm{SH}} = \pm\sqrt{\frac{C_{4,4}\beta_z^2 - \rho^{\mathrm{s}}}{C_{6,6}}}. \qquad (2.63)$$

The substitution $u = rs\beta_r$ ($\partial_u = \partial_r/(s\beta_r)$) can be applied to obtain *Bessel*'s differential equation

$$\left[u^2\partial_u^2 + u\partial_u + \left(u^2 - m^2\right)\right]\tilde{\Psi}^{\mathrm{SH}} = 0. \tag{2.64}$$

The solutions of this differential equation are the modified *Bessel* functions $I_m(u)$ and $K_m(u)$ (e.g., Gradshteyn and Ryzhik, 2007). The first is ascending with increasing argument u, and the latter is descending with increasing argument u. To fulfill the radiation condition, i.e., the potential $\check{\Psi}^{\mathrm{SH}}$ shall vanish when $r \to \infty$, the modified *Bessel* function $K_m(u)$ is chosen as the solution. Applying the inverse spatial *Fourier* transform with respect to the vertical coordinate and the inverse azimuthal *Fourier* transform concerning the azimuth yields the solution

$$\check{\Psi}^{\mathrm{SH}}(r,\theta,z,s) = \mathcal{T}^{\mathrm{SH}}(s)K_m(rs\beta_r^{\mathrm{SH}})\exp\left(\mathrm{i}m\theta\right)\exp\left(s\beta_z z\right). \tag{2.65}$$

The transmission coefficient $\mathcal{T}^{\mathrm{SH}}$ defines the amplitude and has to be determined by applying boundary conditions.

The remaining two partial differential equations (Eq. 2.61a–2.61b) describing the qP- and qSV-wave cannot be solved in the same way because of their coupling. Therefore, an ansatz is chosen that the solutions have the same form as the SH-wave potential

$$\check{\Phi}(r,\theta,z,s) \propto \mathcal{T}^{\mathrm{qP}}(s)K_m(rs\beta_r)\exp\left(\mathrm{i}m\theta\right)\exp\left(s\beta_z z\right), \tag{2.66}$$

$$\check{\Psi}^{\mathrm{qSV}}(r,\theta,z,s) \propto \mathcal{T}^{\mathrm{qSV}}(s)K_m(rs\beta_r)\exp\left(\mathrm{i}m\theta\right)\exp\left(s\beta_z z\right). \tag{2.67}$$

Both equations are substituted into the coupled partial differential equations (Eq. 2.61a–2.61b) to obtain the linear equation system

$$s^2\begin{pmatrix}\mathcal{A}_{1,1} & \mathcal{A}_{1,2}\\ \mathcal{A}_{2,1} & \mathcal{A}_{2,2}\end{pmatrix}\begin{pmatrix}\check{\Phi}\\ \check{\Psi}^{\mathrm{qSV}}\end{pmatrix} = \mathbf{0}, \tag{2.68a}$$

with the matrix elements

$$\mathcal{A}_{1,1} = \beta_r^2 C_{1,1} + (C_{1,3} + 2C_{4,4})\beta_z^2 - \rho^{\mathrm{s}}, \tag{2.68b}$$

$$\mathcal{A}_{1,2} = s\beta_z\left(\beta_r^2\left(C_{1,1} - C_{1,3} - C_{4,4}\right) + C_{4,4}\beta_z^2 - \rho^{\mathrm{s}}\right), \tag{2.68c}$$

$$\mathcal{A}_{2,1} = s\beta_z\left(\beta_r^2\left(C_{1,3} + 2C_{4,4}\right) + C_{3,3}\beta_z^2 - \rho^{\mathrm{s}}\right), \tag{2.68d}$$

$$\mathcal{A}_{2,2} = -s^2\beta_r^2\left(\beta_r^2 C_{4,4} + \left(C_{3,3} - C_{4,4} - C_{1,3}\right)\beta_z^2 - \rho^{\mathrm{s}}\right). \tag{2.68e}$$

The determinant of the matrix must vanish to compute non-trivial solutions. This is equivalent to finding the roots of the characteristic polynomial, which can be expressed after polynomial division in the form

$$s^2\left(\beta_r^2 + \beta_z^2\right)\left(a_1\beta_r^4 + a_2\beta_r^2 + a_3\right) = 0, \tag{2.69a}$$

with

$$a_1 = C_{1,1}C_{4,4}, \tag{2.69b}$$

$$a_2 = \left(C_{1,1}C_{3,3} - C_{1,3}^2 - 2C_{1,3}C_{4,4}\right)\beta_z^2 - \left(C_{1,1} + C_{4,4}\right)\rho^{\mathrm{s}}, \tag{2.69c}$$

$$a_3 = C_{3,3}C_{4,4}\beta_z^4 - \left(C_{3,3} + C_{4,4}\right)\rho^{\mathrm{s}}\beta_z^2 + \left(\rho^{\mathrm{s}}\right)^2. \tag{2.69d}$$

The characteristic polynomial has the roots $s = 0$ and $\beta_r = \pm \mathrm{i}\beta_z$, which do not correspond to a wave motion and are ignored (Tang and Cheng, 2004). Additionally, the polynomial given in the second parenthesis possesses two roots for β_r^2, which indeed correspond to the wave motion of the qP-wave

$$\beta_r = \beta_r^{\mathrm{qP}} = \pm\sqrt{\frac{-a_2 + \sqrt{a_2^2 - 4a_1a_3}}{2a_1}}, \tag{2.70}$$

and the qSV-wave

$$\beta_r = \beta_r^{\mathrm{qSV}} = \pm\sqrt{\frac{-a_2 - \sqrt{a_2^2 - 4a_1a_3}}{2a_1}}. \tag{2.71}$$

The eigenvalues imply that the wave motions of the qP- and qSV-wave cannot be resolved into independent compressional and shear waves (Tang and Cheng, 2004). Indeed, they have to be combined to solve both partial differential given in equations 2.61a and 2.61b. The solutions are given in terms of the potentials Φ and $\check{\Psi}^{\mathrm{qSV}}$ by

$$\begin{pmatrix} \check{\Phi} \\ \check{\Psi}^{\mathrm{qSV}} \end{pmatrix}(r,\theta,z,s) = \begin{pmatrix} 1 & \alpha_2 \\ \alpha_1 & 1 \end{pmatrix} \begin{pmatrix} \mathcal{T}^{\mathrm{qP}} K_m(rs\beta_r^{\mathrm{qP}}) \\ \mathcal{T}^{\mathrm{qSV}} K_m(rs\beta_r^{\mathrm{qSV}}) \end{pmatrix} \exp\left(\mathrm{i}m\theta\right) \exp\left(\mathrm{i}s\beta_z z\right), \tag{2.72a}$$

with

$$\alpha_1 = -\frac{\mathcal{A}_{1,1}(\beta_r^{\mathrm{qP}})}{\mathcal{A}_{1,2}(\beta_r^{\mathrm{qP}})}, \qquad \alpha_2 = -\frac{\mathcal{A}_{1,2}(\beta_r^{\mathrm{qSV}})}{\mathcal{A}_{1,1}(\beta_r^{\mathrm{qSV}})}. \tag{2.72b}$$

The two coefficients α_1 and α_2 result from finding the eigenvectors for the eigenvalues β_r^{qP} and β_r^{qSV}. The solution for the potential Φ shows that anisotropy induces coupling of transverse particle motion to the qP-wave, and the magnitude of the coupling is controlled by the coefficient α_2. Analogously, the solution for the potential $\check{\Psi}^{\mathrm{qSV}}$ indicates the coupling of longitudinal particle motion to the qSV-wave, and the magnitude of the coupling is defined by the coefficient α_1. If the formation is isotropic instead of anisotropic, the coefficients vanish, and the isotropic solutions are obtained. In both cases, the transmission coefficients ($\mathcal{T}^{\mathrm{qP}}$, $\mathcal{T}^{\mathrm{qSV}}$) have to be determined by applying appropriate boundary conditions.

The boundary conditions result from the connection of the above-described solution for the wavefield in unbounded VTI media with the solution in the borehole fluid at the borehole

wall. Since the derivation of solutions for the total acoustic wavefield in the borehole fluid is extensively presented in literature, e.g., Ellefsen et al. (1990), Geerits and Kranz (2017), Hsu and Sinha (1998), and Tang and Cheng (2004), it is omitted in this work. At the borehole interface between the fluid and the formation ($r = R_{\mathrm{H}}$), the boundary conditions are defined by the continuity of the radial particle velocity ($\check{v}_r$) and the radial stress component ($\check{\tau}_{r,r}$). Moreover, the components $\check{\tau}_{r,z}$ and $\check{\tau}_{r,\theta}$ must vanish since the borehole fluid cannot support shear stresses. Hence, the resulting equations are defined as (e.g., Tang and Cheng, 2004)

$$\check{v}_r = \check{v}_r^{\mathrm{f}}, \qquad r = R_{\mathrm{H}}, \tag{2.73a}$$

$$\check{\tau}_{r,r} = \check{\tau}_{r,r}^{\mathrm{f}}, \qquad r = R_{\mathrm{H}}, \tag{2.73b}$$

$$\check{\tau}_{r,z} = 0, \qquad r = R_{\mathrm{H}}, \tag{2.73c}$$

$$\check{\tau}_{r,\theta} = 0, \qquad r = R_{\mathrm{H}}. \tag{2.73d}$$

The solution for the particle velocity vector ($\check{\boldsymbol{v}}$) in the formation is obtained by substituting the solutions for the potentials (Eq. 2.65 and 2.72a) into equation 2.59. Moreover, the stress tensor components ($\check{\boldsymbol{\tau}}$) can be calculated by substituting the solutions for the particle velocity vector into equation 2.54. The substitution of both the radial particle velocity component and the respective stress tensor components into the above-defined boundary conditions yields a matrix equation for the unknown transmission coefficients (Tang and Cheng, 2004)

$$\begin{pmatrix} \mathcal{D}_{1,1} & \mathcal{D}_{1,2} & \mathcal{D}_{1,3} & \mathcal{D}_{1,4} \\ \mathcal{D}_{2,1} & \mathcal{D}_{2,2} & \mathcal{D}_{2,3} & \mathcal{D}_{2,4} \\ \mathcal{D}_{3,1} & \mathcal{D}_{3,2} & \mathcal{D}_{3,3} & \mathcal{D}_{3,4} \\ \mathcal{D}_{4,1} & \mathcal{D}_{4,2} & \mathcal{D}_{4,3} & \mathcal{D}_{4,4} \end{pmatrix} \begin{pmatrix} \mathcal{R}^{\mathrm{f}} \\ \mathcal{T}^{\mathrm{qP}} \\ \mathcal{T}^{\mathrm{SH}} \\ \mathcal{T}^{\mathrm{qSV}} \end{pmatrix} = \begin{pmatrix} \check{v}_r^{\mathrm{f}} \\ \check{\tau}_{r,r}^{\mathrm{f}} \\ 0 \\ 0 \end{pmatrix}. \tag{2.74}$$

Additionally, the reflection coefficient $\mathcal{R}^{\mathrm{f}}$ is included, defining the amplitude of the acoustic wavefield in the borehole fluid, which is reflected from the borehole wall. The right-hand side of the equation is defined by the radial particle velocity $\check{v}_r^{\mathrm{f}}$ and the radial normal stress tensor component $\check{\tau}_{r,r}^{\mathrm{f}}$ in the borehole fluid. The latter is identical to the acoustic pressure $\check{p}$ in the fluid. The explicit components of the matrix $\mathcal{D}$ and the right-hand side can be found in Ellefsen (1990) and Tang and Cheng (2004), using a slightly different notation. From the roots of the boundary condition matrix $\mathcal{D}$, dispersion curves can be obtained. For this reason, the radial phase slowness values β_r are sought at a given frequency s, for which the determinant vanishes

$$\det\left(\mathcal{D}(\beta_r, s)\right) = 0. \tag{2.75}$$

The possibly complex roots of the determinant are calculated numerically, e.g., using *Muller*'s method (Muller, 1956). Once a root is found, it can be tracked to various frequencies to obtain the dispersion curves. While the boundary condition matrix defined in Eq. 2.74 considers a fluid-filled borehole surrounded by a VTI formation in the absence of a logging tool, the

configuration can be extended by several layers to model the LWD tool. This would result in a larger linear equation system, including reflection and transmission coefficients corresponding to the interface between the tool and the fluid (e.g., Geerits and Kranz, 2017).

2.4.2. General case: triclinic symmetry

For anisotropic formations exhibiting symmetries lower than VTI, the corresponding stiffness tensor depends on the azimuth θ, making the *Christoffel* equation challenging to solve. In the case of the most general triclinic symmetry, all twenty-one components of the stiffness tensor are non-zero. Their dependency on the azimuth in cylindrical coordinates is explicitly given in Appendix B.2. When applying partial differentiation with respect to the azimuth according to equation 2.55, the azimuthal derivatives of the stiffness tensor elements are needed to perform the product rule. The resulting *Christoffel* equation is given in Appendix C.2 and contains cosine and sine functions of the azimuth up to the power of four, as well as various products of them. When applying the azimuthal *Fourier* transform, each cosine and sine term has to be transformed separately and convolved with the azimuthal *Fourier* transform of the particle velocity vector according to Appendix A.3. The spatial vertical *Fourier* transform (App. A.2) can be applied in the same way as for the VTI case. The resulting *Christoffel* equation in the (r, m, β_z, s)–domain is defined by

$$\tilde{\Lambda}(r, m, \beta_z, s) = \mathbf{0}, \tag{2.76}$$

where the elements of the matrix Λ are given in Appendix C.2 (Eq. C.21b–C.21j). The azimuthal *Fourier* transforms of the cosine and the sine terms introduce coupling between several mode numbers in the range from $m - 4$ to $m + 4$. The induced mode contaminants depend on the symmetry of the anisotropic formation. If the formation exhibits orthotropic or HTI symmetry, the terms corresponding to the azimuthal wavenumbers $m \pm 1$ and $m \pm 3$ vanish, and only the terms corresponding to even increments of m remain. Furthermore, in the case of VTI symmetry or isotropy, only the terms corresponding to the azimuthal wavenumber m are non-zero since all other terms vanish. This is because the stiffness tensor is azimuthally invariant for VTI or isotropic media, and no cosine and sine terms are azimuthally *Fourier* transformed, and no mode contaminants are induced.

Equation 2.76 represents an ordinary differential equation in the radial coordinate r. In the isotropic or VTI case, *Bessel*'s differential equation can be deduced for which solutions are defined by the (modified) *Bessel* function (Gradshteyn and Ryzhik, 2007). In contrast, it is impossible to deduce *Bessel*'s differential equation if the medium exhibits symmetries lower than VTI. In the latter case, the system of differential equations (Eq. 2.76 and C.21b–C.21j) appears daunting and impossible to decouple. One solution strategy might be transforming the radial coordinate to the radial slowness number β_r to obtain an algebraic equation. For this reason, the *Meijer* transform (Meijer, 1941) defined in Appendix A.4 seemed to be an appropriate integral transform. However, a solution for the differential equation was not successfully found in the scope of this thesis.

3. Finite-difference modeling of wave propagation in anisotropic media

Alternatively to an analytical solution, the anisotropic wave equation can also be solved numerically by the finite-difference (FD) method. This method is a purely numerical method to obtain full wavefield solutions in complex geometries. For simulating the wave propagation in cylindrical boreholes surrounded by anisotropic media, a three-dimensional, time-domain finite-difference code in Cartesian coordinates is used. The code is written in the programming language *C* and was originally developed by *Olaf Hellwig* and *Daniel Köhn* (Köhn et al., 2015). In the scope of this thesis, the code is modified to work correctly for triclinic anisotropic media. Therefore, the implemented spatial FD grid is exchanged, and in consequence of the new grid, the source initialization is modified, and communication between processors is extended for parallelization. This chapter shortly describes the basic concepts of the finite-difference method and explains the new spatial grid in more detail.

3.1. Finite-difference method

The computational domain is covered by a discrete space-time grid in the FD method. A three-dimensional regular spatial grid is defined by the set of positions

$$x^i = x_0 + i\Delta x, \qquad y^j = y_0 + j\Delta y, \qquad z^k = z_0 + k\Delta z. \tag{3.1}$$

The spatial increments are referred to as grid spacing. Analogously, the time grid is defined by

$$t_l = t_0 + l\Delta t, \tag{3.2}$$

with Δt denoting the time step. The functions describing the wavefield, the density, and the stiffness of the medium are represented by their values at the discrete grid positions

$$f_l^{i,j,k} = f(x^i, y^j, z^k, t_l). \tag{3.3}$$

The problem of wave motion in anisotropic media can be expressed by various formulations. One of those is the commonly used velocity-stress formulation, which is given in chapter 2. The governing equations can be derived from equations 2.19, 2.21a, and 2.22 in the form

$$\rho^{\mathrm{s}} \partial_t v_p = \partial_q \tau_{p,q}, \tag{3.4a}$$

$$\partial_t \tau_{p,q} = C_{p,q,i,j} \partial_t \epsilon_{i,j}, \tag{3.4b}$$

$$\partial_t \epsilon_{i,j} = \frac{1}{2} \left(\partial_i v_j + \partial_j v_i \right). \tag{3.4c}$$

The wavefield is expressed by the stress tensor τ and the particle velocity vector $\boldsymbol{v}$.

Finite-difference methods approximate partial differential equations with algebraic finite-difference equations by replacing the partial derivatives with FD formulas. Besides the forward-difference and backward-difference formula, the central-difference formula derived from the *Taylor* series expansion is most common (e.g., Moczo et al., 2004)

$$\partial_u f(u) \approx D_u F(u) = \frac{F(u + \frac{\Delta u}{2}) - F(u - \frac{\Delta u}{2})}{\Delta u}. \tag{3.5}$$

The parameter u can be replaced by any spatial coordinate x, y, z, or the time coordinate t. While the forward- and backward-difference formulas are first-order approximations, the central-difference formula is a second-order approximation (Moczo et al., 2004), where the order of accuracy is defined by the truncation error of the *Taylor* series expansion. Furthermore, it is possible to define non-uniform spatial grids with variable spacing. The FD operator for such grids can also be derived by *Taylor* series expansion and is defined by

$$\partial_u f(u) \approx D_u F(u) = \frac{F(u + \alpha \Delta u) - F(u + (\alpha - 1)\Delta u)}{\Delta u}, \tag{3.6}$$

which is only first-order accurate (Hellwig, 2017). The parameter α ($0 < \alpha < 1$) defines the ratio of the grid spacing of the two involved neighboring grids. If both grid spacings are equal, the parameter is $\alpha = 0.5$, and equation 3.6 reduces to equation 3.5.

The temporal grid is chosen to be uniform, which means that the time step Δt is constant. The central-difference formula for uniform grids (Eq. 3.5) can be rewritten to obtain an explicit time integration scheme

$$F\left(t + \frac{\Delta t}{2}\right) = \Delta t \left[D_t F(t) \right] + F\left(t - \frac{\Delta t}{2}\right). \tag{3.7}$$

The time-stepping can be implemented as an explicit leapfrog time integration, i.e., the particle velocity and the stress tensor are updated at discrete times shifted by half a time step against each other (Hellwig, 2017).

3.2. Spatial finite-difference grids

3.2.1. Standard staggered grid

Analogously to the temporal FD grid, it is advantageous to define the particle velocity components and the stress tensor components not at the same spatial position but shifted by half a grid spacing. For this reason, various spatial FD grids were developed in the past. The most

commonly used grid for isotropic media is the standard staggered grid (SSG) introduced by Virieux (1984, 1986), as displayed in figure 3.1a. The normal components of the stress tensor

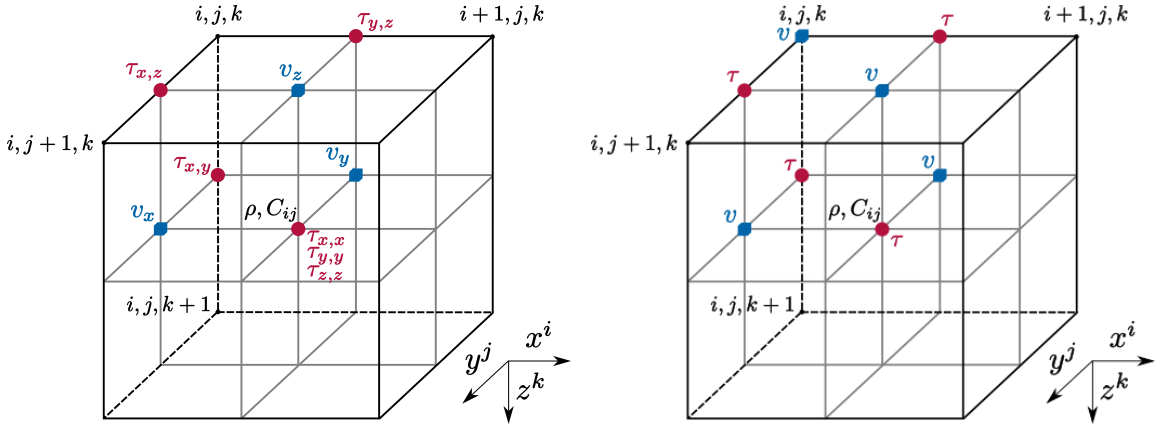

(a) Standard staggered grid (SSG) **(b)** *Lebedev* grid

Fig. 3.1: Spatial finite-difference grids.

$(\tau_{x,x}, \tau_{y,y}, \tau_{z,z})$ are stored together in the center of the grid cell, whereas each shear component of the stress tensor $(\tau_{y,z}, \tau_{x,z}, \tau_{x,y})$ has its position at the edges of the cell. Similarly, each component of the particle velocity vector (v_x, v_y, v_z) is positioned on the faces of the cell. The locations of all components are given by

$$\tau_{u,u}^{i,j,k} = \tau_{u,u}\left(x^{i+\frac{1}{2}}, y^{j+\frac{1}{2}}, z^{k+\frac{1}{2}}\right), \qquad u \in \{x, y, z\}, \tag{3.8a}$$

$$\tau_{y,z}^{i,j,k} = \tau_{y,z}\left(x^{i+\frac{1}{2}}, y^{j}, z^{k}\right), \tag{3.8b}$$

$$\tau_{x,z}^{i,j,k} = \tau_{x,z}\left(x^{i}, y^{j+\frac{1}{2}}, z^{k}\right), \tag{3.8c}$$

$$\tau_{x,y}^{i,j,k} = \tau_{x,y}\left(x^{i}, y^{j}, z^{k+\frac{1}{2}}\right), \tag{3.8d}$$

$$v_{x}^{i,j,k} = v_{x}\left(x^{i}, y^{j+\frac{1}{2}}, z^{k+\frac{1}{2}}\right), \tag{3.8e}$$

$$v_{y}^{i,j,k} = v_{y}\left(x^{i+\frac{1}{2}}, y^{j}, z^{k+\frac{1}{2}}\right), \tag{3.8f}$$

$$v_{z}^{i,j,k} = v_{z}\left(x^{i+\frac{1}{2}}, y^{j+\frac{1}{2}}, z^{k}\right), \tag{3.8g}$$

where i, j, and k in the left-hand sides of the equations are the indices of the cell. In contrast, the indices in the right-hand sides correspond to the actual positions. The advantage of the above-defined positioning is that all derivatives, approximated with the central-difference operator (Eq. 3.6), are calculated at the position where they are needed for further computations. For example, the update of the particle velocity component v_x depends only on the spatial derivatives of the stress tensor components $\tau_{x,x}$, $\tau_{x,y}$, and $\tau_{x,z}$ (Eq. 3.4a)

$$\rho^{\mathrm{s}} \partial_t v_x = \partial_x \tau_{x,x} + \partial_y \tau_{x,y} + \partial_z \tau_{x,z}. \tag{3.9a}$$

The FD method approximates these spatial derivatives by

$$\partial_x \tau_{x,x} \approx \frac{1}{\Delta x}\left(\tau_{x,x}^{i,j,k} - \tau_{x,x}^{i-1,j,k}\right), \tag{3.9b}$$

$$\partial_y \tau_{x,y} \approx \frac{1}{\Delta y}\left(\tau_{x,y}^{i,j+1,k} - \tau_{x,y}^{i,j,k}\right), \tag{3.9c}$$

$$\partial_z \tau_{x,z} \approx \frac{1}{\Delta z}\left(\tau_{x,z}^{i,j,k+1} - \tau_{x,z}^{i,j,k}\right), \tag{3.9d}$$

and a comparison with equation 3.8 or figure 3.1a shows that all derivatives are computed at the location $(x_i, y_{j+\frac{1}{2}}, z_{k+\frac{1}{2}})$ where the particle velocity component v_x is stored. Similarly, the stress tensor shear component $\tau_{x,z}$ can be updated in isotropic media (Eq. 2.16) by

$$\partial_t \tau_{x,z} = 2\mu \partial_t \epsilon_{x,z} = \mu\left(\partial_x v_z + \partial_z v_x\right). \tag{3.10}$$

The equation involves only two spatial partial derivatives of the particle velocity components approximated by the FD operators

$$\partial_x v_z \approx \frac{1}{\Delta x}\left(v_z^{i,j,k} - v_z^{i-1,j,k}\right), \tag{3.11a}$$

$$\partial_z v_x \approx \frac{1}{\Delta z}\left(v_x^{i,j,k} - v_x^{i,j,k-1}\right). \tag{3.11b}$$

The approximations of the derivatives are computed at the position $(x_i, y_{j+\frac{1}{2}}, z_k)$ where the shear stress component $\tau_{x,z}$ is stored. This works for all stress component updates in isotropic media, and no interpolation is required. Besides, the SSG can also be used in anisotropic media exhibiting orthotropic or higher symmetries. All these symmetries, including the isotropic case, are characterized by twelve zero elements of the stiffness tensor (Sec. 2.1)

$$\begin{aligned} C_{1,4} = C_{1,5} = C_{1,6} = C_{2,4} = C_{2,5} = C_{2,6} \\ = C_{3,4} = C_{3,5} = C_{3,6} = C_{4,5} = C_{4,6} = C_{5,6} = 0. \end{aligned} \tag{3.12}$$

In contrast, these elements can become non-zero if the anisotropic medium exhibits monoclinic or triclinic symmetry (Sec. 2.1). In the triclinic case, all elements of the stiffness tensor are non-zero and updating a stress component, e.g., $\tau_{x,z}$, involves all strain components

$$\partial_t \tau_{x,z} = C_{1,5}\epsilon_{x,x} + C_{2,5}\epsilon_{y,y} + C_{3,5}\epsilon_{z,z} + C_{4,5}\epsilon_{y,z} + C_{5,5}\epsilon_{x,z} + C_{5,6}\epsilon_{x,y}. \tag{3.13}$$

Thus, all spatial derivatives of all three components of the particle velocity vector have to be computed. The problem is that these derivatives are, in general, not computed at the position of $\tau_{x,z}$. Consequently, the standard staggered grid does no longer work. Igel et al. (1995) showed that the grid could be repaired by interpolating the strain components to the positions where they are needed for computation. However, these interpolations significantly increase the computational effort and will likely introduce a considerable numerical error (Bansal and Sen, 2008).

3.2.2. Lebedev grid

As an alternative, this thesis proposes more convenient spatial FD grids. One of those grids is the rotated staggered grid originally introduced by Saenger et al. (2000) to circumvent instability problems caused by high contrast discontinuities. Saenger and Bohlen (2004) demonstrated that this rotated staggered grid could also be used to model wave propagation in general anisotropic media, but it is restricted to uniform grids. A second FD grid appropriate for anisotropic media is the grid introduced by Lebedev (1964) to solve different types of partial differential equations. Indeed, the rotated staggered grid can be considered as a modification of the *Lebedev* grid (Lisitsa and Vishnevskiy, 2010). Lisitsa (2007) demonstrated that both grids are equivalent in two dimensions, but in three dimensions, they are fundamentally different (Bernth and Chapman, 2011). In this thesis, only the *Lebedev* grid is explained and applied because it is computationally more efficient and can also be implemented straightforwardly for non-uniform grids.

The *Lebedev* grid displayed in figure 3.1b stores all components of the stress tensor in the center and additionally at the edges of the cell. Similarly, all particle velocity components are stored at the faces and one corner of the cell

$$\tau^{i+\frac{1}{2},j+\frac{1}{2},k+\frac{1}{2}} = \tau(x^{i+\frac{1}{2}}, y^{j+\frac{1}{2}}, z^{k+\frac{1}{2}}), \tag{3.14a}$$

$$\tau^{i+\frac{1}{2},j,k} = \tau(x^{i+\frac{1}{2}}, y^{j}, z^{k}), \tag{3.14b}$$

$$\tau^{i,j+\frac{1}{2},k} = \tau(x^{i}, y^{j+\frac{1}{2}}, z^{k}), \tag{3.14c}$$

$$\tau^{i,j,k+\frac{1}{2}} = \tau(x^{i}, y^{j}, z^{k+\frac{1}{2}}), \tag{3.14d}$$

$$v^{i,j,k} = v(x^{i}, y^{j}, z^{k}), \tag{3.14e}$$

$$v^{i,j+\frac{1}{2},k+\frac{1}{2}} = v(x^{i}, y^{j+\frac{1}{2}}, z^{k+\frac{1}{2}}), \tag{3.14f}$$

$$v^{i+\frac{1}{2},j,k+\frac{1}{2}} = v(x^{i+\frac{1}{2}}, y^{j}, z^{k+\frac{1}{2}}), \tag{3.14g}$$

$$v^{i+\frac{1}{2},j+\frac{1}{2},k} = v(x^{i+\frac{1}{2}}, y^{j+\frac{1}{2}}, z^{k}). \tag{3.14h}$$

The *Lebedev* scheme can also be considered as four overlapping standard staggered grids shifted against each other by half a face diagonal. Since the SSG stores nine quantities (six components of the stress tensor and three components of the particle velocity vector), the *Lebedev* grid stores thirty-six quantities. The advantage of the grid is that all spatial derivatives for the particle velocity can be calculated at all positions of the stress tensor components and vice versa. Consequently, the interpolation of quantities is not required, reducing the numerical error. The solutions for the stress tensor and particle velocity vector can be output at the center of the *Lebedev* grid cell $(i+\frac{1}{2}, j+\frac{1}{2}, k+\frac{1}{2})$, including all four staggered grids. The quantities stored in each SSG are interpolated to the cell center of the *Lebedev* grid first. Subsequently, the arithmetic average of all four interpolated values is computed. The combination of both steps yields the weights displayed in figure 3.2 and which

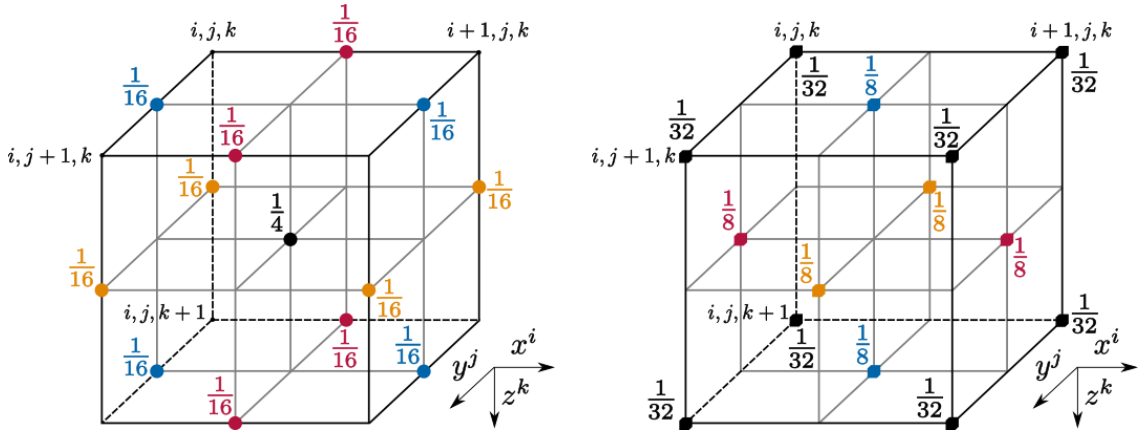

(a) Output of stress tensor components **(b)** Output of particle velocity components

Fig. 3.2: The stress tensor and particle velocity components can be output at the cell center by averaging the stress tensor (a) and particle velocity (b) components stored in all four SSGs. Each SSG is illustrated by a different color.

are applied in the following equations

$$\begin{aligned}\bar{\tau}^{i+\frac{1}{2},j+\frac{1}{2},k+\frac{1}{2}} = \frac{1}{4}\Bigg[&\tau^{i+\frac{1}{2},j+\frac{1}{2},k+\frac{1}{2}} + \frac{\tau^{i+\frac{1}{2},j,k} + \tau^{i+\frac{1}{2},j+1,k} + \tau^{i+\frac{1}{2},j,k+1} + \tau^{i+\frac{1}{2},j+1,k+1}}{4} \\ &+ \frac{\tau^{i,j+\frac{1}{2},k} + \tau^{i+1,j+\frac{1}{2},k} + \tau^{i,j+\frac{1}{2},k+1} + \tau^{i+1,j+\frac{1}{2},k+1}}{4} \\ &+ \frac{\tau^{i,j,k+\frac{1}{2}} + \tau^{i+1,j,k+\frac{1}{2}} + \tau^{i,j+1,k+\frac{1}{2}} + \tau^{i+1,j+1,k+\frac{1}{2}}}{4}\Bigg],\end{aligned} \tag{3.15a}$$

$$\begin{aligned}\bar{v}^{i+\frac{1}{2},j+\frac{1}{2},k+\frac{1}{2}} = \frac{1}{4}\Bigg[&\frac{v^{i,j+\frac{1}{2},k+\frac{1}{2}} + v^{i+1,j+\frac{1}{2},k+\frac{1}{2}}}{2} + \frac{v^{i+\frac{1}{2},j,k+\frac{1}{2}} + v^{i+\frac{1}{2},j+1,k+\frac{1}{2}}}{2} \\ &+ \frac{v^{i+\frac{1}{2},j+\frac{1}{2},k} + v^{i+\frac{1}{2},j+\frac{1}{2},k+1}}{2} \\ &+ \frac{1}{8}\Big(v^{i,j,k} + v^{i+1,j,k} + v^{i,j+1,k} + v^{i+1,j+1,k} \\ &\quad + v^{i,j,k+1} + v^{i+1,j,k+1} + v^{i,j+1,k+1} + v^{i+1,j+1,k+1}\Big)\Bigg].\end{aligned} \tag{3.15b}$$

For isotropic or anisotropic media with orthotropic or higher symmetries, the four SSGs constituting the *Lebedev* grid decouple. Hence, the particle velocity vector and stress tensor components are updated on each grid independently with no interaction between the four grids. Therefore, it is recommended to use the SSG in media with orthotropic or higher symmetries to reduce the computational effort.

3.3. Heterogeneous media

In both grids, the density and stiffness tensor elements of the medium are stored in the cell center. However, for updating the particle velocity or the stress tensor (Eq. 3.4a and 3.4b), the formation parameters are required at their positions. For homogeneous media, this is no problem because they are constant at all positions of the grid. In contrast, the parameters need special treatment for heterogeneous media in order to fulfill the continuity conditions. If a medium possesses a discontinuity, e.g., an interface between two layers with different parameters, the conditions have to be fulfilled at the interface between two neighboring cells. This is achieved by appropriate averaging of the material parameters. Moczo et al. (2002) have shown that arithmetic averaging of the density and harmonic averaging of the stiffness tensor elements are adequate. The averaging of the material parameters is performed at more positions for the *Lebedev* grid than for the SSG resulting in a higher computational effort.

3.4. Finite-difference properties and grid dispersion

The finite-difference equations and their solutions exhibit different properties. FD equations are consistent with the partial differential equation if the difference between both (the truncation error of the *Taylor* series expansion) vanishes as the size of the time step and the grid spacing go to zero (Moczo et al., 2004). An FD equation is stable if it yields bounded solutions if the exact solution is bounded, and it is unstable if the computed solution becomes unbounded. Stability depends on the chosen length of the time step and the grid spacing. Lisitsa and Vishnevskiy (2010) have derived a stability criterion for the *Lebedev* grid

$$\Delta t \cdot \max\left(v^{\mathrm{qP}}\right) \cdot \sqrt{\frac{1}{(\min(\Delta x))^2} + \frac{1}{(\min(\Delta y))^2} + \frac{1}{(\min(\Delta x))^2}} \leq 1, \tag{3.16}$$

where v^{qP} denotes the qP-wave phase velocity. Convergence defines that the solution of the FD equation approaches the exact solution of the partial differential equation as the time step and the spatial grid spacings go to zero (Moczo et al., 2004). Convergence is complicated to prove, but it is related to consistency and stability. Thus, the *Lax* equivalence theorem can be used, expressing that an FD equation that is consistent and stable is also convergent (Lax and Richtmyer, 1956).

Besides, grid dispersion has to be considered. Since the finite-difference solution is discrete, only a limited number of wavenumbers can be represented, and hence, the phase velocity on the FD grid differs from the true velocities in the continuous medium (Moczo et al., 2007). This phenomenon is referred to as grid dispersion and must be taken into account for planning numerical simulations since it has a cumulative effect on the wave propagation. The relative error between the grid velocity and true velocity depends on the *Courant* number and the spatial sampling ratio (Hellwig, 2017). Since both parameters are controlled by the grid spacing, it is necessary to choose appropriate spatial grid spacings to keep the grid dispersion at a prescribed level. For this reason, the minimum wavelength λ_{min} must be resolved with at

least ten grid points for head waves. Moreover, Bohlen and Saenger (2006) have demonstrated that 15 to 30 grid points per minimum wavelength are required to accurately compute *Rayleigh* waves at a planar free surface aligned with the grid. Therefore, it is recommended to use a similar requirement for the finite-difference modeling of borehole-guided waves (Hellwig, 2017). Moczo et al. (2004) have presented the spatial sampling criterion for head waves

$$\max\left(\Delta x, \Delta y, \Delta z\right) < \frac{\lambda_{min}}{10} = \frac{\min(v)}{10 f_{acc}}. \tag{3.17}$$

If this criterion is fulfilled, the finite-difference computation is accurate up to the frequency f_{acc}. The criterion was obtained for the SSG and for the FD scheme, which is second-order accurate in space (Moczo et al., 2004). Since the *Lebedev* grid can be considered as four standard staggered grids, the grid spacing is equivalent, and the dispersion properties of both the standard staggered grid and the *Lebedev* grid coincide (Lisitsa and Vishnevskiy, 2010).

3.5. Initial conditions

The French mathematician *Hadamard* proposed that a model of a physical problem is well-posed if a solution exists, the solution is unique, and its behavior changes continuously with the initial conditions. The existence of solutions of the velocity-stress formulation (Eq. 3.4a–3.4c) is shown in chapter 2. However, to find a unique solution, additional initial and boundary conditions are required. An appropriate initial condition is that all particle velocity and stress tensor components are zero before an instant t_0, at which a source is applied. In the simplest case, a volumetric point source is applied by increment the right-hand side of equation 3.4b. For the SSG, the temporal derivative of the increment is added to the normal components $\tau_{x,x}^{i,j,k}$, $\tau_{y,y}^{i,j,k}$ and $\tau_{z,z}^{i,j,k}$ of the stress tensor to apply a source that acts at the grid cell i, j, k. The midpoint of the volumetric source coincides with the midpoint of this grid cell.

In contrast, this is not as simple for the *Lebedev* scheme. Since it consists of four standard staggered grids, the source must be applied to all four grids. Therefore, two different methods can be used. The most straightforward way is to apply the point source to the normal components of the stress tensor at all four locations with the weight one (Fig. 3.3a). The disadvantage of this method is that the source midpoint is not located in the cell center but at $(x_{i+\frac{1}{4}}, y_{j+\frac{1}{4}}, z_{k+\frac{1}{4}})$. A more elegant solution is to apply the source with the weight one to the SSG that stores the normal components of the stress tensor closest to the defined source location (Fig. 3.3b). Additionally, the source is applied to the four neighboring locations of each remaining SSG with the weight 1/4 (Lisitsa and Vishnevskiy, 2010). As a result, the total source weight of each SSG is one, and the applied source origin is aligned with the grids and not shifted to them.

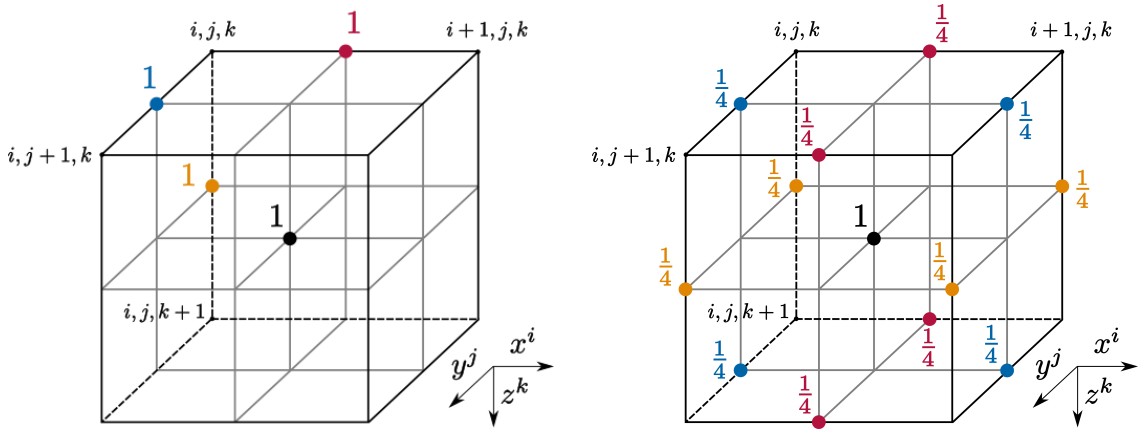

(a) Eccentered source **(b)** Centered source

Fig. 3.3: Application of a volumetric point source to the *Lebedev* grid. The source has to be applied to each SSG displayed in different colors. In the left figure (a), the source is applied to all four SSGs with equal weights, whereas in the right figure (b), the source is applied to the black SSG with the weight one and to four locations of the remaining three SSGs with the weight 1/4.

3.6. Boundary conditions

Additional to the wave equation and initial conditions, boundary conditions are required to define a unique solution of the partial differential equation. The spatial computational domain is limited to a finite grid resulting in a cuboid having six boundaries. Different types of boundary conditions can be set at each boundary face, such as a free surface to implement boundary conditions of the *Dirichlet* type or periodic boundary conditions. Other types are non-reflecting or absorbing boundary conditions for simulations in unbounded domains. By applying such boundary conditions, practical no wavefield energy is transmitted or reflected back from the boundary. Non-reflecting boundary conditions are commonly implemented using complex-frequency shifted perfectly matched layers introduced by Berenger (1994) for electromagnetic waves and applied to seismic modeling by Chew and Liu (1996) and Hastings et al. (1996).

3.7. Parallelization

The finite-difference code is parallelized to simulate the wave propagation on large grids within a reasonable run time. The parallelization is based on a decomposition of the spatial grid into sub-grids of equal size (Bohlen, 2002). The wavefield update is then performed on each sub-grid by a single processing element. On the boundary of each sub-grid, components of the stress tensor and the particle velocity from the neighboring sub-grid are needed. Therefore, communication between processing elements belonging to neighbored sub-grids is required, which is realized using the message passing interface (MPI) (Message Passing Interface Forum, 2012). The MPI is a public library available in the programming languages *C* and *Fortran* and provides various functions for communication. In the FD code used for this thesis, non-blocking communication functions are used to speed up the exchange of variables (Hellwig, 2017).

3.8. Finite-difference parameters

This section gives an overview of the parameters used to model the wavefield in a circular borehole surrounded by various anisotropic formations. The LWD tool is modeled by a cylindrical steel pipe with a fluid core centered in the borehole. Since the FD code is implemented in Cartesian coordinates, the cross-section of the circular borehole has to be discretized with a fine grid spacing of $\Delta x = \Delta y = 1\,\mathrm{mm}$. Using a non-uniform grid, the formation outside the borehole is discretized with larger grid spacing to reduce the total number of grid cells and the computational effort (Fig. 3.4). The maximum size of the grid spacing is limited through the grid dispersion (Sec. 3.4) depending on the required maximum accurate frequency, as well as the acoustic parameters of the surrounding formation, the borehole fluid, and the logging tool. In this thesis, three different anisotropic formations are considered. The Austin Chalk formation is an example of a slow TI formation, whereas the Bakken Shale and Cotton Valley Shale formations represent fast TI formations. Their densities and stiffness tensor elements can be found in table 3.1 based on Sinha et al. (1994, 2006). The borehole fluid parameters are given in table 3.2, and the parameters of the LWD tool modeled by a steel pipe are defined in table 3.3. The source signal is a *Ricker* wavelet (Ricker, 1943) characterized by its center frequency f_c. In theory, the bandwidth of the wavelet is unlimited but frequencies higher than three times the center frequency are insignificant. Thus, it is adequate to set the maximum accurate frequency to $f_{acc} = 3f_c$. Using the spatial sampling criterion (Eq. 3.17), the maximum grid size can be calculated based on the three different formations and the center frequency of the source signal (Tab. 3.4). The minimum velocity is the slow shear wave velocity for the Austin Chalk formation. Since the shear wave velocities of the Bakken Shale and Cotton Valley Shale formations are higher than the compressional velocity of the borehole fluid, the grid spacing depends only on the borehole compressional velocity and the source frequency in fast formations. Since the cross-section of the borehole and steel pipe have to

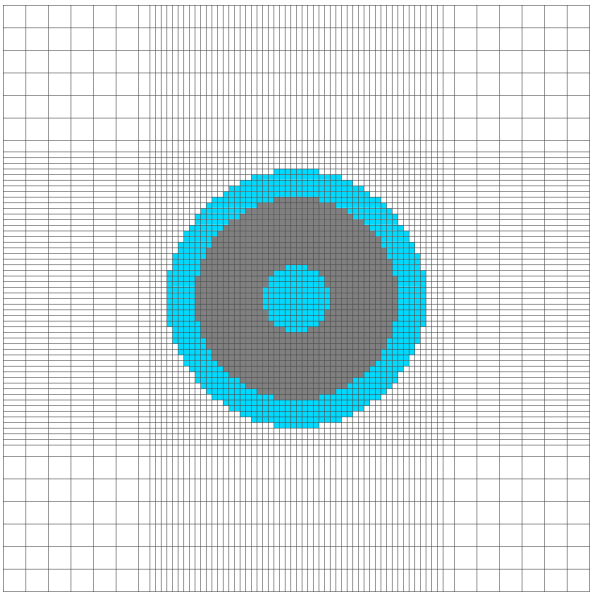

Fig. 3.4: Schematic view of the discretized cross-section of a circular borehole, including a steel pipe using a non-uniform grid in Cartesian coordinates.

Tab. 3.1: Overview of the volumetric mass density, the stiffness tensor elements, the corresponding vertical/horizontal compressional and shear wave velocities, and the *Thomsen* parameters (Thomsen, 1986) of the slow Austin Chalk, fast Bakken Shale, and fast Cotton Valley Shale VTI formations.

Formation		**Austin Chalk**	**Bakken Shale**	**Cotton Valley Shale**
ρ^{s}	$[\mathrm{kg\,m^{-3}}]$	2200	2230	2640
$C''_{1,1}$	[GPa]	22.00	40.90	74.73
$C''_{1,3}$	[GPa]	12.00	8.50	25.29
$C''_{3,3}$	[GPa]	14.00	26.90	58.84
$C''_{4,4}$	[GPa]	2.40	10.50	22.05
$C''_{6,6}$	[GPa]	3.10	15.30	29.99
$v^{\mathrm{P}}_{\mathrm{hor}}$	$[\mathrm{m\,s^{-1}}]$	3162.3	4282.6	5320.4
$(\beta^{\mathrm{P}}_{\mathrm{hor}})$	$([\mu\mathrm{s\,ft^{-1}}])$	(96.4)	(71.2)	(57.3)
$v^{\mathrm{P}}_{\mathrm{ver}}$	$[\mathrm{m\,s^{-1}}]$	2522.6	3473.2	4721.0
$(\beta^{\mathrm{P}}_{\mathrm{ver}})$	$([\mu\mathrm{s\,ft^{-1}}])$	(120.8)	(87.8)	(64.6)
$v^{\mathrm{SH}}_{\mathrm{hor}}$	$[\mathrm{m\,s^{-1}}]$	1187.1	2619.3	3370.4
$(\beta^{\mathrm{SH}}_{\mathrm{hor}})$	$([\mu\mathrm{s\,ft^{-1}}])$	(256.8)	(116.4)	(90.4)
$v^{\mathrm{SH}}_{\mathrm{ver}}$	$[\mathrm{m\,s^{-1}}]$	1044.5	2169.9	2890.0
$(\beta^{\mathrm{SH}}_{\mathrm{ver}})$	$([\mu\mathrm{s\,ft^{-1}}])$	(291.8)	(140.5)	(105.5)
ϵ		0.286	0.260	0.135
γ		0.146	0.229	0.180
δ		0.224	0.104	0.205

Tab. 3.2: Acoustic parameters of the borehole fluid (water) and the borehole radius.

Borehole Fluid		
ρ^{f}	$[\mathrm{kg\,m^{-3}}]$	1000
v^{f}	$[\mathrm{m\,s^{-1}}]$	1500
(β^{f})	$([\mu\mathrm{s\,ft^{-1}}])$	(203.2)
borehole radius R_{H}	[m]	0.107

Tab. 3.3: Acoustic parameters and radii of the LWD tool (steel pipe).

Logging tool		
ρ^{T}	$[\mathrm{kg\,m^{-3}}]$	7850
$v^{\mathrm{P}}_{\mathrm{T}}$	$[\mathrm{m\,s^{-1}}]$	5860
$(\beta^{\mathrm{P}}_{\mathrm{T}})$	$([\mu\mathrm{s\,ft^{-1}}])$	(52.0)
$v^{\mathrm{S}}_{\mathrm{T}}$	$[\mathrm{m\,s^{-1}}]$	3130
$(\beta^{\mathrm{S}}_{\mathrm{T}})$	$([\mu\mathrm{s\,ft^{-1}}])$	(97.4)
inner tool radius $R^{\mathrm{ID}}_{\mathrm{T}}$	[m]	0.025
outer tool radius $R^{\mathrm{OD}}_{\mathrm{T}}$	[m]	0.092

Tab. 3.4: Maximum grid spacings in dependence with the formation and the center frequency f_c of the source signal. The last column displays the maximum time step dependent on the grid spacing Δz.

Formation	f_c [kHz]	$\Delta x = \Delta y$ [mm]	Δz [mm]	Δt_{max} [ns]
Austin Chalk	2	15.0	10.160	120
	4	8.0	8.128	120
	8	4.0	4.064	118
Bakken Shale/ Cotton Valley Shale	2	25.0	20.320	120
	4	10.0	10.160	120
	8	5.0	5.080	119

be discretized with much finer grid spacing to model the curvature more precisely, the grid spacing values obtained in table 3.4 are only useful in the vertical and horizontal directions outside the borehole in the formation. The maximum time step Δt_{max} in the last column of table 3.4 is computed using the stability criterion defined in equation 3.16. Independent of the formation type, the steel pipe possesses the maximum compressional wave velocity in the configuration, and the horizontal minimal grid spacings are $\Delta x = \Delta y = 1\,\text{mm}$. Hence, the maximum time step depends only on the vertical grid spacing Δz, which has no significant influence. The grid dimensions are $2\,\text{m} \times 2\,\text{m} \times 10\,\text{m}$ resulting in a total number of 190 million grid cells. The simulated time of the modeling is 10 ms yielding 100 000 time steps for $\Delta t = 100\,\text{ns}$.

4. Wave propagation in fluid-filled boreholes surrounded by TI media

This chapter investigates the wave propagation in a fluid-filled borehole surrounded by an anisotropic formation exhibiting TI symmetry via time-domain FD modeling (Ch. 3). In the first section, the VTI case is considered, where the TI symmetry axis of the formation coincides with the vertical borehole axis. The second exceptional case is the HTI symmetry characterized by a TI symmetry axis that is perpendicular to the borehole axis. Finally, the most general TTI case is discussed, where the TI symmetry axis is arbitrarily inclined to the borehole axis. The head waves and borehole-guided waves with various azimuthal wavenumbers (e.g., *Stoneley*, flexural, quadrupole) are studied in all cases in the absence and the presence of an LWD tool. For this reason, synthetic time-domain waveform arrays are computed and processed to obtain the phase slowness dispersion curves of the borehole waves (App. D). Additionally, the sensitivities of the phase slowness dispersion curves to particular stiffness tensor elements are investigated in detail. The last section of this chapter deals with anisotropy-induced mode contaminants.

4.1. Vertical transverse isotropy (VTI)

The most straightforward anisotropic borehole configuration consists of a fluid-filled borehole surrounded by a VTI formation, where the symmetry axis (x_3''–axis) is parallel to the borehole axis (x_3–axis), as illustrated in figure 4.1. The wave velocities are azimuthally invariant since the plane transverse to the borehole is the isotropic plane of the TI formation indicated by

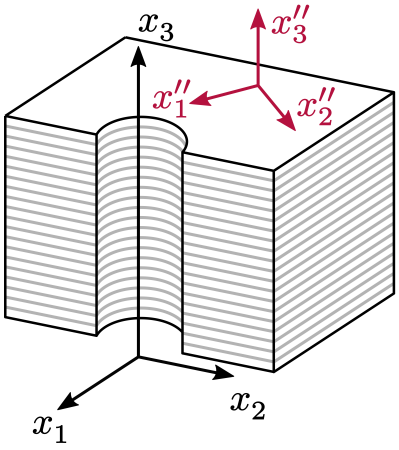

Fig. 4.1: Illustration of the VTI symmetry in the crystallographic reference frame (red) and the tool reference frame (black). The isotropic plane is indicated by the gray lines.

the gray lines in figure 4.1. Hence, the tool and borehole reference frames coincide with the crystallographic reference frame (Sec. 2.2) and $C_{i,j} \equiv C''_{i,j}$. According to equation 2.12, a VTI formation can be fully described by the five stiffness tensor elements $C_{1,1}$, $C_{1,3}$, $C_{3,3}$, $C_{4,4}$, and $C_{6,6}$ plus the density ρ^{s}. As explained in section 2.1.4, the phase velocities of vertically and horizontally propagating P- and SH-waves are defined as

$$\begin{pmatrix} \left(v^{\mathrm{P}}_{\mathrm{hor}}\right)^2 \\ \left(v^{\mathrm{P}}_{\mathrm{ver}}\right)^2 \\ \left(v^{\mathrm{SH}}_{\mathrm{hor}}\right)^2 \\ \left(v^{\mathrm{SH}}_{\mathrm{ver}}\right)^2 \end{pmatrix} = \frac{1}{\rho^{\mathrm{s}}} \begin{pmatrix} C_{1,1} \\ C_{3,3} \\ C_{6,6} \\ C_{4,4} \end{pmatrix}. \tag{4.1}$$

The shear wave velocity of a vertically and horizontally propagating SV-wave is in both cases determined by the stiffness tensor element $C_{4,4}$.

The following sections investigate the wave propagation in a fluid-filled borehole surrounded by slow and fast VTI formations in the absence and presence of an LWD tool. First, the omnidirectional monopole excitation is considered exciting refracted head waves and the borehole-guided *Stoneley* wave. The latter is sensitive to the horizontal SH-wave velocity at low frequencies. In contrast, the flexural and quadrupole waves excited by a dipole and quadrupole source, respectively, are sensitive to the vertical shear wave velocities.

4.1.1. Monopole excitation

The waveform array data excited by a monopole source in a fluid-filled borehole surrounded by the slow Austin Chalk VTI formation in the absence of a logging tool is displayed in figure 4.2a. Similar to the isotropic case (Sec. 1.2), the first arrival corresponds to the refracted P-wave traveling vertically along the borehole wall. Its velocity coincides with the vertical P-wave velocity ($v^{\mathrm{P}}_{\mathrm{ver}}$) determined by the stiffness tensor element $C_{3,3}$. The second arrival corresponds to the axisymmetric *Stoneley* wave showing a dispersive characteristic. Its phase slowness dispersion curve is plotted in figure 4.2c by the solid blue line. Additionally, the dotted and dashed blue lines display the dispersion curves of the *Stoneley* wave, excited in isotropic formations exhibiting a shear modulus of $\mu = C_{4,4}$ and $\mu = C_{6,6}$, respectively. All phase slowness dispersion curves are extracted from the modeled time-domain waveform arrays by a modified matrix pencil method introduced by Ekstrom (1996) (App. D.2.2). The dispersion curve of the *Stoneley* wave excited in the isotropic formation characterized by $\mu = C_{6,6}$ coincides with the dispersion curve modeled in the VTI formation at low frequencies. With increasing frequencies, the latter moves away from the dispersion curve in the isotropic formation ($\mu = C_{6,6}$) and comes closer to the dispersion curve modeled for the isotropic formation defined by $\mu = C_{4,4}$. Consequently, at low frequencies, the slowness of the *Stoneley* wave seems to be dominated by the stiffness tensor element $C_{6,6}$, whereas the influence of $C_{4,4}$ becomes more significant at higher frequencies.

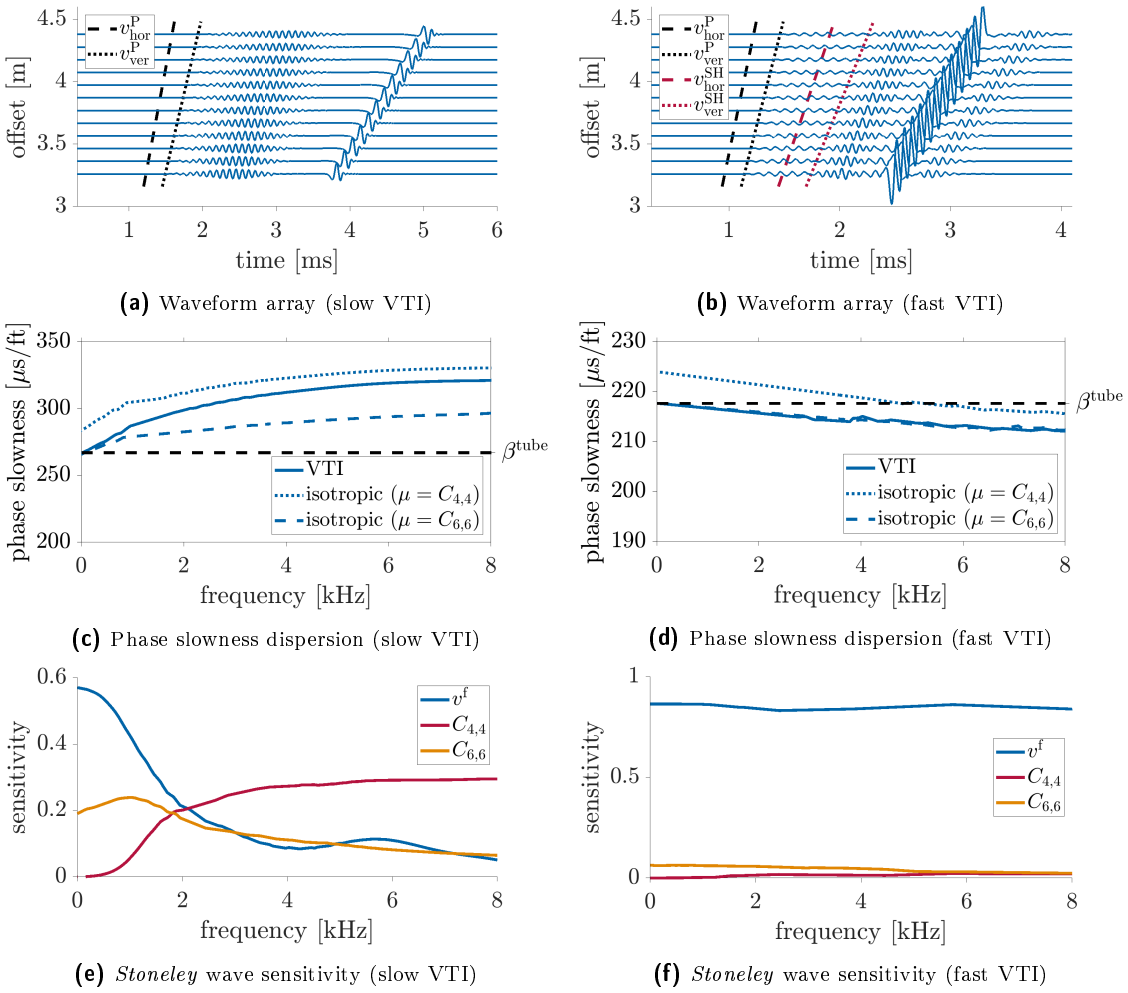

(a) Waveform array (slow VTI)

(b) Waveform array (fast VTI)

(c) Phase slowness dispersion (slow VTI)

(d) Phase slowness dispersion (fast VTI)

(e) *Stoneley* wave sensitivity (slow VTI)

(f) *Stoneley* wave sensitivity (fast VTI)

Fig. 4.2: Waveform array data excited by a monopole source ($f_{\mathrm{c}} = 8\,\mathrm{kHz}$) in a fluid-filled borehole surrounded by the slow Austin Chalk (a) and fast Bakken Shale (b) VTI formations in the absence of a logging tool. The amplitudes of the refracted P-, refracted shear, and *Stoneley* waves are differently amplified for better visibility. The solid lines in the second-row figures (c–d) display the phase slowness dispersion curves of the *Stoneley* wave compared to the isotropic counterparts illustrated by the dotted ($\mu = C_{4,4}$) and dashed ($\mu = C_{6,6}$) blue lines, respectively. The dashed black line represents the tube wave slowness (β^{tube}). The last-row figures (e–f) show the sensitivity of the *Stoneley* wave slowness to the P-wave velocity in the borehole fluid (v^{f}) and the stiffness tensor elements $C_{4,4}$ and $C_{6,6}$ of the formation.

For further investigation, the sensitivity of the *Stoneley* wave phase slowness (β^{St}) to various parameters is computed depending on the frequency s (e.g., Tang and Cheng, 2004)

$$\text{sensitivity} = \frac{\text{parameter}}{\beta(s)} \cdot \frac{\partial \beta(s)}{\partial \text{parameter}}. \tag{4.2}$$

Since the phase slowness of the *Stoneley* wave is computed numerically, the partial derivative is replaced by an FD operator to perform numerical differentiation (Sec. 3.1). The sensitivities of the *Stoneley* wave phase slowness to the stiffness tensor elements $C_{4,4}$, $C_{6,6}$, and the compressional wave velocity of the borehole fluid (v^{f}) are shown in figure 4.2e. As assumed, the sensitivity of the *Stoneley* wave slowness is high to the elastic constant $C_{6,6}$ and zero to $C_{4,4}$ at low frequencies. With increasing frequencies, the *Stoneley* wave slowness becomes less sensitive to $C_{6,6}$ and more to $C_{4,4}$. Moreover, the *Stoneley* wave is also sensitive to the

compressional wave velocity of the fluid. Since the sum of all three sensitivities is less than one, the *Stoneley* wave is indeed sensitive to other parameters (Tang and Cheng, 2004), which are omitted in the figure.

White and Tongtaow (1981) derived a formula to compute the slowness or velocity of the *Stoneley* wave in the low-frequency limit referred to as tube wave velocity (v^{tube})

$$v^{\mathrm{tube}} = \lim_{s\to 0} v^{\mathrm{St}} = v^{\mathrm{f}} \left(1 + \frac{\rho^{\mathrm{f}} \left(v^{\mathrm{f}}\right)^2}{C_{6,6}} \right)^{\left(-\frac{1}{2}\right)} . \tag{4.3}$$

The equation shows that the *Stoneley* wave velocity (v^{St}) in the low-frequency limit depends only on the parameters of the borehole fluid and the elastic constant $C_{6,6}$ of the surrounding VTI formation. Figure 4.2c illustrates the reciprocal of the tube wave velocity, i.e., the tube wave slowness (β^{St}), by the dashed black line, which coincides with the low-frequency limit of the *Stoneley* wave dispersion curve in the VTI formation. The dispersion curve of the *Stoneley* wave in the faster isotropic formation also coincides with the tube wave slowness since the shear modulus is set to $\mu = C_{6,6}$. In contrast, the shear modulus of the slower isotropic formation is $\mu = C_{4,4}$, yielding a higher tube wave slowness.

The right column of figure 4.2 displays, in the same manner, the waveform array, the phase slowness dispersion curves, and the sensitivity analysis of the *Stoneley* wave if the surrounding formation is the fast Bakken Shale VTI formation. The waveforms (Fig. 4.2b) contain the refracted shear wave in addition to the refracted P- and *Stoneley* waves. The refracted shear wave travels similar to the refracted P-wave, vertically along the borehole wall with vertical shear wave velocity ($v_{\mathrm{ver}}^{\mathrm{SH}} = v_{\mathrm{ver}}^{\mathrm{SV}}$) controlled by the elastic modulus $C_{4,4}$. Furthermore, figure 4.2f shows that in fast formations, the *Stoneley* wave is strongly sensitive to the compressional wave velocity of the borehole fluid and only weakly sensitive to the formation parameters. Nevertheless, the sensitivity to the formation parameters is highest to the elastic constant $C_{6,6}$ and zero to the elastic constant $C_{4,4}$ at low frequencies. Moreover, equation 4.3 is still valid to compute the tube wave velocity, as illustrated by the dashed black line in figure 4.2d.

Section 1.3 showed that the presence of an LWD tool strongly affects the slowness dispersion characteristics of the *Stoneley* wave in an isotropic environment. Similar behavior can be observed in a VTI environment. Norris (1990) has shown that the LWD tool can be modeled by an effective modulus M_{T} to compute the tube wave velocity. Tang (2003) has extended the work from isotropic to VTI media. The resulting equations can be used to compute the phase slowness dispersion curves of the *Stoneley* wave by the roots of the boundary condition matrix given in Tang (2003). In the slow Austin Chalk formation, the phase slowness dispersion curve of the *Stoneley* wave is descending instead of ascending (Fig. 4.3a), and the tube wave slowness is strongly increased. Hence, equation 4.3 is not valid in the presence of a tool. Furthermore, figures 4.3c and 4.3d show that the presence of an LWD tool also changes the sensitivities.

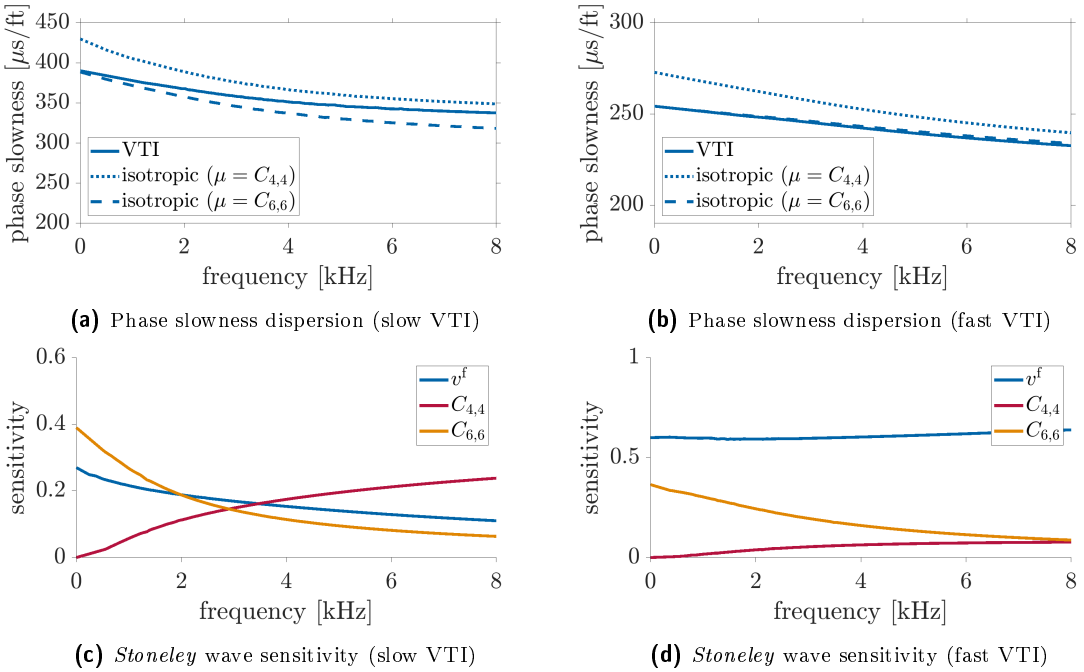

(a) Phase slowness dispersion (slow VTI)

(b) Phase slowness dispersion (fast VTI)

(c) *Stoneley* wave sensitivity (slow VTI)

(d) *Stoneley* wave sensitivity (fast VTI)

Fig. 4.3: Phase slowness dispersion curves and sensitivity analysis of the *Stoneley* waves excited by a monopole source in a fluid-filled borehole surrounded by the slow Austin Chalk (left) and fast Bakken Shale (right) VTI formations in the presence of an LWD tool. The solid lines in the first-row figures (a–b) display the phase slowness dispersion curves of the *Stoneley* wave compared to the isotropic counterparts illustrated by the dotted ($\mu = C_{4,4}$) and dashed ($\mu = C_{6,6}$) lines, respectively. The second-row figures (c–d) show the sensitivity of the *Stoneley* wave slowness to the P-wave velocity in the borehole fluid (v^{f}) and the stiffness tensor elements $C_{4,4}$ and $C_{6,6}$ of the formation.

The *Stoneley* wave is much less sensitive to the P-wave velocity in the borehole fluid since the LWD occupies much space in the borehole remaining only a tiny fluid annulus. Nevertheless, at low frequencies, the sensitivity to the stiffness tensor element $C_{6,6}$ is at a maximum, whereas the sensitivity to the component $C_{4,4}$ is zero. Consequently, it is still possible to obtain the component $C_{6,6}$ from the *Stoneley* wave slowness at low frequencies (Sec. 5.1).

4.1.2. Dipole excitation

Analogous to the monopole excitation, the phase slowness dispersion curve and the sensitivity analysis of the flexural wave excited by an alternate polarity dipole source ($n = 1$) in a fluid-filled borehole surrounded by a VTI formation are displayed in figure 4.4 in the absence of a logging tool. Since the parameters of a VTI formation are azimuthally invariant, the excited directional flexural wave does not depend on the source azimuth. In the low-frequency limit, the flexural wave propagates with the vertical shear wave velocity ($v_{\mathrm{ver}}^{\mathrm{SH}} = v_{\mathrm{ver}}^{\mathrm{SV}} \propto C_{4,4}$) of the formation for both the slow Austin Chalk and the fast Bakken Shale formation. The sensitivity analysis confirms that the flexural wave is mainly controlled by the stiffness tensor element $C_{4,4}$ and only marginal by $C_{6,6}$. Consequently, the flexural wave can only be used to determine the elastic modulus $C_{4,4}$ but not $C_{6,6}$.

Similar to the isotropic case, the presence of an LWD tool strongly affects the formation flexural wave and induces a tool flexural wave (Fig. 4.5). In the slow Austin Chalk formation,

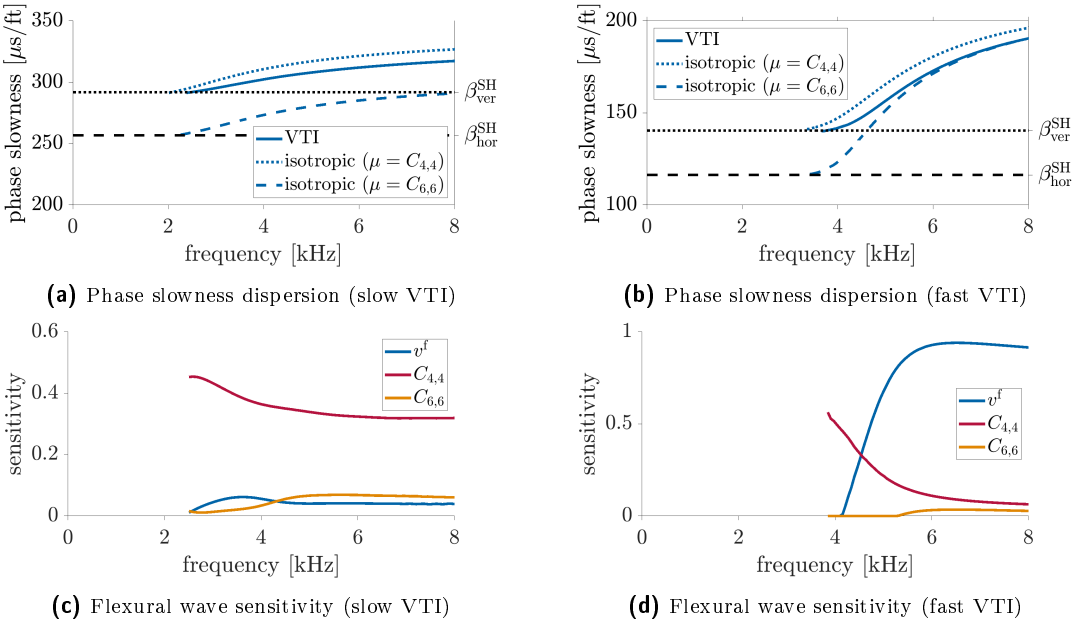

(a) Phase slowness dispersion (slow VTI)

(b) Phase slowness dispersion (fast VTI)

(c) Flexural wave sensitivity (slow VTI)

(d) Flexural wave sensitivity (fast VTI)

Fig. 4.4: Phase slowness dispersion curves and sensitivity analysis of the flexural waves excited by a dipole source in a fluid-filled borehole surrounded by the slow Austin Chalk (left) and fast Bakken Shale (right) VTI formations in the absence of an LWD tool. The solid lines in the first-row figures (a–b) display the phase slowness dispersion curves of the flexural wave compared to the isotropic counterparts illustrated by the dotted ($\mu = C_{4,4}$) and dashed ($\mu = C_{6,6}$) blue lines, respectively. The black lines represent the vertical ($\beta^{\mathrm{SH}}_{\mathrm{ver}}$) and horizontal ($\beta^{\mathrm{SH}}_{\mathrm{hor}}$) SH-wave slowness in the formation. The second-row figures (c–d) show the sensitivity of the flexural wave slowness to the P-wave velocity in the borehole fluid (v^{f}) and the stiffness tensor elements $C_{4,4}$ and $C_{6,6}$.

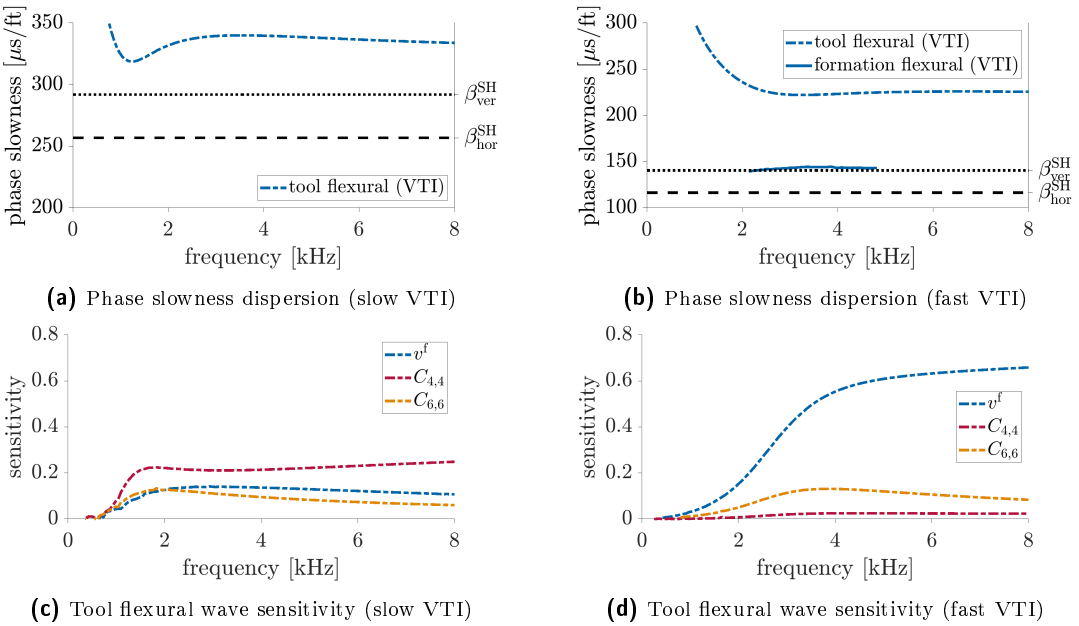

(a) Phase slowness dispersion (slow VTI)

(b) Phase slowness dispersion (fast VTI)

(c) Tool flexural wave sensitivity (slow VTI)

(d) Tool flexural wave sensitivity (fast VTI)

Fig. 4.5: Phase slowness dispersion curves and sensitivity analysis of the flexural waves excited by a dipole source in a fluid-filled borehole surrounded by the slow Austin Chalk (left) and fast Bakken Shale (right) VTI formations in the presence of an LWD tool. The first-row figures (a–b) display the phase slowness dispersion curves of the tool and formation flexural waves by the dashed and solid lines, respectively. The black lines represent the vertical ($\beta^{\mathrm{SH}}_{\mathrm{ver}}$) and horizontal ($\beta^{\mathrm{SH}}_{\mathrm{hor}}$) SH-wave slowness in the formation. The second-row figures (c–d) show the sensitivity of the tool flexural wave slowness to the P-wave velocity in the borehole fluid (v^{f}) and the stiffness tensor elements $C_{4,4}$ and $C_{6,6}$.

only the tool flexural wave is excited, but no formation flexural wave (Fig. 4.5a). In contrast, in the fast Bakken Shale formation, the formation flexural wave is still visible and mainly sensitive to the component $C_{4,4}$ at the cutoff frequency (Fig. 4.5b). Figures 4.5c and 4.5d display the sensitivities of the tool flexural wave to formation shear parameters and the P-wave velocity in the borehole fluid. The tool flexural wave possesses at medium and high frequencies a significant amount of sensitivity to the stiffness tensor elements $C_{4,4}$ and $C_{6,6}$, respectively. Consequently, the tool flexural wave potentially contains valuable information to invert formation VTI parameters.

4.1.3. Quadrupole excitation

The quadrupole wave excited by an alternate polarity quadrupole source ($n = 2$) in a fluid-filled borehole surrounded by a VTI formation in the absence of a logging tool shows a similar behavior as the flexural wave. The phase slowness dispersion curve of the quadrupole wave attains the vertical shear wave velocity controlled by $C_{4,4}$ at the cutoff frequency (Fig. 4.6a and 4.6b). Similarly, the sensitivity analysis shows that the sensitivity to the stiffness tensor element $C_{6,6}$ is close to zero, whereas the sensitivity of the quadrupole wave slowness to the component $C_{4,4}$ is at a maximum at low frequencies (Fig. 4.6c and 4.6d). The same results are obtained if the fluid-filled borehole contains an LWD tool (Fig. 4.7) since the quadrupole tool mode only slightly affects the formation quadrupole mode. Therefore, LWD quadrupole

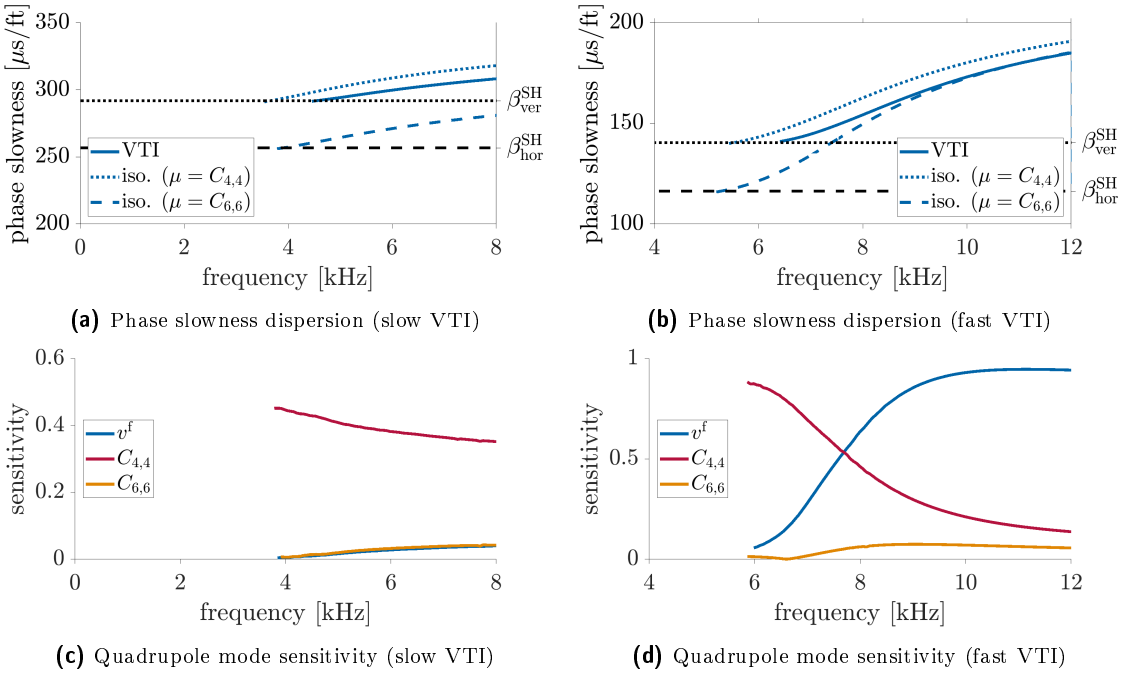

(a) Phase slowness dispersion (slow VTI)

(b) Phase slowness dispersion (fast VTI)

(c) Quadrupole mode sensitivity (slow VTI)

(d) Quadrupole mode sensitivity (fast VTI)

Fig. 4.6: Phase slowness dispersion curves and sensitivity analysis of the quadrupole modes excited by a quadrupole source in a fluid-filled borehole surrounded by the slow Austin Chalk (left) and fast Bakken Shale (right) VTI formations in the absence of an LWD tool. The solid lines in the first-row figures (a–b) display the phase slowness dispersion curves of the quadrupole modes compared to the isotropic counterparts illustrated by the dotted ($\mu = C_{4,4}$) and dashed ($\mu = C_{6,6}$) blue lines, respectively. The black lines represent the vertical ($\beta^{\mathrm{SH}}_{\mathrm{ver}}$) and horizontal ($\beta^{\mathrm{SH}}_{\mathrm{hor}}$) SH-wave slowness in the formation. The second-row figures (c–d) show the sensitivity of the quadrupole mode slowness to the P-wave velocity in the borehole fluid (v^{f}) and the stiffness tensor elements $C_{4,4}$ and $C_{6,6}$.

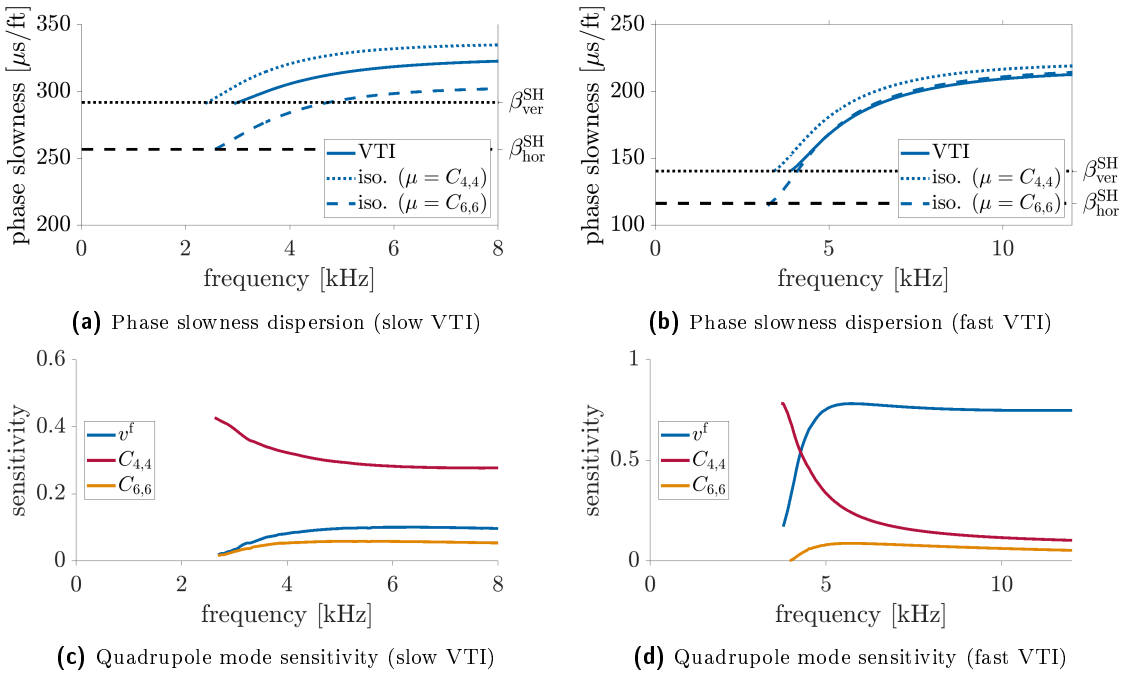

(a) Phase slowness dispersion (slow VTI)

(b) Phase slowness dispersion (fast VTI)

(c) Quadrupole mode sensitivity (slow VTI)

(d) Quadrupole mode sensitivity (fast VTI)

Fig. 4.7: Phase slowness dispersion curves and sensitivity analysis of the quadrupole modes excited by a quadrupole source in a fluid-filled borehole surrounded by the slow Austin Chalk (left) and fast Bakken Shale (right) VTI formations in the presence of an LWD tool. The first-row figures (a–b) display the phase slowness dispersion curves of the formation quadrupole waves by the dashed and solid lines, respectively. The black lines represent the vertical ($\beta^{\mathrm{S}}_{\mathrm{ver}}$) and horizontal ($\beta^{\mathrm{S}}_{\mathrm{hor}}$) SH-wave slowness in the formation. The second-row figures (c–d) show the sensitivity of the formation quadrupole mode slowness to the P-wave velocity in the borehole fluid (v^{f}) and the stiffness tensor elements $C_{4,4}$ and $C_{6,6}$.

measurements are more convenient to obtain the vertical shear wave velocity than LWD dipole logging, especially in slow formations where the formation flexural wave may not be present.

4.1.4. Summary

Tab. 4.1 gives an overview of the sensitivity analysis of the refracted and borehole-guided (e.g., *Stoneley*, flexural, quadrupole) waves to the stiffness tensor elements characterizing a VTI formation. The sensitivity analysis is helpful to determine which waves can be used to obtain particular stiffness tensor elements. The table treats both the absence and the presence of an LWD tool as well as slow and fast VTI formations.

First, the configuration without a logging tool is considered as it is valuable for WL measurements since the slim WL tool has only little effect on the borehole waves. The refracted P-wave is emitted, e.g., by a monopole source, and travels vertically along the borehole wall at vertical P-wave velocity defined by the stiffness tensor element $C_{3,3}$. The vertical S-wave velocity controlled by the stiffness tensor element $C_{4,4}$ can be obtained from the refracted shear wave in fast formations or from the low-frequency limits of the flexural and quadrupole waves in both formation types. The *Stoneley* wave is the only borehole wave sensitive to the horizontal SH-wave velocity defined by the stiffness tensor element $C_{6,6}$ in the low-frequency limit. At higher frequencies, the sensitivity to $C_{4,4}$ becomes greater than to $C_{6,6}$. While the sensitivities to $C_{6,6}$ and $C_{4,4}$ are significant in slow formations, they are weak in fast forma-

Tab. 4.1: Overview of the phase slowness sensitivities of particular waves to stiffness tensor elements characterizing a VTI formation. The table considers the absence and presence of an LWD tool as well as fast and slow formations. The bold variables denote a strong sensitivity to the respective stiffness tensor elements, whereas the parentheses indicate that the sensitivity is weak.

	wave mode	**slow formation**	**fast formations**
no tool	refracted P	$\boldsymbol{C_{3,3}}$	$\boldsymbol{C_{3,3}}$
	Stoneley	$\boldsymbol{C_{6,6}}$ (low freq.), $C_{4,4}$(high freq.)	($C_{6,6}$)
	flexural	$\boldsymbol{C_{4,4}}$	$\boldsymbol{C_{4,4}}$
	quadrupole	$\boldsymbol{C_{4,4}}$	$\boldsymbol{C_{4,4}}$
LWD tool	refracted P	$\boldsymbol{C_{3,3}}$	$\boldsymbol{C_{3,3}}$
	Stoneley	$\boldsymbol{C_{6,6}}$ (low freq.),$C_{4,4}$ (high freq.)	$\boldsymbol{C_{6,6}}$
	formation flexural	not present	$\boldsymbol{C_{4,4}}$
	tool flexural	$\boldsymbol{C_{4,4}}$, $\boldsymbol{C_{6,6}}$	($C_{6,6}$)
	formation quadrupole	$\boldsymbol{C_{4,4}}$	$\boldsymbol{C_{4,4}}$

tions since the *Stoneley* wave is mainly sensitive to the compressional wave velocity in the borehole fluid.

In the LWD configuration, the refracted P-wave is sensitive to the stiffness tensor element $C_{3,3}$, like in the absence of a tool. Moreover, the vertical shear wave velocity proportional to $C_{4,4}$ can be obtained from the low-frequency limit of the formation flexural wave in fast formations. In slow formations, the formation flexural wave is not present, but the stiffness tensor element $C_{4,4}$ can be obtained from a model-based inversion method of the tool flexural wave, which also exhibits a considerable sensitivity to $C_{6,6}$. In contrast, the tool flexural wave is only weakly sensitive to formation parameters in fast formations since the sensitivity to the P-wave velocity in the borehole fluid dominates. Alternatively, the stiffness tensor element $C_{4,4}$ can be obtained from the low-frequency limit of the formation quadrupole wave in both slow and fast formations.

While the stiffness tensor elements $C_{3,3}$, $C_{4,4}$, and $C_{6,6}$ can be determined by processing different refracted and borehole-guided waves, it is not possible to obtain the stiffness tensor elements $C_{1,1}$ and $C_{1,3}$ from borehole acoustic measurements in VTI formations. This is because the borehole acoustic configuration can only measure P-waves propagating on a vertical travel path but not in horizontal or other directions.

4.2. Horizontal transverse isotropy (HTI)

The second exceptional case is the HTI symmetry characterized by a TI symmetry axis (x_3''–axis) that is perpendicular to the borehole axis (x_3'–axis), as visualized in figure 4.8. Since the compressional and shear wave velocities change with azimuth, the HTI symmetry is in some literature referred to as azimuthal anisotropy (e.g., Sinha et al., 1994). The stiffness tensor elements can be transformed from the crystallographic reference frame ($\boldsymbol{x}''$) to the borehole reference frame ($\boldsymbol{x}'$) via a rotation around the x_1''–axis by $\pi/2$ radians (Sec. 2.2). In this way, the TI symmetry axis (x_3''–axis) coincides with the x_2'–axis. The stiffness tensor given in the borehole reference is defined by

$$C'_{i,j} = \begin{pmatrix} C''_{1,1} & C''_{1,3} & C''_{1,1} - 2C''_{6,6} & 0 & 0 & 0 \\ & C''_{3,3} & C''_{1,3} & 0 & 0 & 0 \\ & & C''_{1,1} & 0 & 0 & 0 \\ & & & C''_{4,4} & 0 & 0 \\ & \text{sym} & & & C''_{6,6} & 0 \\ & & & & & C''_{4,4} \end{pmatrix}, \tag{4.4}$$

where the single elements are expressed in the crystallographic reference frame. While the wave velocity of a vertically propagating P-wave is controlled by the stiffness tensor element $C''_{1,1}$ ($= C'_{3,3}$), the velocity of a horizontally propagating P-wave depends on the azimuth and has to be computed by solving the *Christoffel* equation (Eq. 2.36) in general. Nevertheless, for two principal directions, the wave velocities can be computed directly from particular stiffness tensor elements. One of those principal directions coincides with the TI symmetry axis (parallel to the x_2'–axis), and the wave velocity of a P-wave propagating in that direction is controlled by the stiffness tensor element $C''_{3,3}$ ($= C'_{2,2}$). The second principal direction lies horizontally perpendicular to the symmetry axis in the isotropic plane (parallel to the

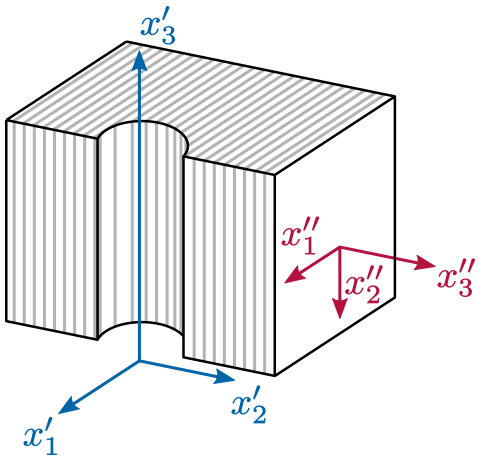

Fig. 4.8: Illustration of the TI symmetry in the crystallographic reference frame (red) and the borehole reference frame (blue), where the symmetry axis is perpendicular to the vertical borehole axis (HTI). The isotropic plane is indicated by the gray lines.

x_1'–axis), and the P-wave velocity is defined by the stiffness tensor element $C_{1,1}''$ ($= C_{1,1}'$) for that direction.

Furthermore, the wave velocities of vertically propagating shear waves in HTI formations depend on their polarization directions. The SV-wave is polarized perpendicular to the isotropic plane of the TI formation and thus parallel to the TI symmetry axis (x_2'–axis). In contrast, the SH-wave is polarized in the isotropic plane of the TI formations, i.e., perpendicular to the symmetry axis and parallel to the x_1'–axis. While the stiffness tensor element $C_{4,4}''$ determines the shear wave velocity of the vertically propagating SV-wave, the velocity of the vertically propagating SH-wave is determined by $C_{6,6}''$

$$\begin{pmatrix} \left(v_{\mathrm{ver}}^{\mathrm{P}}\right)^2 \\ \left(v_{\mathrm{ver}}^{\mathrm{SV}}\right)^2 \\ \left(v_{\mathrm{ver}}^{\mathrm{SH}}\right)^2 \end{pmatrix} = \frac{1}{\rho^{\mathrm{s}}} \begin{pmatrix} C_{1,1}'' \\ C_{4,4}'' \\ C_{6,6}'' \end{pmatrix}. \tag{4.5}$$

These shear wave velocities are often referred to as the slow shear wave velocity $v_{\mathrm{slow}}^{\mathrm{S}}$ and the fast shear wave velocity $v_{\mathrm{fast}}^{\mathrm{S}}$, characterizing the HTI formation. The shear wave polarization directions of the SH- and SV-wave are the mutually perpendicular principal directions of the HTI formation. The direction corresponding to the fast shear wave velocity is referred to as the fast principal direction, whereas the direction corresponding to the slow shear wave velocity is referred to as the slow principal direction. If a vertically propagating shear wave, who's polarization direction is not aligned with one of the principal directions, enters an HTI formation, it splits into the SH- and SV-waves. The first one is polarized in the fast principal direction propagating with fast shear wave velocity, whereas the latter is polarized in the slow principal direction propagating with slow shear wave velocity. This behavior is referred to as shear wave splitting or birefringence phenomenon.

While the shear wave splitting is well-understood for plane waves, the following sections investigate the behavior of borehole-guided waves in HTI formations. The first section investigates the omnidirectional *Stoneley* wave excited by a monopole source, which is not dependent on the source azimuth and does not split. However, its velocity in the low-frequency limit is sensitive to a known combination of stiffness tensor elements. The next section mathematically derives the theory of cylindrical wave splitting of borehole-guided waves with azimuthal wavenumbers higher than zero. It is shown that all cylindrical waves ($m > 0$) split into a fast and a slow principal wave when they enter an HTI formation. The theory is verified by FD modeling of synthetic time-domain waveforms for flexural, quadrupole, and hexapole waves in the subsequent sections. For all borehole waves, the phase slowness dispersion curves extracted from the waveform array and their sensitivities to particular stiffness tensor elements are systematically investigated in both the absence and presence of an LWD tool.

4.2.1. Monopole excitation

Figure 4.9a displays the synthetic waveform array of the borehole wavefield excited by a monopole source in a fluid-filled borehole surrounded by the fast Bakken Shale HTI formation in the absence of a logging tool. While the excited *Stoneley* wave is clearly visible, the amplitudes of the refracted P- and refracted shear waves are comparably small. However, slowness time coherence (STC) processing (App. D.1) shows different maxima corresponding to these refracted waves (Fig. 4.9c). The maximum corresponding to the refracted P-wave is located at the vertical P-wave slowness controlled by the elastic constant $C''_{1,1}$. Additionally, two maxima are found corresponding to the refracted shear waves. One maximum is located at the slowness of the vertically propagating SH-wave proportional to $C''_{6,6}$, and one maximum is located at the slowness of the vertically propagating SV-wave proportional to $C''_{4,4}$. Consequently, a monopole source excites a refracted shear wave polarized in the fast principal direction (SH-wave) and a refracted shear wave polarized in the slow principal direction (SV-wave) in fast HTI formations. Theoretically, these two refracted shear waves can be used to obtain the slow and fast principal shear wave slowness values and, thus, the stiffness tensor elements $C''_{4,4}$ and $C''_{6,6}$. However, the amplitudes of the refracted shear waves are small in the presence of an LWD tool, and it is not possible to reliably extract the refracted shear waves in real measurements because of the interference with the strong drilling noise. The upper right maximum corresponds to the *Stoneley* wave, which dispersion curve is displayed in figure 4.9b.

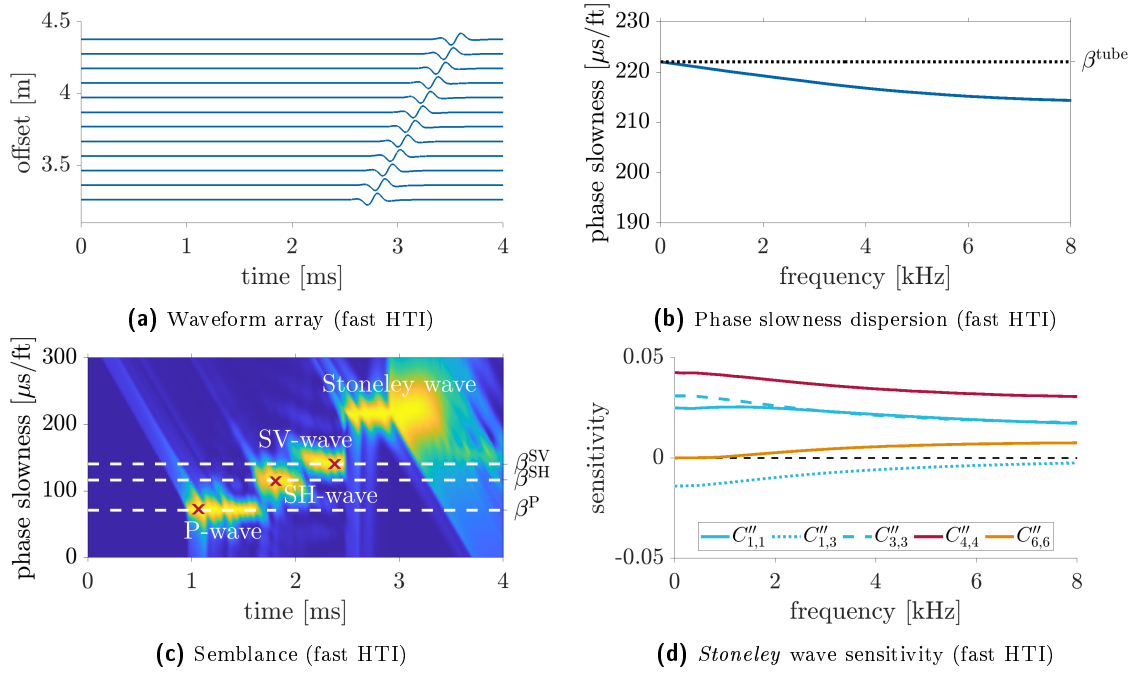

(a) Waveform array (fast HTI)

(b) Phase slowness dispersion (fast HTI)

(c) Semblance (fast HTI)

(d) *Stoneley* wave sensitivity (fast HTI)

Fig. 4.9: Monopole excitation in a fluid-filled borehole surrounded by the fast Bakken Shale HTI formation in the absence of a logging tool. The left figures display the waveform array (a) and semblance analysis (App. D.1) of the array data containing the refracted P-, refracted shear, and *Stoneley* waves (c). The right figures show the phase slowness dispersion characteristics of the *Stoneley* wave (b) and its sensitivity to formation parameters (d).

The slowness of the *Stoneley* wave in the low-frequency limit corresponds to the tube wave slowness indicated by the dotted black line. Norris and Sinha (1993) have derived a formula to compute the tube wave velocity in general TI media, which can also be applied to the HTI symmetry. Their equation is originally given in the borehole reference frame but can be straightforwardly transformed to the crystallographic reference frame, yielding

$$v^{\mathrm{tube}} = \lim_{s\to 0} v^{\mathrm{St}} = v^{\mathrm{f}} \left(1 + \frac{8\rho^{\mathrm{f}} \left(v^{\mathrm{f}}\right)^2}{C''_{1,1} + C''_{3,3} - 2C''_{1,3} + 4C''_{4,4}} \right)^{\left(-\frac{1}{2}\right)} . \tag{4.6}$$

The equation can be qualitatively validated by the sensitivity analysis of the *Stoneley* wave slowness dispersion curve to the stiffness tensor elements of the formation. While the phase slowness of the *Stoneley* wave is highly sensitive to the borehole fluid in the range 0.8–0.9 at all frequencies (omitted in Fig. 4.9d), it is less sensitive to the formation parameters displayed in figure 4.9d. Nevertheless, the sensitivity to the formation parameters is highest to the stiffness tensor elements $C''_{4,4}$ and zero to $C''_{6,6}$ at low frequencies. While the sensitivity to the elements $C''_{1,1}$ and $C''_{3,3}$ has a similar magnitude, the sensitivity to $C''_{1,3}$ has an opposite sign. These results are consistent with equation 4.6, where the components $C''_{1,1}$ and $C''_{3,3}$ are multiplied by one, the component $C''_{1,3}$ is subtracted, and the component $C''_{4,4}$ has the largest factor.

The presence of an LWD tool strongly alters the tube wave velocity, as displayed in figure 4.10a, and causes that equation 4.6 is no longer valid. Nevertheless, the sensitivity of the *Stoneley* wave slowness to the stiffness tensor elements is similar as in the absence of a logging tool (Fig. 4.10b). The sensitivity to the stiffness tensor elements is higher in the LWD configuration, whereas the *Stoneley* wave is less sensitive to the compressional wave velocity in the borehole fluid. The reason for this is that the borehole fluid occupies only a small fluid annulus in the presence of the large LWD tool.

Besides, the *Stoneley* wave is not sensitive to azimuthal variations in the shear wave velocities due to its omnidirectional nature (Fig. 1.2d). Hence, the azimuthal excitation direction of the monopole source relative to the principal directions of the HTI formation does not influence the *Stoneley* wave dispersion curve.

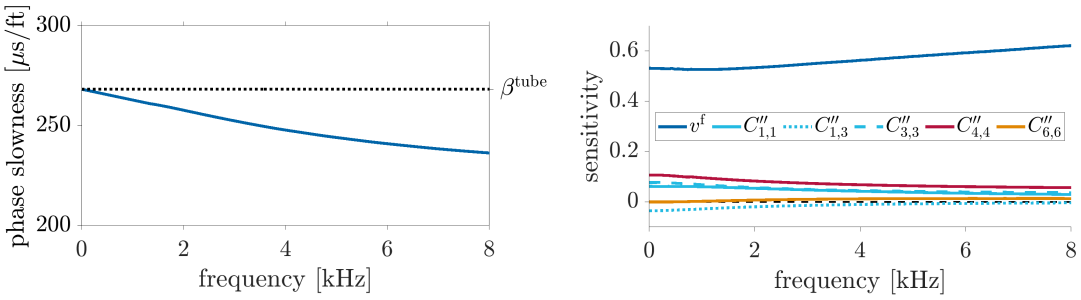

(a) Phase slowness dispersion (fast HTI)

(b) *Stoneley* wave sensitivity (fast HTI)

Fig. 4.10: Monopole excitation in a fluid-filled borehole surrounded by the fast Bakken Shale HTI formation in the presence of an LWD tool. The figures display the phase slowness dispersion curve of the *Stoneley* wave (a) and its sensitivity to formation parameters (b).

4.2.2. Theory of cross-multipole shear wave splitting

While the *Stoneley* wave exhibits an omnidirectional directivity, the flexural wave ($m = 1$) and higher-order modes are directional, and their directivities are defined by $\cos(m\theta)$ (Fig. 1.2e and 1.2f). Consequently, these wave modes $m \geq 1$ depend on the azimuthal source excitation direction relative to the principal directions of the HTI formation. Esmersoy et al. (1994) and Mueller et al. (1994) have shown that in HTI formations, two principal flexural waves exist, which propagate with different velocities. A dipole source aligned with the fast principal direction of the HTI formation excites the fast principal flexural wave C_1^{F}, whereas a dipole source aligned with the slow principal direction excites the slow principal flexural wave C_1^{S}. This is analogous to the vertically propagating SH- and SV-waves in HTI media, which are polarized in the fast and slow principal directions, respectively. Furthermore, if the dipole excitation direction is not aligned with the principal directions, the excited flexural wave splits into the slow and the fast principal flexural wave, such as a vertically propagating shear wave.

This section explains that the fundamental concept of dipole shear wave splitting in HTI formations can be generalized to all higher-order cylindrical waves. The following work was previously published in the form of an expanded abstract for the 90th annual meeting of the *Society of Exploration Geophysicists* (SEG) in Demmler et al. (2020). The starting point for explaining the theory is a summary of the fundamental results that apply to the borehole acoustic pressure due to an alternate polarity double multipole excitation in isotropic formations (Przebindowska and Geerits, 2019). Based on this, the four-component cross-multipole pressure data matrix is defined. Subsequently, the concept of HTI shear wave splitting is generalized to alternate polarity multipole modes ($m > 0$).

Alternate polarity double multipole excitation in isotropic formations

Figure 4.11 illustrates a cross-section of an alternate polarity cross-multipole source or receiver of the excitation order n. The double multipole source consists of two single multipole sources azimuthally shifted from each other by $\pi/(2n)$ radians. While the blue multipole source

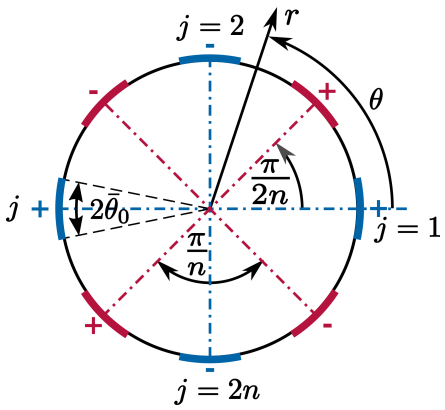

Fig. 4.11: Schematic view of the cross-section of an alternate polarity double multipole source/receiver consisting of one single X-multipole source/receiver (blue) and one single Y-multipole source/receiver (red) separated azimuthally by $\pi/(2n)$ radians.

is referred to as the X-multipole source, the red multipole source is referred to as the Y-multipole source. The azimuthal locations of the single constituting sources are defined for the X-multipole source as

$$\theta_j^X = (j-1)\frac{\pi}{n}, \qquad j = 1, ..., 2n, \tag{4.7a}$$

and for the Y-multipole source as

$$\theta_j^Y = \frac{\pi}{2n} + (j-1)\frac{\pi}{n}, \qquad j = 1, ..., 2n. \tag{4.7b}$$

Accordingly, the azimuthal location of the first constituting source of the X-multipole source is $\theta_1^X = 0$. The azimuthal locations of the constituent multipole sources and receivers are coincident.

Przebindowska and Geerits (2019) expressed the acoustic pressure of the wavefield emitted by such an alternate polarity double multipole surface source in a homogeneous and isotropic formation as

$$\check{p}(r,\theta,z,s) = \overbrace{\sum_{k=\text{odd}} \check{C}_{kn}(r,z,s)\cos(kn\theta)}^{\check{p}_X} \pm \overbrace{\sum_{k=\text{odd}} \check{C}_{kn}(r,z,s)\sin(kn\theta)}^{\check{p}_Y} \begin{cases} k = 1,5,9,\dots \\ k = 3,7,11,\dots \end{cases}. \tag{4.8}$$

According to equation 4.8, the borehole acoustic pressure $\check{p}$ is a superposition of that originating from the X-multipole source ($\check{p}_X$) and the Y-multipole source ($\check{p}_Y$). The relationship between the effective cylinder functions $\check{C}_{kn}$ and the excitation functions $\check{C}_{kn}^{q'}$ is given by (Geerits and Kranz, 2017)

$$\check{C}_{kn}(r,z,s) = \frac{2nA_p\check{a}_0(s)}{4\pi^2}\rho^{\mathrm{s}}2\check{C}_{kn}^{q'}(r,z,s)W_{kn}(\bar{\theta}_0). \tag{4.9}$$

In this equation 4.9, A_p represents the surface area of a single, cylindrically shaped surface source, and $\check{a}_0$ represents its associated uniform acceleration. The wavefield weighting function W_{kn} describes the azimuthal filtering effect caused by the finite azimuthal aperture ($\bar{\theta}_0$) of the constituting sources (Geerits and Kranz, 2017).

Four-component multipole data matrix

The four-component multipole pressure data matrix $\check{\mathcal{P}}$ is defined as

$$\check{\mathcal{P}}(r,z_0,s) = \begin{pmatrix} \check{p}_{XX} & \check{p}_{XY} \\ \check{p}_{YX} & \check{p}_{YY} \end{pmatrix}. \tag{4.10}$$

The matrix contains the two in-line components, $\check{p}_{XX}$ and $\check{p}_{YY}$, and the two cross-line components, $\check{p}_{XY}$ and $\check{p}_{YX}$. The first subscript letter of these components refers to the multipole source and the second subscript letter refers to the multipole receiver. For instance, the component $\check{p}_{XX}$ describes the acoustic pressure of the wavefield emitted by the X-multipole

source and received by the X-multipole receiver. The pressure values received at the single constituting receivers are stacked using an alternating polarity according to

$$\check{p}_{XX}(r,z_0,s)=\sum_{j=1}^{2n}(-1)^{(j-1)}\hat{p}_X(r,\theta_j^X,z_0,s)=2n\sum_{k=\text{odd}}\check{C}_{kn}(r,z,s). \tag{4.11a}$$

The acoustic pressure emitted by the X-multipole source is defined by the first term in equation 4.8, and the azimuthal locations of the constituting receiver are defined in equation 4.7a. Similarly, the in-line component $\check{p}_{YY}$ is defined as

$$\check{p}_{YY}(r,z_0,s)=\sum_{j=1}^{2n}(-1)^{(j-1)}\hat{p}_Y(r,\theta_j^Y,z_0,s)=$$

$$\pm\,2n\sum_{k=\text{odd}}\check{C}_{kn}(r,z,s),\ \begin{cases}k=1,5,9,\ldots,\text{etc.}\\ k=3,7,11,\ldots,\text{etc.}\end{cases}, \tag{4.11b}$$

using the second term of equation 4.8 and the receiver azimuths defined in equation 4.7b. In contrast, the cross-line components vanish

$$\check{p}_{XY}(r,z_0,s)=\sum_{j=1}^{2n}(-1)^{(j-1)}\hat{p}_X(r,\theta_j^Y,z_0,s)=0, \tag{4.11c}$$

$$\check{p}_{YX}(r,z_0,s)=\sum_{j=1}^{2n}(-1)^{(j-1)}\hat{p}_Y(r,\theta_j^X,z_0,s)=0. \tag{4.11d}$$

The generalization to HTI media

The above results that apply in isotropic formations can be extended to HTI media by making fundamental assumptions. In analogy to the two principal polarization directions of a vertically propagating shear wave, it is assumed that there are two principal excitation functions. The first is associated with the fast principal direction denoted by $\check{C}_{kn}^{\text{F}}$, whereas the second is associated with the slow principal direction denoted by $\check{C}_{kn}^{\text{S}}$. Assuming the fast principal direction corresponds to the azimuth $\theta=0$, it can be postulated that the X-multipole source excites the fast principal wave and the Y-multipole source excites the slow principal wave

$$\check{p}_X(r,\theta,z,s)=\sum_{k=\text{odd}(>0)}\check{C}_{kn}^{\text{F}}(r,z,s)\cos(kn\theta), \tag{4.12}$$

$$\check{p}_Y(r,\theta,z,s)=\pm\sum_{k=\text{odd}(>0)}\check{C}_{kn}^{\text{S}}(r,z,s)\sin(kn\theta),\ \begin{cases}k=1,5,9,\ldots,\text{etc.}\\ k=3,7,11,\ldots,\text{etc.}\end{cases}. \tag{4.13}$$

For the following explanations, only the leading term $k=1$ is considered ($m=kn$). Figure 4.12a illustrates the leading term of the fast principal wave $C_n^{\text{F}}(r,z,s)\cos(n\theta)$ and the slow principal wave $C_n^{\text{S}}(r,z,s)\sin(n\theta)$. The azimuth measurement unit in the figure is $n\theta$

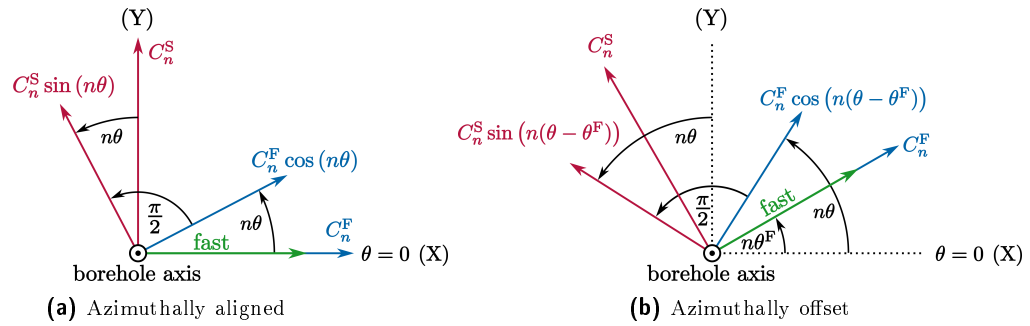

(a) Azimuthally aligned **(b)** Azimuthally offset

Fig. 4.12: Illustration of multipole shear wave splitting in terms of the principal fast (C_n^F) and slow (C_n^S) cylindrical waves, where the X-multipole source is aligned to the fast principal direction (a) and azimuthally offset by the angle $n\theta^F$ to it (b). The azimuth measurement unit in the figures is $n\theta$ instead of θ.

instead of θ, which justifies the notion that the fast principal wave is orthogonal to the slow principal wave independent of the excitation order n for all angles $n\theta$. Since the X-multipole source, which first constituting source azimuth coincides with $n\theta = 0$, only excites the fast principal wave, the multipole source is aligned with the fast principal direction. Analogously, the Y-multipole source, which first constituting source azimuth coincides with $n\theta = \pi/2$, is aligned with the slow principal direction because it excites only the slow principal wave.

In the general case, neither the X- nor the Y-multipole source is aligned with the principal directions of the formation (Fig. 4.12b). Thus, both the fast and the slow principal waves are excited, irrespective of which of the two multipole sources is fired. Consequently, any multipole source that is not aligned with the principal directions of the HTI formation excites a weighted superposition of the fast and slow principal waves. The weights are defined by projecting the amplitudes of the fast and slow principal waves onto the X- and Y-excitation directions, respectively. According to figure 4.12b, the acoustic pressure of the wavefield emitted by the X-multipole source that is not aligned with a principal direction can be postulated by

$$\begin{aligned}\check{p}_X(r,\theta,z,s) = &\cos\left(n\theta^F\right)\check{C}_n^F(r,z,s)\cos\left(n\left(\theta-\theta^F\right)\right)\\ &-\sin\left(n\theta^F\right)\check{C}_n^S(r,z,s)\sin\left(n\left(\theta-\theta^F\right)\right).\end{aligned} \tag{4.14}$$

Similarly, an equation can be derived for the azimuthal offset Y-multipole excitation

$$\begin{aligned}\check{p}_Y(r,\theta,z,s) = &\sin\left(n\theta^F\right)\check{C}_n^F(r,z,s)\cos\left(n\left(\theta-\theta^F\right)\right)\\ &+\cos\left(n\theta^F\right)\check{C}_n^S(r,z,s)\sin\left(n\left(\theta-\theta^F\right)\right).\end{aligned} \tag{4.15}$$

The angle θ^F denotes the azimuth between the first constituting source of the X-multipole source and the fast principal direction of the formation (Fig. 4.12b).

The generalized formula for the Alford Rotation

For the definition of the four-component pressure data matrix in HTI formations, the definitions from equations 4.11a–4.11d are used, in which equations 4.14 and 4.15 are substituted.

The resulting data matrix components are given by

$$\check{p}_{XX}(r,z_0,s) = 2n\left[\check{C}_n^{\mathrm{F}}(r,z_0,s)\cos^2(n\theta^{\mathrm{F}}) + \check{C}_n^{\mathrm{S}}(r,z_0,s)\sin^2(n\theta^{\mathrm{F}})\right], \quad (4.16a)$$

$$\check{p}_{YY}(r,z_0,s) = 2n\left[\check{C}_n^{\mathrm{F}}(r,z_0,s)\sin^2(n\theta^{\mathrm{F}}) + \check{C}_n^{\mathrm{S}}(r,z_0,s)\cos^2(n\theta^{\mathrm{F}})\right], \quad (4.16b)$$

$$\check{p}_{XY}(r,z_0,s) = \check{p}_{YX}(r,z_0,s) = 2n\left[\check{C}_n^{\mathrm{F}}(r,z_0,s) - \check{C}_n^{\mathrm{S}}(r,z_0,s)\right]\sin(n\theta^{\mathrm{F}})\cos(n\theta^{\mathrm{F}}). \quad (4.16c)$$

Using the matrix definition (Eq. 4.10), the above equations can be rewritten into matrix form

$$\check{\mathcal{P}}(r,z_0,s) = \mathcal{R}(n\theta^{\mathrm{F}})\check{\mathcal{G}}_n(r,z_0,s)\mathcal{R}^{\mathrm{T}}(n\theta^{\mathrm{F}}), \quad (4.17a)$$

where

$$\mathcal{R}(n\theta^{\mathrm{F}}) = \begin{pmatrix} \cos(n\theta^{\mathrm{F}}) & -\sin(n\theta^{\mathrm{F}}) \\ \sin(n\theta^{\mathrm{F}}) & \cos(n\theta^{\mathrm{F}}) \end{pmatrix}, \quad (4.17b)$$

and

$$\check{\mathcal{G}}_n(r,z_0,s) = 2n\begin{pmatrix} \check{C}_n^{\mathrm{F}} & 0 \\ 0 & \check{C}_n^{\mathrm{S}} \end{pmatrix}(r,z_0,s). \quad (4.17c)$$

Equations 4.17a–4.17c represent a generalization of the *Alford* rotation (Alford, 1986). The original formula was introduced by Alford (1986) for the excitation order $n = 1$, wherefore it only applies to flexural waves. In contrast, this generalization applies to all vector-cylindrical waves, which can all be considered as scaled dipoles, thereby excluding the monopole having the azimuthal wavenumber zero.

Non-orthogonal firings

The above-presented generalized formula for the *Alford* rotation assumes an orthogonal firing of the cross-multipole source, i.e., the X- and Y-multipole source firings are azimuthally separated by $\pi/(2n)$. Since the X- and Y-multipole sources cannot be fired simultaneously, they are fired in sequence. However, in LWD measurements, the tool rotates between the X- and the Y-multipole source firings. Thus, the fast tool rotation prevents orthogonal firings, and both excitations are, in general, non-orthogonal. The advantage of the tool rotation is that a cross-multipole source is not necessary since one multipole source can be fired in sequence at different azimuths utilizing the tool rotation. For both firings, the four-component pressure data matrix is measured by the in-line and cross-line multipole receivers that are still orthogonal to each other.

The above-defined formulas for the *Alford* rotation are extended to apply for non-orthogonal firings according to figure 4.13 illustrating the multipole shear wave splitting for the two non-orthogonal X-multipole and Y*-multipole excitations. The star indicates that the Y*-multipole excitation is not necessarily orthogonal to the X-multipole excitation. The azimuth

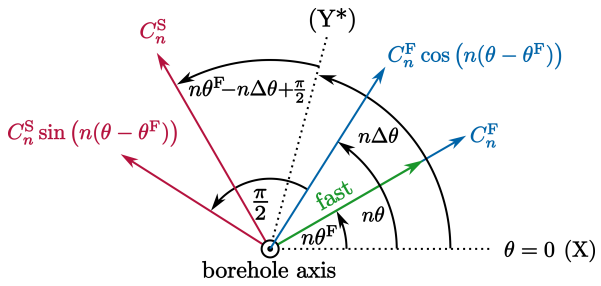

Fig. 4.13: Illustration of multipole shear wave splitting in terms of the principal fast (C_n^{F}) and slow (C_n^{S}) cylindrical waves, where the X- and Y*-multipole sources are not fired orthogonal to each other. Both excitation directions are azimuthally offset to the principal directions of the formation. The azimuth measurement unit in the figures is $n\theta$ instead of θ.

between both sources is referred to as $\Delta\theta$. In the general case, neither of the multipole sources is aligned with the principal directions of the formation. Consequently, both sources excite a weighted superposition of the fast and slow principal cylindrical waves. As explained above, the weights are defined by the projection of the principal wave's amplitudes onto the X- and Y*-excitation directions, respectively. While Eq. 4.14 for the acoustic pressure of the wavefield emitted by the X-multipole source does not change, equation 4.15 is changed to a more general form according to figure 4.13

$$\begin{aligned}\check{p}_{Y^*}(r,\theta,z,s) = &\cos\left(n\left(\theta^{\mathrm{F}}-\Delta\theta\right)\right)\check{C}_n{}^{\mathrm{F}}(r,z,s)\cos\left(n\left(\theta-\theta^{\mathrm{F}}\right)\right)\\ &-\sin\left(n\left(\theta^{\mathrm{F}}-\Delta\theta\right)\right)\check{C}_n{}^{\mathrm{S}}(r,z,s)\sin\left(n\left(\theta-\theta^{\mathrm{F}}\right)\right).\end{aligned} \tag{4.18}$$

In the next step, the elements of the four-component data matrix are computed. Therefore, it must be noted that the azimuthal locations of the cross-line receivers for the X-multipole excitation (θ_j^Y) are different from the azimuthal locations of the in-line receivers for the Y*-multipole excitation ($\theta_j^{Y^*}$). The other way around, the locations of the cross-line receivers ($\theta_j^{X^*}$) for the Y*-multipole excitation do not coincide with the in-line receivers for the X-multipole excitation (θ_j^X). The azimuthal locations of the in-line and cross-line receivers for the X-multipole excitations are defined in equations 4.7a and 4.7b, whereas the locations of the in-line and cross-line receivers for the Y*-multipole excitation are given by

$$\theta_j^{Y^*} = \Delta\theta + (j-1)\frac{\pi}{n}, \qquad \theta_j^{X^*} = \Delta\theta - \frac{\pi}{2n} + (j-1)\frac{\pi}{n}, \qquad j = 1,...,2n. \tag{4.19}$$

These receiver positions are used for stacking the components of the in-line and cross-line components of the four-component data matrix

$$\check{p}_{XX}(r,z_0,s) = 2n\left[\check{C}_n^{\mathrm{F}}(r,z_0,s)\cos^2(n\theta^{\mathrm{F}}) + \check{C}_n^{\mathrm{S}}(r,z_0,s)\sin^2(n\theta^{\mathrm{F}})\right], \tag{4.20a}$$

$$\check{p}_{XY}(r,z_0,s) = 2n\left[\check{C}_n^{\mathrm{F}}(r,z_0,s) - \check{C}_n^{\mathrm{S}}(r,z_0,s)\right]\sin(n\theta^{\mathrm{F}})\cos(n\theta^{\mathrm{F}}), \tag{4.20b}$$

$$\begin{aligned}\check{p}_{Y^*Y^*}(r,z_0,s) = 2n\Big[&\check{C}_n^{\mathrm{F}}(r,z_0,s)\cos^2\left(n\left(\theta^{\mathrm{F}}-\Delta\theta\right)\right)\\ &+\check{C}_n^{\mathrm{S}}(r,z_0,s)\sin^2\left(n\left(\theta^{\mathrm{F}}-\Delta\theta\right)\right)\Big],\end{aligned} \tag{4.20c}$$

$$\check{p}_{Y^*X^*}(r,z_0,s) = 2n\left[\check{C}_n^{\mathrm{S}}(r,z_0,s) - \check{C}_n^{\mathrm{F}}(r,z_0,s)\right]\sin\left(n\left(\theta^{\mathrm{F}}-\Delta\theta\right)\right)\cos\left(n\left(\theta^{\mathrm{F}}-\Delta\theta\right)\right). \tag{4.20d}$$

These equations for the in-line and cross-line components can also be rewritten into the matrix-vector form

$$\begin{bmatrix} (\check{p}_{XX},\ \check{p}_{XY}) \\ (\check{p}_{Y^*X^*},\ \check{p}_{Y^*Y^*})\,\mathcal{R}^{\mathrm{T}}(n\Delta\theta - \frac{\pi}{2}) \end{bmatrix} (r, z_0, s) = \mathcal{Q}(n\Delta\theta)\mathcal{R}(n\theta^{\mathrm{F}})\check{\mathcal{G}}_n(r, z_0, s)\mathcal{R}^{\mathrm{T}}(n\theta^{\mathrm{F}}). \quad (4.21a)$$

While the rotation matrix $\mathcal{R}$ and the matrix $\check{\mathcal{G}}_n$, containing the principal cylindrical waves, are defined in equation 4.17b and 4.17c, respectively, the matrix $\mathcal{Q}$ is defined as

$$\mathcal{Q}(n\Delta\theta) = \begin{pmatrix} 1 & 0 \\ \cos(n\Delta\theta) & \sin(n\Delta\theta) \end{pmatrix}. \quad (4.21b)$$

The matrix $\mathcal{Q}$ is composed of the first row of the unity matrix and the second row of the rotation matrix $\mathcal{R}^{\mathrm{T}}(n\Delta\theta - \pi/2)$. If the X- and Y-multipole sources are orthogonal ($n\Delta\theta = \pi/2$), the matrix $\mathcal{Q}$ becomes the unity matrix, and equation 4.21a reduces to the formula for an orthogonal cross-multipole excitation (Eq. 4.17a).

4.2.3. Dipole excitation

According to the above theory, a dipole source aligned with the fast principal direction of the formation only excites the fast principal flexural wave C_1^{F}, whereas a dipole source aligned with the slow principal direction excited the slow principal flexural wave C_1^{S} (Fig. 4.14a–4.14b). Consequently, the four-component data matrix $\mathcal{P}$ of the wavefield excited by an aligned cross-

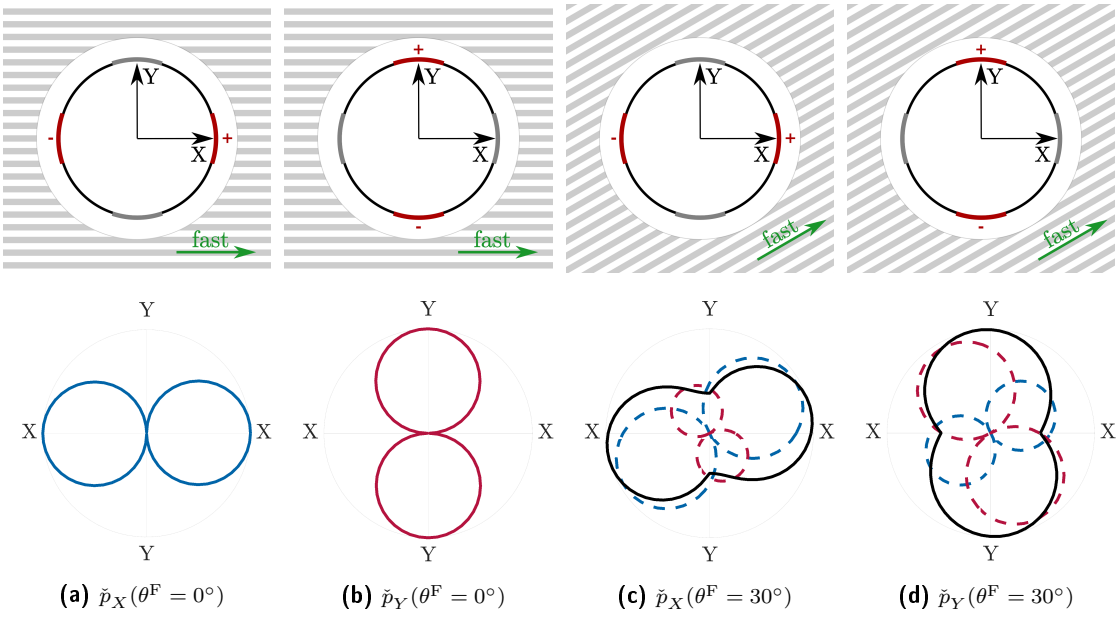

Fig. 4.14: Directivities of the flexural waves excited by cross-dipole sources aligned with the formation's principal directions (a–b) and azimuthally offset to them by $\theta^{\mathrm{F}} = 30°$ (c–d). The directivity is computed from the maximum absolute amplitude of the functions $\check{p}_X$ (Eq. 4.14) and $\check{p}_Y$ (Eq. 4.15), respectively, at a fixed radius and the axial offset $z_0 = 3.262\,\mathrm{m}$. The directivity of the fast principal flexural wave is displayed in blue, whereas the slow one is plotted in red. In the azimuthally offset case (c–d), the excited flexural wave splits into the fast and slow principal flexural waves, as indicated by the dashed lines.

dipole source equals the matrix $\mathcal{G}_1$, where the off-diagonal elements are zero, and the diagonal elements contain the fast and slow principal flexural waves, respectively. Figure 4.15 shows the time-domain waveforms of this matrix, which are excited by a cross-dipole source aligned with the principal directions of the slow Austin Chalk HTI formation. The source is centered in a fluid-filled borehole in the absence of a logging tool, and the receiver is axially offset by $z_0 = 3.262\,\mathrm{m}$.

The phase slowness dispersion curves of both principal flexural waves are displayed in figure 4.16a by the solid lines. In comparison, the dashed lines illustrate the dispersion curves of the flexural waves, which are excited in isotropic formations having the shear modulus $\mu = C''_{6,6}$ and $\mu = C''_{4,4}$, respectively. The dispersion curves of the fast and slow principal flexural waves excited in HTI formations lie at all frequencies between the dispersion curves of their isotropic counterparts. Furthermore, the low-frequency limit of the fast principal flexural wave corresponds to the fast shear wave slowness $\beta^{\mathrm{S}}_{\mathrm{fast}}$ proportional to $C''_{6,6}$, whereas the slow principal flexural wave attains the slow shear wave slowness $\beta^{\mathrm{S}}_{\mathrm{slow}}$ proportional to $C''_{4,4}$ at the cutoff frequency. Additionally, it can be seen that the cutoff frequency of the slow principal flexural wave is slightly higher than the cutoff frequency of the fast principal flexural wave. The sensitivities of the fast and slow principal flexural wave dispersion curves to the stiffness tensor elements $C''_{4,4}$, $C''_{6,6}$, and to the fluid compressional velocity v^{f} are displayed in figures 4.16c and 4.16e, respectively. As expected, the sensitivity of the fast principal flexural wave dispersion curve is highest to the elastic constant $C''_{6,6}$ and zero to $C''_{4,4}$ at low frequencies.

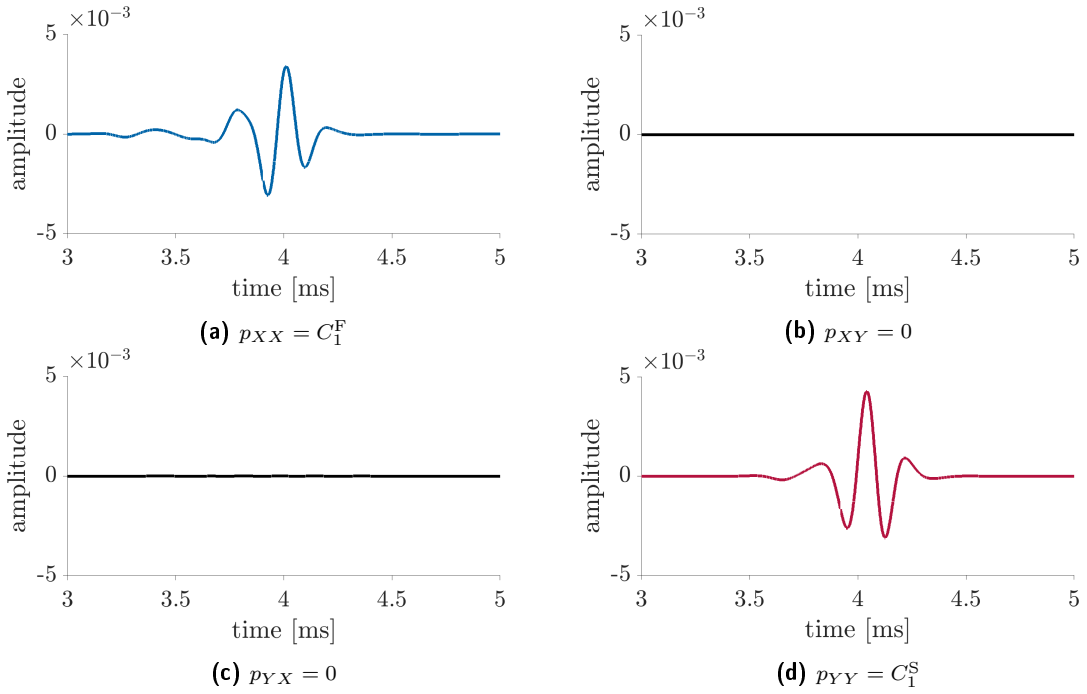

Fig. 4.15: Four-component pressure data matrix of the time-domain waveforms excited by a cross-dipole source aligned to the principal directions of the slow Austin Chalk HTI formation. The source ($f_{\mathrm{c}} = 4\,\mathrm{kHz}$) is centered in a fluid-filled borehole in the absence of a logging tool, and the axial offset between the cross-dipole source and the cross-dipole receiver is $z_0 = 3.262\,\mathrm{m}$. The in-line components (a, d) contain the waveforms of the fast and slow principal flexural waves plotted in blue and red, respectively.

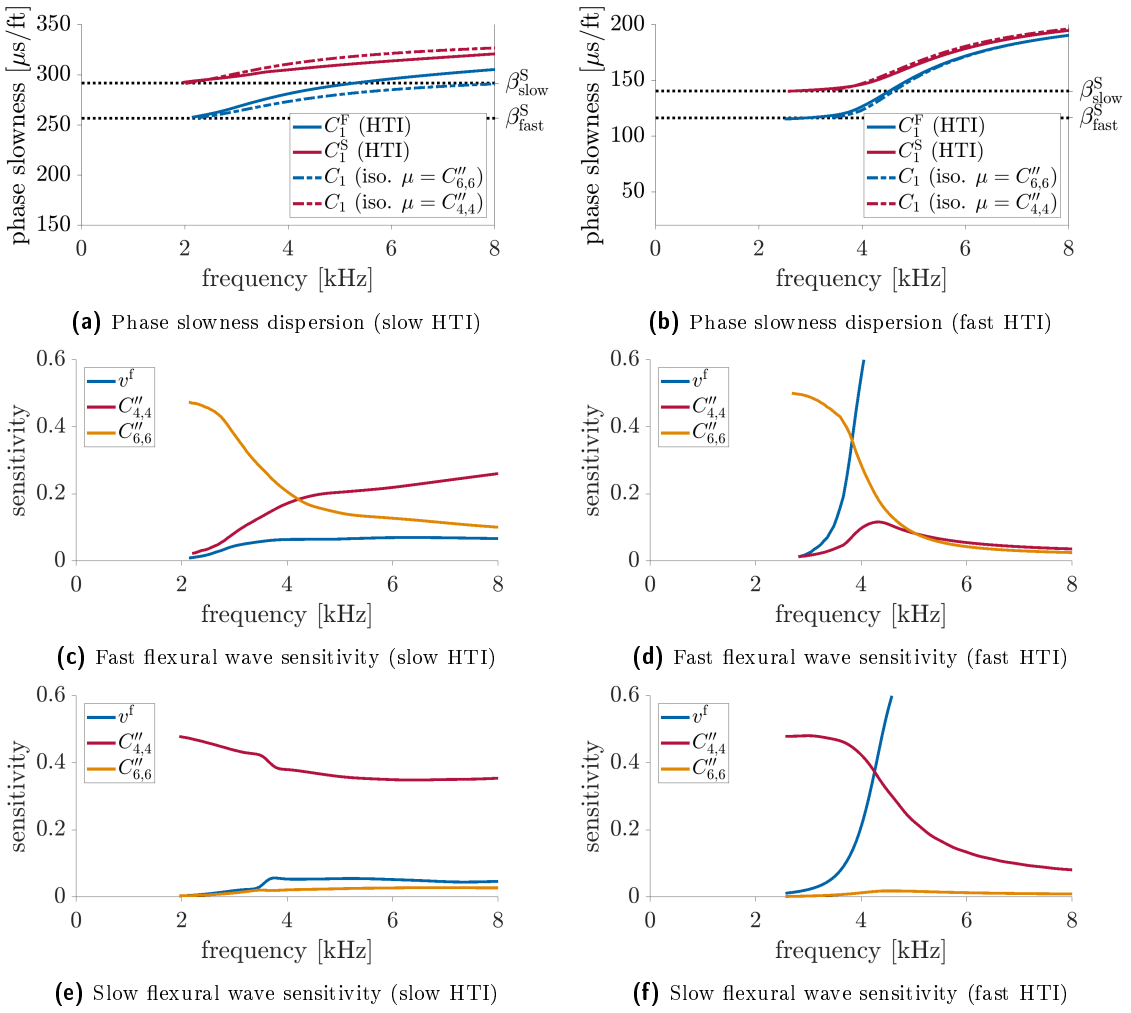

(a) Phase slowness dispersion (slow HTI)

(b) Phase slowness dispersion (fast HTI)

(c) Fast flexural wave sensitivity (slow HTI)

(d) Fast flexural wave sensitivity (fast HTI)

(e) Slow flexural wave sensitivity (slow HTI)

(f) Slow flexural wave sensitivity (fast HTI)

Fig. 4.16: Phase slowness dispersion curves and sensitivity analysis of the principal flexural waves excited in a fluid-filled borehole surrounded by the slow Austin Chalk (left) and fast Bakken Shale (right) HTI formations in the absence of an LWD tool. The solid lines in the first-row figures (a–b) display the phase slowness dispersion curves of the fast and slow principal flexural waves compared to the isotropic counterparts illustrated by the dashed red ($\mu = C''_{4,4}$) and blue ($\mu = C''_{6,6}$) lines, respectively. The black lines represent the formation's fast (β^{S}_{fast}) and slow (β^{S}_{slow}) shear wave slowness. The bottom figures show the sensitivity of the fast (c–d) and slow (e–f) principal flexural wave slowness to the P-wave velocity in the borehole fluid (v^f) and the stiffness tensor elements $C''_{4,4}$ and $C''_{6,6}$ of the formation.

At higher frequencies, the sensitivity to $C''_{6,6}$ decreases, and the sensitivity to $C''_{4,4}$ increases. In contrast, the sensitivity of the slow principal flexural wave dispersion curve is highest to $C''_{4,4}$ and zero to $C''_{6,6}$ at the cutoff frequency. The sensitivity to $C''_{4,4}$ remains dominant also at higher frequencies.

If the slow Austin Chalk HTI formation is replaced by the fast Bakken Shale HTI formation, similar behavior is observed. The fast principal flexural wave attains the fast shear wave slowness at the cutoff frequency, while the low-frequency limit of the slow principal flexural wave corresponds to the slow shear wave slowness (Fig. 4.16b). Furthermore, it is visualized that the phase slowness dispersion curves of the fast and slow principal flexural waves are very similar to their corresponding isotropic counterparts. At low frequencies, the sensitivity of the fast principal flexural wave dispersion curve is highest to $C''_{6,6}$ and zero to $C''_{4,4}$, whereas

the slow flexural wave dispersion curve is highest sensitive to $C''_{4,4}$ and zero to $C''_{6,6}$. Besides, both principal flexural wave dispersion curves are much more sensitive to the borehole fluid compressional velocity in the fast Bakken Shale formation than in the slow Austin Chalk formation.

The sensitivity analysis and the phase slowness dispersion curves of the fast and slow principal dipole waves have shown that the first one is suitable for determining the formation's fast shear wave slowness, whereas the latter can be used to obtain the slow shear wave slowness of the formation. However, the problem in real measurements is that the azimuth of the fast and slow principal direction is unknown. Consequently, the dipole excitation is, in general, not aligned with a principal direction, and a weighted superposition of the fast and the slow flexural wave is excited according to the theory in section 4.2.2 and figures 4.14c–4.14d. Figure 4.17 displays the time-domain waveforms of the four-component pressure data matrix, which are excited by a cross-dipole source azimuthally offset to the principal directions of the slow Austin Chalk HTI formation by $\theta^{\mathrm{F}} = 30°$. Since both the fast and the slow principal waves are excited, the cross-line components p_{XY} and p_{YX} of the four-component data matrix become non-zero. The blue lines illustrate the time-domain waveforms obtained from FD modeling of an azimuthally offset cross-dipole source. In comparison, the red waveforms are computed by rotating the FD modeled fast and slow principal flexural waves (Fig. 4.15a and 4.15d) utilizing the formula for the *Alford* rotation (Eq. 4.17). The coincidence of the waveforms for all components validates this equation. Using the inverse formula of the *Alford*

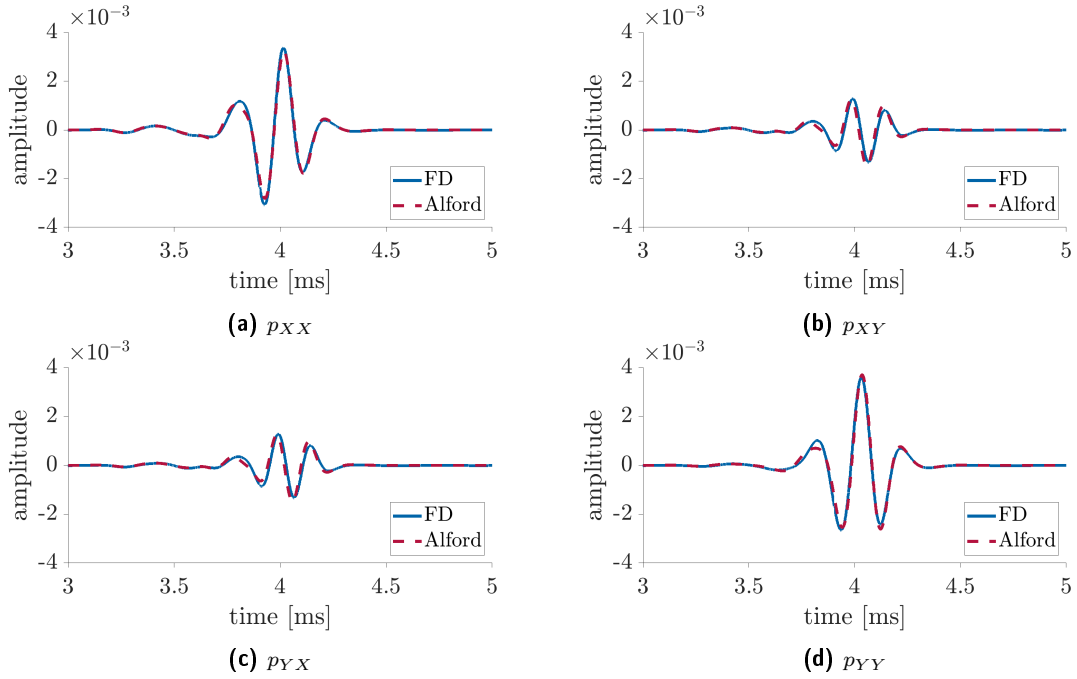

Fig. 4.17: Four-component pressure data matrix of the time-domain waveforms excited by a cross-dipole source azimuthally offset to the principal directions of the slow Austin Chalk HTI formation by $\theta^{\mathrm{F}} = 30°$. The source ($f_{\mathrm{c}} = 4\,\mathrm{kHz}$) is centered in a fluid-filled borehole in the absence of a logging tool, and the axial offset between the cross-dipole source and the cross-dipole receiver is $z_0 = 3.262\,\mathrm{m}$. The blue waveforms result from FD modeling using an azimuthally offset cross-dipole source, whereas the red waveforms are computed by rotating the modeled waveforms of the principal flexural waves (Fig. 4.15) via the *Alford* rotation.

rotation, it is possible to obtain the fast and slow principal flexural waves from cross-dipole measurements that are azimuthally offset to the fast and slow principal directions (Sec. 5.2). Subsequently, the formation's fast and slow shear wave slowness can be obtained from the phase slowness dispersion curves of both principal waves in the low-frequency limit.

While the above investigation assumes an open fluid-filled borehole without a logging tool, the results become different in an LWD environment. The presence of the LWD tool causes tool flexural waves, which strongly affect the formation flexural waves, as discussed in section 1.3 for the isotropic case. Similar to the VTI case, the formation flexural wave is not present in the slow Austin Chalk HTI formation (Fig. 4.18a) and thus cannot be used to determine the fast and slow shear wave slowness. Nevertheless, figure 4.18a presents that the tool flexural wave excited by a dipole source aligned with the formation's fast principal direction differs from the tool flexural wave excited by a dipole source aligned with the formation's slow principal

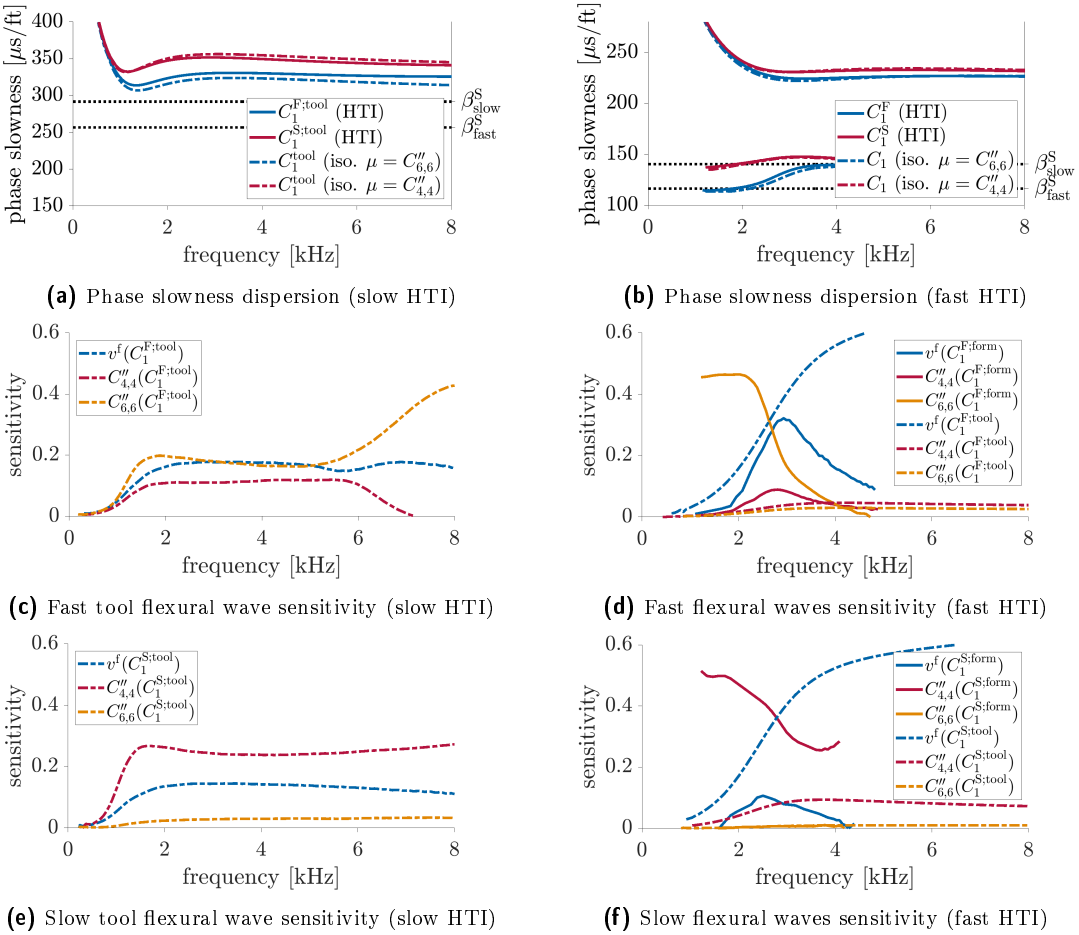

Fig. 4.18: Phase slowness dispersion curves and sensitivity analysis of the principal tool and formation flexural waves excited in a fluid-filled borehole surrounded by the slow Austin Chalk (left) and fast Bakken Shale (right) HTI formations in the presence of an LWD tool. The solid lines in the first-row figures (a–b) display the phase slowness dispersion curves of the fast and slow principal tool and formation flexural waves compared to their isotropic counterparts illustrated by the dashed red ($\mu = C''_{4,4}$) and blue ($\mu = C''_{6,6}$) lines, respectively. The black lines represent the formation's fast ($\beta^{\mathrm{S}}_{\mathrm{fast}}$) and slow ($\beta^{\mathrm{S}}_{\mathrm{slow}}$) shear wave slowness. The bottom figures (c–f) show the sensitivity of the principal tool (dashed lines) and formation (solid lines) flexural wave slowness to the P-wave velocity in the borehole fluid (v^{f}) and the stiffness tensor elements $C''_{4,4}$ and $C''_{6,6}$ of the formation.

direction. Consequently, the tool flexural wave must also be sensitive to formation parameters. The sensitivity analysis of the fast tool flexural wave (Fig. 4.18c) shows the sensitivity of its phase dispersion curve to the elastic constants $C''_{4,4}$ and $C''_{6,6}$ at frequencies greater than 1 kHz. The sensitivity to the elastic modulus $C''_{6,6}$ controlling the fast shear wave slowness is higher than to the elastic modulus $C''_{4,4}$ defining the slow shear wave slowness. Analogously, the sensitivity of the dispersion curve of the slow tool flexural wave is higher to the elastic constant $C''_{4,4}$ than to $C''_{6,6}$ (Fig. 4.18e).

The right column of Fig. 4.18 displays the same plots for the fast Bakken Shale HTI formation. In contrast to the slow Austin Chalk formation, both the tool and formation flexural waves are excited by a dipole source. The phase slowness dispersion curve of the formation flexural wave exhibits similar behavior as in the absence of a logging tool. The fast principal formation flexural wave C_1^{F} attains the formation's fast shear wave slowness at the cutoff frequency, whereas the slowness of the slow principal formation flexural wave C_1^{S} coincides with the slow shear wave in the low-frequency limit. The sensitivities of their phase slowness dispersion curves to the formation parameters are displayed in figures 4.18d and 4.18f by the solid lines. As expected, the fast principal formation flexural wave is most sensitive to the elastic constant $C''_{6,6}$ at low frequencies, whereas the slow principal formation flexural wave has its maximum sensitivity to the elastic constant $C''_{4,4}$. Furthermore, the difference between the phase slowness dispersion curves of the fast and slow tool flexural waves also implies that they are sensitive to formation parameters. The sensitivities of the dispersion curves of the principal tool flexural waves to formation parameters are displayed in figures 4.18d and 4.18f by the dashed lines. Since the sensitivity is much higher to the fluid compressional velocity in fast formations than in slow formations, the sensitivity to the formation parameters is significantly lower. While the dispersion curve of the fast principal tool flexural wave exhibits similar sensitivity to $C''_{4,4}$ and $C''_{6,6}$, the dispersion curve of the slow principal tool flexural wave is more sensitive to $C''_{4,4}$ than to $C''_{6,6}$.

In summary, the tool flexural wave is also sensitive to formation anisotropy parameters and may contain useful information to determine the fast and slow shear wave slowness of an HTI formation (Wang et al., 2016). Moreover, the *Alford* rotation can be applied to the waveforms of both the tool flexural waves and the formation flexural waves. The sensitivity of the tool flexural wave to the formation parameters is higher in slow than in fast HTI formations. On the other hand, the formation flexural wave is excited additionally to tool flexural wave in fast formations, which can be used to read both slowness values directly from their phase slowness dispersion curves at the cutoff frequency.

4.2.4. Quadrupole excitation

The theory of cross-multipole shear wave splitting (Sec. 4.2.2) implies that there exists two principal waves for all excitation orders ($n > 0$) in HTI media. Consequently, a cross-quadrupole source aligned with the formation's principal directions excites the fast and slow principal quadrupole modes, respectively. While the X-quadrupole source aligned with the

fast principal direction only excites the fast principal quadrupole mode C_2^{F} (Fig. 4.19a), the Y-quadrupole source aligned with the slow principal direction only excites the slow principal quadrupole mode C_2^{S} (Fig. 4.19b). A quadrupole source is referred to as aligned with the fast principal direction if the source excitation direction is parallel to the formation's principal directions. In contrast, a quadrupole source is referred to as aligned with the slow principal direction if its excitation direction is $\pi/4 = 45°$ rotated to the principal directions in the θ–space. These notations follow from the theory utilizing the $n\theta$–space where the X- and Y-quadrupole sources are orthogonal. Blyth et al. (2016) introduced the notation symmetric quadrupole corresponding to the fast principal quadrupole mode and antisymmetric quadrupole corresponding to the slow principal quadrupole mode.

The four-component data matrix of the time-domain waveforms emitted and received by an LWD cross-quadrupole measurement aligned with the principal directions of the slow Austin Chalk HTI formation is displayed in figure 4.20. As expected, the cross-line components are zero, and the in-line component p_{XX} contains the fast principal quadrupole mode C_2^{F}, whereas the in-line component p_{YY} is defined by the slow principal quadrupole mode C_2^{S}.

The dispersion curves of both principal quadrupole modes are illustrated in figure 4.21a by the solid blue and red lines, respectively. The dashed lines display the dispersion curves of the quadrupole modes excited in isotropic formations that have the shear modulus $\mu = C''_{6,6}$ and $\mu = C''_{4,4}$, respectively. Like the flexural waves, the fast and slow principal quadrupole mode dispersion curves lie at all frequencies between the dispersion curves of their isotropic

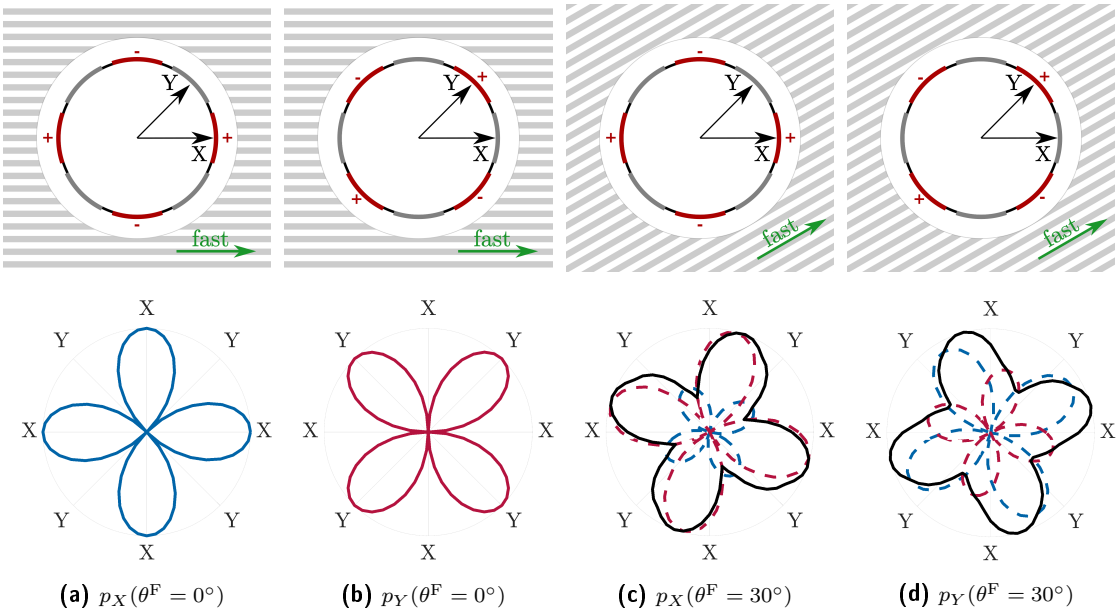

(a) $p_X(\theta^{\mathrm{F}} = 0°)$ **(b)** $p_Y(\theta^{\mathrm{F}} = 0°)$ **(c)** $p_X(\theta^{\mathrm{F}} = 30°)$ **(d)** $p_Y(\theta^{\mathrm{F}} = 30°)$

Fig. 4.19: Directivities of the quadrupole modes excited by a cross-quadrupole source aligned with the formation's principal directions (a–b) and azimuthally offset to them by $\theta^{\mathrm{F}} = 30°$ (c–d). The directivity is computed from the maximum absolute amplitude of the functions $\check{p}_X$ (Eq. 4.14) and $\check{p}_Y$ (Eq. 4.15), respectively, at a fixed radius and the axial offset $z_0 = 3.262\,\mathrm{m}$. The directivity of the fast principal quadrupole mode is displayed in blue, whereas the slow one is plotted in red. In the azimuthally offset case (c–d), the excited quadrupole mode splits into the fast and slow principal quadrupole modes indicated by the dashed lines.

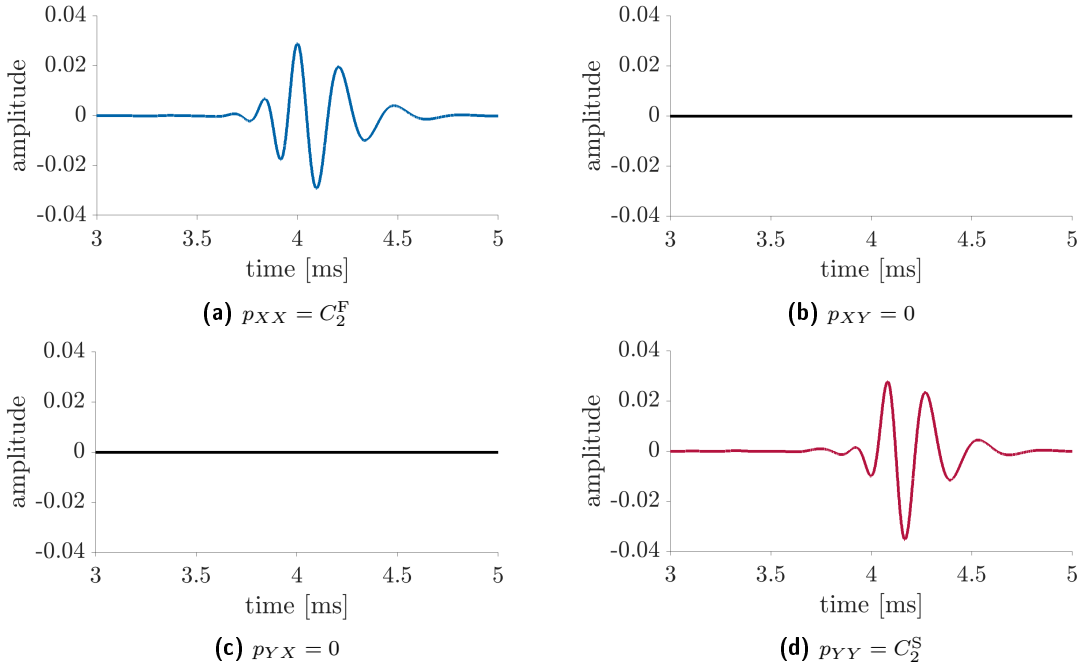

Fig. 4.20: Four-component pressure data matrix of the time-domain waveforms excited by a cross-quadrupole source aligned to the principal directions of the slow Austin Chalk HTI formation. The source ($f_c = 4\,\mathrm{kHz}$) is centered in a fluid-filled borehole in the absence of a logging tool, and the axial offset between the cross-quadrupole source and the cross-quadrupole receiver is $z_0 = 3.262\,\mathrm{m}$. The in-line components (a, d) contain the waveforms of the fast and slow principal quadrupole modes plotted in blue and red, respectively.

counterparts. Furthermore, the fast principal quadrupole dispersion curve attains the formation's fast shear wave slowness $\beta^{\mathrm{S}}_{\mathrm{fast}}$ at the cutoff frequency. In contrast, the slow principal quadrupole slowness becomes much lower than the formation's slow shear wave slowness at low frequencies. Therefore, it is not possible to read the formation's slow shear wave slowness directly from the dispersion curves. The sensitivity analysis displayed in figures 4.21c and 4.21e shows that the slowness dispersion curve of the fast principal quadrupole mode is only sensitive to the elastic modulus $C''_{6,6}$ and zero to $C''_{4,4}$ in the low-frequency limit. The other way around, the slowness dispersion curve of the slow principal quadrupole mode is highly sensitive to the elastic constant $C''_{4,4}$ and zero to $C''_{6,6}$ at the cutoff frequency. All in all, the fast and slow principal quadrupole modes exhibit a similar sensitivity as the principal flexural waves. If the slow Austin Chalk formation is replaced by the fast Bakken Shale formation, similar dispersion characteristics of the principal quadrupole modes can be observed (Fig. 4.21b). However, the fast and slow principal quadrupole dispersion curves are almost identical except at low frequencies and are hard to distinguish. The results of the sensitivity analysis of the principal quadrupole wave slowness to the formation parameters presented in Fig. 4.21d and 4.21f are similar to that in the slow formation.

Analogous to the cross-dipole logging, the cross-quadrupole source is, in general, not azimuthally aligned with the formation's fast or slow principal direction and a weighted superposition of both principal quadrupole modes is excited (Fig. 4.19c and 4.19d). Consequently, the cross-components p_{XY} and p_{YX} of the four-component data matrix become non-zero. Figure 4.22 displays the time-domain waveforms of the four-component pressure data matrix,

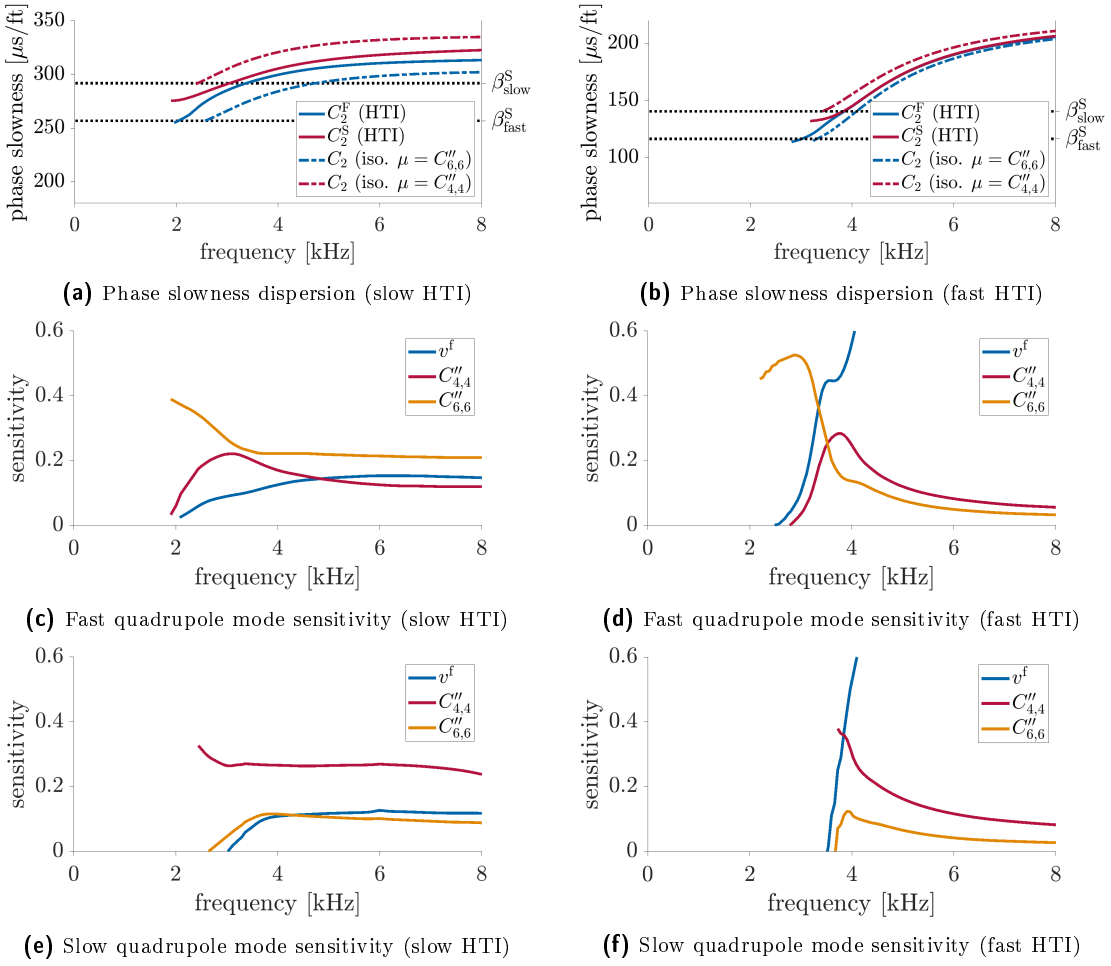

(a) Phase slowness dispersion (slow HTI)

(b) Phase slowness dispersion (fast HTI)

(c) Fast quadrupole mode sensitivity (slow HTI)

(d) Fast quadrupole mode sensitivity (fast HTI)

(e) Slow quadrupole mode sensitivity (slow HTI)

(f) Slow quadrupole mode sensitivity (fast HTI)

Fig. 4.21: Phase slowness dispersion curves and sensitivity analysis of the principal formation quadrupole modes excited in a fluid-filled borehole surrounded by the slow Austin Chalk (left) and fast Bakken Shale (right) HTI formations in the presence of an LWD tool. The solid lines in the first-row figures (a–b) display the phase slowness dispersion curves of the fast and slow principal formation quadrupole modes compared to their isotropic counterparts illustrated by the dashed red ($\mu = C''_{4,4}$) and blue ($\mu = C''_{6,6}$) lines, respectively. The black lines represent the formation's fast (β^S_{fast}) and slow (β^S_{slow}) shear wave slowness. The bottom figures (c–f) show the sensitivity of the principal formation quadrupole mode slowness to the P-wave velocity in the borehole fluid (v^f) and the stiffness tensor elements $C''_{4,4}$ and $C''_{6,6}$ of the formation.

which are excited by a cross-quadrupole source azimuthally offset to the principal directions of the slow Austin Chalk HTI formation by $\theta^F = 30°$. The blue lines illustrate the waveforms obtained from FD modeling of an azimuthally offset cross-quadrupole source. In contrast, the red waveforms are computed by rotating the FD modeled fast and slow principal quadrupole modes (Fig. 4.20a and 4.20d) utilizing the generalized formula for the *Alford* rotation (Eq. 4.17). The coincidence of the waveforms for all components verifies that this equation is not only valid for flexural waves but also for higher-order cylindrical waves such as quadrupole modes. Via the inverse formula for the generalized *Alford* rotation, the fast and slow principal quadrupole modes can be obtained from cross-quadrupole measurements that have an arbitrary azimuthal offset to the formation's fast and slow principal directions (Sec. 5.2). However, the formation's principal shear wave slowness values cannot be read directly from the phase slowness dispersion curves of the principal quadrupole modes in the low-frequency limit.

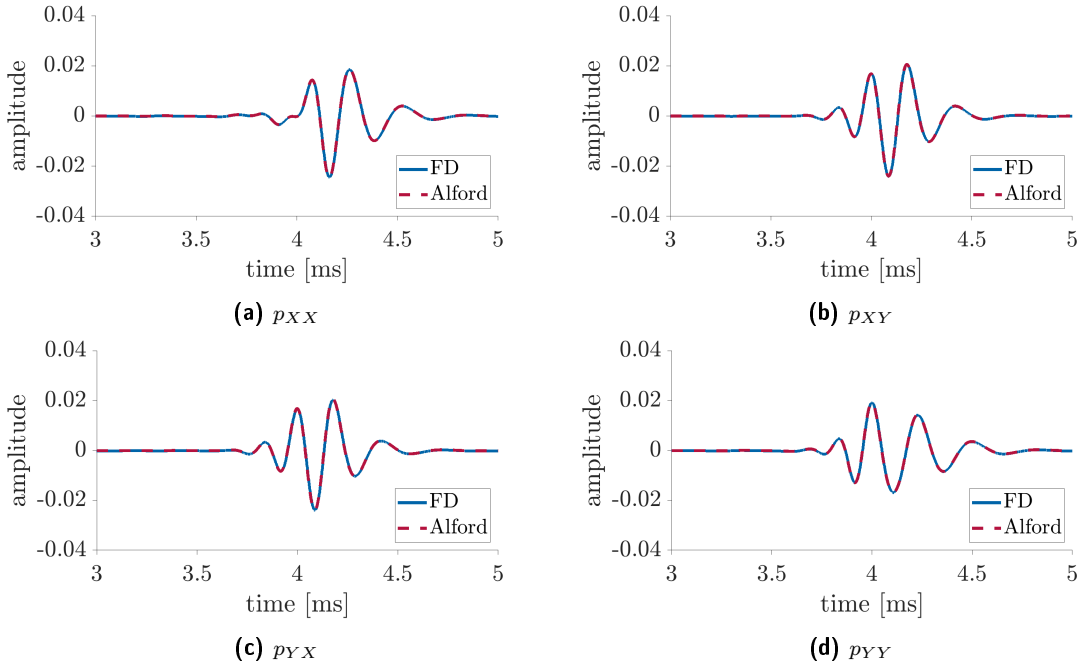

Fig. 4.22: Four-component pressure data matrix of the time-domain waveforms excited by a cross-quadrupole source azimuthally offset to the principal directions of the slow Austin Chalk HTI formation by $\theta^{\mathrm{F}} = 30°$. The source ($f_{\mathrm{c}} = 4\,\mathrm{kHz}$) is centered in a fluid-filled borehole in the presence of an LWD tool, and the axial offset between the cross-quadrupole source and the cross-quadrupole receiver is $z_0 = 3.262\,\mathrm{m}$. The blue waveforms result from FD modeling using an azimuthally offset cross-quadrupole source, whereas the red waveforms are computed by rotating the waveforms of the principal quadrupole modes (Fig. 4.20) via the *Alford* rotation.

4.2.5. Hexapole waves

The next higher-order borehole waves are hexapole waves having the azimuthal wavenumber $m = 3$ (e.g., Geerits et al., 2010) and behave similarly to the quadrupole modes in HTI formations. A cross-hexapole source aligned with the principal directions of the formation excites only the fast (C_3^{F}) and the slow (C_3^{S}) principal hexapole wave, respectively (Fig. 4.23a–4.23b). On the other hand, if the cross-hexapole source is not aligned with the principal directions, a weighted superposition of both principal hexapole modes is excited, as displayed in figures 4.23c and 4.23d. The corresponding four-component data pressure matrix is shown in figure 4.24. While the blue waveforms are obtained from the FD modeling of an azimuthally offset hexapole source ($\theta^{\mathrm{F}} = 10°$), the red waveforms are obtained by applying the generalized formula for the *Alford* rotation (Eq. 4.17) using the FD modeled fast and slow principal hexapole waves. The perfect coincidence of both waveforms for all components once again validates the generalization of the *Alford* rotation.

The main problem of the hexapole mode in real measurements is that it cannot be directly excited by a hexapole source since standard LWD tools possess only four piezoelectric source segments (Sec. 1.1). In contrast, a hexapole excitation of the order $n = 3$ requires six source segments azimuthally separated from each other by $\pi/3$ radians. On the other hand, a dipole source ($n = 1$) excites not only the flexural wave ($m = 1$) as the leading term but additionally all odd multiples $m = kn$ ($k = 1, 3, 5, ...$) (Eq. 4.8). Consequently, a dipole source always

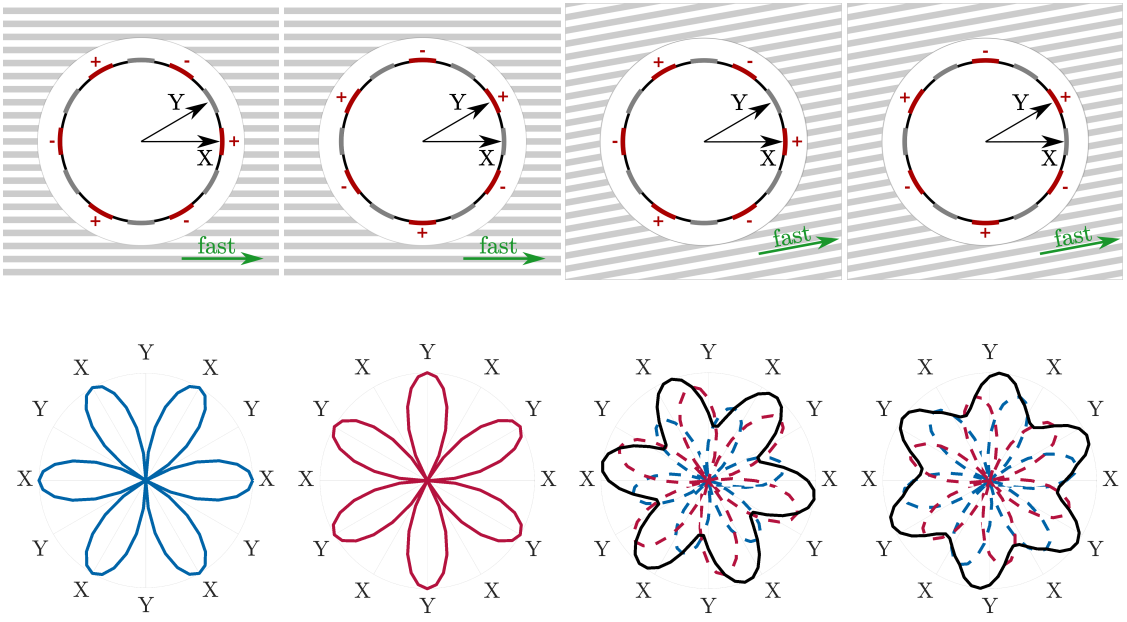

(a) $p_X(\theta^{\mathrm{F}} = 0°)$ (b) $p_Y(\theta^{\mathrm{F}} = 0°)$ (c) $p_X(\theta^{\mathrm{F}} = 10°)$ (d) $p_Y(\theta^{\mathrm{F}} = 10°)$

Fig. 4.23: Directivities of the hexapole modes excited by a cross-hexapole source aligned with the formation's principal directions (a–b) and azimuthally offset to them by $\theta^{\mathrm{F}} = 10°$ (c–d). The directivity is computed from the maximum absolute amplitude of the functions $\check{p}_X$ (Eq. 4.14) and $\check{p}_Y$ (Eq. 4.15), respectively, at a fixed radius and the axial offset $z_0 = 3.262\,\mathrm{m}$. The directivity of the fast principal hexapole mode is displayed in blue, whereas the slow one is plotted in red. In the azimuthally offset case (c–d), the excited hexapole mode splits into the fast and slow principal hexapole modes indicated by the dashed lines.

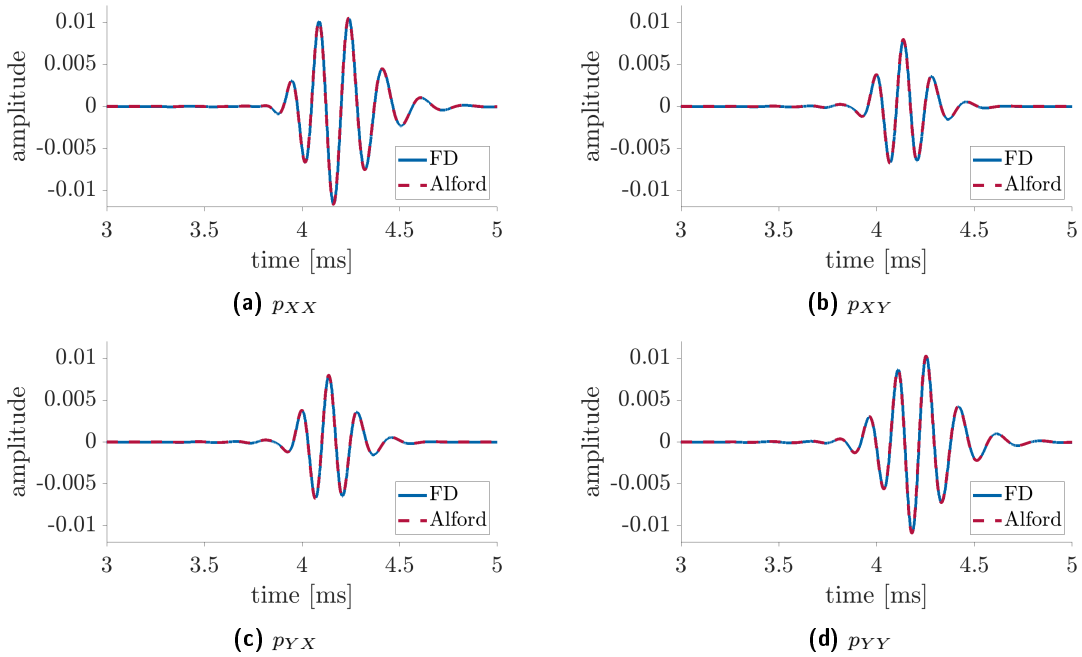

(a) p_{XX} (b) p_{XY}

(c) p_{YX} (d) p_{YY}

Fig. 4.24: Four-component pressure data matrix of the time-domain waveforms excited by a cross-hexapole source azimuthally offset to the principal directions of the slow Austin Chalk HTI formation by $\theta^{\mathrm{F}} = 10°$. The source ($f_{\mathrm{c}} = 4\,\mathrm{kHz}$) is centered in a fluid-filled borehole in the absence of a logging tool, and the axial offset between the cross-hexapole source and the cross-hexapole receiver is $z_0 = 3.262\,\mathrm{m}$. The blue waveforms result from FD modeling using an azimuthally offset cross-hexapole source, whereas the red waveforms are computed by rotating the waveforms of the principal hexapole modes via the *Alford* rotation.

excites a hexapole wave ($m = 3$) as the higher-order cylindrical wave following the leading flexural wave. Figure 4.25 displays the directivities of the flexural and hexapole waves excited by a cross-dipole source in a fluid-filled borehole surrounded by an HTI formation. The dipole source aligned with the formation's fast principal direction excites the fast principal flexural wave and the fast principal hexapole wave. Analogously, a dipole source aligned with the formation's slow principal direction excites the slow principal flexural wave and the slow principal hexapole wave. The latter has an opposite polarity ($-C_3^{\mathrm{S}}$) to the slow principal hexapole wave excited by a hexapole source aligned with the formation's slow principal direction (Fig. 4.23b). This follows directly from equation 4.13 or by consideration of the source polarities.

If the dipole source is not aligned with the principal directions, a weighted superposition of the slow and fast principal flexural waves is excited. Additionally, it seems that the same is true for the hexapole wave. However, since the azimuthal offset of the dipole source is $\theta^{\mathrm{F}} = 30°$, the source azimuth is $n\theta^{\mathrm{F}} = 90°$ in the $n\theta$–space for the hexapole wave ($n = 3$). Consequently, the source azimuth is azimuthally offset to the principal directions for the flexural waves but aligned to them for the hexapole modes. However, figures 4.25c–4.25d show that instead of a principal hexapole mode, a weighted superposition of the slow and the fast hexapole is excited. The problem is that these weights are not defined by the generalized *Alford* rotation but are unknown. Hence, the generalized formula for the *Alford* rotation applies for all excitation orders n only to the leading term $k = 1$ ($m = kn$).

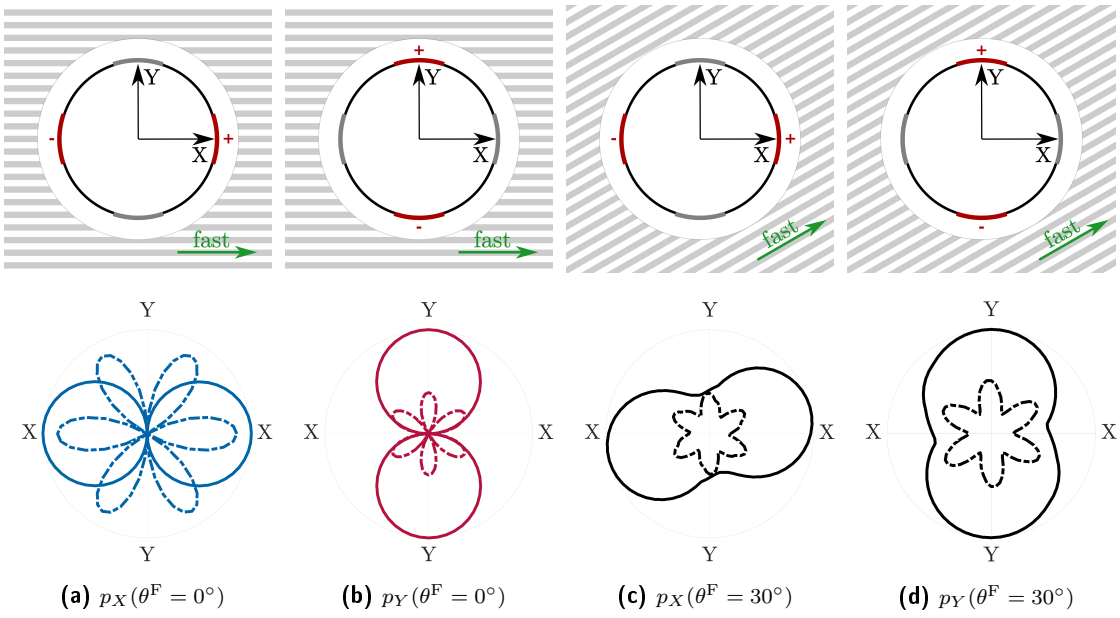

Fig. 4.25: Directivities of the hexapole modes excited by a cross-dipole source aligned with the formation's principal directions (a–b) and azimuthally offset to them by $\theta^{\mathrm{F}} = 30°$ (c–d). The directivity is computed from the maximum absolute amplitude of the functions $\check{p}_X$ and $\check{p}_Y$, respectively, at a fixed radius and the axial offset $z_0 = 3.262\,\mathrm{m}$. The directivities of the fast principal flexural and hexapole waves are displayed in blue, whereas the slow ones are plotted in red. In the azimuthally offset case (c–d), the cross-dipole source excites a weighted superposition of the principal flexural and hexapole modes, respectively.

The phase slowness dispersion curves of the fast and slow principal tool and formation flexural waves are displayed in figure 4.26 compared to the dispersion characteristics of the fast and slow principal formation hexapole waves. Similar to the quadrupole modes, the principal hexapole waves do not attain the true fast and slow shear wave values of the HTI formation at the cutoff frequency. Moreover, the difference of the slowness dispersion curves between the fast and slow principal hexapole mode is minimal in the slow Austin Chalk formation, and in the fast Bakken Shale formation, both are almost identical. Thus, the hexapole mode is not appropriate for the determination of the formation's HTI parameters.

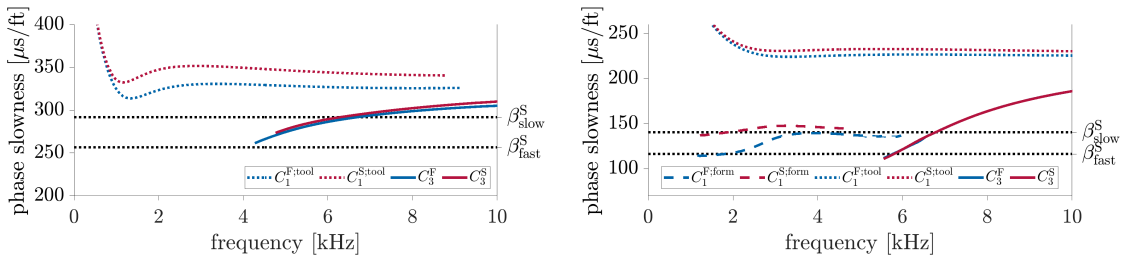

(a) Phase slowness dispersion (slow HTI)

(b) Phase slowness dispersion (fast HTI)

Fig. 4.26: Phase slowness dispersion curves of the principal flexural and hexapole waves excited by a cross-dipole source in a fluid-filled borehole surrounded by the slow Austin Chalk (a) and fast Bakken Shale (b) HTI formations in the presence of an LWD tool. The principal tool and formation flexural waves are illustrated by the dotted and dashed lines, respectively. The solid lines display the principal formation hexapole modes. The black lines represent the formation's fast (β^{S}_{fast}) and slow (β^{S}_{slow}) shear wave slowness.

4.2.6. Summary

The results of the sensitivity analysis for different refracted and borehole waves (*Stoneley*, flexural, quadrupole) in HTI formations are summarized in table 4.2. The configuration without a logging tool corresponds to WL logging because the WL tool has only little effect on the sensitivities of the borehole waves. The refracted P-wave propagating vertically along the borehole wall can be used to determine the vertical P-wave velocity defined by the stiffness tensor element $C''_{1,1}$ expressed in the crystallographic reference frame. The *Stoneley* wave is sensitive to a combination of the stiffness tensor elements $C''_{1,1}$, $C''_{1,3}$, $C''_{3,3}$, and $C''_{4,4}$ in the low-frequency limit. The flexural wave splits into the fast and slow principal flexural waves. While the low-frequency limit of the fast principal flexural wave coincides with the vertical SH-wave velocity that is proportional to the stiffness tensor element $C''_{6,6}$, the slow principal flexural wave attains, at the cutoff frequency, the vertical SV-wave velocity defined by the stiffness tensor element $C''_{4,4}$.

In the LWD configuration, the sensitivities of the refracted P- and *Stoneley* waves are similar to those in the absence of a tool. However, the presence of an LWD tool alters the slowness of the *Stoneley* wave in the low-frequency limit. Moreover, the LWD tool causes that formation flexural waves are not present in slow formations. In that case, the fast principal tool flexural wave is sensitive to the stiffness tensor element $C''_{6,6}$, whereas the slow principal tool flexural wave is sensitive to $C''_{4,4}$. Thus, the elements $C''_{4,4}$ and $C''_{6,6}$ may be obtained by applying a model-based inversion method on the principal tool flexural waves. In fast formations,

Tab. 4.2: Overview of the phase slowness sensitivities of particular waves to stiffness tensor elements characterizing an HTI formation. The table considers the absence and presence of an LWD tool as well as fast and slow formations. The bold variables denote a strong sensitivity to the respective stiffness tensor elements, whereas the parentheses indicate that the sensitivity is weak.

	wave mode	slow formation	fast formations
no tool	refracted P	$\boldsymbol{C''_{1,1}}$	$\boldsymbol{C''_{1,1}}$
	Stoneley	$C''_{1,1}$, $C''_{1,3}$, $C''_{3,3}$, $C''_{4,4}$	$C''_{1,1}$, $C''_{1,3}$, $C''_{3,3}$, $C''_{4,4}$
	fast flexural	$\boldsymbol{C''_{6,6}}$, $C''_{4,4}$	$\boldsymbol{C''_{6,6}}$
	slow flexural	$\boldsymbol{C''_{4,4}}$	$\boldsymbol{C''_{4,4}}$
LWD tool	refracted P	$\boldsymbol{C''_{1,1}}$	$\boldsymbol{C''_{1,1}}$
	Stoneley	$C''_{1,1}$, $C''_{1,3}$, $C''_{3,3}$, $C''_{4,4}$	$C''_{1,1}$, $C''_{1,3}$, $C''_{3,3}$, $C''_{4,4}$
	fast formation flexural	not present	$\boldsymbol{C''_{6,6}}$
	slow formation flexural	not present	$\boldsymbol{C''_{4,4}}$
	fast tool flexural	$\boldsymbol{C''_{6,6}}$, $(C''_{4,4})$	$(C''_{4,4}, C''_{6,6})$
	slow tool flexural	$\boldsymbol{C''_{4,4}}$	$(C''_{4,4})$
	fast formation quadrupole	$\boldsymbol{C''_{6,6}}$, $(C''_{4,4})$	$C''_{6,6} \approx C''_{4,4}$
	slow formation quadrupole	$\boldsymbol{C''_{4,4}}$, $(C''_{6,6})$	$C''_{4,4} \approx C''_{6,6}$

the principal tool flexural waves exhibit only weak sensitivity to formation parameters, but the principal formation flexural waves can be used for the determination of $C''_{4,4}$ and $C''_{6,6}$. Analogous to the flexural wave, the quadrupole mode splits into the slow and fast principal quadrupole modes. Accordingly, the principal fast formation quadrupole mode is sensitive to the stiffness tensor element $C''_{6,6}$, and the slow principal formation quadrupole mode to $C''_{4,4}$ in slow formations. In fast formations, the fast and slow principal quadrupole modes exhibit similar sensitivities to the stiffness tensor elements $C''_{4,4}$ and $C''_{6,6}$ and thus can not be distinguished except at very low frequencies, which is not useful in real LWD measurements.

4.3. Tilted transverse isotropy (TTI)

This section treats the general TTI case, where the formation's TI symmetry axis (x_3''–axis) is arbitrarily inclined to the vertical borehole axis (x_3'–axis), as displayed in Fig. 4.27. The

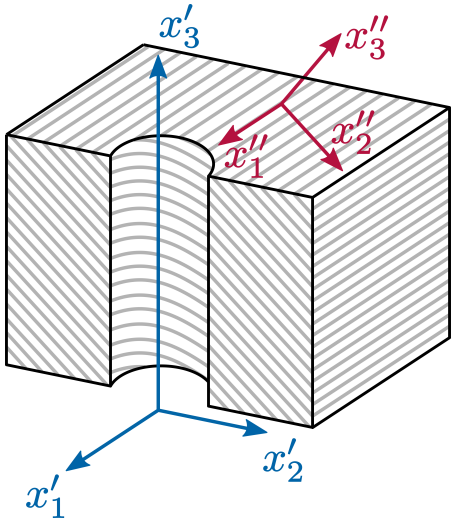

Fig. 4.27: Illustration of the TI symmetry in the crystallographic reference frame (red) and the borehole reference frame (blue), where the symmetry axis is arbitrarily inclined to the borehole axis (TTI). The isotropic plane is indicated by the gray lines.

stiffness tensor elements given in the crystallographic reference frame ($\boldsymbol{x}''$) can be transformed to the borehole reference frame ($\boldsymbol{x}'$) by a rotation around the x_1''–axis by the inclination angle ψ_0 (Sec. 2.2). The resulting stiffness tensor exhibits monoclinic symmetry in the borehole reference frame, where the x_2'–x_3' plane is the plane of mirror symmetry

$$C'_{i,j} = \begin{pmatrix} C'_{1,1} & C'_{1,2} & C'_{1,3} & C'_{1,4} & 0 & 0 \\ & C'_{2,2} & C'_{2,3} & C'_{2,4} & 0 & 0 \\ & & C'_{3,3} & C'_{3,4} & 0 & 0 \\ & & & C'_{4,4} & 0 & 0 \\ & \text{sym} & & & C'_{5,5} & C'_{5,6} \\ & & & & & C'_{6,6} \end{pmatrix}. \tag{4.22}$$

The elements of the stiffness tensor given in the borehole reference frame can be expressed by the stiffness tensor elements in the crystallographic reference frame dependent on the inclination angle ψ_0

$$C'_{1,1} = C''_{1,1}, \tag{4.23a}$$

$$C'_{1,2} = C''_{1,2}\cos^2\psi_0 + C''_{1,3}\sin^2\psi_0, \tag{4.23b}$$

$$C'_{1,3} = C''_{1,2}\sin^2\psi_0 + C''_{1,3}\cos^2\psi_0, \tag{4.23c}$$

$$C'_{1,4} = \left(C''_{1,3} - C''_{1,2}\right)\cos\psi_0\sin\psi_0, \tag{4.23d}$$

$$C'_{2,2} = C''_{1,1}\cos^4\psi_0 + C''_{3,3}\sin^4\psi_0 + (2C''_{1,3} + 4C''_{4,4})\sin^2\psi_0\cos^2\psi_0, \tag{4.23e}$$

$$C'_{2,3} = C''_{1,3} + (C''_{1,1} + C''_{3,3} - 2C''_{1,3} - 4C''_{4,4})\sin^2\psi_0\cos^2\psi_0, \tag{4.23f}$$

$$C'_{2,4} = (C''_{1,3} - C''_{1,1} + 2C''_{4,4})\cos^3\psi_0\sin\psi_0 + (C''_{3,3} - C''_{1,3} - 2C''_{4,4})\cos\psi_0\sin^3\psi_0, \tag{4.23g}$$

$$C'_{3,3} = C''_{1,1}\sin^4\psi_0 + C''_{3,3}\cos^4\psi_0 + (2C''_{1,3} + 4C''_{4,4})\sin^2\psi_0\cos^2\psi_0, \tag{4.23h}$$

$$C'_{3,4} = (C''_{3,3} - C''_{1,3} - 2C''_{4,4})\cos^3\psi_0\sin\psi_0 + (C''_{1,3} - C''_{1,1} + 2C''_{4,4})\cos\psi_0\sin^3\psi_0, \tag{4.23i}$$

$$C'_{4,4} = C''_{4,4} + (C''_{1,1} + C''_{3,3} - 2C''_{1,3} - 4C''_{4,4})\sin^2\psi_0\cos^2\psi_0, \tag{4.23j}$$

$$C'_{5,5} = C''_{4,4}\cos^2\psi_0 + C''_{6,6}\sin^2\psi_0, \tag{4.23k}$$

$$C'_{5,6} = (C''_{4,4} - C''_{6,6})\cos\psi_0\sin\psi_0, \tag{4.23l}$$

$$C'_{6,6} = C''_{4,4}\sin^2\psi_0 + C''_{6,6}\cos^2\psi_0. \tag{4.23m}$$

Figure 4.28a displays the compressional moduli $C'_{1,1}$, $C'_{2,2}$, and $C'_{3,3}$ characterizing the slow Austin Chalk TI formation dependent on the inclination angle ψ_0. Since the stiffness tensor elements are rotated from the crystallographic reference frame to the borehole reference frame around the x'_1–axis, the latter always lies in the isotropic plane, and the elastic modulus $C'_{1,1}$ is constant for all inclinations (Eq. 4.23a). In contrast, the stiffness tensor elements $C'_{2,2}$ and $C'_{3,3}$ change with the inclination angle in a complementary manner (Eq. 4.23e and 4.23h). If

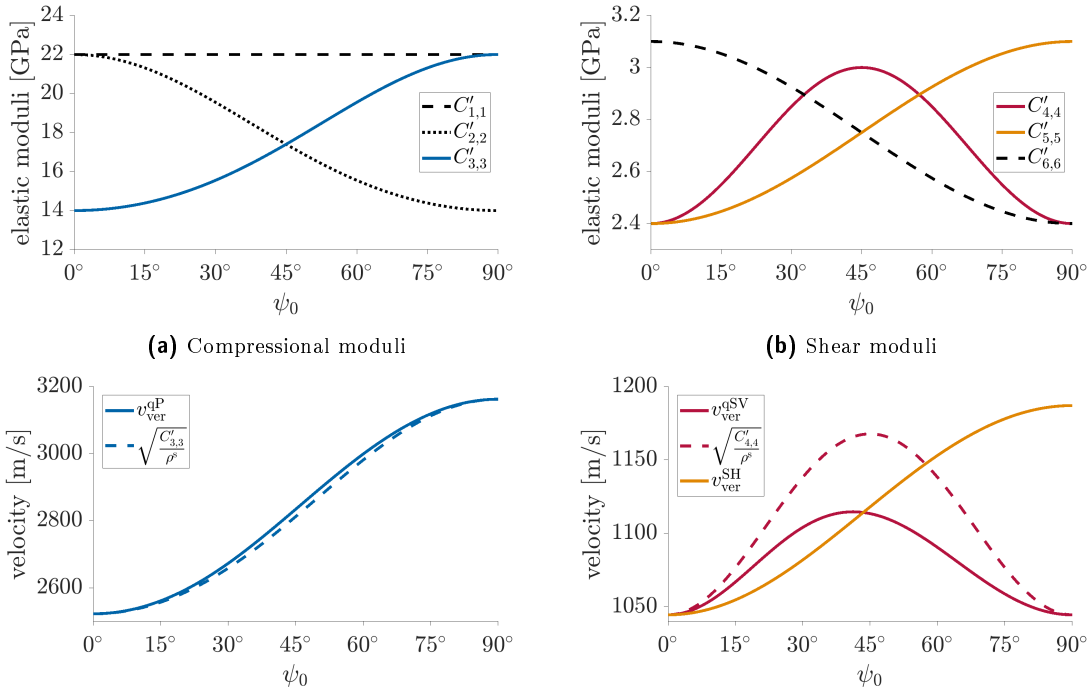

(a) Compressional moduli **(b)** Shear moduli

(c) Compressional wave velocity **(d)** Shear wave velocities

Fig. 4.28: The figures display various stiffness tensor elements characterizing the slow Austin Chalk TI formation (a–b) and the corresponding velocities of the vertically propagating qP-, qSV- and SH-waves (c–d) dependent on the inclination angle ψ_0. The exact wave velocities obtained by solving the *Christoffel* equation are plotted by the solid lines, whereas the dashed lines display approximated wave velocities using single stiffness tensor elements expressed in the borehole reference frame.

the inclination angle is zero (VTI), the elements $C'_{2,2}$ and $C'_{1,1}$ coincide because, in this case, both define the P-wave velocity in the isotropic plane. The element $C'_{3,3}$ has a lower value and controls the velocity of the vertically propagating P-wave parallel to the vertical symmetry axis. On the other hand, if the inclination attains $\psi_0 = 90°$ (HTI), the components $C'_{1,1}$ and $C'_{3,3}$ are equal because the x'_1–x'_3 plane defines the isotropic plane in this case, and the component $C'_{2,2}$ becomes equal to $C''_{3,3}$ defining the P-wave velocity in x'_2–direction parallel to the TI symmetry axis.

The elastic shear moduli of the slow Austin Chalk formation are displayed in figure 4.28b in relation to the inclination angle. Similar to the compressional moduli $C'_{2,2}$ and $C'_{3,3}$, the shear moduli $C'_{5,5}$ and $C'_{6,6}$ show a complementary ascending and descending behavior, respectively (Eq. 4.23k and 4.23m). The stiffness tensor element $C'_{4,4}$ is symmetric at $\psi_0 = 45°$, where it attains its maximum value. If the inclination angle is zero (VTI), the elastic moduli $C'_{4,4}$ and $C'_{5,5}$ coincide and define the shear wave velocities of the vertically propagating shear waves. On the other hand, if the inclination angle is $\psi_0 = 90°$ (HTI), the value of the elastic modulus $C'_{5,5}$ controlling the vertical SH-wave velocity is higher than that of the shear modulus $C'_{4,4}$ defining the vertical SV-wave velocity.

For arbitrary inclinations, the velocities of vertically propagating qP- and qSV-waves are not defined by single stiffness tensor elements because they are no longer pure modes. For instance, the compressional motion (parallel to the propagation direction) of the vertical qP-wave is controlled by the stiffness tensor element $C'_{3,3}$, whereas the shear motion involves additional stiffness tensor elements, e.g., $C'_{3,4}$ and $C'_{4,4}$. Analogously, the shear motion (transverse to the propagation direction) of the qSV-wave is defined by the stiffness tensor element $C'_{4,4}$, whereas the compressional motion involves the stiffness tensor element $C'_{3,3}$. Consequently, the *Christoffel* equation must be solved to obtain the exact velocities or slowness values of the qP- and qSV-waves (Eq. 2.39). Figures 4.28c and 4.28d display the exact velocities for the vertically propagating qP-, qSV-, and SH-waves dependent on the inclination angle ψ_0 by the solid lines. The dashed blue line in figure 4.28c illustrates an approximated velocity for the qP-wave defined only by the stiffness tensor element $C'_{3,3}$

$$v_{ver}^{\mathrm{qP};*}(\psi_0) = \sqrt{\frac{C'_{3,3}(\psi_0)}{\rho^{\mathrm{s}}}}. \tag{4.24}$$

The approximated velocity coincides with the true velocity for the VTI ($\psi_0 = 0°$) and HTI ($\psi_0 = 90°$) symmetry because, in these cases, the qP-wave becomes a pure compressional wave. For arbitrary inclinations ($0° < \psi_0 < 90°$), the approximated velocity is slightly lower than the true velocity since the shear motion is not considered in the former. Similarly, an approximated velocity for the vertically propagating qSV-wave is proposed that involves only the shear motion and depends only on the stiffness tensor element $C'_{4,4}$

$$v_{ver}^{\mathrm{qSV};*}(\psi_0) = \sqrt{\frac{C'_{4,4}(\psi_0)}{\rho^{\mathrm{s}}}}. \tag{4.25}$$

The approximated velocity of the vertical qSV-wave is displayed by the dashed red line in figure 4.28d in comparison to the true velocity plotted by the solid red line. The velocities are identical for the VTI and HTI symmetries since the qSV-wave becomes a pure shear wave. For inclination angles in between, the approximated velocity significantly deviates from the true velocity because of the significant compressional particle motion. In contrast to the qP- and qSV-wave, the vertically propagating SH-wave is always a pure shear wave in TI media, independent of the inclination angle. The SH-wave is polarized parallel to the x_1'–axis that is perpendicular to the plane of mirror symmetry, defining the monoclinic symmetry. Therefore, the vertical SH-wave velocity is only controlled by the stiffness tensor element $C'_{5,5}$, and the true velocity is defined by

$$v_{ver}^{\mathrm{SH}}(\psi_0) = \sqrt{\frac{C'_{5,5}(\psi_0)}{\rho^{\mathrm{s}}}}. \tag{4.26}$$

The solid orange line in figure 4.28d illustrates the vertical SH-wave velocity dependent on the inclination. Furthermore, it is shown that the vertically propagating SH-wave can become slower than the vertically propagating qSV-wave for particular inclinations. For inclinations smaller than $\psi_0 = 43.5°$, the qSV-wave velocity is greater than the SH-wave velocity, and for greater inclinations, the SH-wave becomes the faster wave. Therefore, the fast and slow principal directions depend on the inclination angle for the TTI symmetry. In borehole acoustics, the principal directions are always defined on the plane transverse to the borehole (x_1'–x_2' plane), as illustrated in figure 4.29. The SH-wave is always polarized in the isotropic plane parallel to the x_1''–axis ($= x_1'$–axis) and defines the fast principal direction ($\boldsymbol{v}^{\mathrm{fast}}$) of the Austin Chalk TI formation for inclinations higher than $\psi_0 > 43.5°$. The slow principal direction ($\boldsymbol{v}^{\mathrm{slow}}$) is defined by the polarization direction of the qSV-wave (lying in the x_2'–x_3' plane) that is projected onto the plane transverse to the borehole (parallel to the x_2'–axis). If the inclination angle is smaller than $\psi_0 < 43.5°$, the polarization direction of the SH-wave defines the slow principal direction, whereas the fast principal direction is defined by the projected

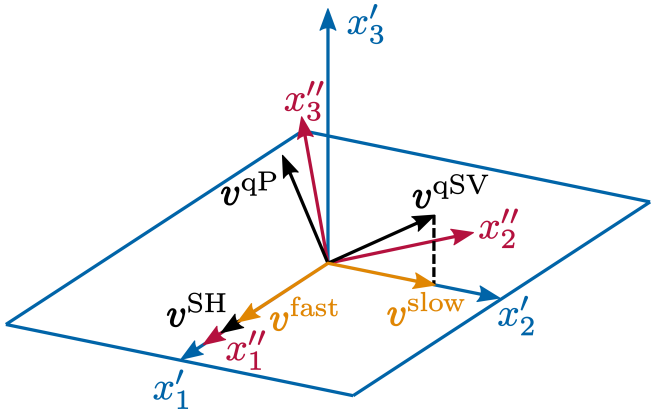

Fig. 4.29: The principal directions ($\boldsymbol{v}^{\mathrm{fast}}$ and $\boldsymbol{v}^{\mathrm{slow}}$) of a TI formation, which symmetry axis (x_3'') is arbitrarily inclined to the borehole axis (x_3'), are defined, in borehole acoustics, by the polarization direction of the SH-wave ($\boldsymbol{v}^{\mathrm{SH}}$) and the polarization direction of the qSV-wave ($\boldsymbol{v}^{\mathrm{qSV}}$) that is projected onto the plane transverse to the borehole (x_1'–x_2' plane). The figure displays the case where the SH-wave propagates faster than the qSV-wave.

qSV-wave polarization direction. Thus, the fast and the slow principal direction interchange when the inclination changes from $\psi_0 < 43.5°$ to $\psi_0 > 43.5°$, or vice versa.

The elastic compressional and shear moduli of the fast Bakken Shale formation exhibit similar behavior to those of the slow Austin Chalk formation. Hence, the velocities of the vertically propagating qP-, qSV- and SH-waves and their approximations are very similar and are thus omitted here. In contrast, different behavior of the elastic moduli can be observed for the fast Cotton Valley Shale formation, which parameters are given in table 3.1. While the compressional moduli exhibit similar behavior (Fig. 4.30a), the shear modulus $C'_{4,4}$ is different (Fig. 4.30b) because it decreases with an increasing inclination for $\psi_0 < 45°$ to values lower than in the VTI and HTI cases. Moreover, the vertically propagating qSV-wave is for all inclinations ($\psi_0 > 0°$) slower than the vertically propagating SH-wave (Fig. 4.30d). Thus, the SH-wave polarization direction always corresponds to the formation's fast principal direction, whereas the projection of the qSV-wave polarization direction defines the slow principal direction independent of the inclination angle (Fig. 4.29). The difference between the approximated and true velocities of the qP- and qSV-waves is smaller than for the slow Austin Chalk formation and less than 1 %. The reason for this is that the qP-wave has less particle motion transverse to the propagation direction, and the qSV-wave has less particle motion parallel to the propagation direction in the fast Cotton Valley Shale formation. Consequently, the approximated velocities may be used for an inversion method instead of the true ones.

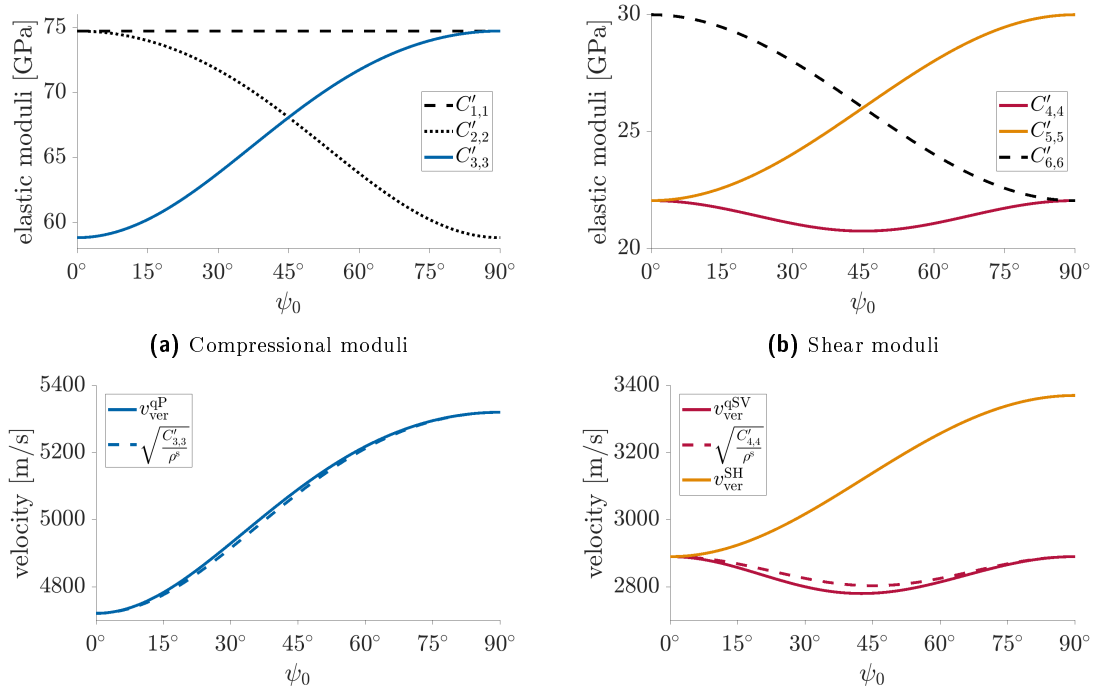

Fig. 4.30: The figures display various stiffness tensor elements characterizing the fast Cotton Valley Shale TI formation (a–b) and the corresponding velocities of the vertically propagating qP-, qSV- and SH-waves (c–d) dependent on the inclination angle ψ_0. The exact wave velocities obtained by solving the *Christoffel* equation are plotted by the solid lines, whereas the dashed lines display approximated wave velocities using single stiffness tensor elements expressed in the borehole reference frame.

The following section investigates the borehole wavefield excited by a monopole source. It is presented that the refracted qSV- and SH-waves, traveling at slightly different velocities, are hard to distinguish for low inclination angles. Furthermore, the velocity of the *Stoneley* wave in the low-frequency limit is defined by the azimuthal average of the stiffness tensor element $C_{6,6}$. The next sections show that the behavior of the flexural and quadrupole waves in the TTI case is similar to the HTI case. All cylindrical waves split into a fast and a slow principal cylindrical wave. Their difference in the waveforms and phase slowness dispersion curves depends on the inclination angle of the TI symmetry axis to the vertical borehole axis.

4.3.1. Monopole excitation

Figure 4.31a displays the semblance analysis (App. D.1) of the head waves and the *Stoneley* wave excited by a monopole source in an open fluid-filled borehole surrounded by the fast Bakken Shale TTI formation, where the symmetry axis is inclined to the borehole axis by $\psi_0 = 75°$. Like in the HTI case, the semblance plot shows one maximum corresponding to the refracted qP-wave and two maxima corresponding to the refracted SH- and qSV-wave. The SH-wave is faster than the qSV-wave, which is also true for an inclination of $\psi_0 = 60°$, but the difference in the shear wave velocities becomes smaller, as illustrated in figure 4.31b. The maxima corresponding to the refracted qSV- and SH-waves are not clearly separated and are hard to distinguish. If the inclination angle further decreases, only one maximum for the

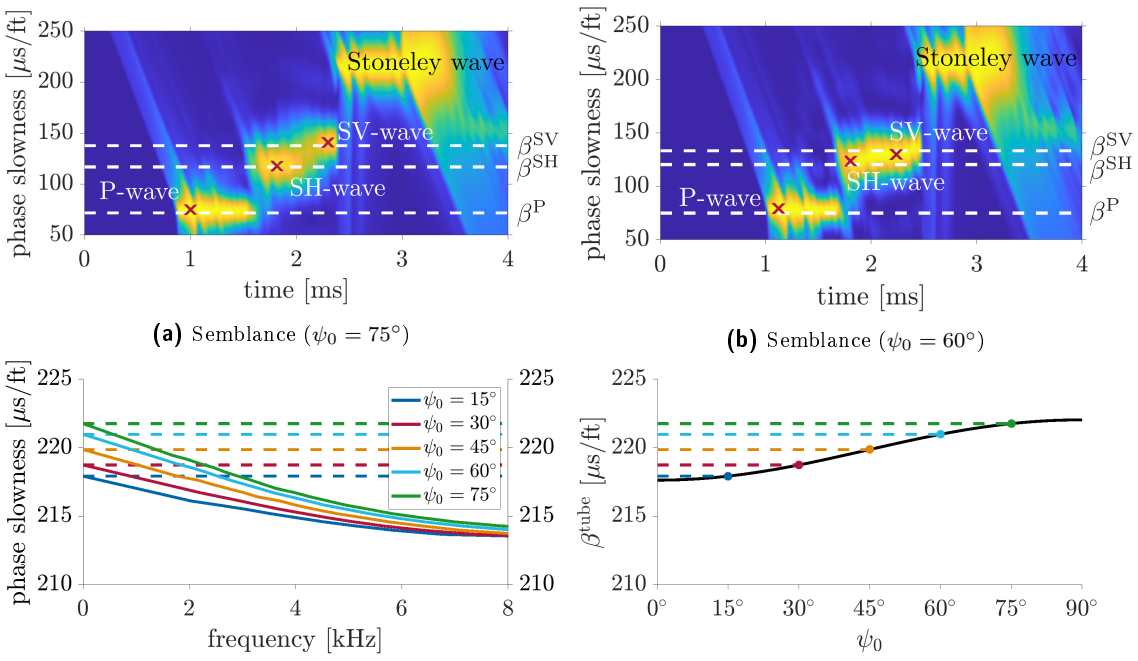

(a) Semblance ($\psi_0 = 75°$)

(b) Semblance ($\psi_0 = 60°$)

(c) Phase slowness dispersion

(d) Tube wave slowness

Fig. 4.31: Monopole excitation in a fluid-filled borehole surrounded by the fast Bakken Shale TTI formation in the absence of a logging tool. The first-row figures (a–b) display the semblance analysis (App. D.1) of the refracted P-, refracted shear, and *Stoneley* waves for two different inclination angles ($\psi_0 = 75°$ (a) and $\psi_0 = 60°$ (b)). The bottom left figure (c) illustrated the phase slowness dispersion curve of the *Stoneley* wave for various inclination angles ψ_0. The corresponding tube wave slowness (β^{tube}) is displayed in relation to the inclination angle in the bottom right figure (d).

shear waves can be found, and the SH- and qSV-wave velocities cannot be separated in the semblance plot. The large maximum in the upper right corner in the semblance plots belongs to the dispersive *Stoneley* wave, with dispersion characteristic displayed in figure 4.31c for different inclination angles. The tube wave slowness denoting the low-frequency limit of the *Stoneley* wave increases with increasing inclination angles.

Equation 4.3 in section 4.1.1 explains that, in VTI formations, the tube wave velocity depends only on the elastic modulus $C''_{6,6}$ defining the velocity of a horizontally propagating SH-wave. In TTI formations, this elastic modulus $C_{6,6}$ depends on the inclination angle ψ_0 and the azimuth θ_0. Norris and Sinha (1993) have demonstrated that the tube wave velocity is controlled by the azimuthal average ($\overline{C}_{6,6}$) of the modulus $C_{6,6}$ since the *Stoneley* wave exhibits an omnidirectional directivity

$$v^{\mathrm{tube}} = \lim_{s\to 0} v^{\mathrm{St}} = v^{\mathrm{f}} \left(1 + \frac{\rho^{\mathrm{f}} \left(v^{\mathrm{f}}\right)^2}{\overline{C}_{6,6}} \right)^{\left(-\frac{1}{2}\right)}, \tag{4.27a}$$

$$\overline{C}_{6,6} = \frac{1}{2\pi} \int_{\theta_0=0}^{2\pi} C_{6,6}(\theta_0) \mathrm{d}\theta_0, \tag{4.27b}$$

$$= \frac{1}{8} \left[C_{1,1} + C_{2,2} - 2C_{1,2} + 4C_{6,6} \right], \tag{4.27c}$$

$$\begin{aligned} = \frac{1}{8} \big[& C''_{1,1} \left(1 - 2\cos^2\psi_0 + \cos^4\psi_0\right) + 2C''_{1,3} \sin^2\psi_0 \left(\cos^2\psi_0 - 1\right) \\ & + C''_{3,3} \sin^4\psi_0 + 4C''_{4,4} \sin^2\psi_0 \left(\cos^2\psi_0 + 1\right) + 8C''_{6,6} \cos^2\psi_0 \big]. \end{aligned} \tag{4.27d}$$

The averaged value $\overline{C}_{6,6}$ can be explicitly calculated via equation 4.27b, including azimuthal integration of equation B.16v (App. B.2). The result is given in equation 4.27c, valid in both the tool ($\boldsymbol{x}$) and the borehole ($\boldsymbol{x}'$) reference frame. Additionally, equation 4.27d expresses the formula in the crystallographic reference frame ($\boldsymbol{x}''$) dependent on the inclination angle ψ_0. Figure 4.31d displays the tube wave slowness for an open fluid-filled borehole surrounded by the fast Bakken Shale TI formation depending on the inclination angle. As indicated, the tube wave slowness values coincide with the low-frequency limits of the *Stoneley* wave dispersion curves displayed in figure 4.31c. If a slow TI formation surrounds the borehole, similar behavior of the tube wave slowness is observed, and equations 4.27a–4.27d are still valid. In contrast, the presence of an LWD tool strongly alters the tube wave slowness and makes equation 4.27d invalid. Thus, the above equations cannot be used to develop an inversion method for LWD monopole measurements.

4.3.2. Dipole excitation

The flexural waves excited by a dipole source in a fluid-filled borehole surrounded by a TTI formation depend on the source azimuth, similar to the HTI case. If the dipole source is either aligned with the polarization direction of the SH-wave or with the polarization direc-

tion of the qSV-wave projected onto the plane transverse to the borehole (Fig. 4.29), only the fast and slow principal flexural waves are excited. The association of the polarization directions to the fast and slow principal waves depends on the inclination angle ψ_0 and the corresponding slowness values for the SH- and qSV-wave. Moreover, Figures 4.32a–4.32b display the dispersion characteristic of both principal flexural waves in the slow Austin Chalk TI formation, whose symmetry axis is inclined to the borehole axis by $\psi_0 = 15°$ and $\psi_0 = 30°$, respectively. The principal flexural wave aligned with the projected qSV-wave polarization direction (red) is at low frequencies slightly faster than the principal flexural wave aligned with the SH-wave polarization direction (blue). Consequently, the fast principal direction coincides with the qSV-wave polarization direction projected onto the plane transverse to the borehole, and the associated flexural wave is referred to as the fast principal flexural wave. In contrast, for higher inclination angles (Fig. 4.32c–4.32e), the flexural wave aligned with

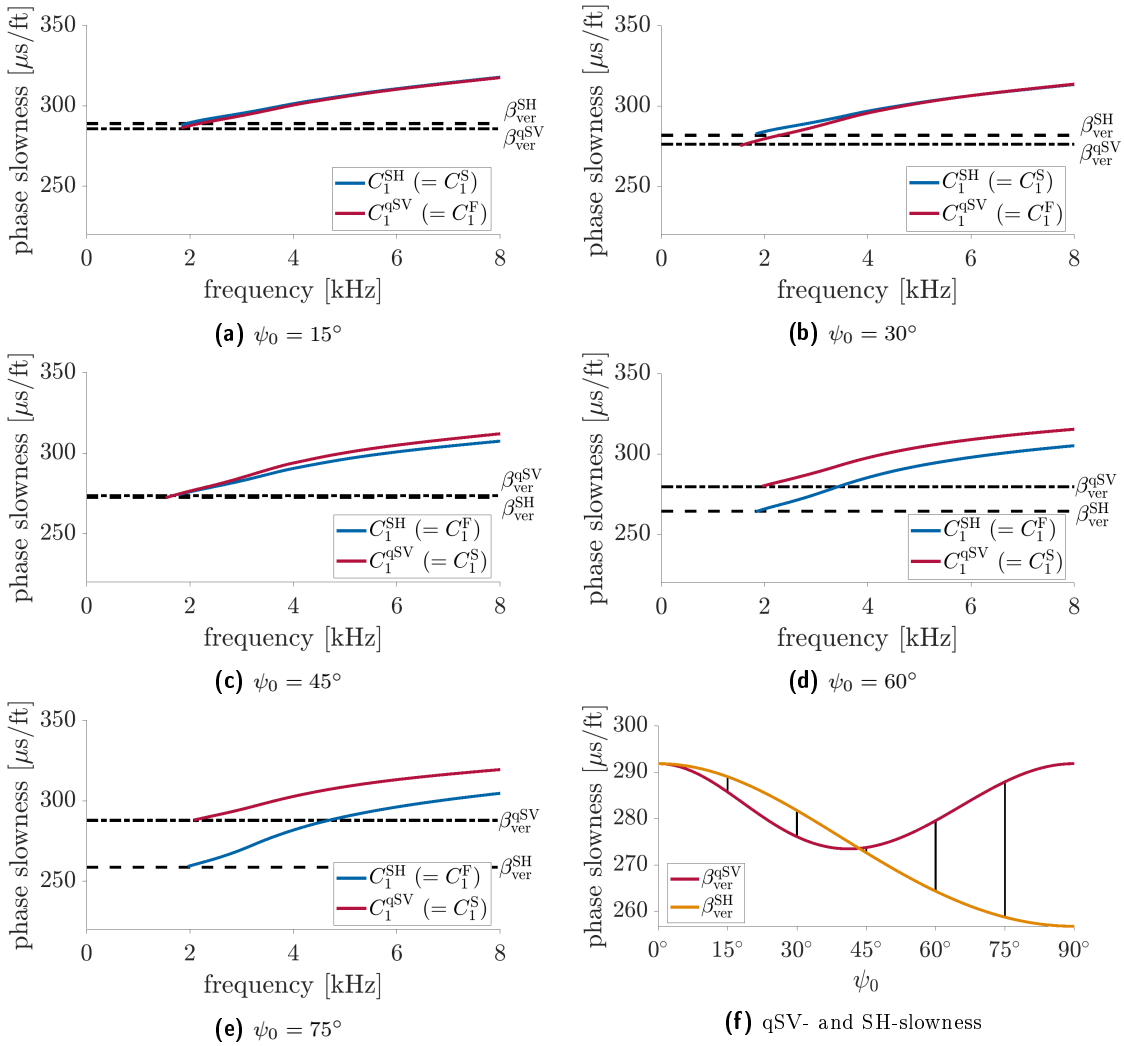

(a) $\psi_0 = 15°$ **(b)** $\psi_0 = 30°$ **(c)** $\psi_0 = 45°$ **(d)** $\psi_0 = 60°$ **(e)** $\psi_0 = 75°$ **(f)** qSV- and SH-slowness

Fig. 4.32: Phase slowness dispersion curves of the principal fast and slow flexural waves excited in a fluid-filled borehole surrounded by the slow Austin Chalk TI formation for various inclinations ($\psi_0 = 15°$ (a), $30°$ (b), $45°$ (c), $60°$ (d), and $75°$ (e)) in the absence of a logging tool. The principal flexural waves are aligned with the (projected) polarization directions of the vertically propagating SH- and qSV-waves, respectively. The black lines represent their slowness values, additionally displayed in the last figure (f) in relation to the inclination angle ψ_0.

the SH-wave polarization direction (blue) is the faster one and is thus referred to as the fast principal flexural wave. Moreover, figure 4.32f illustrates the slowness values of the qSV- and SH-waves dependent on the inclination. Accordingly, for inclinations smaller than 43.5°, the fast principal flexural wave is aligned with the projected qSV-wave polarization direction while it is, for higher inclination angles, aligned with the SH-wave polarization direction. For slight differences in the qSV- and SH-wave slowness values, e.g., at $\psi_0 = 45°$, the dispersion curves of the fast and slow principal waves become hard to distinguish.

The sensitivity analysis of the dispersion curves of the principal flexural waves to the stiffness tensor elements is displayed in figure 4.33 for the inclination angle $\psi_0 = 60°$. As expected, the slowness of the fast principal flexural wave is highly sensitive to the elastic constant $C'_{5,5}$ ($\propto v^{\mathrm{SH}}$) and zero to $C'_{4,4}$ in the low-frequency limit (Fig. 4.33a). In contrast, the slowness dispersion curve of the slow principal flexural wave is sensitive only to the modulus $C'_{4,4}$ at the cutoff frequency (Fig. 4.33b).

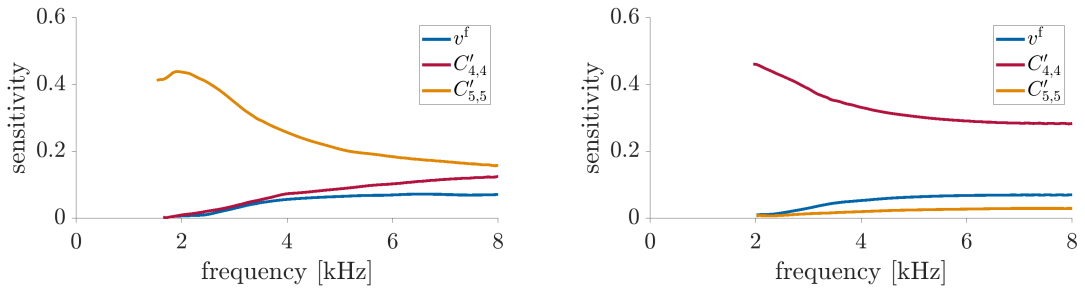

(a) Fast flexural wave sensitivity **(b)** Slow flexural wave sensitivity

Fig. 4.33: Sensitivity analysis of the phase slowness dispersion curves of the principal fast (a) and slow (b) flexural waves to the P-wave velocity in the borehole fluid (v^{f}), and the elastic moduli $C'_{4,4}$ and $C'_{6,6}$ of the Austin Chalk TTI formation exhibiting an inclination of $\psi_0 = 60°$.

If the fast Bakken Shale formation is considered instead of the slow Austin Chalk formation, the results are quite similar because the dependency of the shear wave velocities on the inclination angle is similar. For this reason, the Cotton Valley Shale formation is investigated instead of the Bakken Shale formation as an example of fast TTI formations. Figure 4.34f displays the slowness of the vertically propagating SH- and qSV-waves dependent on the inclination angle ψ_0. In contrast to the slow Austin Chalk formation, the slowness of the qSV-wave is for all inclinations higher than the slowness of the SH-wave. Hence, a dipole source aligned with the polarization direction of the SH-wave excites only the fast principal flexural wave for all inclination angles ($\psi_0 > 0$). Analogously, the slow principal flexural wave is always polarized parallel to the projected polarization direction of the qSV-wave (Fig. 4.32a–4.32e). If the inclination angle vanishes (VTI), the SH- and qSV-wave velocities coincide, and only one flexural wave is excited.

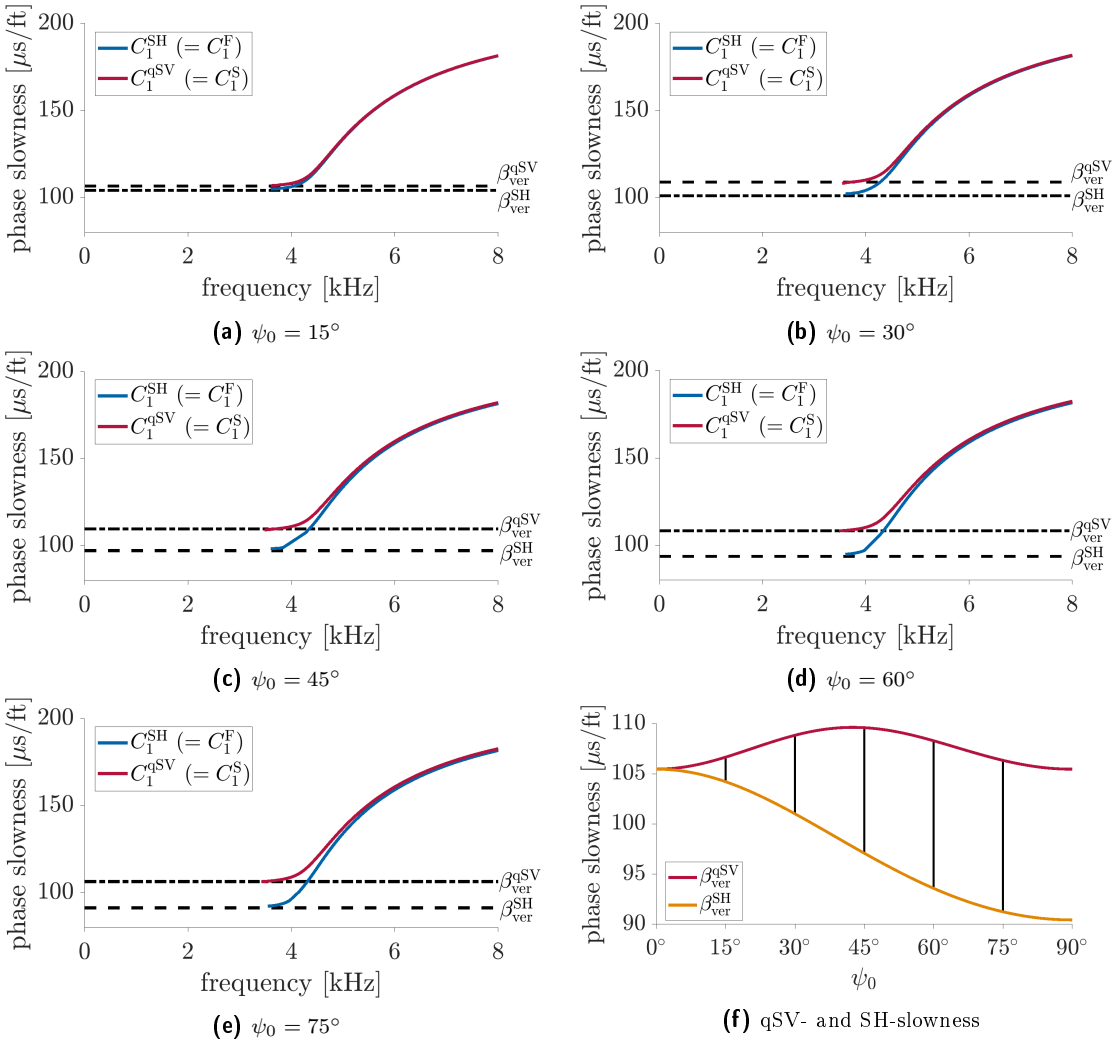

Fig. 4.34: Phase slowness dispersion curves of the principal fast and slow flexural waves excited in a fluid-filled borehole surrounded by the fast Cotton Valley Shale TI formation for various inclinations ($\psi_0 = 15°$ (a), $30°$ (b), $45°$ (c), $60°$ (d), and $75°$ (e)) in the absence of a logging tool. The principal flexural waves are aligned with the (projected) polarization directions of the vertically propagating SH- and qSV-waves, respectively. The black lines represent their slowness values, additionally displayed in the last figure (f) in relation to the inclination angle ψ_0.

The presence of an LWD tool has a strong influence on the dispersion characteristics of the flexural waves in the TTI case, like in the HTI case. Figure 4.35 displays the phase slowness dispersion curves of the principal flexural waves in the presence of an LWD tool for inclination angles of $\psi_0 = 30°$ and $\psi_0 = 60°$. In the slow Austin Chalk formation, only the principal tool flexural waves are present (Fig. 4.35a and 4.35c), whereas the formation flexural waves are additionally visible in the fast Cotton Valley Shale formation (Fig. 4.35b and 4.35d). These principal formation flexural waves attain the true shear wave slowness values of the formation at the cutoff frequency, in the same manner as in the absence of a tool. Hence, in fast formations, the formation flexural wave might be used to determine formation TI parameters. The fast and slow tool flexural waves differ only marginally and are thus not sensitive to TI parameters. In contrast, the phase slowness dispersion curves of the principal tool flexural waves are different in the slow Austin Chalk formation. The difference in the dispersion curves

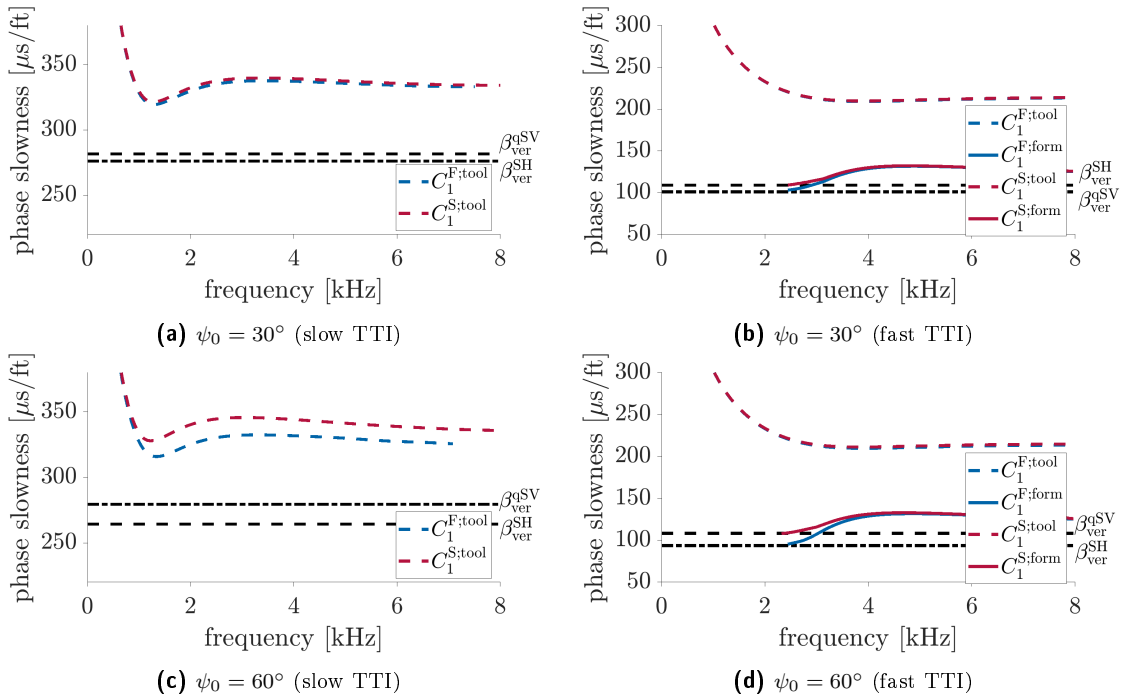

(a) $\psi_0 = 30°$ (slow TTI) **(b)** $\psi_0 = 30°$ (fast TTI)

(c) $\psi_0 = 60°$ (slow TTI) **(d)** $\psi_0 = 60°$ (fast TTI)

Fig. 4.35: Phase slowness dispersion curves of the principal tool and formation flexural waves excited in a fluid-filled borehole surrounded by the slow Austin Chalk (left) and fast Cotton Valley Shale (right) TI formation for various inclinations ($\psi_0 = 30°$ (a–b), $60°$ (c–d)) in the presence of an LWD tool. The principal tool and formation flexural waves (if they are present) are aligned with the (projected) polarization directions of the vertically propagating SH- and qSV-waves, respectively. The black lines represent their slowness.

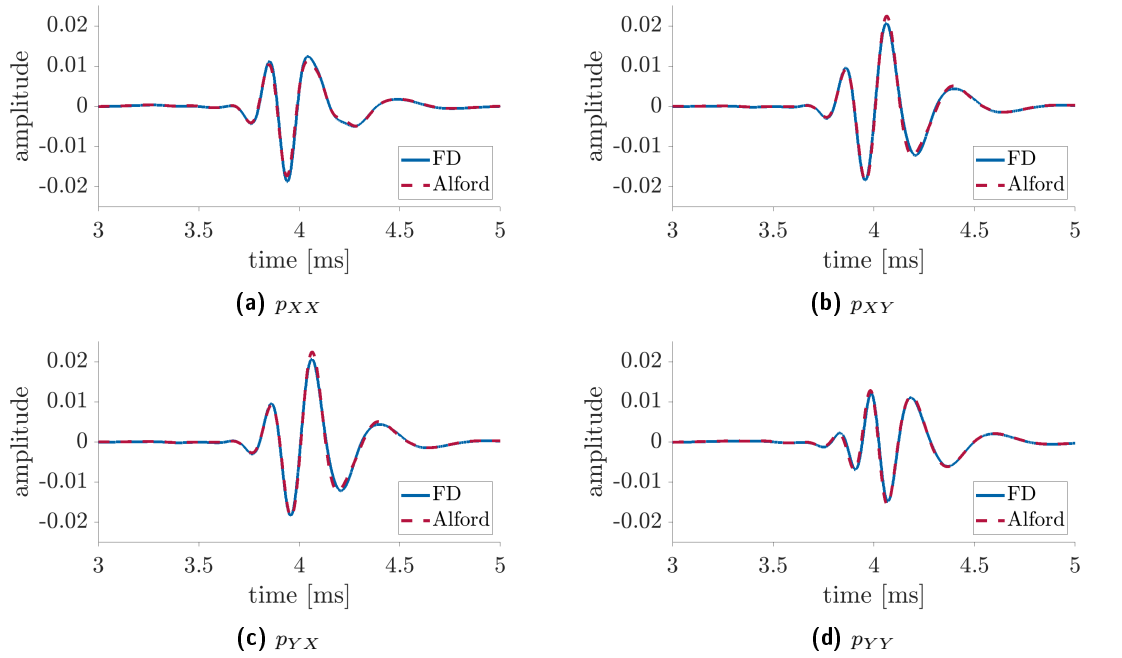

(a) p_{XX} **(b)** p_{XY}

(c) p_{YX} **(d)** p_{YY}

Fig. 4.36: Four-component data matrix of the time-domain waveforms excited by an LWD cross-dipole source azimuthally offset to the principal directions of the slow Austin Chalk TTI formation ($\psi_0 = 60°$) by $\theta^{\mathrm{F}} = 30°$. The source ($f_{\mathrm{c}} = 4\,\mathrm{kHz}$) is centered in a fluid-filled borehole in the presence of an LWD tool, and the axial offset between the cross-dipole source and the cross-dipole receiver is $z_0 = 3.262\,\mathrm{m}$. The blue waveforms result from FD modeling using an azimuthally offset cross-dipole source, whereas the red waveforms are computed by rotating the waveforms of the principal tool and formation flexural waves via the *Alford* rotation.

of both tool modes implies that they are sensitive to formation TI parameters, especially if the inclination angle is $\psi_0 = 60°$, for which the difference of the shear wave slowness values is higher than for an inclination of $\psi_0 = 30°$. Hence, the principal tool flexural waves might be used to determine the TI parameters in slow formations.

Moreover, figure 4.36 shows that the generalized formula for the *Alford* rotation does not only apply in HTI formations but also in TTI formations. The blue waveforms are simulated using FD modeling of an azimuthally offset LWD cross-dipole source in the Austin Chalk formation ($\psi_0 = 60°$). The dashed red waveforms are obtained by applying the generalized *Alford* rotation in which the FD modeled fast and slow principal flexural waves are substituted. The marginal deviation of both waveforms is induced by numerical errors.

4.3.3. Quadrupole excitation

Since the general characteristic of the flexural waves is similar in TTI and HTI formations, the same is expected for the quadrupole waves. Accordingly, the fast principal quadrupole mode is excited by a quadrupole source, with constituent sources aligned with the polarization directions of the SH- and qSV-waves. The polarization direction of the latter is projected onto the plane transverse to the borehole (Fig. 4.29). On the other hand, the slow principal quadrupole mode is azimuthally rotated to the fast principal quadrupole mode by 45° in the θ–space as described in section 4.2.4. Figure 4.37 displays the directivities of both principal quadrupole waves excited by an aligned cross-quadrupole source in a fluid-filled borehole surrounded by the slow Austin Chalk TI formation, with symmetry axis inclined to the borehole axis by $\psi_0 = 30°$ (Fig. 4.37a–4.37b) and $\psi_0 = 60°$ (Fig. 4.37e–4.37f), respectively. A cross-quadrupole source aligned with the polarization directions of the SH- and qSV-wave in TTI formations only excites the fast and slow principal quadrupole mode, respectively.

Figures 4.37c and 4.37d illustrate the directivities of the quadrupole modes excited by an azimuthal offset cross-quadrupole source ($\theta^{\mathrm{F}} = 30°$) for an inclination angle $\psi_0 = 30°$. In contrast to the HTI case, the offset cross-quadrupole source excites mainly an in-line quadrupole mode. Consequently, the cross-components of the four-component data matrix are close to zero. Equation 4.16 explains that the cross-components either vanish if the source azimuth corresponds to a principal direction ($n\theta^{\mathrm{F}} = k\pi/2,\ k \in \mathbb{Z}$) or if the fast and slow principal waves are identical. Since the cross-components are zero independent of the azimuth, the latter must be true, which is verified by figure 4.38c displaying the waveforms of both principal waves. The coincidence of both waveforms implies that the fast and slow principal quadrupole modes are almost identical ($C_2^{\mathrm{F}} \approx C_2^{\mathrm{S}}$). Thus, the distinction between fast and slow is no longer meaningful because only one quadrupole mode C_2 is excited independently of the source azimuth, such as in isotropic formations. The phase slowness dispersion curve of this quadrupole mode (Fig. 4.38d) illustrates that its low-frequency limit coincides with the phase slowness of the qSV-wave, which is for the inclination $\psi_0 = 30°$ faster than the SH-wave. If the inclination angle becomes greater, the quadrupole wave characteristic becomes more similar to the HTI case. Figure 4.37g and 4.37h illustrate the directivities of

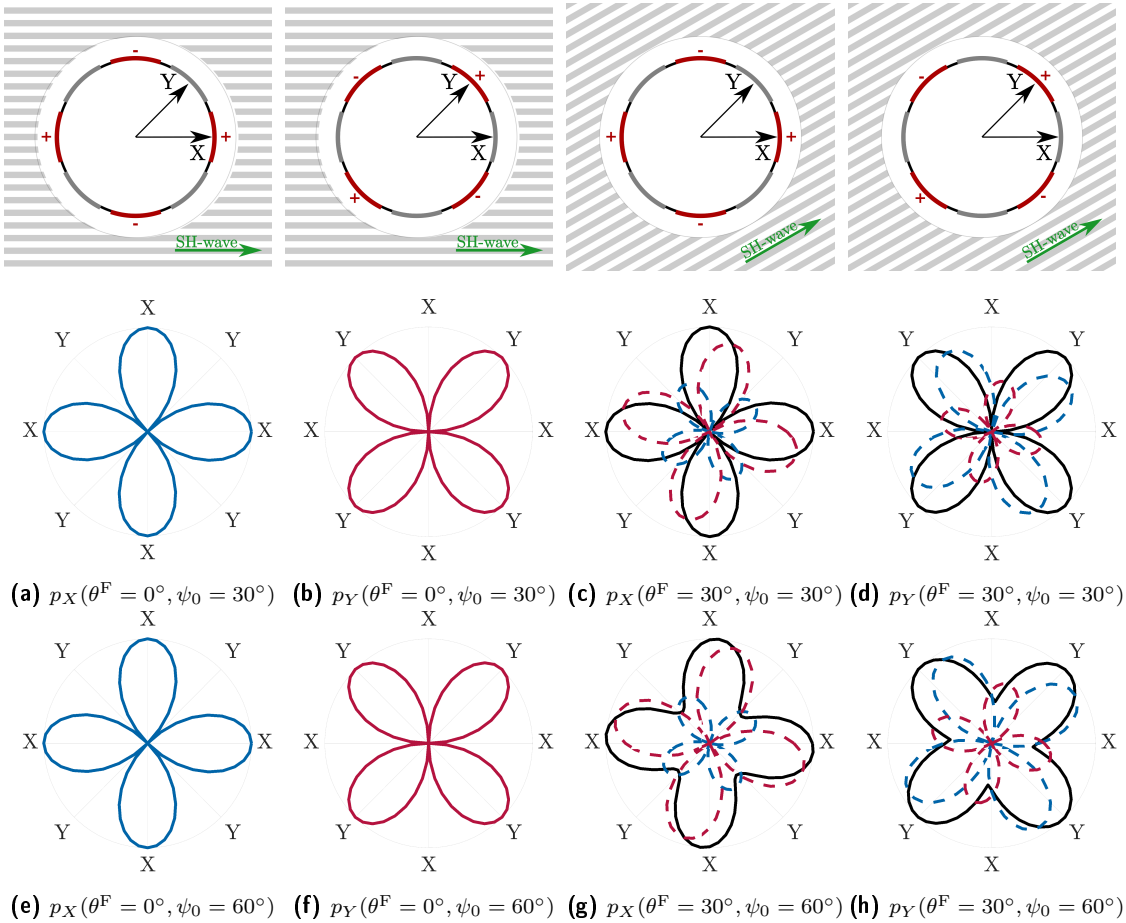

Fig. 4.37: Directivities of the quadrupole modes excited by a cross-quadrupole source aligned with the principal directions of the Austin Chalk TTI formation (a, b, e, f) and azimuthally offset to them by $\theta^F = 30°$ (c, d, g, h). The directivity is computed from the maximum absolute amplitude of the functions $\check{p}_X$ (Eq. 4.14) and $\check{p}_Y$ (Eq. 4.15), respectively, at a fixed radius and the axial offset $z_0 = 3.262\,\text{m}$. The directivity of the fast principal quadrupole mode is displayed in blue, whereas the slow one is plotted in red. In the azimuthally offset case, the excited quadrupole mode splits into the fast and slow principal quadrupole modes indicated by the dashed lines. All directivities are displayed for the inclination angles $\psi_0 = 30°$ (a–d) and $\psi_0 = 60°$ (e–h).

the quadrupole modes excited by an azimuthally offset cross-quadrupole source ($\theta^F = 30°$) for the inclination angle $\psi_0 = 60°$. The cross-components of the four-component matrix are non-zero in this case, and the principal waves are distinguishable into the fast and the slow principal quadrupole mode. Fig. 4.38g shows that the waveforms are different, especially at earlier arrival times corresponding to lower frequencies. Accordingly, the phase slowness dispersion curves of both principal quadrupole modes are distinct. While the fast quadrupole mode propagates at low frequencies with the fast SH-wave slowness, the low-frequency limit of the slow principal quadrupole does not attain the slow qSV-wave slowness. Instead, the slow principal quadrupole mode propagates faster than the qSV-wave, such as in the HTI case (Fig. 4.21a). Figure 4.38 gives an overview of the waveforms and phase slowness dispersion curves of the fast and slow principal quadrupole modes excited in a fluid-filled borehole in the presence of an LWD tool surrounded by the slow Austin Chalk TTI formation exhibiting inclinations of $\psi_0 = 15°, 30°, 45°, 60°$ and $75°$. For inclinations smaller than $60°$, the difference in the slowness values of the SH- and the qSV-waves are small (Fig. 4.38a–4.38f), wherefore

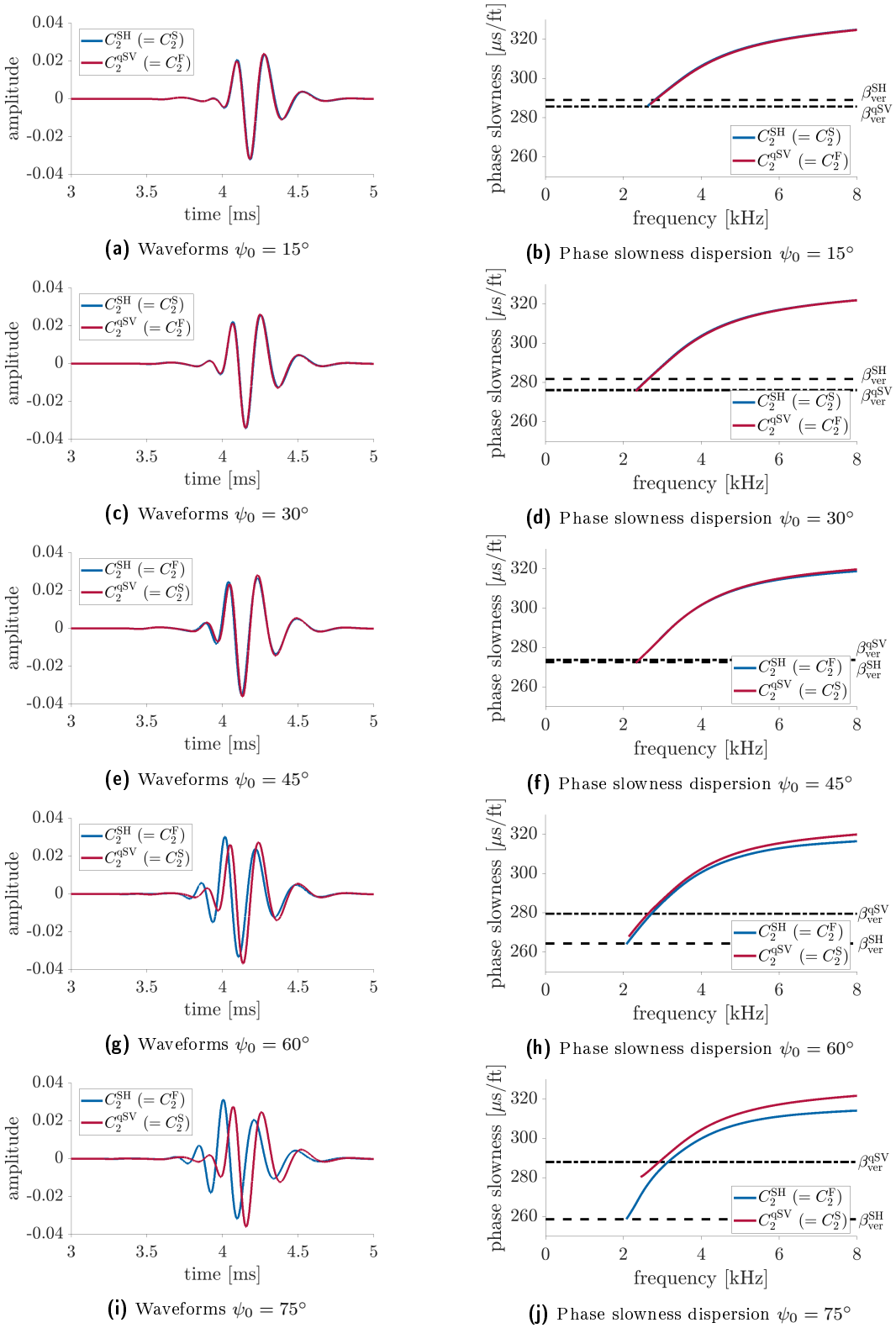

(a) Waveforms $\psi_0 = 15°$ **(b)** Phase slowness dispersion $\psi_0 = 15°$

(c) Waveforms $\psi_0 = 30°$ **(d)** Phase slowness dispersion $\psi_0 = 30°$

(e) Waveforms $\psi_0 = 45°$ **(f)** Phase slowness dispersion $\psi_0 = 45°$

(g) Waveforms $\psi_0 = 60°$ **(h)** Phase slowness dispersion $\psi_0 = 60°$

(i) Waveforms $\psi_0 = 75°$ **(j)** Phase slowness dispersion $\psi_0 = 75°$

Fig. 4.38: Waveforms (left) and phase slowness dispersion curves (right) of the principal formation quadrupole modes excited in a fluid-filled borehole surrounded by the slow Austin Chalk TI formation for various inclinations ($\psi_0 = 15°$ (a–b), $30°$ (c–d), $45°$ (e–f), $60°$ (g–h), and $75°$ (i–j)) in the presence of an LWD tool. The principal quadrupole modes are aligned with the (projected) polarization directions of the vertically propagating SH- and qSV-waves, respectively. The black lines represent their slowness values.

the fast and the slow principal quadrupole modes cannot be distinguished. For higher inclination angles ($\psi_0 = 60°$ or $\psi_0 = 75°$), the difference of the SH- and qSV-wave slowness become greater, and the fast and slow principal quadrupole modes are different (Fig. 4.38g–4.38j).

Figure 4.39 displays the sensitivity analysis of the phase slowness dispersion curves of the principal quadrupole modes to the formation's TI parameters ($\psi_0 = 60°$) given in the borehole reference frame ($\boldsymbol{x}'$) and in the crystallographic reference frame ($\boldsymbol{x}''$), respectively. It is expected that the fast principal quadrupole wave is maximally sensitive to the elastic modulus $C'_{5,5}$ in the low-frequency limit, controlling the fast shear wave (SH-wave) slowness. In contrast, the slow principal quadrupole mode should be maximally sensitive to the stiffness tensor element $C'_{4,4}$ at the cutoff frequency, which mainly determines the slow shear wave (qSV-wave) slowness. However, figures 4.39a and 4.39c show different behavior. While the sensitivity of the slow principal quadrupole wave dispersion curve is higher to the elastic modulus $C'_{4,4}$ than to $C'_{5,5}$, the fast principal quadrupole dispersion curve exhibits a strong sensitivity to both moduli. Thus, it is quite complicated to obtain true formation shear wave slowness values from quadrupole measurements in TTI formations. Furthermore, figures 4.39b and 4.39d display the sensitivities of the dispersion curves to the stiffness tensor elements given in the crystallographic reference frame. The dispersion curves of both principal quadrupole modes are sensitive to all five parameters, and a quantitative relation, such as for the tube wave velocity, cannot be derived.

If the slow Austin Chalk TI formation is replaced by the fast Cotton Valley Shale TI formation, the fast and the slow principal modes become even harder to distinguish. Figure 4.40 displays

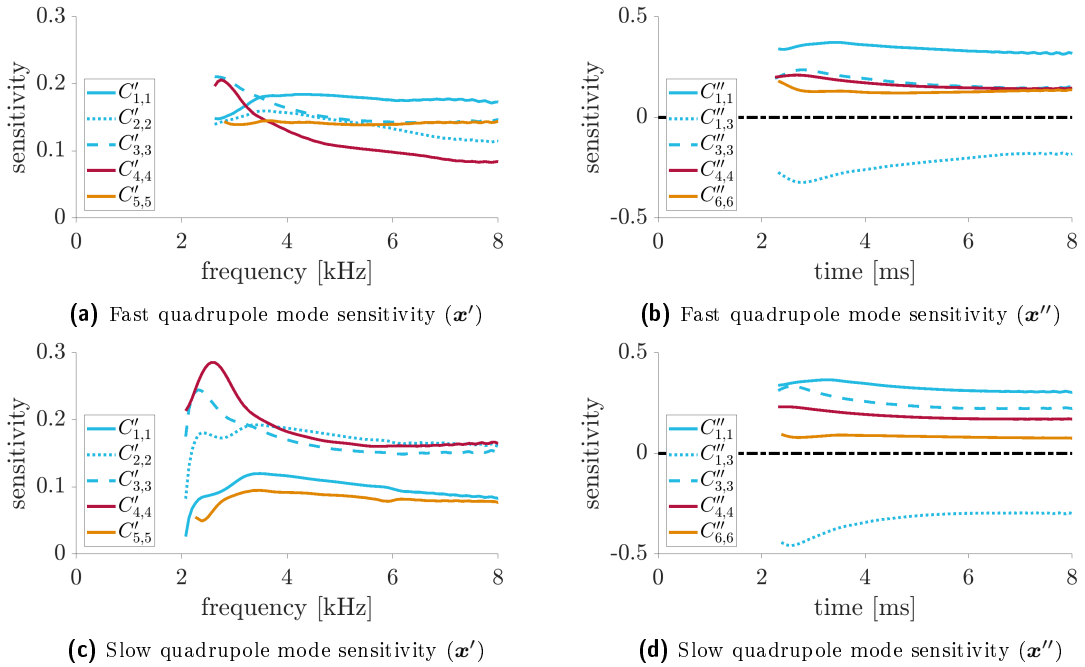

(a) Fast quadrupole mode sensitivity ($\boldsymbol{x}'$)

(b) Fast quadrupole mode sensitivity ($\boldsymbol{x}''$)

(c) Slow quadrupole mode sensitivity ($\boldsymbol{x}'$)

(d) Slow quadrupole mode sensitivity ($\boldsymbol{x}''$)

Fig. 4.39: Sensitivity analysis of the phase slowness dispersion curves of the principal fast (a–b) and slow (c–d) quadrupole modes to the elastic moduli of the Austin Chalk TTI formation expressed in the borehole $\boldsymbol{x}''$ (left) and crystallographic reference frame $\boldsymbol{x}'$ (right), respectively. The inclination angle is $\psi_0 = 60°$.

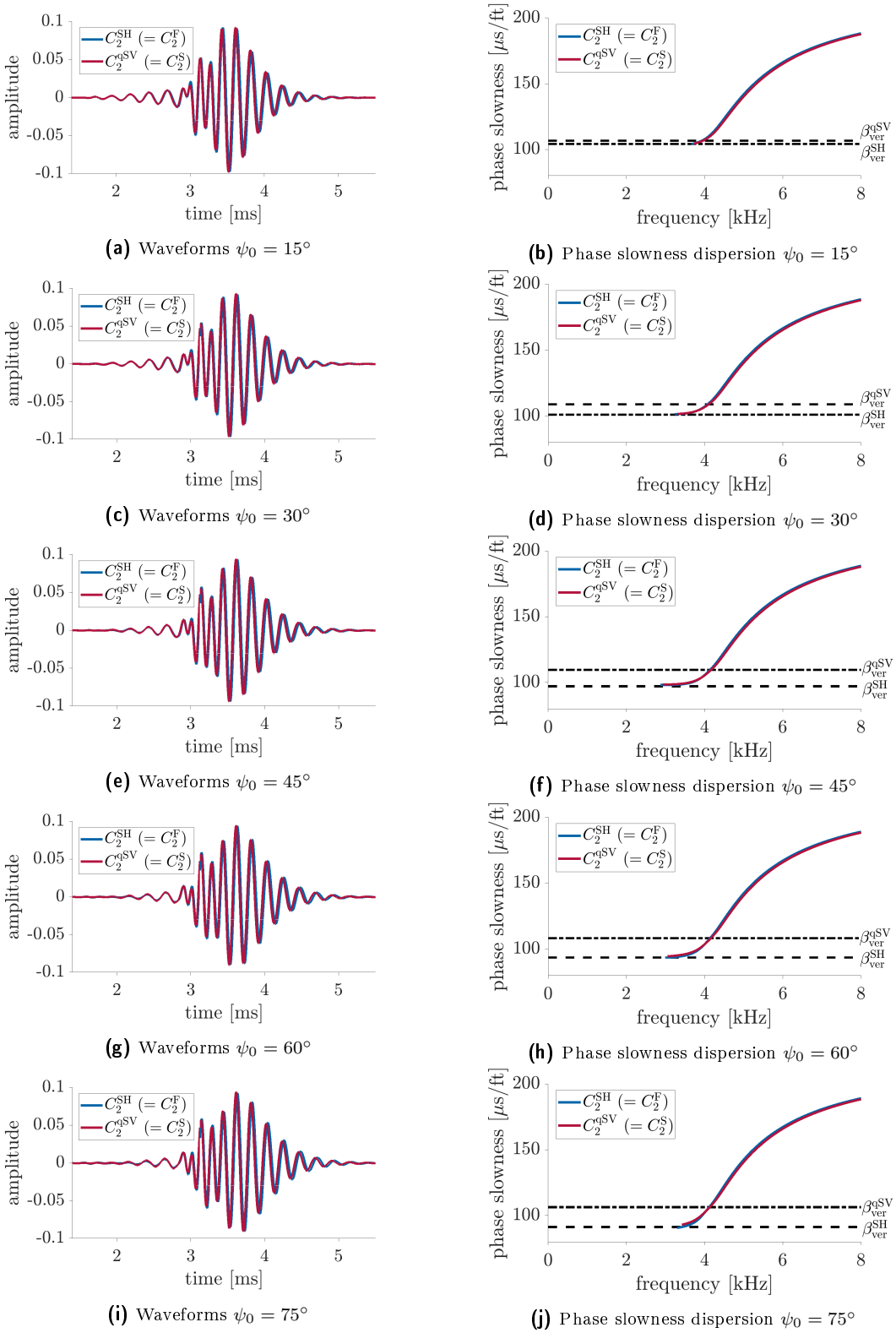

(a) Waveforms $\psi_0 = 15°$ **(b)** Phase slowness dispersion $\psi_0 = 15°$

(c) Waveforms $\psi_0 = 30°$ **(d)** Phase slowness dispersion $\psi_0 = 30°$

(e) Waveforms $\psi_0 = 45°$ **(f)** Phase slowness dispersion $\psi_0 = 45°$

(g) Waveforms $\psi_0 = 60°$ **(h)** Phase slowness dispersion $\psi_0 = 60°$

(i) Waveforms $\psi_0 = 75°$ **(j)** Phase slowness dispersion $\psi_0 = 75°$

Fig. 4.40: Waveforms (left) and phase slowness dispersion curves (right) of the principal formation quadrupole modes excited in a fluid-filled borehole surrounded by the fast Cotton Valley Shale TI formation for various inclinations ($\psi_0 = 15°$ (a–b), $30°$ (c–d), $45°$ (e–f), $60°$ (g–h), and $75°$ (i–j)) in the presence of an LWD tool. The principal quadrupole modes are aligned with the (projected) polarization directions of the vertically propagating SH- and qSV-waves, respectively. The black lines represent their slowness values.

the waveforms and phase slowness dispersion curves of the principal quadrupole modes excited in a fluid-filled borehole in the presence of an LWD tool surrounded by the fast Cotton Valley Shale TI formation exhibiting various inclination angles. It can be seen that even for the highest displayed inclination angle $\psi_0 = 75°$, the waveforms (Fig. 4.40i) are almost identical, and the dispersion curves (Fig. 4.40j) are only slightly different in the low-frequency limit. Thus, the quadrupole mode seems to be not appropriate to determine TI parameters in fast formations.

4.3.4. Summary

In contrast to the VTI and HTI cases, it is not possible to summarize the sensitivities of the refracted and borehole waves to particular stiffness tensor elements in a table for the general TTI case. The problem is that the velocities of vertically propagating plane waves are no longer defined by single stiffness tensor elements but by a combination of them dependent on the inclination between the TI symmetry axis and the vertical borehole axis. Consequently, the borehole-guided *Stoneley*, flexural, and quadrupole waves can be sensitive to all stiffness tensor elements expressed in the crystallographic reference frame dependent on the inclination angle ψ_0.

In the absence of a logging tool, the slowness of the *Stoneley* wave in the low-frequency limit is defined by the azimuthal average of the stiffness tensor element $C'_{6,6}$ expressed in the borehole reference frame. However, this elastic constant itself depends on several stiffness tensor elements given in the crystallographic reference frame and the inclination angle. Furthermore, the flexural waves split into fast and slow principal flexural waves like in the HTI case. The principal waves propagate at the cutoff frequency with the slowness of vertically propagating qSV- and SH-waves. Their slowness values also depend on several stiffness tensor elements given in the crystallographic reference frame and the inclination angle.

The presence of an LWD tool alters the slowness of the *Stoneley* wave in the low-frequency limit, such as in the VTI and HTI cases. The tool flexural waves split like the formation flexural waves in fast and slow principal tool flexural waves, which are sensitive to formation parameters at intermediate and high frequencies in slow formations. Thus, the slowness values of the vertically propagating qSV- and SH-waves may be obtained from the principal tool flexural waves using a model-based inversion method. In fast formations, the low-frequency limit of the formation flexural waves can be used to obtain the shear slowness values since the principal tool flexural waves are almost identical. The formation quadrupole mode splits into the fast and the slow principal formation quadrupole mode like the flexural wave. However, their phase slowness dispersion curves do not attain the slowness values of the vertically propagating qSV- and SH-waves at the cutoff frequency. Moreover, the principal quadrupole modes are almost identical in fast formations and for low inclination angles. Consequently, the quadrupole waves are only helpful in slow formations and at high inclination angles.

4.4. Anisotropy-induced mode contaminants

An exactly centered multipole source in a perfectly cylindrical, fluid-filled borehole surrounded by an isotropic formation excites only a limited number of borehole modes. Geerits and Kranz (2017) derived a formula for the acoustic pressure in the borehole fluid expressed as

$$\check{p}(r,\theta,z,s) = \sum_k \epsilon_k \check{C}_{kn}(r,z,s)\cos(kn\theta), \qquad k = \begin{cases} 0,2,4,... \text{ if } \sigma = 1 \\ 1,3,5,... \text{ if } \sigma = -1 \end{cases}, \tag{4.28}$$

where the effective cylinder functions $\check{C}_{kn}$ are defined in equation 4.9, and ϵ_k is the *Neumann* factor defined by

$$\epsilon_k = \begin{cases} 1 & \text{if } \ k = 0 \\ 2 & \text{else} \end{cases}. \tag{4.29}$$

The equation for the acoustic pressure considers both an equal polarity excitation ($\sigma = 1$) and an alternate polarity excitation ($\sigma = -1$). Accordingly, an alternate polarity multipole source of the order n excites all borehole modes having azimuthal wavenumbers, which are odd multiples of n ($m = kn$, $k = 1,3,5,...$). Hence, a dipole source ($n = 1$) excites additional to the leading flexural wave ($m = 1$) also the hexapole wave ($m = 3$), as discussed in section 4.2.5, the decapole wave ($m = 5$), and all higher odd multiples of $n = 1$. Analogously, a quadrupole source ($n = 2$) excites the leading quadrupole wave ($m = 2$), the dodecapole wave ($m = 6$), and higher odd multiples of $n = 2$. In all cases, the amplitudes of the excited borehole modes rapidly decrease with increasing azimuthal wavenumbers. Thus, only the first multiple of n might be detectable in real measurements. On the other hand, an equal polarity multipole source consisting of $2n$ source segments excites all borehole modes with azimuthal wavenumbers equal to even multiples of n ($m = kn$, $k = 0,2,4,...$). Consequently, all equal polarity multipole sources excite a *Stoneley* wave having the azimuthal wavenumber $m = 0$ independent of the source order n. The latter determines which higher-order modes are additionally excited. For instance, a monopole source consisting of two source segments ($n = 1$) excites in addition to the *Stoneley* wave, a quadrupole wave ($m = 2$), an octupole wave ($m = 4$), and all higher even multiples of one. If the monopole source consists of four source segments ($n = 2$), the excited next higher-order mode following the *Stoneley* wave is the octupole wave, and the quadrupole mode is not excited.

The above-explained mode excitations are only valid for a perfect azimuthal symmetry, which means that the cross-section of the borehole is perfectly circular, the tool is exactly centered, and the source signals of the constituting sources are perfectly matched in amplitude and phase. Norris (1990) and Nicoletis et al. (1990) investigated the effect of non-circular boreholes on the *Stoneley* wave velocity in the low-frequency limit. Additionally, Randall (1991) modeled the *Stoneley* and flexural borehole waves in elliptical boreholes using FD modeling. Leslie and Randall (1990), as well as Byun and Toksöz (2003), investigated the effect of an

eccentric tool, and Geerits et al. (2010) quantified the effect of source imbalances. The result of their investigation is that a non-circular borehole, an eccentric tool, or source imbalances induce mode contaminants, and the above-described mode excitation patterns are violated, e.g., an alternate polarity multipole source may also excite even multiples of n or modes that have azimuthal wavenumbers lower than n. The other way around, equal polarity multipole sources may excite odd multiples of n if the symmetry is disturbed.

Another mechanism that induces mode contaminants is formation anisotropy. Norris and Sinha (1996) have shown that the *Stoneley* and flexural waves couple in TI formations if the symmetry axis is inclined to the borehole axis ($0 < \psi_0 < \pi/2$). They concluded that the coupling seemed to be stronger in the slow Austin Chalk formation than in the fast Bakken Shale formation. In the following section, the anisotropy-induced mode contaminants are investigated in addition to the *Stoneley* and flexural waves also for higher-order cylindrical waves, such as the quadrupole, hexapole, and octupole waves. For this reason, synthetic waveforms of borehole waves are modeled, which are excited by centered multipole sources of different excitation orders in a circular fluid-filled borehole. The surrounding formation is chosen to be the slow Austin Chalk formation for better visualization since the amplitudes of the mode contaminants are greater in slow formations than in fast formations. Moreover, the two exceptional VTI and HTI symmetries, as well as the general TTI symmetry, are investigated separately. The synthetic waveforms are modeled at an offset of $z_0 = 3.26\,\mathrm{m}$ at seventy-two receivers ($N = 72$) azimuthally separated from each other by $\Delta\theta^{\mathrm{rec}} = 5°$. A discrete version of the azimuthal *Fourier* transform (App. A.3) is used to extract the different borehole modes from the waveforms (Geerits et al., 2018)

$$\tilde{p}_m(r,z,t) = \frac{1}{N}\sum_{j=0}^{N-1} \exp\left(-\mathrm{i}m\theta_j\right) p(r,\theta_j,z,t), \tag{4.30a}$$

$$p(r,\theta_j,z,t) = \mathrm{Re}\left[\sum_{j=0}^{N-1} \exp\left(\mathrm{i}m\theta_j\right) \epsilon_m \check{p}_m(r,z,t)\right], \tag{4.30b}$$

$$\theta_j = \frac{2\pi j}{N}, \qquad \epsilon_m = \begin{cases} 1 & \text{if } m = 0 \\ 2 & \text{else} \end{cases}.$$

First, a particular borehole mode having the azimuthal wavenumber m is extracted from the waveforms using equation 4.30a. Next, the output is inversely transformed via equation 4.30b to obtain the azimuthal directivity of the extracted mode. Subsequently, the maximum absolute amplitudes of the resulting waveforms are plotted in relation to the azimuth to obtain the directivity of the excited borehole modes. The amplitudes of the borehole modes are not normalized in the figures to visualize the amplitude ratio of the mode contaminants. The following sections investigate the anisotropy-induced mode contaminants in a systematic way for the VTI, HTI, and TTI symmetries. An overview of the results is given in the last section.

4.4.1. Vertical transverse isotropy (VTI)

Figure 4.41a displays the directivities of the borehole waves excited by an equal polarity LWD monopole source in a fluid-filled borehole surrounded by the slow Austin Chalk VTI formation. In agreement with the isotropic case, the monopole source of the order $n = 2$ excites only a strong *Stoneley* wave ($m = 0$) and a weak octupole wave ($m = 4$) as the next higher-order mode. Similarly, an alternate polarity dipole source ($n = 1$) excites only a flexural wave ($m = 1$) and a hexapole wave ($m = 3$) in VTI formations (Fig. 4.41b). The quadrupole source ($n = 2$) excites the dominating quadrupole wave ($m = 2$), as displayed in figure 4.41c, whereas the excited higher-order dodecapole wave ($m = 6$) has amplitudes that are too weak to be visible in the plot. Since all three sources excite the same modes as in the isotropic case, it can be concluded that anisotropy of the VTI type does not induce mode contaminants. The reason for this is the azimuthal invariance of the wave velocities in VTI formations since the plane transverse to the borehole coincides with the isotropic plane of a TI formation.

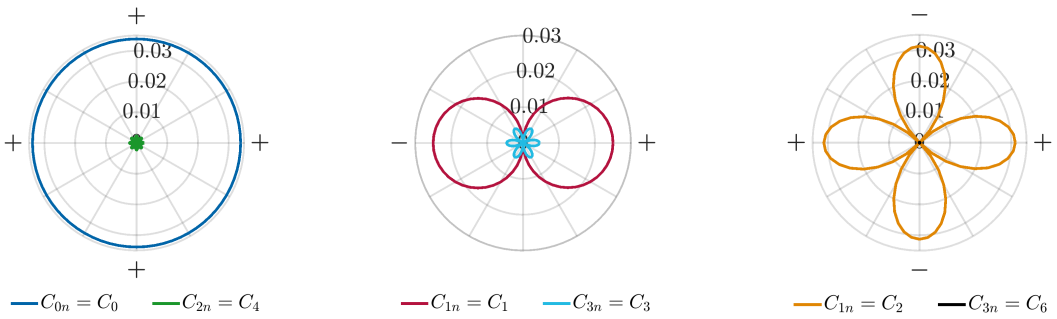

(a) Monopole excitation **(b)** Dipole excitation **(c)** Quadrupole excitation

Fig. 4.41: Directivities of the borehole waves excited by an equal polarity monopole ($n = 2$, $\sigma = 1$) (a), an alternate polarity dipole ($n = 1$, $\sigma = -1$) (b), and an alternate polarity quadrupole ($n = 2$, $\sigma = -1$) (c) source in a fluid-filled borehole surrounded by the slow Austin Chalk VTI formation in the presence of an LWD tool.

4.4.2. Horizontal transverse isotropy (HTI)

In the next step, the HTI symmetry is considered. Figure 4.42 displays the directivities of the borehole waves emitted by LWD monopole, quadrupole, and octupole sources, respectively. In all cases, the sources are either aligned with the formation's fast principal direction (Fig. 4.42b–4.42c) or aligned with the formation's slow principal direction (Fig. 4.42e–4.42f). The omnidirectional monopole source excites independent of its source azimuth relative to the formation's principal directions, the dominating *Stoneley* wave ($m = 0$), the fast principal quadrupole wave ($m = 2$), the fast principal octupole wave ($m = 4$), and higher-order fast principal cylindrical waves with even azimuthal wavenumbers. The latter are omitted in the figures because their amplitudes are too small for visualization. Further investigation shows that a monopole source always excites all cylindrical waves with even azimuthal wavenumbers in HTI formations independent of the excitation order n. This is different from the isotropic case, where the source order determines which higher-order cylindrical waves are excited. For

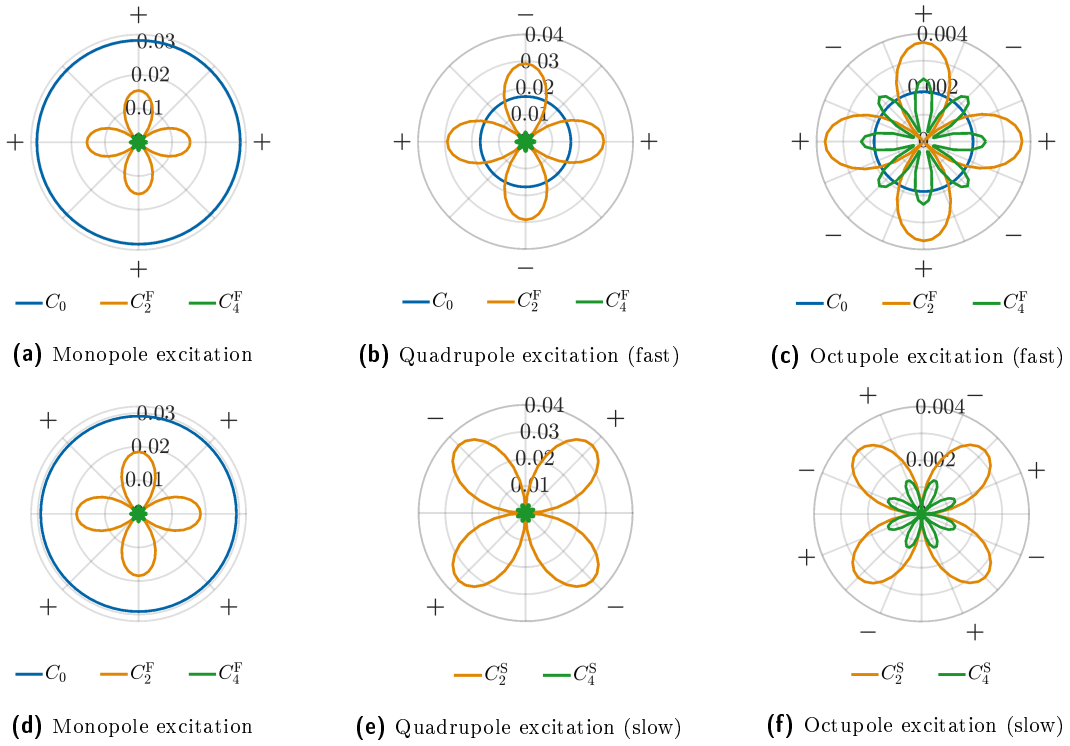

(a) Monopole excitation **(b)** Quadrupole excitation (fast) **(c)** Octupole excitation (fast)

(d) Monopole excitation **(e)** Quadrupole excitation (slow) **(f)** Octupole excitation (slow)

Fig. 4.42: Directivities of the borehole waves excited by equal polarity monopole ($n = 2$, $\sigma = 1$) (a, d), alternate polarity quadrupole ($n = 2$, $\sigma = -1$) (b, e), and alternate polarity octupole ($n = 4$, $\sigma = -1$) (c, f) sources in a fluid-filled borehole surrounded by the slow Austin Chalk HTI formation in the presence of an LWD tool. The multipole sources are aligned with the formation's fast (a–c) and slow (d–f) principal directions, respectively. The monopole excitation is invariant to the source azimuth.

instance, the monopole source of order $n = 2$ displayed in figures 4.42a and 4.42d excites the *Stoneley* wave and the octupole wave, but no quadrupole mode in the isotropic formation. Consequently, the excited fast principal quadrupole wave in the HTI formation is anisotropy-induced. The other way around, a quadrupole source ($n = 2$) aligned with the formation's fast principal direction (Fig. 4.42b) excites the *Stoneley* wave, the dominating fast principal quadrupole wave, the fast principal octupole wave, and higher-order cylindrical waves with even azimuthal wavenumbers. Since a quadrupole source excites only the quadrupole wave and the next higher-order dodecapole wave in isotropic or VTI formations (Fig. 4.41c), the emitted *Stoneley* wave and the fast principal octupole wave are anisotropy-induced. This HTI-induced coupling between the *Stoneley* wave and all fast principal cylindrical waves with even azimuthal wavenumbers can be further verified by figure 4.42c, displaying the directivities of the borehole waves excited by an octupole source ($n = 4$) aligned with the formation's fast principal direction. In contrast to the isotropic or VTI case, this octupole source excites the anisotropy-induced fast principal quadrupole wave and the *Stoneley* wave. Besides, if the quadrupole or octupole source is aligned with the formation's slow principal direction, only the slow principal quadrupole wave, the slow principal octupole wave, and higher-order slow principal cylindrical waves with even azimuthal wavenumbers are excited, but not the *Stoneley* wave (Fig. 4.42e–4.42f).

Further investigation of the *Stoneley* wave excited by a quadrupole source that is azimuthally offset to the fast principal direction of the formation shows that the amplitude of the *Stoneley* wave depends on this azimuth θ^{F}. The blue circles in figure 4.43 display the maximum amplitude of the *Stoneley* wave excited by a quadrupole source in relation to the azimuthal source offset θ^{F} to the formation's fast principal direction. The negative maximum amplitudes mean that the excited *Stoneley* wave has the opposite polarity. While the amplitude is at a maximum if the quadrupole source is aligned with the formation's fast principal direction, it vanishes if the quadrupole source is aligned with the formation's slow principal direction. The figure deduces that the *Stoneley* wave amplitude follows a $\cos(2\theta^{\mathrm{F}})$–dependency plotted by the solid blue line. Hence, the amplitudes of the *Stoneley* wave excited by a quadrupole source contain valuable information about the azimuths of the formation's principal directions. Similarly, it can be deduced that the amplitude of the *Stoneley* excited by an octupole source is proportional to $\cos(4\theta^{\mathrm{F}})$. Consequently, the dependency of the *Stoneley* wave amplitude excited by sources of higher even orders is defined by $\cos(n\theta^{\mathrm{F}})$ $(n = 2, 4, 6, ...)$.

While above only considers cylindrical waves with even azimuthal wavenumbers, the flexural and the hexapole waves having odd azimuthal wavenumbers are discussed in this part. Figures 4.44a and 4.44c show the directivities of the borehole waves excited by a dipole source $(n = 1)$ aligned with the fast and the slow principal direction of the formation, respectively. In both cases, only the principal flexural waves $(m = 1)$, the principal hexapole waves $(m = 3)$, and principal higher-order cylindrical waves with odd azimuthal wavenumbers are excited identical to the isotropic case. Additionally, figures 4.44b and 4.44d show that the aligned hexapole sources $(n = 3)$ excite the respective principal hexapole waves $(m = 3)$ and also the respective principal flexural $(m = 1)$ and decapole waves $(m = 5)$. Since the latter two are not excited by a hexapole source in isotropic or VTI formations, both are anisotropy-induced.

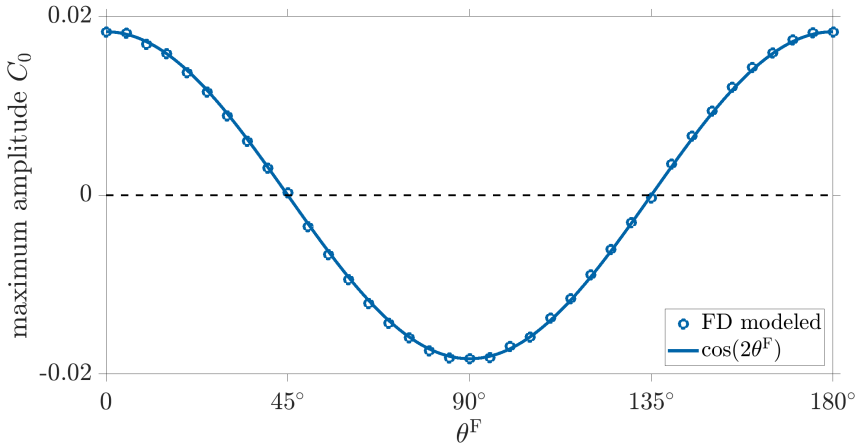

Fig. 4.43: Maximum amplitude of the anisotropy-(HTI-)induced *Stoneley* wave (C_0) excited by a quadrupole source dependent on the azimuth θ^{F} between the quadrupole excitation direction and the formation's fast principal direction. Negative amplitude values mean opposite polarity of the *Stoneley* wave.

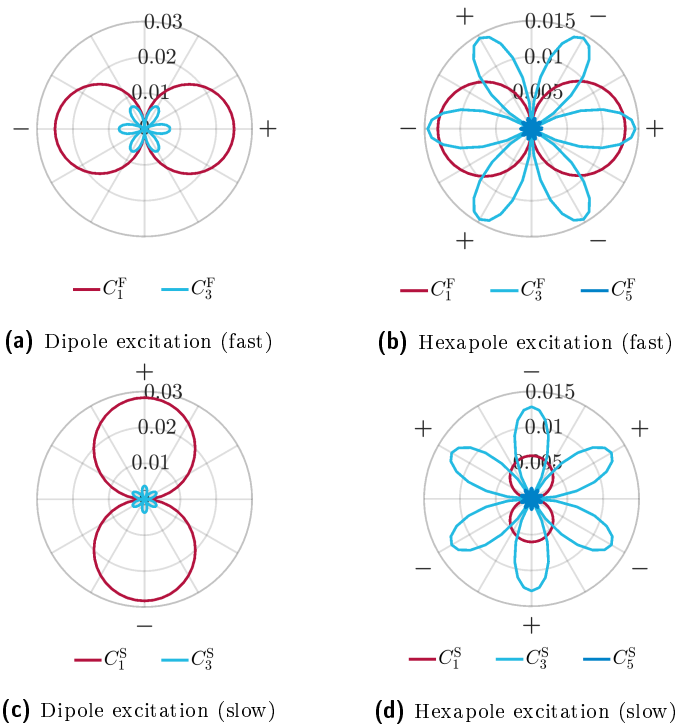

(a) Dipole excitation (fast) **(b)** Hexapole excitation (fast)

(c) Dipole excitation (slow) **(d)** Hexapole excitation (slow)

Fig. 4.44: Directivities of the borehole waves excited by alternate polarity dipole ($n = 1$, $\sigma = -1$) (a, c) and hexapole ($n = 3$, $\sigma = -1$) (b, d) sources in a fluid-filled borehole surrounded by the slow Austin Chalk HTI formation in the presence of an LWD tool. The multipole sources are aligned with the formation's fast (a–b) and slow (c–d) principal directions, respectively.

In summary, formation anisotropy of the HTI type causes coupling between all fast principal cylindrical waves having odd azimuthal wavenumbers as well as coupling between all slow principal cylindrical waves having odd azimuthal wavenumbers. Besides, coupling exists also between all slow principal cylindrical waves having even azimuthal wavenumbers ($m > 0$). The anisotropy-induced coupling between all fast principal cylindrical waves with even azimuthal wavenumbers is special because they are also coupled to the *Stoneley* wave. A multipole source azimuthally offset to the formation's principal direction excites a weighted superposition of the fast and slow principal waves for all anisotropy-induced mode contaminants. However, the weights of the principal waves are defined by the generalized formula for the *Alford* rotation (Eq. 4.17) only for the leading term ($m = n$), but not for the mode contaminants.

The amplitude ratios of the mode contaminants depend on different parameters. One important parameter is the source spectrum since some cylindrical waves will not be excited if the source spectrum contains only frequencies below its cutoff frequency. Moreover, the diameter and the elastic parameters of the LWD tool also influence the amplitudes of the mode contaminants. Another crucial parameter is the type of HTI formation. While in the above examples, only the slow Austin Chalk formation is considered, the amplitudes of the anisotropy-induced modes are significantly smaller for the fast Bakken Shale formation. Nevertheless, the explained mode contaminants and the dependency of the anisotropy-induced *Stoneley* wave are still valid.

Further numerical experiments have deduced an analogy between anisotropy-induced mode contaminants and those induced by an elliptical borehole. For this investigation, FD modeling of cylindrical waves excited by multipole sources with various excitation orders is performed. The cross-section of the fluid-filled borehole is defined by an ellipse instead of a circle, and the surrounding formation is isotropic (Fig. 4.45a–4.45b). The semi-major axes of the ellipse are analogous to the principal directions of an HTI formation. For instance, an omnidirectional monopole source excites the dominant *Stoneley* wave as well as an ellipticity-induced X-quadrupole wave and the X-octupole wave, which are aligned with the semi-major axes. These modes are analogous to the fast principal quadrupole and octupole waves. Similarly, an X-quadrupole source aligned with the semi-major axis excites the X-quadrupole wave, an ellipticity-induced *Stoneley* wave, and an ellipticity-induced X-octupole wave. On the other hand, a Y-quadrupole source 45° rotated to the semi-major axes excites only the Y-quadrupole and the ellipticity-induced Y-octupole wave but not the *Stoneley* wave. The Y-quadrupole and Y-octupole waves are analogous to the slow principal waves in an HTI formation. Indeed, the $\cos(n\theta^{\mathrm{F}})$–dependency of the amplitude of the induced *Stoneley* wave is still valid in elliptical boreholes, where the angle θ^{F} is, in analogy, the azimuth between the excitation direction and the larger semi-major axis of the ellipse. The ellipticity-induced coupling between the cylindrical waves having odd azimuthal wavenumbers also shows an identical behavior to the HTI-induced coupling and is therefore omitted here. The analogy between ellipticity-induced and anisotropy-(HTI-)induced mode coupling can be explained by the non-circular-shaped phase slowness surfaces of the shear waves in the plane transverse to the borehole. For instance, figure 2.4c illustrates that the SH-wave slowness has an elliptical shape in the Austin Chalk HTI formation. The discussed analogy causes the problem that the reason for mode contaminants in real measurements cannot be distinguished between ellipticity-induced or anisotropy-induced. Thus, additional measurements are necessary to exclude or quantify the borehole ellipticity.

Besides, not only an elliptical borehole but also an off-centered tool induces mode contaminants (Wang and Tang, 2003) similar to the anisotropy-induced ones. In this thesis, numerical modeling of various borehole modes is performed, which are excited by a multipole source of an off-centered LWD tool in a fluid-filled circular borehole surrounded by a slow isotropic formation. The tool is shifted from the borehole center in X-direction by $d = 6.5\,\mathrm{mm}$, whereby the

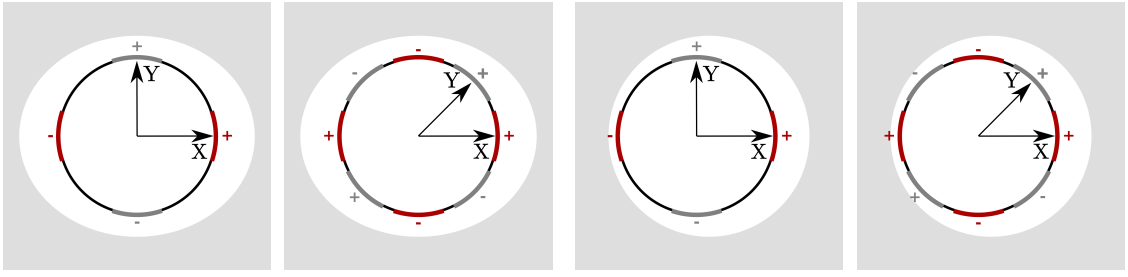

(a) Dipole sources **(b)** Quadrupole sources **(c)** Dipole sources **(d)** Quadrupole sources

Fig. 4.45: Schematic view of centered alternate polarity multipole sources/receivers in an elliptical borehole (a–b) and for an off-centered tool in a circular borehole (c–d).

total distance between the borehole radius and the outer tool radius is $R_{\mathrm{H}} - R_{\mathrm{T}}^{\mathrm{OD}} = 15\,\mathrm{mm}$. Furthermore, different excitation directions relative to the tool eccentricity are considered, as illustrated by figures 4.45c and 4.45d. The X-multipole sources are aligned with the tool eccentricity since the excitation direction of the first constituting source is parallel to the shift of the tool from the borehole center. In contrast, the Y-multipole sources of the order n are referred to as orthogonal to the tool eccentricity since the first constituting source is azimuthally offset to the eccentricity direction by $\pi/(2n)$ radians. The FD simulations show that the alternate polarity X-multipole source aligned with the tool eccentricity excites all aligned X-borehole waves and the *Stoneley* wave. The same modes are excited if a monopole source is fired. On the other hand, if the alternate polarity Y-multipole source is fired that is orthogonal to the tool eccentricity, all orthogonal Y-borehole waves are excited but not the *Stoneley* wave. This is similar to the HTI-induced mode contaminants, where the *Stoneley* wave is only excited by a multipole source aligned with the fast principal direction but not by one aligned with the slow principal direction. Indeed, it can be shown that the amplitude of the eccentricity-induced *Stoneley* wave follows the same $\cos(n\theta^{\mathrm{F}})$–dependency as for the anisotropic case, where the angle θ^{F} denotes the azimuth between the tool shift and the excitation direction in this case. While this dependency of the *Stoneley* wave's amplitude is true for all source orders if the LWD tool is off-centered, it applies in the HTI case only for alternate polarity multipole sources having even orders. In this way, the eccentricity-induced mode coupling might be distinguished from the HTI-induced mode coupling.

4.4.3. Tilted transverse isotropy (TTI)

Finally, the anisotropy-induced mode contaminants are investigated in TTI formations, where the symmetry axis is inclined to the borehole axis. Figure 4.46a shows that in TTI formations, a monopole source excites the *Stoneley* wave, the fast principal quadrupole wave, and all higher-order fast principal cylindrical waves having an even azimuthal wavenumber similar to the HTI case. However, the slow principal flexural wave and all higher-order slow principal cylindrical waves with odd azimuthal wavenumbers are additionally excited in TTI formations. This coupling between the *Stoneley* wave and the flexural wave in TTI formations was first discovered by Norris and Sinha (1996). Moreover, figure 4.46 illustrates that not only the *Stoneley* wave and the flexural wave couple but all cylindrical waves, following a specific pattern. All fast principal cylindrical waves with even azimuthal wavenumbers are coupled with the *Stoneley* wave and all slow principal cylindrical waves with odd azimuthal wavenumbers

$$C_0 \Leftrightarrow C_{2j-1}^{\mathrm{S}} \Leftrightarrow C_{2j}^{\mathrm{F}}, \qquad j \in \mathbb{N}^*. \tag{4.31}$$

These cylindrical waves are always excited independently of the source order. For instance, a dipole or hexapole source aligned with the formation's slow principal direction excites the same wave modes as a quadrupole or octupole source aligned with the formation's fast principal direction (Fig. 4.46b–4.46e). Only the amplitudes of the excited cylindrical waves depend on the source excitation.

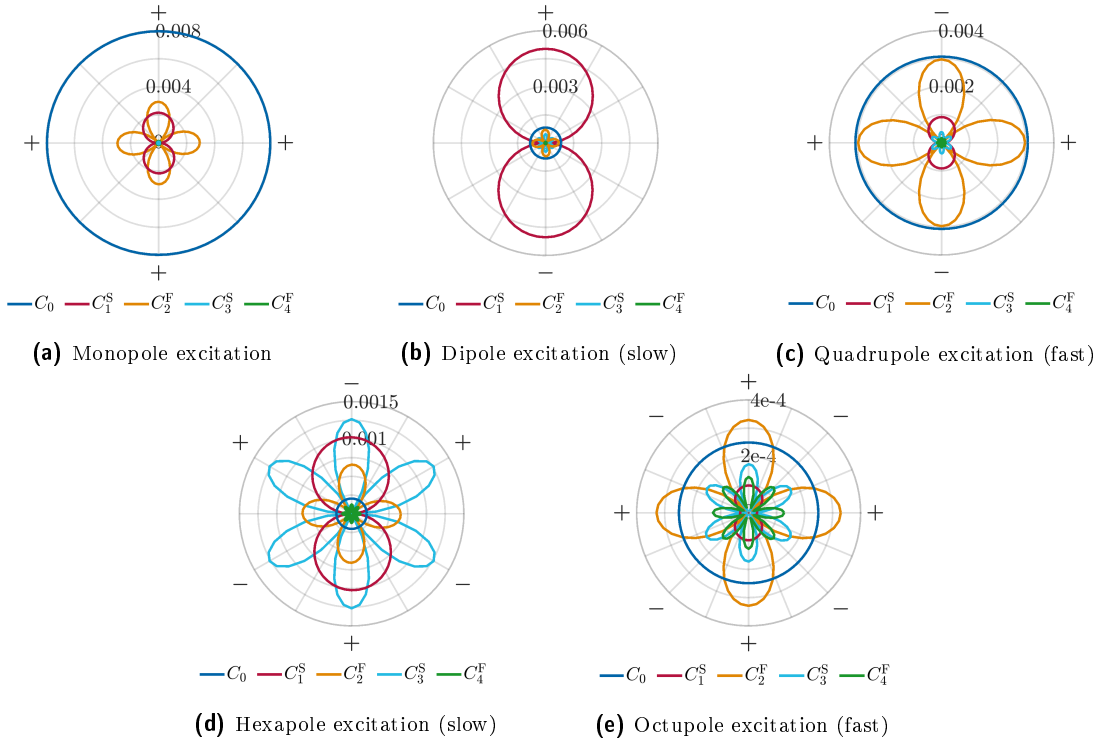

(a) Monopole excitation **(b)** Dipole excitation (slow) **(c)** Quadrupole excitation (fast)

(d) Hexapole excitation (slow) **(e)** Octupole excitation (fast)

Fig. 4.46: Directivities of the borehole waves excited by an equal polarity monopole ($n = 2$, $\sigma = 1$) (a), an alternate polarity dipole ($n = 1$, $\sigma = -1$) (b), quadrupole ($n = 2$, $\sigma = -1$) (c), hexapole ($n = 3$, $\sigma = -1$) (d), and octupole ($n = 4$, $\sigma = -1$) (e) source in a fluid-filled borehole surrounded by the slow Austin Chalk TTI formation in the absence of an LWD tool. While the multipole sources of even excitation orders are aligned with the formation's fast principal direction (c, e), the multipole sources of odd excitation orders are aligned with the formation's slow principal directions (b, d). The monopole excitation is invariant to the source azimuth.

The other way around, figure 4.47 illustrates the anisotropy-induced coupling between all fast principal cylindrical waves with odd azimuthal wavenumbers and all slow principal cylindrical waves with even azimuthal wavenumbers

$$C_{2j-1}^{\mathrm{F}} \Leftrightarrow C_{2j}^{\mathrm{S}}, \qquad j \in \mathbb{N}^*. \tag{4.32}$$

Hence, a dipole or hexapole source aligned with the formation's fast principal direction excites the same cylindrical waves that are excited by a quadrupole or octupole source aligned with the formation's slow principal direction.

The presence of an LWD tool does not change the general behavior of the mode coupling, but the amplitudes of the anisotropy-induced mode contaminants become much smaller. Therefore, figures 4.46 and 4.47 display the mode coupling in the absence of a logging tool for better visualization. Moreover, the $\cos(2\theta^{\mathrm{F}})$–dependency of the amplitude of the *Stoneley* wave excited by a quadrupole source is also valid in TTI formations, as displayed in figure 4.48. It can be seen that the amplitude of the anisotropy-induced *Stoneley* wave also highly depends on the inclination angle ψ_0 between the TI symmetry axis to the borehole axis. Figure 4.48 illustrates that higher inclination angles cause larger *Stoneley* wave ampli-

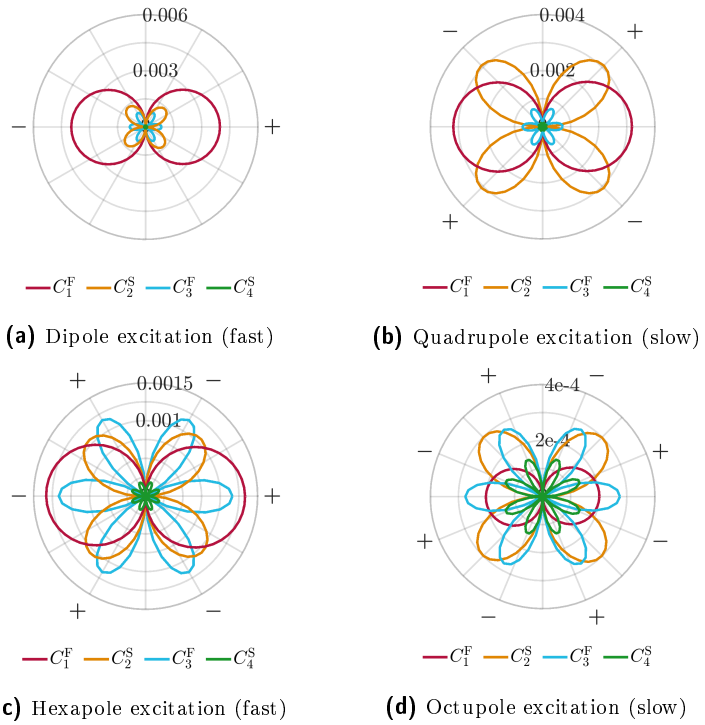

(a) Dipole excitation (fast)

(b) Quadrupole excitation (slow)

(c) Hexapole excitation (fast)

(d) Octupole excitation (slow)

Fig. 4.47: Directivities of the borehole waves excited by an alternate polarity dipole ($n = 1$, $\sigma = -1$) (a), quadrupole ($n = 2$, $\sigma = -1$) (b), hexapole ($n = 3$, $\sigma = -1$) (c), and octupole ($n = 4$, $\sigma = -1$) (d) source in a fluid-filled borehole surrounded by the slow Austin Chalk TTI formation in the absence of an LWD tool. While the multipole sources of odd excitation orders are aligned with the formation's fast principal direction (a, c), the multipole sources of even excitation orders are aligned with the formation's slow principal directions (b, d).

tudes. The reason for this can be explained by considering the phase slowness surfaces of the shear waves on the plane transverse to the borehole (Fig. 4.49). For small inclination angles, such as $\psi_0 = 15°$ (Fig. 4.49a), the phase slowness curves are nearly circular, and thus, the anisotropy-induced borehole waves are weak. However, with increasing inclinations, the

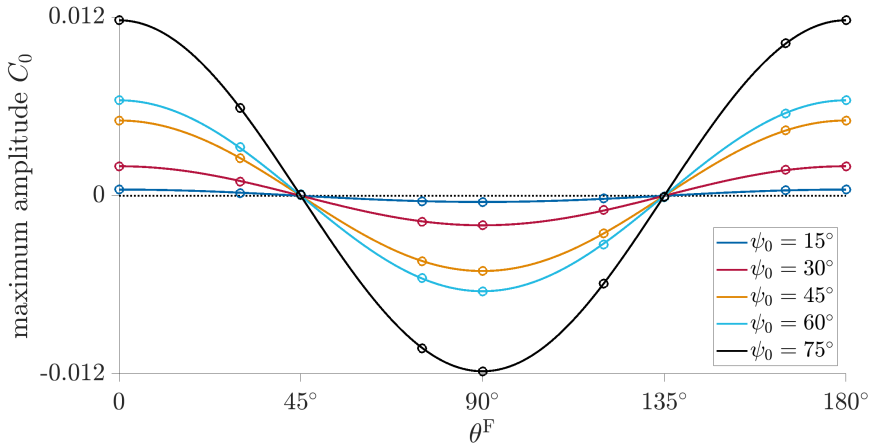

Fig. 4.48: Maximum amplitude of the anisotropy-(TTI-)induced *Stoneley* wave (C_0) excited by a quadrupole source for various inclination angles ψ_0 dependent on the azimuth θ^F between the quadrupole excitation direction and the formation's fast principle direction. Negative amplitude values mean opposite polarity of the *Stoneley* wave.

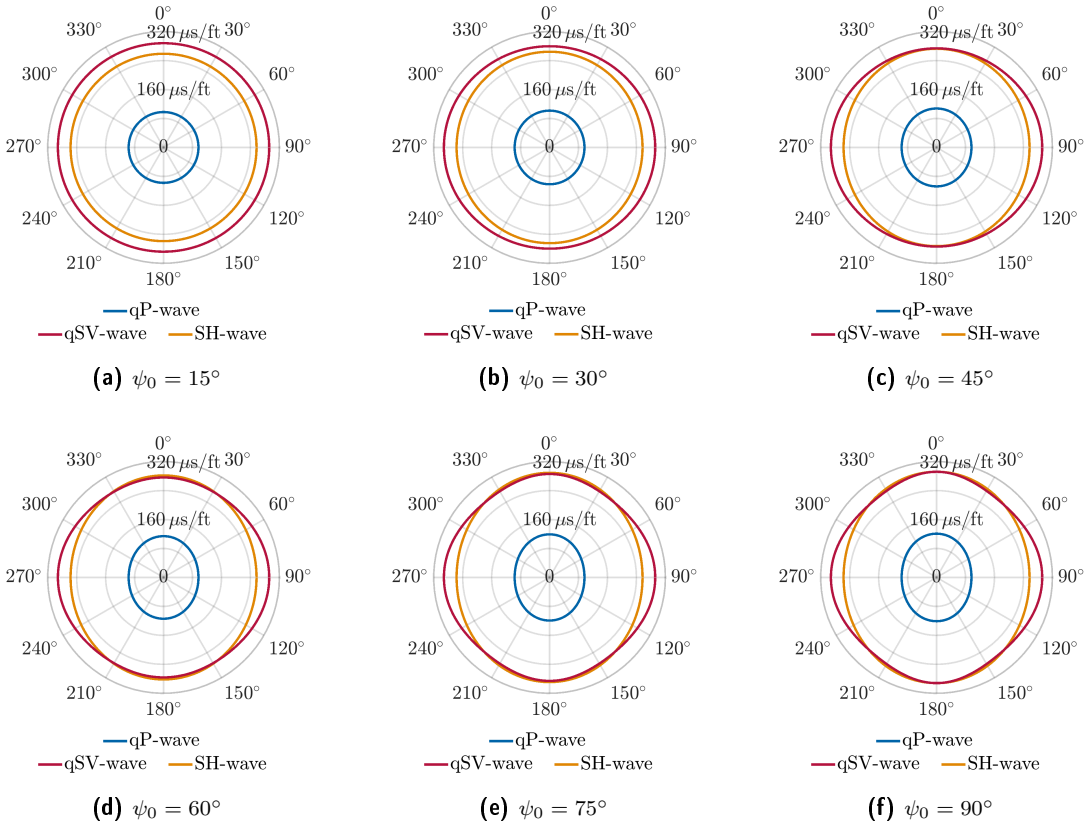

(a) $\psi_0 = 15°$ **(b)** $\psi_0 = 30°$ **(c)** $\psi_0 = 45°$

(d) $\psi_0 = 60°$ **(e)** $\psi_0 = 75°$ **(f)** $\psi_0 = 90°$

Fig. 4.49: Slices of the phase slowness surfaces through the plane transverse to the borehole axis (x_1'–x_2' plane) for the slow Austin Chalk TTI formation at different inclination angles ψ_0.

slowness curves increasingly deviate from a circular shape. Consequently, the amplitudes of the anisotropy-induced borehole modes become more significant and reach their maximum at an inclination of $\psi_0 = 90°$ (HTI), where the deviation of the phase slowness curves from circles is at a maximum.

4.4.4. Summary

The mode contaminants induced by the formation anisotropy are summarized in table 4.3 for the HTI and TTI cases. While the excitation direction of the omnidirectional equal polarity monopole source is invariant to the source azimuth, the alternate polarity sources are assumed to be either aligned with the fast or the slow principal direction, respectively. For the HTI symmetry, an aligned alternate polarity multipole source of an odd order excites all corresponding (fast or slow) principal multipole waves having odd azimuthal wavenumbers. Analogously, an aligned alternate polarity multipole source of an even order ($n > 0$) excites all respective principal multipole waves having even azimuthal wavenumbers. An exceptional case is the *Stoneley* wave having the azimuthal wavenumber zero, which is excited by an alternate polarity source of even order that is aligned with the fast principal direction, but not if the source is aligned with the slow principal direction. The mode contaminants induced by an HTI formation are also excited for the TTI symmetry. In the latter case, additionally to the principal waves having odd azimuthal wavenumbers, the opposite principal

Tab. 4.3: Summary of the anisotropy-induced mode contaminants excited by different LWD multipole sources in a fluid-filled borehole surrounded by an HTI or TTI formation.

	HTI	TTI
Monopole source ($n = 2$, $\sigma = 1$)	C_0, C_2^{F}, C_4^{F}, ...	C_0, C_1^{S}, C_2^{F}, C_3^{S}, C_4^{F}, ...
Dipole source aligned with fast direction ($n = 1$, $\sigma = -1$)	C_1^{F}, C_3^{F}, C_5^{F}, ...	C_1^{F}, C_2^{S}, C_3^{F}, C_4^{S}, ...
Dipole source aligned with slow direction ($n = 1$, $\sigma = -1$)	C_1^{S}, C_3^{S}, C_5^{S}, ...	C_0, C_1^{S}, C_2^{F}, C_3^{S}, C_4^{F}, ...
Quadrupole source aligned with fast direction ($n = 2$, $\sigma = -1$)	C_0, C_2^{F}, C_4^{F}, ...	C_0, C_1^{S}, C_2^{F}, C_3^{S}, C_4^{F}, ...
Quadrupole source aligned with slow direction ($n = 2$, $\sigma = -1$)	C_2^{S}, C_4^{S}, ...	C_1^{F}, C_2^{S}, C_3^{F}, C_4^{S}, ...
Hexapole source aligned with fast direction ($n = 3$, $\sigma = -1$)	C_1^{F}, C_3^{F}, C_5^{F}, ...	C_1^{F}, C_2^{S}, C_3^{F}, C_4^{S}, ...
Hexapole source aligned with slow direction ($n = 3$, $\sigma = -1$)	C_1^{S}, C_3^{S}, C_5^{S}, ...	C_0, C_1^{S}, C_2^{F}, C_3^{S}, C_4^{F}, ...
Octupole source aligned with fast direction ($n = 4$, $\sigma = -1$)	C_0, C_2^{F}, C_4^{F}, ...	C_0, C_1^{S}, C_2^{F}, C_3^{S}, C_4^{F}, ...
Octupole source aligned with slow direction ($n = 4$, $\sigma = -1$)	C_2^{S}, C_4^{S}, ...	C_1^{F}, C_2^{S}, C_3^{F}, C_4^{S}, ...

waves having even azimuthal wavenumbers are excited. For instance, the fast principal waves having even azimuthal wavenumbers are coupled with the slow principal waves having odd azimuthal wavenumbers and vice versa. Besides, if the alternate polarity multipole sources are azimuthally offset to the formation's principal directions, it cannot be divided between the slow and fast principal waves since a weighted superposition of both is excited. The weights are defined by the generalized *Alford* rotation (Eq. 4.17) only for the leading wave but not for the mode contaminants.

The investigated anisotropy-induced mode contaminants utilizing FD modeling can also be described by the *Christoffel* equation expressed in cylindrical coordinates after applying an azimuthal *Fourier* transform (Eq. 2.76). If the symmetry axis of the surrounding TI formation is parallel to the borehole, the stiffness tensor elements defining this VTI symmetry cause that only the coefficients of $\hat{v}_{\odot}^{m}$ ($\odot \in \{r, \theta, z\}$) are non-zero, and all other terms ($\hat{v}_{\odot}^{m\pm j}$, $j = 1, 2, 3, 4$) vanish. Consequently, the VTI symmetry does not induce mode contaminants. In contrast, if the formation exhibits HTI symmetry, only the coefficients of the terms $\hat{v}_{\odot}^{m\pm1}$ and $\hat{v}_{\odot}^{m\pm3}$ vanish, whereas the terms with an even increment for the azimuthal wavenumber ($\hat{v}_{\odot}^{m\pm j}$, $j = 0, 2, 4$) are non-zero. Thus, the HTI symmetry induces the coupling between the excited cylindrical wave having the azimuthal wavenumber m and all cylindrical waves having an even increment or decrement of m. For instance, the quadrupole wave ($m = 2$) is coupled with the *Stoneley* wave ($m = 0$) and the octupole wave ($m = 4$), or the hexapole wave

($m = 3$) couples with the flexural wave ($m = 1$) and the decapole wave ($m = 5$). Finally, if the formation's TI symmetry axis is arbitrarily inclined, all terms of the *Christoffel* equation are non-zero, and all modes are coupled. This shows that the numerical experiments are in agreement with the theory. However, the different coupling between fast and slow principal cylindrical waves cannot be seen by the partial differential equation.

5. Inversion methods

While the previous chapter investigates the waveforms and phase slowness dispersion curves of the borehole waves obtained from forward (FD) modeling, this chapter deals with the inversion of waveforms and dispersion curves to obtain the anisotropy parameters of the formation. The ultimate goal is to determine the five stiffness tensor elements in the crystallographic reference frame ($\boldsymbol{x''}$) characterizing a TI formation from LWD measurements for arbitrary inclination angles of the TI symmetry axis relative to the borehole axis. It is assumed that the formation's density ρ^{s} is known from gamma-ray logging. Moreover, the borehole radius is assumed to be known from caliper logs, whereas the dimensions and elastic parameters of the tool are defined by the used LWD tool. Besides, the density and P-wave velocity of the borehole fluid is assumed to be known and depend on the used drilling mud. Hence, only the stiffness tensor elements $C''_{1,1}$, $C''_{1,3}$, $C''_{3,3}$, $C''_{4,4}$, and $C''_{6,6}$ have to be determined in the crystallographic reference frame. Therefore, it is also necessary to determine the azimuthal angle θ_0 ($\propto \theta^{\mathrm{F}}$) and the inclination angle ψ_0 describing the rotation of the stiffness tensor elements from the tool reference frame ($\boldsymbol{x}$) to the crystallographic reference frame ($\boldsymbol{x''}$) according to section 2.2. In many cases, it can be assumed that the inclination angle ψ_0 is known from ultrasonic measurements.

In the following sections, different inversion methods are theoretically explained and discussed for the VTI, HTI, and TTI configurations. The first section discusses an inversion method for the VTI case utilizing the phase slowness dispersion of the *Stoneley* wave, which was originally developed by Tang (2003). The subsequent section presents a model-based inversion method for the HTI case introduced by Wang et al. (2016) using both the tool and formation flexural waves if the latter is present. In analogy with this method, an inversion method using non-orthogonal cross-quadrupole firings is developed. Since this inversion method cannot be applied to current LWD tools yet, an alternative inversion method is proposed using the amplitudes of the anisotropy-induced *Stoneley* waves excited by quadrupole sources at different azimuths. The last section discusses some challenges and limitations of the methods that occur in real measurements.

5.1. Vertical transverse isotropy (VTI)

Since the wave velocities are azimuthally invariant for the VTI case, the excited borehole waves do not depend on the source azimuth, and the stiffness tensor elements are equal in the crystallographic and tool reference frames. For the determination of these components, monopole and quadrupole excitations are helpful. The problem of dipole excitations is the interference between the formation and tool flexural waves, especially in slow formations.

Section 4.1.3 shows that the quadrupole mode propagates with the true vertical shear wave slowness ($\beta^{\mathrm{S}}_{\mathrm{ver}}$) defined by the elastic modulus $C''_{4,4}$ at the cutoff frequency. Consequently, the slowness of the quadrupole mode in the low-frequency limit can be used to obtain the value for $C''_{4,4}$ via

$$C''_{4,4} = \rho^{\mathrm{s}} \left(v^{\mathrm{S}}_{\mathrm{ver}}\right)^2 = \frac{\rho^{\mathrm{s}}}{\left(\beta^{\mathrm{S}}_{\mathrm{ver}}\right)^2}. \tag{5.1}$$

Furthermore, an omnidirectional monopole source can be used to excite refracted P-waves, which travel vertically along the borehole wall with vertical P-wave velocity $v^{\mathrm{P}}_{\mathrm{ver}}$ defined by the elastic modulus $C''_{3,3}$. The vertical P-wave velocity or slowness can be determined by STC processing, e.g., semblance analysis (Kimball and Marzetta, 1984) of the wavefield (App. D.1). Using the obtained velocity, the stiffness tensor element $C''_{3,3}$ can be computed via

$$C''_{3,3} = \rho^{\mathrm{s}} \left(v^{\mathrm{P}}_{\mathrm{ver}}\right)^2 = \frac{\rho^{\mathrm{s}}}{\left(\beta^{\mathrm{P}}_{\mathrm{ver}}\right)^2}. \tag{5.2}$$

Moreover, in section 4.1.1 is presented that the *Stoneley* wave excited by an omnidirectional monopole source is in the low-frequency limit highly sensitive to the elastic modulus $C''_{6,6}$. However, equation 4.3 cannot be used for the inversion because the presence of the LWD tool strongly alters the tube wave velocity (Fig. 4.3). Nevertheless, Tang (2003) developed an inversion method that accounts for the logging tool. The *Stoneley* wave dispersion curves are modeled by the roots of the boundary condition matrix, where the logging tool is modeled by an effective tool modulus. Tang (2003) has explained that the effective tool modulus of a real logging tool can be obtained from a calibration method. Furthermore, it is assumed that all parameters are known for the modeling except the stiffness tensor element $C''_{6,6}$. The problem is that only the elastic moduli $C''_{3,3}$ and $C''_{4,4}$ are determined from the above-described inversion methods. Hence, the stiffness tensor elements $C''_{1,1}$ and $C''_{1,3}$ have to be approximated. Tang (2003) suggested that the ratio of the stiffness tensor elements $C''_{4,4}$ and $C''_{6,6}$, controlling the vertical and horizontal SH-wave velocities, is similar to the ratio of the elastic constants $C''_{3,3}$ and $C''_{1,1}$, controlling the vertical and horizontal P-wave velocities. Consequently, the component $C''_{1,1}$ can be parameterized by $C''_{6,6}$ via

$$C''_{1,1} \approx \frac{C''_{3,3} C''_{6,6}}{C''_{4,4}}. \tag{5.3a}$$

Moreover, Tang (2003) proposed an approximation for the elastic modulus $C''_{1,3}$

$$C''_{1,3} \approx C''_{3,3} - 2C''_{4,4}. \tag{5.3b}$$

The latter approximation becomes true for an isotropic formation characterized by $\lambda + 2\mu = C''_{3,3}$ and $\mu = C''_{4,4}$. Using both approximations, the modeling of the *Stoneley* wave dispersion curve depends only on the elastic constant $C''_{6,6}$. In the next step, the weighted spectral

average theorem introduced by Geerits and Tang (2003) is considered

$$\bar{\beta}^{\mathrm{St}} = \frac{\int\limits_{s\in\mathrm{Br}} \beta^{\mathrm{St}}(s, C''_{6,6}) A^2(s)\mathrm{d}s}{\int\limits_{s\in\mathrm{Br}} s^2 A^2(s)\mathrm{d}s}, \tag{5.4}$$

where β^{St} represents the phase slowness dispersion curve of the *Stoneley* wave, s denotes the frequency, and $A(s)$ is the amplitude spectrum of the *Stoneley* wave. The integration over the frequencies can be performed by evaluating the *Bromwich* integral (Br) in the complex s plane (App. A.1). The left-hand side slowness value $\bar{\beta}^{\mathrm{St}}$ is the phase slowness of the *Stoneley* wave obtained from non-dispersive STC processing (App. D.1). Since the *Stoneley* wave is highly dispersive, especially at low frequencies (Fig. 4.3), non-dispersive processing is not appropriate. However, the slowness value resulting from a non-dispersive STC processing method is the weighted spectral average of the *Stoneley* wave's phase slowness dispersion curve over the frequency range of the wave spectrum (Geerits and Tang, 2003). Tang (2003) utilized equation 5.4 to develop an inversion method. The only unknown quantity in the equation is the stiffness tensor element $C''_{6,6}$. The left-hand side ($\bar{\beta}^{\mathrm{St}}$) is computed by STC processing of the measured *Stoneley* waveforms. Additionally, the amplitude spectrum of the *Stoneley* wave $A(s)$ can be determined by applying the *Laplace* transform (Sec. A.1) or a temporal *Fourier* transform to the measured waveforms. Subsequently, the phase slowness dispersion curve of the *Stoneley* wave β^{St} is forward modeled using an initial guess for $C''_{6,6}$. After integration and dividing the nominator and denominator, the resulting slowness value is compared to the slowness value $\bar{\beta}^{\mathrm{St}}$ obtained from non-dispersive STC processing. If both values are different, the phase slowness dispersion curve of the *Stoneley* wave is modeled using a different value for $C''_{6,6}$, and the resulting value is again compared to $\bar{\beta}^{\mathrm{St}}$. This procedure is repeated until the elastic modulus $C''_{6,6}$ is found, for which the left-hand side and right-hand side of equation 5.4 are equal (Tang, 2003).

The above-described inversion method is tested for the slow Austin Chalk VTI formation. The waveforms of the *Stoneley* wave are displayed in figure 5.1a. These waveforms represent the received signals in real measurements but are FD modeled in this thesis. Figure 5.1c displays the semblance analysis using a long time window ($T_w = 10\,\mathrm{ms}$). The maximum semblance value is found at the phase slowness value $\bar{\beta}^{\mathrm{St}}$ at all time samples. An alternative illustration of the semblance is the combined correlogram shown in figure 5.1b. For this figure, the semblance is stacked over all time samples and divided by their number. Hence, a function for the semblance is obtained in relation to the phase slowness. The maximum of this function corresponds to the centroid phase slowness $\bar{\beta}^{\mathrm{St}}$ and defines the left-hand side of equation 5.4. Next, the right-hand side has to be determined. Therefore, the *Stoneley* wave's amplitude spectrum is computed by applying the *Laplace* transform (App. A.1) to the waveforms displayed in figure 5.1a. Next, the phase slowness dispersion curve of the *Stoneley* wave is modeled for different values for the elastic modulus $C''_{6,6}$. For the modeling, two different values for $C''_{1,1}$ and $C''_{1,3}$ are used, respectively. While one modeling is done with the true values (Tab. 3.1), the second modeling is performed with the approximated values proposed by (Tang, 2003)

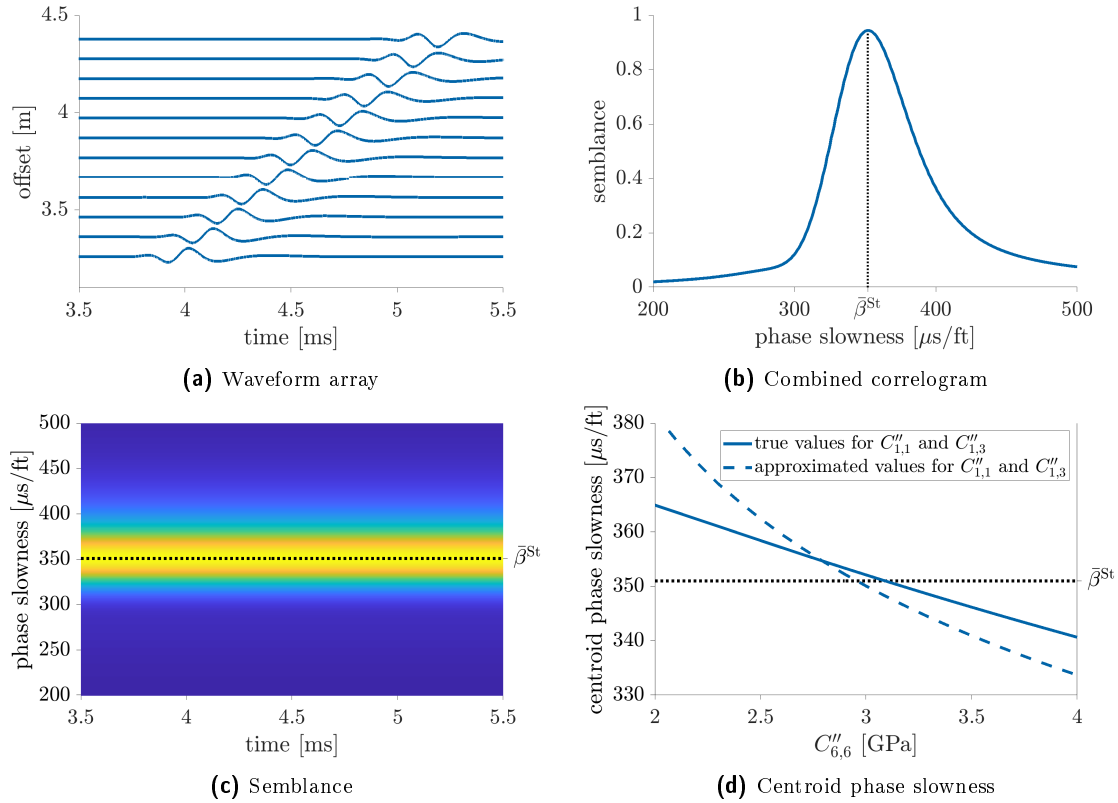

(a) Waveform array **(b)** Combined correlogram

(c) Semblance **(d)** Centroid phase slowness

Fig. 5.1: Illustration of an inversion method to obtain the elastic modulus $C''_{6,6}$ from *Stoneley* wave data. The time-domain waveform array (a) containing the *Stoneley* wave is processed by semblance processing (App. D.1) (c). The semblance values are stacked over all time samples to obtain the combined correlogram (b). The maximum semblance value corresponds to the centroid phase slowness, which is compared to the slowness computed from forward modeling of the *Stoneley* wave dispersion curves dependent on the elastic modulus $C''_{6,6}$. The blue lines in the last figure (d) illustrate the slowness value obtained from forward modeling using the exact and approximated (Eq. 5.3a and 5.3b) values for $C''_{1,1}$ and $C''_{1,3}$, respectively. The intersection of the modeled slowness value and the centroid phase slowness plotted by the dotted black line corresponds to the sought value for $C''_{6,6}$.

and defined in equations 5.3a and 5.3b. For each modeling, the right-hand side is computed according to equation 5.4, whereby numerical integration is used. In this way, the centroid phase slowness is computed in relation to the elastic modulus $C''_{6,6}$ for both modelings, as displayed in figure 5.1d by the solid and dashed lines, respectively. The input of the true values for $C''_{1,1}$ and $C''_{1,3}$ causes a linear relation between the centroid phase slowness and the elastic modulus $C''_{6,6}$. In contrast, if the respective approximated values are used, the dependency becomes non-linear since the approximation for $C''_{1,1}$ itself depends on $C''_{6,6}$. Finally, the intersection between these functions and the centroid phase slowness obtained from the semblance analysis is sought to obtain the true value for $C''_{6,6}$. This can be performed by subtracting the right-hand side from $\bar{\beta}^{St}$ and applying any root-finding algorithm subsequently. When using the true values for $C''_{1,1}$ and $C''_{1,3}$, the intersection is located at $C''_{6,6} = 3.1\,\text{GPa}$, which coincides with the true value (Tab. 3.1). In contrast, if the approximated values for $C''_{1,1}$ and $C''_{1,3}$ are used as modeling input, the intersection is located at $C''_{6,6} = 2.96\,\text{GPa}$ representing a deviation of 4.5 % from the true value.

In summary, it is possible to obtain the elastic moduli $C''_{3,3}$, $C''_{4,4}$, and $C''_{6,6}$ for the VTI symmetry using the refracted P-wave, the quadrupole wave, and the *Stoneley* wave, respectively. In contrast, the elastic moduli $C''_{1,1}$ and $C''_{1,3}$ cannot be directly determined by LWD measurements using classical kinematic inversion methods. The approximations for both moduli (Eq. 5.3a–5.3b) are good enough to model the phase slowness dispersion curves of the *Stoneley* wave since this mode is only marginally sensitive to $C''_{1,1}$ and $C''_{1,3}$ (Tang, 2003). On the other hand, for seismic migration and imaging using P-waves, the elastic modulus $C''_{1,1}$ is required more precisely, and the correlation with the ratio of the shear wave velocities may be insufficient. For instance, considering the Austin Chalk formation, the approximated values for $C''_{1,1}$ and $C''_{1,3}$ differ from their true values by 17 % and 23 %, respectively. This causes a maximal difference in the horizontal P-wave velocity of 9 %, which is in the range of anisotropy for weak anisotropic formations.

As an alternative, Bazulin et al. (2020) have presented an inversion method to obtain all five moduli characterizing a VTI formation using an inversion method based on a convolutional neural network. This network predicts the elastic moduli from the input data given by the waveforms excited by a monopole source. The advantage of their method is that both the kinematic characteristics and the amplitudes of the received waveforms are used for the inversion. However, they tested their neural network only in the absence of a logging tool and only in fast formations. Hence, it is not verified if it also works in an LWD environment or for slow formations, where refracted shear waves are not present.

5.2. Horizontal transverse isotropy (HTI)

The HTI symmetry, as the second exceptional case, has the advantage that the wave velocities depend on the azimuth, and different source azimuths can be utilized to determine the elastic moduli characterizing an HTI formation. Section 4.2.1 demonstrates that a monopole source in a fluid-filled borehole surrounded by an HTI formation dominantly excites a refracted P-wave and the *Stoneley* wave. In fast formations, two refracted shear waves (SV- and SH-wave) are additionally emitted. In theory, these waves can be used to determine the elastic moduli $C''_{4,4}$ and $C''_{6,6}$ but are in real measurements barely investigated and usually not consistent (Blyth et al., 2016). Thus, both refracted shear waves are not considered in the following sections. Nevertheless, the refracted P-wave is well detectable in real measurements in both fast and slow formations and propagates with true vertical P-wave velocity. This velocity is determined by the element $C'_{3,3}$ of the stiffness tensor given in the borehole reference frame ($\boldsymbol{x}'$). From equation 4.4 can be deduced that this element is equal to the elastic modulus $C''_{1,1}$ in the crystallographic reference frame ($\boldsymbol{x}''$). Therefore, the value for this elastic modulus can be obtained from the velocity of the vertically propagating refracted P-wave by the inverse formula of equation 4.5

$$C''_{1,1} = C'_{3,3} = \rho^{\mathrm{s}} \left(v^{\mathrm{P}}_{\mathrm{ver}}\right)^2 = \frac{\rho^{\mathrm{s}}}{\left(\beta^{\mathrm{P}}_{\mathrm{ver}}\right)^2}. \tag{5.5}$$

Besides, section 4.2.1 explains that the low-frequency limit of the *Stoneley* wave is controlled by a combination of the four elastic moduli $C''_{1,1}$, $C''_{3,3}$, $C''_{1,3}$, and $C''_{4,4}$ (Eq. 4.6) given in the crystallographic reference frame. However, this equation 4.6 is not valid for the LWD configuration because the presence of the LWD tool strongly alters the tube wave slowness. Moreover, the tool effect cannot be estimated since an analytical solution to fast model the *Stoneley* wave dispersion curves exists only for the VTI symmetry (Sec. 2.4.1). Consequently, it is not possible to develop an inversion method based on the formula for the centroid phase slowness (Eq. 5.4), as discussed in the VTI case.

5.2.1. Inverse generalized Alford rotation

Therefore, higher-order modes are required to determine further parameters of an HTI formation because these higher-order modes, such as the dipole or quadrupole mode, are sensitive to the azimuthal variations of the wave velocities. Section 4.2.2 demonstrates that for all excitation orders $n > 0$, two principal cylindrical waves exist in the HTI case. From these two principal waves, it is possible to determine the principal shear slowness values characterizing an HTI formation. However, the problem in real measurements is that, in general, a weighted superposition of both principal waves is excited since the azimuths of the fast and slow principal directions are unknown. The generalized *Alford* rotation (Eq. 4.17) can be used to develop a straightforward inversion method to obtain these azimuths and the principal cylindrical waves. The formula can be easily inverted to

$$\check{\mathcal{G}}_n(r, z_0, s) = \mathcal{R}^{\mathrm{T}}(n\theta^{\mathrm{F}})\check{\mathcal{P}}(r, z_0, s)\mathcal{R}(n\theta^{\mathrm{F}}), \tag{5.6}$$

utilizing the orthonormal property of the rotation matrix $\mathcal{R}$ ($\mathcal{R}\mathcal{R}^{\mathrm{T}} = \mathcal{R}^{\mathrm{T}}\mathcal{R} = I$). Equation 5.6 presents that the principal cylindrical waves contained in $\check{\mathcal{G}}_n$ can be obtained from the measured four-component data matrix ($\check{\mathcal{P}}$) by a rotation over the angle $n\theta^{\mathrm{F}}$. This unknown angle can be obtained by seeking the angle $n\theta^{\mathrm{F}}$ for which the off-diagonal elements of the matrix $\check{\mathcal{G}}_n$ vanish. The sum of both off-diagonal elements is given in the expanded form by (Demmler et al., 2020)

$$0 = (\check{p}_{YY} - \check{p}_{XX}) \sin\left(2n\theta^{\mathrm{F}}\right) + (\check{p}_{XY} + \check{p}_{YX}) \cos\left(2n\theta^{\mathrm{F}}\right). \tag{5.7}$$

The roots of the above equation are defined by

$$\theta^{\mathrm{F}} = \frac{1}{2n} \arctan\left(\frac{\hat{p}_{XY} + \hat{p}_{YX}}{\hat{p}_{XX} - \hat{p}_{YY}}\right) \tag{5.8}$$

after applying some basic trigonometric relations. The angle is sought in the range $0 \leq \theta^{\mathrm{F}} < \pi$. Because of the periodicity of the tangent function ($\tan(x) = \tan(x + j\pi), j \in \mathbb{Z}$) it follows

$$\theta^{\mathrm{F}} = \theta^{\mathrm{F}} + j\frac{\pi}{2n}, \;\; j = 0, 1, \ldots, 2n-1, \; n \geq 1. \tag{5.9}$$

For the flexural wave ($n = 1$), equation 5.9 yields two angles shifted by $\pi/2$ radians to each other. One angle corresponds to the polarization direction of the fast principal flexural wave

and one angle to the polarization direction of the slow one. For higher-order cylindrical waves, there are $2n$ angles shifted by $\pi/(2n)$ radians to each other, for which the off-diagonal elements in equation 5.6 vanish. This implies there are n fast angles and n slow angles ($n \geq 1$). This is referred to as angle ambiguity. The ultimate goal is to resolve this ambiguity to determine which angles belong to the fast and slow principal direction of the formation, respectively.

The standard technique to determine formation anisotropy parameters in WL logging is to use cross-dipole measurements (Esmersoy et al., 1994; Mueller et al., 1994). For this purpose, two orthogonal dipole sources are fired in sequence. The waveforms emitted by each dipole firing are received at the four azimuthal receivers of each receiver unit and are appropriately stacked to obtain the four-component pressure data matrix. The azimuths of the fast and slow principal directions of the formation are obtained from this matrix by the above-described inversion method. Additionally, the fast and slow shear slowness values are obtained from the low-frequency limit of the fast and slow principal flexural wave, respectively. Based on this inversion procedure, further improved inversion methods were developed, e.g., a simultaneous inversion method (Tang and Chunduru, 1999) to determine the azimuths of the principal directions and the principal slowness values simultaneously.

In contrast, the usage of cross-dipole excitations has some problems in the LWD configuration. One problem is that the formation flexural wave strongly interferes with the tool flexural wave and may be absent in slow formations (Sec. 4.2.3). Moreover, the fast tool rotation while logging prevents exact orthogonal cross-multipole firings, and the non-orthogonal formula for the *Alford* rotation (Eq. 4.21a) has to be applied. On the other hand, the rotation of the LWD tool has the advantage that the multipole sources can be fired at different azimuths. Market and Bilby (2012) have demonstrated that LWD dipole sources can be used to determine the shear slowness values dependent on the azimuth in fast formations. For the determination of the slowness values, they used non-dispersive STC processing and subsequently applied dispersion corrections. However, they did not investigate the coupling of the formation flexural wave and the tool flexural wave in more detail.

Wang et al. (2016) presented an inversion workflow using LWD dipole measurements to output the fast and slow principal slowness values and the azimuth of the principal directions characterizing an HTI formation. They considered a dipole source firing two times in sequence. Since the tool rotates between both firings, the dipole excitations are azimuthally separated from each other by the angle $\Delta\theta$. This angle depends on the rotation velocity of the tool and the time interval between both firings. Hence, the two dipole excitations are, in general, not orthogonal, and the non-orthogonal version of the formula for the *Alford* rotation (Eq. 4.21) has to be utilized to develop an inversion method. Inverting the formula for the

non-orthogonal *Alford* rotation yields

$$\check{\mathcal{G}}_n(r,z_0,s) = \mathcal{R}^{\mathrm{T}}(n\theta^{\mathrm{F}})\mathcal{Q}^{-1}(n\Delta\theta)\begin{bmatrix} (\check{p}_{XX},\ \check{p}_{XY}) \\ (\check{p}_{Y^*X^*},\ \check{p}_{Y^*Y^*})\,\mathcal{R}^{\mathrm{T}}(n\Delta\theta-\frac{\pi}{2}) \end{bmatrix}(r,z_0,s)\mathcal{R}(n\theta^{\mathrm{F}}), \tag{5.10a}$$

where the orthonormal property of the rotation matrix $\mathcal{R}$ is utilized, and the inverse of the matrix $\mathcal{Q}$ is defined by

$$\mathcal{Q}^{-1}(n\Delta\theta) = \begin{pmatrix} 1 & 0 \\ -\cot(n\Delta\theta) & (\sin(n\Delta\theta))^{-1} \end{pmatrix}. \tag{5.10b}$$

With the help of equations 5.10a and 5.10b, the principal cylindrical waves can be computed from two non-orthogonal multipole excitations. The problem is that the azimuth θ^{F} of the first X-multipole excitation to the formation's fast principle direction is unknown, and the angle $\Delta\theta$ between the X- and Y*-multipole excitations may not be known precisely. Fortunately, both angles can be simultaneously determined by seeking the angles for which the off-diagonal elements of the matrix $\check{\mathcal{G}}_n$ vanish

$$\begin{aligned} 0 = {} & [\check{p}_{XY} + \check{p}_{Y^*X^*} + \cot(n\Delta\theta)\,(\check{p}_{Y^*Y^*} - \check{p}_{XX})]\cos\left(2n\theta^{\mathrm{F}}\right) \\ & + [\check{p}_{Y^*Y^*} - \check{p}_{XX} - \cot(n\Delta\theta)\,(\check{p}_{XY} + \check{p}_{Y^*X^*})]\sin\left(2n\theta^{\mathrm{F}}\right). \end{aligned} \tag{5.11}$$

In real measurements, the in-line and cross-line components of the wavefield emitted by the X- and Y*-multipole excitations contain many time samples in the time domain or frequencies (s) in the *Laplace* transformed domain. Furthermore, the waveforms are received at N receivers of the receiver array having different offsets z_k ($k = 1, ..., N$). Therefore, Wang et al. (2016) defined a minimization problem to numerically compute the angles θ^{F} and $\Delta\theta$, which is generalized to apply for all cylindrical waves ($n > 0$)

$$\begin{aligned} \min_{\theta^{\mathrm{F}},\Delta\theta} \Bigg[\sum_{k=1}^{N} \int_{s\in\mathrm{Br}} \Bigg(& \big[\check{p}_{XY}(r,z_k,s) + \check{p}_{Y^*X^*}(r,z_k,s) \\ & + \cot(n\Delta\theta)\,(\check{p}_{Y^*Y^*}(r,z_k,s) - \check{p}_{XX}(r,z_k,s))\,\big]\cos\left(2n\theta^{\mathrm{F}}\right) \\ & + \big[\check{p}_{Y^*Y^*}(r,z_k,s) - \check{p}_{XX}(r,z_k,s) \\ & - \cot(n\Delta\theta)\,(\check{p}_{XY}(r,z_k,s) + \check{p}_{Y^*X^*}(r,z_k,s))\,\big]\sin\left(2n\theta^{\mathrm{F}}\right) \Bigg)\mathrm{d}s \Bigg]. \end{aligned} \tag{5.12}$$

While the azimuth θ^{F} between the X-multipole excitation direction and the formation's fast principal direction is sought in the range $0 \leq \theta^{\mathrm{F}} < \pi$, the azimuth $\Delta\theta$ between the X- and Y*-multipole excitation is sought only in the range $0 < \Delta\theta < \pi/n$. The reason for this is the nature of the cotangent function, which is involved in equation 5.12. Figure 5.2a illustrates that the cotangent function possesses discontinuities at $n\Delta\theta = k\pi$ ($k \in \mathbb{Z}$). Consequently,

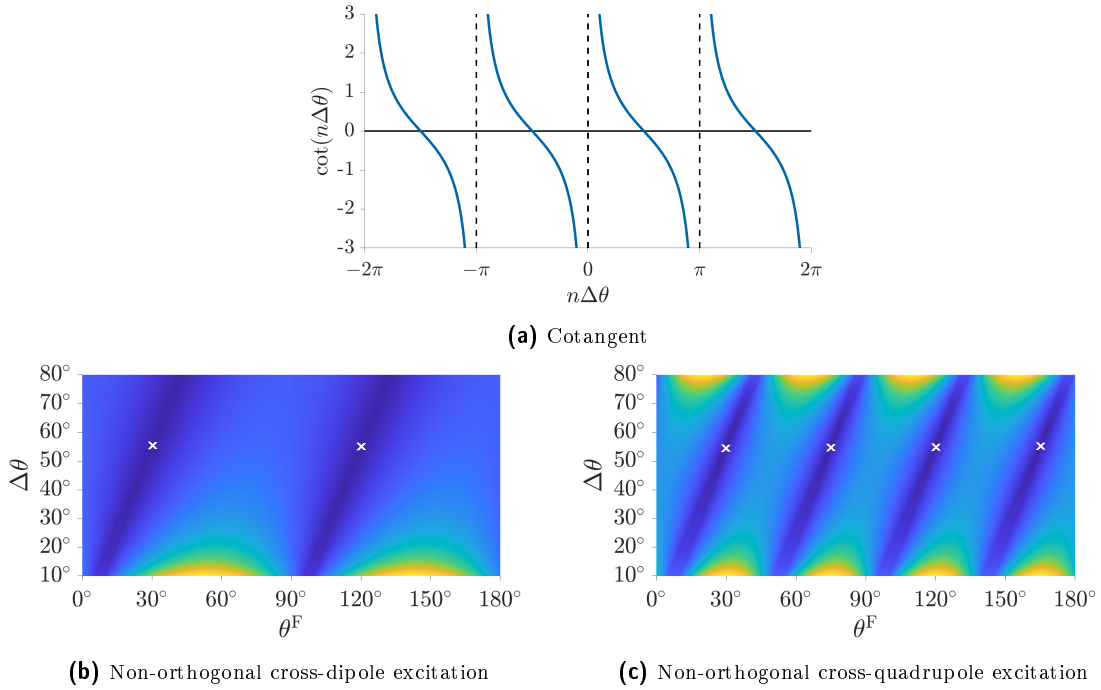

(a) Cotangent

(b) Non-orthogonal cross-dipole excitation

(c) Non-orthogonal cross-quadrupole excitation

Fig. 5.2: The upper figure (a) shows the cotangent function in the range from -2π to 2π. The bottom figures display examples of the error function computed via equation 5.12 depending on the angles θ^{F} and $\Delta\theta$. For the examples, non-orthogonal cross-dipole (b) and cross-quadrupole (c) excitations are considered, respectively, having the azimuths $\theta^{\mathrm{F}} = 30°$ and $\Delta\theta = 55°$. The white crosses indicate the minima of the error function, and their locations correspond to the actual input values for θ^{F} and $\Delta\theta$.

the inverse formula for the non-orthogonal *Alford* rotation (Eq. 5.10a) is not defined for these angles, which is reasonable since at these angles, the azimuths of the X- and Y*-multipole excitations are identical, and both may only differ in opposite polarity.

5.2.2. Inversion method based on dipole excitations

Figure 5.2b shows an example for the error function in relation to the azimuths θ^{F} and $\Delta\theta$ for two non-orthogonal dipole excitations ($n = 1$). The X-dipole source is azimuthally offset to the formation's fast principal direction by $\theta^{\mathrm{F}} = 30°$, and the azimuthal offset between the X- and Y*-dipole excitations is set to $\Delta\theta = 55°$. The white crosses in the figure indicate the two minima of the error function. Since both minima are located at the angle $\Delta\theta = 55°$, the azimuthal offset between the X- and Y*-excitation is uniquely determined in the range $0 < \Delta\theta < \pi$. In contrast, the azimuthal angle θ^{F} shows the beforehand described angle ambiguity. Accordingly, one angle corresponds to the formation's fast principal direction, and one angle corresponds to the formation's slow principal direction. This ambiguity is resolved by substituting the obtained angle for $\Delta\theta$ and one of the two angles for θ^{F} into the inverse formula for the non-orthogonal *Alford* rotation (Eq. 5.10a) to compute the fast and slow principal flexural waves. From the rotated waveform array data, the phase slowness dispersion curves of the tool flexural and formation flexural wave, if the latter is present, are extracted using the modified matrix pencil method (Ekstrom, 1996). Alternatively, Wang et al. (2016) proposed various broadband approaches to compute the phase slowness dispersion curves (Aeron et al., 2011; Wang and Bose, 2013), which are computational more efficient. In section 4.2.3 is

demonstrated that both the principal formation flexural and the principal tool flexural waves are sensitive to the HTI parameters of the formation (Fig. 4.18). While the formation flexural waves, if they are present, are more sensitive to the formation anisotropy parameters at lower frequencies, the tool flexural waves exhibit a higher sensitivity at intermediate and high frequencies. Since the drilling noise interferes with the waveforms much stronger at low frequencies, it seems advantageous to use the tool flexural waves for an inversion method. From the comparison of both tool flexural waves, it can be determined which one is the fast and the slow principal tool flexural wave, and the angle ambiguity can be resolved. If equation 5.10a, in which the angle θ^{F} was substituted, yields the correct order of the principal waves, i.e., $\check{\mathcal{G}}_{1,1} = 2\check{C}_1^{\mathrm{F}}$ and $\check{\mathcal{G}}_{2,2} = 2\check{C}_1^{\mathrm{S}}$, the substituted angle θ^{F} is associated with the formation's fast principal direction. The other way around, if the order of the principal waves is interchanged, i.e., $\check{\mathcal{G}}_{1,1} = 2\check{C}_1^{\mathrm{S}}$ and $\check{\mathcal{G}}_{2,2} = 2\check{C}_1^{\mathrm{F}}$, the substituted angle is associated with the formation's slow principal direction.

While in this way, the angle ambiguity is resolved, the principal shear wave slowness cannot be read directly from the dispersion curves of the principal tool flexural waves. For this reason, Wang et al. (2016) suggested a model-based inversion method. Therefore, the phase slowness dispersion curves of the formation and tool flexural waves are modeled by the roots of the boundary condition matrix dependent on various parameters. The model used by Wang et al. (2016) consists of a centered cylindrical steel pipe in a fluid-filled borehole surrounded by a homogeneous and isotropic formation. They assume that all parameters are known except the formation shear wave slowness which has to be determined. For the inversion method, the phase slowness values of the tool flexural wave at different frequency samples s_j are used as the input to compute the boundary condition matrix $\mathcal{D}$. Then, the determinant of the boundary condition is minimized in relation to the formation shear wave slowness $|\boldsymbol{\beta}^{\mathrm{S}}|$ to find its true value (Wang et al., 2016)

$$\min_{|\boldsymbol{\beta}^{\mathrm{S}}|} \left(\sum_{j=1}^{N} \left| \mathcal{D}(\beta(s_j), s_j, |\boldsymbol{\beta}^{\mathrm{S}}|) \right| \right). \tag{5.13}$$

It is also possible to use both the principal tool flexural and principal formation flexural waves for the inversion if the latter is present. The problem of this inversion method is that the measured phase slowness dispersion curves in anisotropic (HTI) formations are input in an isotropic model. Figures 4.18a and 4.18b illustrate that the dispersion curves of the flexural waves in anisotropic formations differ from their isotropic counterparts, especially in slow formations. Consequently, the usage of an isotropic model introduces an additional error in the inversion of the principal shear wave slowness values.

An alternative would be to use an anisotropic (HTI) model to compute the phase slowness dispersion curves. The problem is that an analytical solution does not exist if the formation exhibits anisotropy with symmetry lower than VTI, and thus, the boundary condition matrix cannot be computed analytically. For this reason, alternative methods were developed, such

as the perturbation method (Ellefsen, 1990; Sinha et al., 1994). The problem of anisotropic modeling of slowness dispersion curves is that more parameters are required which characterize the HTI formation. While for the isotropic modeling, only the density and the P-wave slowness of the formation must be known, the elastic moduli $C''_{1,1}$, $C''_{1,3}$, $C''_{3,3}$, and $C''_{4,4}$ or $C''_{6,6}$, respectively, are required for the anisotropic modeling. The vertical P-wave slowness corresponding to the modulus $C''_{1,1}$ can be obtained from the slowness of the vertically propagating refracted P-wave excited by a monopole source. Furthermore, the elastic moduli $C''_{4,4}$ and $C''_{6,6}$ controlling the shear wave slowness values may be inverted simultaneously by a joint inversion of the fast and slow principal tool flexural waves. However, the stiffness tensor elements $C''_{3,3}$ and $C''_{1,3}$ are unknown and cannot be obtained from borehole measurements. Consequently, both parameters have to be approximated analogously to section 5.1 by

$$C''_{3,3} = \frac{C''_{1,1} C''_{4,4}}{C''_{6,6}}, \tag{5.14a}$$

and

$$C''_{1,3} = C''_{1,1} - 2C''_{6,6}. \tag{5.14b}$$

Since the principal tool flexural waves exhibit only minor sensitivity to these elastic moduli, the approximations might introduce a smaller error than the usage of an isotropic model. However, such a model-based inversion method using an anisotropic (HTI) model was not tested in the scope of this thesis since an analytical solution has not been implemented yet.

5.2.3. Inversion method based on quadrupole excitations

Cross-quadrupole measurements

Since the quadrupole wave is commonly used in LWD to obtain the shear wave slowness of isotropic formations, the following sections discuss different inversion methods to determine the HTI parameters of the formation using quadrupole excitations. Like in LWD dipole measurements, the fast tool rotation can be utilized to fire two quadrupole sources in sequence, which are azimuthally offset by $\Delta\theta$. This angle and the azimuth θ^{F} between the excitation direction of the first X-quadrupole source and the formation's fast principal direction can be determined by solving the minimization problem given in equation 5.12 using $n = 2$. Figure 5.2c illustrates an example for the error function for two non-orthogonal quadrupole excitations ($n = 2$) using the input azimuths $\theta^{\mathrm{F}} = 30°$ and $\Delta\theta = 55°$. In contrast to non-orthogonal dipole excitations (Fig. 5.2b), the error function corresponding to the non-orthogonal quadrupole excitation possesses four minima instead of two indicated by the white crosses. Since all four minima are located at the angle $\Delta\theta = 55°$, the azimuthal offset between the X- and Y*-excitation is again uniquely determined in the range $0 < \Delta\theta < \pi/2$. However, the azimuth θ^{F} that shows the beforehand described angle ambiguity, can only be distinguished into two angles potentially corresponding to the formation's fast principal direction and two angles potentially corresponding to the formation's slow principal direction. Similarly to the dipole

logging, the obtained angle for $\Delta\theta$ and one of the angles for θ^{F} are substituted into the inverse formula for the non-orthogonal *Alford* rotation (Eq. 5.10a) to compute the fast and slow principal quadrupole waves. Their phase slowness dispersion curves can be extracted from the waveform array data using the modified matrix pencil method (App. D.2.2) or alternative methods mentioned above. While the principal formation quadrupole mode propagating at a lower slowness, especially at the cutoff frequency, corresponds to the fast principal quadrupole mode, the other one is the slow principal quadrupole mode. If the substituted angle θ^{F} yields the correct order of the principal waves, i.e., $\check{\mathcal{G}}_{1,1} = 4\check{C}_2^{\mathrm{F}}$ and $\check{\mathcal{G}}_{2,2} = 4\check{C}_2^{\mathrm{S}}$, this angle θ^{F} is associated with the formation's fast principal direction. In contrast, if the substituted angle yields the interchanged order of the fast and slow principal quadrupole modes, the angle is associated with the slow principal direction. In this way, the four angles obtained from the locations of the minima of the error function can be divided into two fast and two slow angles. However, it is not possible to determine which one of both fast or which one of both slow angles is the correct one. For this distinction, further information is required, e.g., provided by ultrasonic measurements.

Inversion of anisotropy-induced Stoneley waves

Another problem of the above-described inversion method is that it requires eight azimuthal receivers per receiver unit, which is not implemented in modern LWD tools. Thus, an alternative inversion method is developed, which utilizes the anisotropy-induced *Stoneley* wave excited by a multipole source having an even order. In section 4.4 is shown that the amplitude of the *Stoneley* wave depends on the angle between the fast principal direction and the multipole excitation direction. The amplitudes are measured of the *Stoneley* waves ($\check{C}_0$) excited by several even alternate polarity multipole sources at different source azimuths. For the development of an inversion method, a tool reference frame is introduced that is fixed for all firings and which azimuth $\theta = 0$ can be arbitrarily defined. The angle θ_0 is the azimuth between the fixed tool reference frame and the first constituting source of the respective multipole excitations. The azimuth θ^{F} defines the azimuth between the formation's fast principal direction and the tool reference frame in the following. Accordingly, the amplitude of the *Stoneley* wave is proportional to the $\cos(n(\theta_0 - \theta^{\mathrm{F}}))$–function (Fig. 4.43)

$$\check{C}_0(r, \theta_0, z_0, s) = \check{C}_0^{\max}(r, z_0, s) \cos\left(n(\theta_0 - \theta^{\mathrm{F}})\right) \quad (n \,\text{even}). \tag{5.15}$$

The anisotropy-induced *Stoneley* wave having the largest amplitude ($\check{C}_0^{\max}$) is excited if the multipole source is aligned with the fast principal direction of the formation ($\theta_0 = \theta^{\mathrm{F}}$). Using basic trigonometric relations, equation 5.15 can be rewritten into

$$\check{C}_0(r, \theta_0, z_0, s) = a(r, z_0, s)\cos(n\theta_0) + b(, z_0, s)\sin(n\theta_0) \quad (n \,\text{even}), \tag{5.16a}$$

$$\begin{pmatrix} a \\ b \end{pmatrix}(r, z_0, s) = \check{C}_0^{\max}(r, z_0, s) \begin{pmatrix} \cos(n\theta^{\mathrm{F}}) \\ \sin(n\theta^{\mathrm{F}}) \end{pmatrix}. \tag{5.16b}$$

For the following inversion method, the multipole source is assumed to be a quadrupole source ($n = 2$) excited at several azimuths θ_0. The inversion method requires at least two quadrupole firings at different azimuths, but more excitations at more different azimuths are recommended since the inversion method becomes more robust against noise. For all excitations, the quadrupole waves ($\check{C}_2(r, \theta_0, z, s)$) and the *Stoneley* waves ($\check{C}_0(r, \theta_0, z, s)$) are acquired from the four azimuthal receivers by appropriate stacking. While the quadrupole waves are obtained by stacking the waveforms received at the single receivers with alternating polarity between neighboring receivers, the *Stoneley* waves are obtained using equal polarity stacking. The obtained *Stoneley* wave data is used to solve equation 5.16a for a and b in the least-squared sense and in an appropriate frequency range

$$\begin{pmatrix} \cos\left(n\theta_0^{[1]}\right) & \sin\left(n\theta_0^{[1]}\right) \\ \cos\left(n\theta_0^{[2]}\right) & \sin\left(n\theta_0^{[2]}\right) \\ \vdots & \vdots \\ \cos\left(n\theta_0^{[M]}\right) & \sin\left(n\theta_0^{[M]}\right) \end{pmatrix} \begin{pmatrix} a \\ b \end{pmatrix} (r, z_0, s) = \begin{pmatrix} \check{C}_0\left(r, \theta_0^{[1]}, z_0, s\right) \\ \check{C}_0\left(r, \theta_0^{[2]}, z_0, s\right) \\ \vdots \\ \check{C}_0\left(r, \theta_0^{[M]}, z_0, s\right) \end{pmatrix}. \tag{5.17}$$

Once the coefficients a and b are determined, the azimuthal angle of the formation's fast principal direction can be computed from equation 5.16b via

$$\theta^{\mathrm{F}} = \frac{1}{n} \arctan\left(\frac{b}{a}\right). \tag{5.18}$$

Since this formula for θ^{F} involves the arctangent function, such as equation 5.8, the angle ambiguity problem remains (Eq. 5.9). In the next step, the principal quadrupole waves are computed using one of the obtained angles for θ^{F}. However, the inverse formula for the *Alford* rotation defined in equation 5.6 cannot be used since only the component $\check{p}_{XX}(r, \theta_0, z_0, s)$ is measured. Nevertheless, a least-squares problem can be formulated to compute the principal cylindrical waves $\check{C}_n^{\mathrm{F}}$ and $\check{C}_n^{\mathrm{S}}$ ($n = 2$)

$$\begin{pmatrix} \cos^2\left(n\left(\theta_0^{[1]} - \theta^{\mathrm{F}}\right)\right) & \sin^2\left(n\left(\theta_0^{[1]} - \theta^{\mathrm{F}}\right)\right) \\ \cos^2\left(n\left(\theta_0^{[2]} - \theta^{\mathrm{F}}\right)\right) & \sin^2\left(n\left(\theta_0^{[2]} - \theta^{\mathrm{F}}\right)\right) \\ \vdots & \vdots \\ \cos^2\left(n\left(\theta_0^{[M]} - \theta^{\mathrm{F}}\right)\right) & \sin^2\left(n\left(\theta_0^{[M]} - \theta^{\mathrm{F}}\right)\right) \end{pmatrix} \begin{pmatrix} 2n\check{C}_n^{\mathrm{F}} \\ 2n\check{C}_n^{\mathrm{S}} \end{pmatrix} (r, z_0, s) = \begin{pmatrix} \check{C}_n\left(r, \theta_0^{[1]}, z_0, s\right) \\ \check{C}_n\left(r, \theta_0^{[2]}, z_0, s\right) \\ \vdots \\ \check{C}_n\left(r, \theta_0^{[M]}, z_0, s\right) \end{pmatrix}. \tag{5.19}$$

If the substituted angle θ^{F} is associated with the fast or slow principal direction can be again distinguished by comparing the phase slowness dispersion curves of the computed principal cylindrical waves.

Inversion of formation parameters from principal quadrupole waves

The output of both above-described inversion methods utilizing quadrupole excitations are the azimuths of the formation's principal directions and the principal quadrupole waves. Next, these waves must be inverted to obtain TI parameters of the formation. Section 4.2.4 demonstrates that the principal fast and slow shear wave slowness values cannot be read directly from the phase slowness dispersion curves, since the principal quadrupole waves do not necessarily attain these slowness values at the cutoff frequency. Besides, the amplitudes of the principal quadrupole waves are small at low frequencies, and interfere with the drilling noise in real measurements. Hence, the low-frequency portion of the quadrupole waves is not convenient to obtain the principal shear slowness values characterizing the HTI formation. Thus, model-based inversion methods are required to obtain these values, or directly the corresponding elastic moduli $C''_{4,4}$ and $C''_{6,6}$. For instance, the determinant of the boundary condition matrix might be minimized in relation to unknown formation parameters (Eq. 5.13). Alternatively, the generalized semblance method presented by Kimball (1998) could be used based on slowness-frequency-coherence (App. D.2.1). However, the main problem of the model-based inversion methods is that they require a fast modeling tool to model the phase slowness dispersion curves of the quadrupole waves in an HTI formation. Unfortunately, such a modeling tool does not currently exist because of the lack of an analytical solution for symmetries lower than VTI. The modeling of the dispersion curves using FD modeling is not appropriate since the computational effort is too high and the run time much too long. Alternatively, an isotropic model may be used for the inversion method (e.g., Eq. 5.13). However, an inversion based on an isotropic model will introduce some errors since the dispersion curves of the principal quadrupole waves are different in HTI formations from them obtained in isotropic formations (Fig. 4.21). Moreover, an inversion method to obtain the principal slowness values from principal quadrupole waves at intermediate and high frequencies (>4 kHz) would fail in fast HTI formations since the dispersion curves of both principal quadrupole waves are almost identical at these frequencies (Fig. 4.21b). Hence, an inversion method would only work for slow formations where the fast and slow principal quadrupole waves are distinct at all frequencies (Fig. 4.21a).

An alternative method to extract the principal slowness values in fast formations seems to be using the second order quadrupole wave. Geerits et al. (2010) have shown that in fast isotropic formations a second-order quadrupole mode exists attaining the true formation shear wave slowness at the cutoff frequency. The advantage of this second order quadrupole mode is that the cutoff frequency is higher than for the first-order quadrupole mode resulting in a weaker interference with the drilling noise dominant at lower frequencies. Furthermore, the second-order quadrupole mode is less dispersive in the low-frequency limit, which is advantageous for processing. This second-order wave is not only observed for the quadrupole excitation but also for dipole excitations. Wang et al. (2017) proposed an inversion method using second-order flexural waves excited by dipole sources. The advantage of their inversion method is that it is model-independent, i.e., the forward modeling of dispersion curves is not required.

Consequently, in the scope of this thesis a similar inversion method was looked for the principal quadrupole waves. Unfortunately, it is difficult to reliably extract the second-order principal quadrupole modes from the waveform array data emitted by LWD quadrupole excitations, and the phase slowness dispersion curves of the second-order principal quadrupole waves are almost identical, such as the first-order principal quadrupole waves in fast formations.

5.3. Tilted transverse isotropy (TTI)

In the third section of this chapter, the most general TTI case is treated, where the formation's TI symmetry axis is arbitrarily inclined to the vertical borehole axis. Thus, the wave velocities of the plane waves propagating vertically along the borehole depend on the inclination angle ψ_0. Moreover, the wave velocities depend also on the azimuth like for the HTI symmetry and therefore the same inversion methods can be used as presented in the previous section. The monopole excitation is utilized to excite refracted qP-waves, traveling vertical along the borehole wall at vertical qP-wave velocity ($v_{\mathrm{ver}}^{\mathrm{qP}}$). This velocity or its inverse, the vertical qP-wave slowness, can be obtained by an STC method (App. D.1) as described in section 4.3.1. For determining the shear wave velocities of the vertically propagating qSV- and SH-wave, cross-dipole or cross-quadrupole measurements are appropriate. In sections 4.3.2 and 4.3.3 is outlined that the generalized formula for the *Alford* rotation originally developed for HTI formations also applies to TTI media. The principal directions of the TI formation are defined by the polarization direction of the vertically propagating SH-wave and the projected polarization direction of the vertically propagating qSV-wave onto the horizontal plane transverse to the borehole, as explained in section 4.3 (Fig. 4.29). Consequently, all inversion methods presented in the previous section can be used to obtain the principal shear wave velocities or slowness values corresponding to the (projected) principal directions. Also, the azimuth of the formation's fast principal direction relative to the tool azimuth can be computed by the same inversion methods as for HTI configurations. However, the difference in the phase slowness dispersion curves of the projected fast and the projected slow principal waves highly depend on the inclination angle, as displayed in figures 4.32, 4.34, 4.38, and 4.40. Hence, the inversion methods are very sensitive to noise in the waveforms at small inclinations, whereas the methods become more robust for higher inclinations.

The output of the inversion methods are the vertical wave velocities of the qP-, qSV-, and SH-wave. Unfortunately, their wave velocities are not defined by single elastic moduli given in the crystallographic reference frame ($\boldsymbol{x}''$), but by a combination of them in dependence with the inclination angle ψ_0. The exact values for the wave velocities can be calculated by solving the *Christoffel* equation (2.36). Daley and Hron (1977) derived explicit formulas to calculate the phase velocities of vertically propagating qP-, qSV-, and SH-waves in TTI media, which depend on the stiffness tensor elements expressed in the crystallographic reference frame, the inclination angle ψ_0, and the density ρ^{s}. The corrected formulas are given by (Thomsen, 1986)

$$v_{\mathrm{ver}}^{\mathrm{qP}}(\psi_0) = \sqrt{\frac{C''_{3,3} + C''_{4,4} + (C''_{1,1} - C''_{3,3})\sin^2\psi_0 + D(\psi_0)}{2\rho^{\mathrm{s}}}}, \tag{5.20a}$$

$$v_{\mathrm{ver}}^{\mathrm{qSV}}(\psi_0) = \sqrt{\frac{C''_{3,3} + C''_{4,4} + (C''_{1,1} - C''_{3,3})\sin^2\psi_0 - D(\psi_0)}{2\rho^{\mathrm{s}}}}, \tag{5.20b}$$

$$v_{\mathrm{ver}}^{\mathrm{SH}}(\psi_0) = \sqrt{\frac{C''_{6,6}\sin^2\psi_0 + C''_{4,4}\cos^2\psi_0}{\rho^{\mathrm{s}}}}, \tag{5.20c}$$

$$\begin{aligned} D(\psi_0) = \Big[& (C''_{3,3} - C''_{4,4})^2 \\ & + 2\left(2(C''_{1,3} + C''_{4,4})^2 - (C''_{3,3} - C''_{4,4})(C''_{1,1} + C''_{3,3} - 2C''_{4,4})\right)\sin^2\psi_0 \\ & + \left((C''_{1,1} + C''_{3,3} - 2C''_{4,4})^2 - 4(C''_{1,3} + C''_{4,4})^2\right)\sin^4\psi_0 \Big]^{\frac{1}{2}}. \end{aligned} \tag{5.20d}$$

The above-presented equations are helpful to invert the stiffness tensor elements from the vertical plane wave velocities assuming that the formation's density ρ^{s} and the inclination angle ψ_0 are known from other measurements. The problem is that there are five unknown stiffness tensor elements characterizing a TI formation but only three equations for the qP-, qSV- and SH- wave velocities. Consequently, an inversion method results in an underdetermined nonlinear equation system. In the VTI and HTI cases, this problem was solved by approximating two elastic moduli, respectively. For the modeling of the *Stoneley* wave dispersion curves in the VTI case, the elastic moduli $C''_{1,1}$ and $C''_{1,3}$ are approximated by formulas depending only on $C''_{3,3}$, $C''_{4,4}$, and $C''_{6,6}$ (Eq. 5.3a and 5.3b). Analogous approximations (Eq. 5.14a and 5.14b) are proposed for the anisotropic modeling of flexural and quadrupole slowness dispersion curves in the HTI case. However, these approximations only work for both exceptional TI cases since the sensitivities of the respective borehole modes are low to the approximated elastic moduli. While the vertical SH-wave velocity depends only on the elastic moduli $C''_{4,4}$ and $C''_{6,6}$ in the TTI case, the sensitivity of the vertical qP- and qSV-wave velocities is high to all elastic moduli, and the proposed approximations would introduce an enormous error, as displayed in figure 5.3. The solid lines denote the velocities of the vertically propagating qP- and qSV-waves if the exact stiffness tensor values are used for the calculation. In comparison, the dashed and dotted lines represent the same wave velocities, if for their computation the elastic moduli $C''_{1,1}$ and $C''_{1,3}$ are approximated by Eq. 5.3a and 5.3b (VTI), and the elastic moduli $C''_{3,3}$ and $C''_{1,3}$ are approximated by Eq. 5.14a and 5.14b (HTI), respectively. These approximations induce errors in the qP- and qSV-wave velocities up to 10 % and 23 %, respectively. Consequently, approximations cannot be used to reduce the number of elastic moduli which have to be determined.

An alternative seems to be involving the tube wave velocity in the inversion. This velocity is defined by the low-frequency limit of the *Stoneley* wave's dispersion curve and depends on a

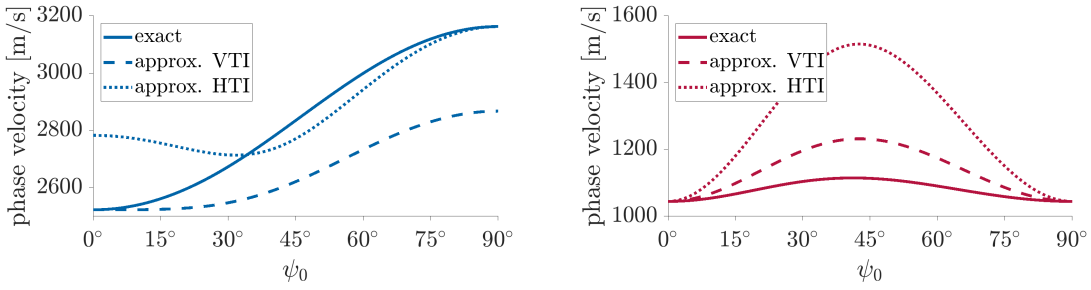

(a) qP-wave velocity **(b)** qSV-wave velocity

Fig. 5.3: The solid lines in the figures display the phase velocities of the vertically propagating qP- (a) and qSV-wave (b) dependent on the inclination angle ψ_0. The dotted lines represent the values for the velocities when using approximated values for $C''_{1,1}$ and $C''_{1,3}$ (VTI: Eq. 5.3a and 5.3b) or for $C''_{3,3}$ and $C''_{1,3}$ (HTI: Eq. 5.14a and 5.14b).

known combination of all five elastic moduli given in the crystallographic reference frame and the inclination angle ψ_0 (Eq. 4.27d). In this way, a fourth equation is obtained, and only one elastic modulus must be known a priori. However, this equation holds only in the absence of a logging tool since the presence of an LWD strongly alters the tube wave velocity. Like in the HTI case, this effect of the presence of a logging tool cannot be modeled because of the lack of an analytical solution for the TTI case.

In conclusion, this means that two elastic moduli must be known a priori in the crystallographic reference frame, preferably the modulus $C''_{1,3}$ and either $C''_{1,1}$ or $C''_{3,3}$. Assuming that the elastic moduli $C''_{1,1}$ and $C''_{1,3}$ of the TI formation, as well as the inclination angle ψ_0 and the formation density ρ^{s} are precisely known, the elastic moduli $C''_{3,3}$ and $C''_{4,4}$ can be simultaneously inverted by solving the minimization problem

$$\min_{C''_{3,3},C''_{4,4}} \Big\{ \big|\big| 2\rho^{\mathrm{s}} \left(v_{\mathrm{ver}}^{\mathrm{qP}}(\psi_0)\right)^2 - C''_{3,3} - C''_{4,4} - (C''_{1,1} - C''_{3,3}) \sin^2\psi_0 - D(\psi_0) \big|\big| + \big|\big| 2\rho^{\mathrm{s}} \left(v_{\mathrm{ver}}^{\mathrm{qSV}}(\psi_0)\right)^2 - C''_{3,3} - C''_{4,4} - (C''_{1,1} - C''_{3,3}) \sin^2\psi_0 + D(\psi_0) \big|\big| \Big\}, \tag{5.21}$$

where $D(\psi_0)$ is defined in equation 5.20d. Figure 5.4 displays examples of the error function defined by the minimization problem. For both the slow Austin Chalk formation and the fast Bakken Shale formation, the correct values for $C''_{3,3}$ and $C''_{4,4}$ (Tab. 3.1) are obtained by the location of the minimum indicated by the white crosses, respectively. Once the elastic modulus $C''_{4,4}$ is determined, it can be substituted in the inverse formula of equation 5.20c to compute the stiffness tensor element $C''_{6,6}$

$$C''_{6,6} = \frac{\left(v_{\mathrm{ver}}^{\mathrm{SH}}(\psi_0)\right)^2 \rho^{\mathrm{s}}}{\sin^2\psi_0} - C''_{4,4} \cot^2\psi_0. \tag{5.22}$$

In this way, the three elastic moduli $C''_{3,3}$, $C''_{4,4}$, and $C''_{6,6}$ can be computed if the stiffness tensor elements $C''_{1,1}$ and $C''_{1,3}$, the inclination angle ψ_0, and the formation density are precisely known. The problem with this naive inversion method is that it is highly susceptible to errors

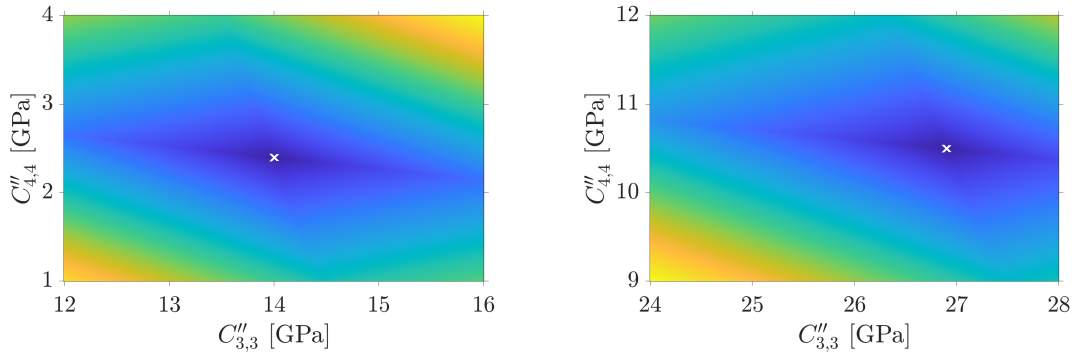

(a) Austin Chalk **(b)** Bakken Shale

Fig. 5.4: Error functions defined by the minimization problem in equation 5.21 for the slow Austin Chalk (a) and fast Bakken Shale (b) TTI formations. The location of the minimum corresponds to the values for the elastic moduli $C''_{3,3}$ and $C''_{4,4}$.

in the input parameters. For instance, a deviation of only one degree from the exact inclination angle will cause the failure of the inversion method. The same is true if the vertical wave velocities are not determined precisely. As a result, the inversion method cannot be applied to data obtained from real measurements because of its high sensitivity to minor errors and noise.

Alternatively, it is possible to invert not the stiffness tensor elements itself but the *Thomsen* parameters ϵ, γ, and δ (Thomsen, 1986). These three dimensionless parameters and the wave velocities of the compressional and shear waves, propagating parallel to the TI symmetry axis, characterize a TI formation (Sec. 2.1.4). However, this results in the same problem that there are five unknowns but only three equations for the vertical qP, qSV- and SH-wave velocities. Thus, it must also be assumed that two parameters are known a priori. Norris and Sinha (1993) proposed an inversion method to invert the elastic moduli for a weakly anisotropic TTI formation from monopole measurements in the absence of a logging tool. Thus, they could use the tube wave velocity in their inversion algorithm to get a fourth equation. Nevertheless, they presented that their inversion method is also highly susceptible to errors in the inclination angle ψ_0.

The main problem of the inversion of TI elastic moduli in the crystallographic reference frame from borehole acoustic measurements is that only one travel path along the borehole wall of the compressional and shear waves can be measured. Consequently, information is only available at one inclination angle ψ_0. As a result, the inclination angle must be precisely known to invert elastic moduli from the vertical wave velocities correctly. If there would be more travel paths at various inclination angles, the sensitivity to the inclination angle could be reduced, or the angle could even be obtained from the measurements. For this reason, Hornby et al. (2003), Walsh et al. (2006) and Horne et al. (2012) combined borehole acoustic measurements from several boreholes having different deviations or from one deviated borehole exhibiting parts with different inclinations. However, their methods work only for specific problems and cannot be generalized. For a single borehole acoustic measurement it is not possible to measure velocities of compressional or shear waves that do not propagate along the borehole wall.

The only exemption is the *Stoneley* wave which is also sensitive to the horizontal SH-wave velocity. Nevertheless, this information is not useful for an inversion method since the effect of the logging tool cannot be fast modeled.

In conclusion, it would be necessary to invert the full phase slowness dispersion curves of the *Stoneley*, flexural, quadrupole waves for the reliable determination of TI elastic moduli. The problem is that this also requires a fast modeling tool to model the dispersion curves of the borehole waves in a fluid-filled borehole surrounded by a TTI formation and in the presence of an LWD tool. While the FD method presented in this thesis is too slow for such an inversion method, an analytical solution would be the best method for fast forward modeling.

5.4. Challenges in real measurements

5.4.1. Signal-to-noise ratio (SNR)

While the above-presented inversion methods for the VTI, HTI, and TTI symmetries are only theoretically verified, some problems will exist in real measurements. One problem is that the signal-to-noise ratio (SNR) is lower in LWD measurements because of the intense noise induced by the drill bit, especially at low frequencies. This problem is solved in isotropic formations by firing the multipole source several times and stacking the results of all firings to increase the SNR significantly. In contrast, this does not work in azimuthally anisotropic formations since the tool rotates between the subsequent firings, and the azimuthal information would get lost. For instance, the integration of the generalized formula for the *Alford* rotation (Eq. 4.17) over all azimuths yields

$$\bar{p}_{XX} = 2n \int_{\theta^{\mathrm{F}}=0}^{2\pi} \left(\check{C}_n^{\mathrm{F}} \cos^2(n\theta^{\mathrm{F}}) + \check{C}_n^{\mathrm{S}} \sin^2(n\theta^{\mathrm{F}}) \right) \mathrm{d}\theta^{\mathrm{F}} = 2\pi n \left(\check{C}_n^{\mathrm{F}} + \check{C}_n^{\mathrm{S}} \right), \tag{5.23a}$$

$$\bar{p}_{YX} = \bar{p}_{XY} = 2n \int_{\theta^{\mathrm{F}}=0}^{2\pi} \left(\check{C}_n^{\mathrm{F}} - \check{C}_n^{\mathrm{S}} \right) \sin(n\theta^{\mathrm{F}}) \cos(n\theta^{\mathrm{F}}) \mathrm{d}\theta^{\mathrm{F}} = 0, \tag{5.23b}$$

$$\bar{p}_{YY} = 2n \int_{\theta^{\mathrm{F}}=0}^{2\pi} \left(\check{C}_n^{\mathrm{S}} \cos^2(n\theta^{\mathrm{F}}) + \check{C}_n^{\mathrm{F}} \sin^2(n\theta^{\mathrm{F}}) \right) \mathrm{d}\theta^{\mathrm{F}} = 2\pi n \left(\check{C}_n^{\mathrm{F}} + \check{C}_n^{\mathrm{S}} \right). \tag{5.23c}$$

Consequently, if the waveforms excited by multipole sources are stacked over all source azimuths, the in-line components of the four-component data matrix contain the sum of the fast and slow principal waves, whereas the off-diagonal components vanish. Unfortunately, it is impossible to separate the fast and slow principal cylindrical waves from their sum without further information. A solution for the low SNR ratio problem could be future LWD tools, which can precisely determine the source azimuth relative to a reference frame and fire the source at the same azimuths several times. However, the disadvantage of this solution is that the vertical resolution decreases since the tool moves downwards during the repeated firings.

5.4.2. Tool eccentricity

Another main challenge in LWD measurements is that the logging tool is usually not perfectly centered in the fluid-filled borehole. While WL tools are almost perfectly centered in the borehole using centralizers, they cannot be used for LWD tools because of the fast tool rotation. In the latter case, stabilizers are used instead of centralizers, which allow a higher eccentricity. Wang and Tang (2003) as well as section 4.4 have shown that such a tool eccentricity induces mode contaminants in isotropic formations. Furthermore, Zheng et al. (2004) and Pardo et al. (2013) found that the flexural and quadrupole waves split into two waves with different phase slowness dispersion curves, such as in anisotropic environments. However, they showed that the difference of the dispersion curves is marginal and not significant. Within the scope of this thesis, several numerical experiments were performed which show that the phase slowness dispersion curves of the principal flexural and quadrupole waves are also only minor affected by the tool eccentricity in anisotropic environments. On the other hand, Zheng et al. (2004) and Pardo et al. (2013) outlined that the tool eccentricity strongly affects the velocity of the *Stoneley* wave at low frequencies in isotropic formations. Further investigation shows that this is not only true in isotropic formations but also in anisotropic media. Therefore, tool eccentricity must be carefully treated when using the tube wave velocity to invert elastic moduli, e.g., as described in section 5.1.

While the phase slowness dispersion curves of the cylindrical waves ($n > 0$) are only slightly sensitive to tool eccentricity, the *Alford* rotation assumes a perfect symmetry and might not apply to cylindrical waves excited by off-centered cross-multipole sources. Numerical experiments have shown that the generalized formula can be only applied without any errors to the cylindrical waves measured by an off-centered tool which center is shifted from the borehole center parallel to the formation's fast or slow principal direction. However, in the case of an arbitrary tool eccentricity, i.e., the tool center is offset from the borehole center in an arbitrary direction relative to the formation's principal directions, the *Alford* rotation cannot be applied exactly. Consequently, this leads to errors in the inversion methods for the determination of the azimuth θ^{F}. For instance, figure 5.5a displays the error function computed from the flexural waves excited by two non-orthogonal dipole sources of an off-centered LWD tool. The azimuth between the excitation direction of the X-dipole source and the formation's fast principal direction is $\theta^{\mathrm{F}} = 30°$, and the azimuth between both dipole excitations is $\Delta\theta = 25°$, which is indicated by the white dots. In comparison, the white crosses in the figure represent the minima of the error function which strongly deviate from the true values. Hence, the tool eccentricity causes considerable errors in the determination of both azimuths θ^{F} and $\Delta\theta$, as illustrated by the gray lines. Consequently, LWD dipole logging is not appropriate to obtain the azimuths of the fast and slow principal directions characterizing an HTI formation if the LWD tool is off-centered.

On the other hand, figure 5.5b illustrates that the tool eccentricity-induced error in the obtained azimuth θ^{F} is much lower when using non-orthogonal LWD quadrupole firings. While

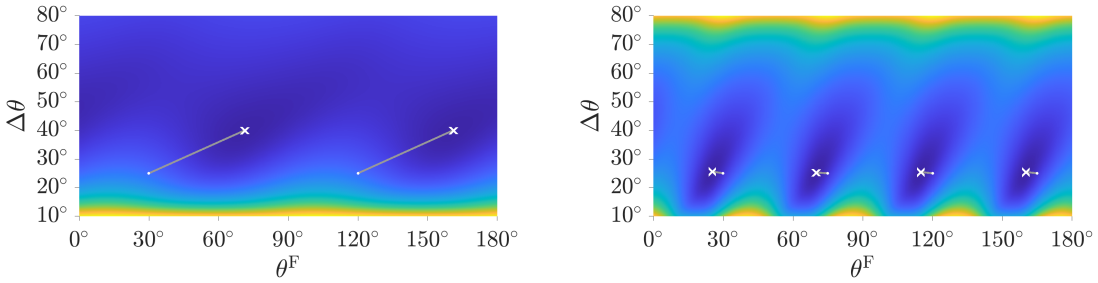

(a) Non-orthogonal off-centered dipole excitation **(b)** Non-orthogonal off-centered quadrupole excitation

Fig. 5.5: Examples of the error function computed via equation 5.12 in relation to the angles θ^{F} and $\Delta\theta$. For the examples, non-orthogonal cross-dipole (a) and cross-quadrupole (b) excitations are considered, respectively, having the azimuths $\theta^{\mathrm{F}} = 30°$ and $\Delta\theta = 55°$. Both sources are off-center from the borehole center by 6.5 mm. Since the difference between the borehole radius and the outer tool radius is 15 mm, the tool eccentricity comes to about 43 %. The minima of the error function are indicated by the white crosses, whereas the white dots correspond to the actual input values for θ^{F} and $\Delta\theta$. The gray lines indicate the error induced by the tool eccentricity.

the angle between the X- and Y*-excitation directions is determined correctly despite the tool eccentricity, the error in the obtained azimuth θ^{F} is only 4.8°. Since the identical amount of tool eccentricity is used for both examples ($d = 6.5\,\mathrm{mm}$), it can be concluded that the determination of the azimuth from LWD cross-quadrupole logging is much less sensitive to tool eccentricity than an inversion method utilizing LWD cross-dipole measurements.

Nevertheless, tool eccentricity-induced mode contaminants cause problems if the amplitudes of the anisotropy-induced *Stoneley* waves excited by quadrupole sources are used to obtain the azimuth θ^{F} (Sec. 5.2.3). Figure 5.6 illustrates the interference of the anisotropy- and eccentricity-induced *Stoneley* waves excited by an off-centered LWD quadrupole source in HTI media. The tool center is shifted from the borehole center by $d = 6.5\,\mathrm{mm}$ along a direction 45° rotated to the formation's principal directions. It is shown that the $\cos(2\theta^{\mathrm{F}})$ dependency of the anisotropy-induced *Stoneley* wave's amplitude (Fig. 4.43) is disturbed due to the tool eccentricity. Considering the slow Austin Chalk formation (Fig. 5.6a), the

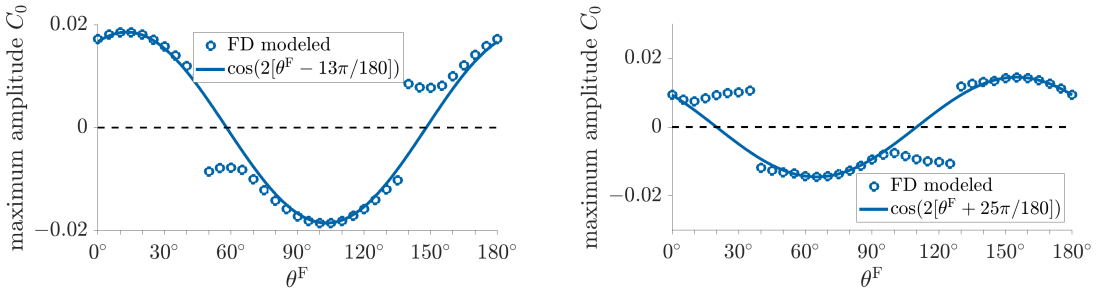

(a) Austin Chalk **(b)** Bakken Shale

Fig. 5.6: Maximum amplitude of the anisotropy-(HTI-)induced *Stoneley* wave (C_0) excited by a generally off-centered LWD quadrupole source in a fluid-filled borehole surrounded by the slow Austin Chalk (a) and fast Bakken Shale (b) HTI formations. The maximum amplitudes are displayed by the blue circles in relation to the azimuth θ^{F} between the quadrupole excitation direction and the formation's fast principle direction. Negative amplitude values mean opposite polarity of the *Stoneley* wave. The solid lines illustrate the $\cos(2\theta^{\mathrm{F}})$–dependency that is phase-shifted due to the tool eccentricity.

amplitude values follow, at the most azimuths, a $\cos(2\theta^{\mathrm{F}})$–function phase-shifted by 13°. However, for azimuths between $50° \leq \theta^{\mathrm{F}} \leq 70°$ (or $140° \leq \theta^{\mathrm{F}} \leq 160°$) the amplitude values deviate from this dependency. Similar behavior is observed for the fast Bakken Shale formation in figure 5.6b. The cosine dependency is shifted by about 25°, and the amplitude values not following this function are located at azimuths between $10° \leq \theta^{\mathrm{F}} \leq 35°$ and $100° \leq \theta^{\mathrm{F}} \leq 125°$. Thus, it is difficult to find the cosine dependency from measurements at only a few azimuths, and even if this dependency is found, the maximum and zero values of *Stoneley* wave amplitude do not correspond to the formation's principal directions because of the phase shift. Thus, when applying the inversion method based on the *Stoneley* wave amplitudes excited by a quadrupole source of an off-centered LWD tool, the phase shift of the cosine function will be the error in determining the azimuth θ^{F}, which is significant especially in fast formations. An extraordinary case occurs if the tool eccentricity is aligned with the principal directions of the HTI formation. This means that the tool center is shifted from the borehole center in a direction parallel to the formation's fast or slow principal direction. Then, the tool eccentricity-induced *Stoneley* wave amplitudes follow a $\cos(2\theta^{\mathrm{F}})$–function that has the same phase as the $\cos(2\theta^{\mathrm{F}})$–dependency of the anisotropy-induced *Stoneley* wave. Hence, the interference results only in a change of the amplitude but not in the phase, and the inversion method presented in section 5.2.3 works perfectly. However, since there is only little control of the direction of tool eccentricity, this cannot be exploited in real measurements.

6. Conclusions

The main objective of this thesis is the investigation of the feasibility on the determination of elastic TI parameters from LWD acoustic measurements. For this reason, borehole-guided and refracted waves are systematically investigated in anisotropic environments, and the effect of the LWD tool is treated additionally. The investigation is based on synthetic waveforms that are modeled for various anisotropic parameters and symmetries. For the VTI configuration, an analytical solution of the *Christoffel* equation can be derived in cylindrical coordinates. It was also tried to find an analytical solution for triclinic anisotropic media, which was not successful since the governing partial differential equation could not be solved in cylindrical coordinates. Alternatively, a new ansatz was developed, but there was no time to implement and test the underlying ideas in the scope of this thesis. Consequently, FD modeling was used to model the wavefield if the anisotropic formation exhibits HTI or TTI symmetry. Dependent on the type of anisotropy, different spatial FD grids must be utilized. The commonly used standard staggered grid (SSG) works correctly only for anisotropic media with at least orthotropic symmetry, including the HTI case. In contrast, if the anisotropic formation exhibits monoclinic or triclinic symmetry, which is the case if the TI symmetry axis is inclined to the borehole axis, the *Lebedev* grid consisting of four SSGs must be applied.

The investigation of the FD modeled waveforms results in a detailed overview of the behavior of the *Stoneley*, flexural, and quadrupole waves in TI formations. While the *Stoneley* and flexural waves have already been well-understood, the quadrupole wave was only little investigated in anisotropic environments. One of the major discoveries of the investigation is that not only the flexural waves split into two principal waves in HTI and TTI formations, but analogously all higher-order cylindrical waves. The mathematical derivation of this multipole cylindrical wave splitting has been successfully verified by FD modeling of quadrupole and hexapole waves. Based on the multipole cylindrical wave splitting theorem, the well-known *Alford* rotation (Alford, 1986) originally developed for flexural waves has been generalized to apply for all cylindrical waves ($m > 0$). Besides, the formula for the *Alford* rotation was extended to apply for non-orthogonal firings.

Based on the inverse formula for the generalized *Alford* rotation, a simple inversion method is proposed utilizing non-orthogonal cross-quadrupole measurements. The inversion method is compared to a similar inversion method utilizing non-orthogonal cross-dipole measurements developed by Wang et al. (2016). In both cases, the inverse formula for the *Alford* rotation is used to obtain the azimuths of the formation's principal directions and the principal borehole waves. The quadrupole inversion method has the disadvantage that the azimuths for

the formation's principal directions cannot be determined uniquely because of an angle ambiguity that cannot be resolved without further information. In contrast, this type of angle ambiguity does not exist for the dipole inversion method, which yields one azimuth corresponding to the fast principal direction and one azimuth corresponding to the slow principal direction. Consequently, the inversion method using LWD cross-dipole excitations seems to be the better option for determining the azimuths between the excitation direction and the formation's principal directions, even in slow formations where only the tool flexural wave might be present. This is because the tool flexural wave is also sensitive to the formation's anisotropy parameters at intermediate and high frequencies ($> 2\,\mathrm{kHz}$).

The proposed LWD cross-quadrupole inversion method requires eight azimuthal receivers causing a technical problem since modern LWD tools have a receiver array with only four azimuthal receivers. For that reason, a second inversion method is developed exploiting anisotropy-induced mode contaminants. Besides the investigation of phase slowness dispersion curves of various borehole waves, this thesis has also extensively investigated the mode contaminants induced by the formation anisotropy. While these anisotropy-induced mode contaminants were predominately studied using FD modeling, the results can be perfectly described by the governing differential equations (*Christoffel* equation) in cylindrical coordinates after applying an azimuthal *Fourier* transform. The most useful discovery is that a quadrupole source excites a *Stoneley* wave in HTI and TTI media, which amplitude depends on the azimuth between the quadrupole excitation direction and the formation's principal directions. In this way, the anisotropy-induced *Stoneley* wave amplitudes provide information about the azimuths of the principal directions. Based on this, an alternative inversion method has been developed to obtain the azimuths and the principal quadrupole waves. The advantage of this method is that it requires only four azimuthal receivers, which are already installed in modern LWD tools. Nevertheless, the problem of the angle ambiguity remains and cannot be solved.

Furthermore, solution strategies and limitations in determining both true principal phase slowness values from the dispersion curves of the obtained principal quadrupole waves are discussed. This work illustrates that the principal slowness values cannot be read directly from the low-frequency limits of the quadrupole phase slowness dispersion curves. Alternatively, Wang et al. (2016) proposed a model-based inversion method to obtain the phase slowness values from the flexural wave dispersion curves. While they approximate the dispersion curves measured in anisotropic media by an isotropic model, this introduces errors for the quadrupole inversion method since the dispersion curves of the principal quadrupole waves deviate significantly from their isotropic counterparts. Thus, it would be advantageous to invert the dispersion curves by using an anisotropic model. The problem is that such an inversion method requires a fast modeling tool, e.g., an analytical solution, to forward model the dispersion curves for different anisotropic parameters. Because such an analytical solution does not exist for the HTI or TTI configuration, it is difficult to reliably determine TI formations anisotropy parameters from LWD cross-quadrupole acoustic measurements. Be-

sides, it is presented that the quadrupole wave splitting can be primarily observed in slow TI formations, whereas the difference between the fast and slow principal quadrupole waves is marginal in fast TI formations. Moreover, the flexural and quadrupole waves are highly sensitive to the borehole fluid slowness in fast formations. Since this slowness value is input in the model-based inversion methods, it must be known precisely to prevent introducing significant errors in the inversion methods.

Moreover, even if the azimuths of the principal directions and the principal phase slowness values are correctly determined, it is impossible to invert elastic moduli in the crystallographic reference frame for the TTI case without knowing the inclination between the TI symmetry axis and the borehole axis precisely. While this inclination angle can be determined, e.g., by ultrasonic measurements, the inversion methods for the elastic moduli are highly sensitive to errors and not practicable in real measurements. Hence, it is proposed to use the full phase slowness dispersion curves of several borehole waves instead of single principal slowness values to reliably obtain the elastic moduli of the TI formation. The problem is that such an inversion method also requires a fast modeling tool (analytical solution) for modeling the dispersion curves for different input parameters.

Bazulin et al. (2020) have shown that neural networks might be an alternative to conventional inversion methods. Their advantage is that an analytical solution is not required since the neural network simulates the involved physics. The latter can be trained with synthetic waveform array data obtained, for instance, by FD modeling for known elastic moduli. Another advantage of neural networks is that both the kinematics and the amplitudes of the wavefield are processed in the inversion. Since the application of neural networks in borehole acoustics is a relatively new topic, the future will show all advantages and limitations of such inversion methods.

Despite all problems and limitations, cross-quadrupole measurements are useful in anisotropic formations to validate cross-dipole logging results in real measurements. For instance, one problem discussed in this work is tool eccentricity, which can lead to great errors in determining the azimuths of the formation's principal directions from cross-dipole measurements. In contrast, the cross-quadrupole inversion methods are less sensitive to tool eccentricity. Nevertheless, a combination of acoustic LWD measurements with ultrasonic measurements would be good practice in the future. The ultrasonic measurements may be used not only to image the borehole wall but additionally to position the tool relative to the borehole. In the best case, the LWD tool is positioned in the center, but if this is technically not possible, the tool can be placed at different positions to quality control the anisotropic parameters obtained from LWD dipole or quadrupole measurements. Besides, quadrupole shear wave splitting and anisotropy-induced mode coupling provide indicators to detect formation anisotropy.

In a future step, the theoretical results presented in this thesis can be tested in real measurements. Ideally, LWD cross-quadrupole measurements are performed in a fluid-filled borehole

surrounded by a slow HTI formation, which anisotropic parameters are known. The LWD tool must contain eight azimuthal receivers instead of four to investigate if the quadrupole wave splitting can be observed in reality. On the other hand, the amplitude dependency of the anisotropy-induced *Stoneley* wave excited by quadrupole sources can be validated with current LWD tools possessing four azimuthal receivers. For the tests, the logging tool must be exactly centered, the borehole must be perfectly circular, and the four constituting sources must be amplitude and phase-matched to exclude other mode contaminants that interfere with the anisotropy-induced ones.

Besides, further work is required to obtain an analytical solution to quickly model the borehole waves and their phase slowness dispersion curves in general anisotropic media exhibiting the lowest triclinic symmetry. One solution strategy is trying to solve the *Christoffel* equation given in cylindrical coordinates by transforming the spatial radial coordinate by an appropriate integral transform to obtain an algebraic equation. The *Meijer* transform (Meijer, 1941) might be such an integral transform. However, the resulting equations depend on different azimuthal wavenumbers causing additional problems to find a solution. Hence, a more promising solution strategy is to transform the plane wave solutions of the *Christoffel* equation given in Cartesian coordinates into cylindrical coordinates. This investigation is in an early stage but has shown that, also in the triclinic anisotropic case, it is possible to expand the Cartesian propagation factor ($\exp(s\beta_q x_q)$, Eq. 2.41) as an infinite summation of (generalized) modified *Bessel* functions. In this way, the plane wave solution can be transformed to cylindrical coordinates, and the boundary conditions can be applied to obtain an analytical solution for the borehole acoustic problem. Further research will show if this solution strategy is successful. An analytical solution would be essential to develop inversion methods that are more robust and may provide a fast tool to model waveforms for given parameters to train neural networks.

References

Aeron, S., Bose, S., Valero, H.-P., and Saligrama, V. (2011). "Broadband dispersion extraction using simultaneous sparse penalization". In: *IEEE Transactions on Signal Processing* 59.10, pp. 4821–4837. DOI: 10.1109/TSP.2011.2160632.

Alford, R. M. (1986). "Shear data in the presence of azimuthal anisotropy: Dilley, Texas". In: *SEG Technical Program Expanded Abstracts 1986*, pp. 476–479. DOI: 10.1190/1.1893036.

Auld, B. A. (1973). *Acoustic fields and waves in solids*. John Wiley and Sons. ISBN: 0-471-03702-8.

Backus, G. E. (1962). "Long-wave elastic anisotropy produced by horizontal layering". In: *Journal of Geophysical Research* 67.11, pp. 4427–4440. DOI: 10.1029/JZ067i011p04427.

Bansal, R. and Sen, M. K. (2008). "Finite-difference modelling of S-wave splitting in anisotropic media". In: *Geophysical Prospecting* 56.3, pp. 293–312. DOI: 10.1111/j.1365-2478.2007.00693.x.

Bateman Manuscript Project (1954). *Tables of integral transforms: based in part on notes left by Harry Bateman and compiled by the staff of the Bateman manuscript project*. McGraw-Hill.

Bazulin, M., Sabitov, D., and Charara, M. (2020). "VTI parameters determination from synthetic sonic logging data using a convolutional neural network". In: *SEG Technical Program Expanded Abstracts 2020*. Society of Exploration Geophysicists, pp. 445–449. DOI: 10.1190/segam2020-3427984.1.

Berenger, J.-P. (1994). "A perfectly matched layer for the absorption of electromagnetic waves". In: *Journal of Computational Physics* 114.2, pp. 185–200. DOI: 10.1006/jcph.1994.1159.

Bernth, H. and Chapman, C. (2011). "A comparison of the dispersion relations for anisotropic elastodynamic finite-difference grids". In: *Geophysics* 76.3, WA43–WA50. DOI: 10.1190/1.3555530.

Biot, M. A. (1952). "Propagation of elastic waves in a cylindrical bore containing a fluid". In: *Journal of Applied Physics* 23.9, pp. 997–1005. DOI: 10.1063/1.1702365.

Blyth, M., Sakiyama, N., Iritani, R., Yamamoto, H., and Valero, H.-P. (2016). "Understanding LWD quadrupole shear in anisotropic environments". In: *22nd Formation Evaluation Symposium of Japan (JFES16)*. SPWLA.

Bohlen, T. (2002). "Parallel 3-D viscoelastic finite difference seismic modelling". In: *Computers & Geosciences* 28.8, pp. 887–899. DOI: 10.1016/S0098-3004(02)00006-7.

Bohlen, T. and Saenger, E. H. (2006). "Accuracy of heterogeneous staggered-grid finite-difference modeling of Rayleigh waves". In: *Geophysics* 71.4, T109–T115. DOI: 10.1190/1.2213051.

Braunisch, H., Habashy, T. M., Sinha, B. K., Pabon, J., and Kong, J. A. (2004). "Inversion of guided-wave dispersion data with application to borehole acoustics". In: *The Journal of the Acoustical Society of America* 115.1, pp. 269–279. DOI: 10.1121/1.1625683.

Brodov, L. Y., Kuznetsov, V. M., Slater, C., and Crampin, S. (1993). "Observations of anisotropic cusps in a clay reservoir". In: *55th EAEG Meeting*. DOI: 10.3997/2214-4609.201411454.

Byun, J. and Toksöz, M. N. (2003). "Numerical modeling of effects of tool eccentricity on multi-component monopole and dipole logging". In: *SEG Technical Program Expanded Abstracts 2003*. Society of Exploration Geophysicists, pp. 289–292. DOI: 10.1190/1.1817900.

Chan, A. K. and Tsang, L. (1983). "Propagation of acoustic waves in a fluid-filled borehole surrounded by a concentrically layered transversely isotropic formation". In: *The Journal of the Acoustical Society of America* 74.5, pp. 1605–1616. DOI: 10.1121/1.390122.

Cheng, C. H. and Toksöz, M. N. (1981). "Elastic wave propagation in a fluid-filled borehole and synthetic acoustic logs". In: *Geophysics* 46.7, pp. 1042–1053. DOI: 10.1190/1.1441242.

Cheng, N., Cheng, C. H., and Toksöz, M. N. (1995). "Borehole wave propagation in three dimensions". In: *The Journal of the Acoustical Society of America* 97.6, pp. 3483–3493. DOI: 10.1121/1.412996.

Chew, W. C. and Liu, Q. H. (1996). "Perfectly matched layers for elastodynamics: a new absorbing boundary condition". In: *Journal of Computational Acoustics* 4.4, pp. 341–359. DOI: 10.1142/S0218396X96000118.

Chi, S. and Tang, X. (2006). "Stoneley-wave speed modeling in general anisotropic formations". In: *Geophysics* 71.4, F67–F77. DOI: 10.1190/1.2216928.

Crampin, S. (1985). "Evaluation of anisotropy by shear-wave splitting". In: *Geophysics* 50.1, pp. 142–152. DOI: 10.1190/1.1441824.

Daley, P. F. and Hron, F. (1977). "Reflection and transmission coefficients for transversely isotropic media". In: *Bulletin of the Seismological Society of America* 67.3, pp. 661–675.

Demmler, C., Geerits, T., Hellwig, O., and Buske, S. (2020). "Logging-while-drilling cross-multipole measurements in anisotropic media". In: *SEG Technical Program Expanded Abstracts 2020*. Society of Exploration Geophysicists, pp. 400–404. DOI: 10.1190/segam2020-3426574.1.

Ekstrom, M. P. (1996). "Dispersion estimation from borehole acoustic arrays using a modified matrix pencil algorithm". In: *Conference Record of the Twenty-Ninth Asilomar Conference*

on Signals, Systems and Computers. Vol. 1. IEEE, pp. 449–453. DOI: 10.1109/ACSSC.1995.540589.

Ellefsen, K. J. (1990). "Elastic wave propagation along a borehole in an anisotropic medium." PhD thesis. Department of Earth and Planetary Sciences.

Ellefsen, K. J., Cheng, C. H., and Toksöz, M. N. (1990). "Elastic wave propagation along a borehole in an anisotropic medium". In: *SEG Technical Program Expanded Abstracts 1990*. Society of Exploration Geophysicists, pp. 14–17. DOI: 10.1190/1.1890038.

– (1991). "Effects of anisotropy upon the normal modes in a borehole". In: *The Journal of the Acoustical Society of America* 89.6, pp. 2597–2616. DOI: 10.1121/1.400699.

Esmersoy, C., Koster, K., Williams, M., Boyd, A., and Kane, M. (1994). "Dipole shear anisotropy logging". In: *SEG Technical Program Expanded Abstracts 1994*. Society of Exploration Geophysicists, pp. 1139–1142. DOI: 10.1190/1.1822720.

Fang, X., Fehler, M. C., and Cheng, A. (2014). "Simulation of the effect of stress-induced anisotropy on borehole compressional wave propagation". In: *Geophysics* 79.4, pp. D205–D216. DOI: 10.1190/geo2013-0186.1.

Geerits, T. W. and Kranz, B. (2017). "Impedance loading and radiation of finite aperture multipole sources in fluid filled boreholes". In: *Journal of Sound and Vibration* 393, pp. 114–132. DOI: 10.1016/j.jsv.2016.12.046.

Geerits, T. W. and Tang, X. (2003). "Centroid phase slowness as a tool for dispersion correction of dipole acoustic logging data". In: *Geophysics* 68.1, pp. 101–107. DOI: 10.1190/1.1543197.

Geerits, T. W., Tang, X., Hellwig, O., and Bohlen, T. (2010). "Multipole borehole acoustic theory: Source imbalances and the effects of an elastic logging tool". In: *Journal of Applied Geophysics* 70.2, pp. 113–143. DOI: 10.1016/j.jappgeo.2009.10.004.

Geerits, T., Colista, T., and Jensen, N. (2018). "Water tank measurements on an experimental LWD multipole acoustic tool". In: *SEG Technical Program Expanded Abstracts 2018*. Society of Exploration Geophysicists, pp. 729–733. DOI: 10.1190/segam2018-2995849.1.

Gradshteyn, I. S. and Ryzhik, I. M. (2007). *Table of integrals, series, and products*. 7th ed. Academic press. ISBN: 978-0-12-373637-6.

Hastings, F. D., Schneider, J. B., and Broschat, S. L. (1996). "Application of the perfectly matched layer (PML) absorbing boundary condition to elastic wave propagation". In: *The Journal of the Acoustical Society of America* 100.5, pp. 3061–3069. DOI: 10.1121/1.417118.

Hellwig, O. (2017). "Seismic exploration ahead of boreholes using borehole-guided waves - a feasibility study". PhD thesis. TU Bergakademie Freiberg.

van der Hijden, J. H. M. T. (1987). "Radiation from an impulsive line source in an unbounded homogeneous anisotropic medium". In: *Geophysical Journal International* 91.2, pp. 355–372. DOI: 10.1111/j.1365-246X.1987.tb05232.x.

de Hoop, A. T. (1995). *Handbook of radiation and scattering of waves: Acoustic waves in fluids, elastic waves in solids, electromagnetic waves*. Academic Press. ISBN: 0-12-208655-4.

Hornby, B. E., Howie, J. M., and Ince, D. W. (2003). "Anisotropy correction for deviated-well sonic logs: Application to seismic well tie". In: *Geophysics* 68.2, pp. 464–471. DOI: 10.1190/1.1567212.

Horne, S., Walsh, J., and Miller, D. (2012). "Elastic anisotropy in the Haynesville Shale from dipole sonic data". In: *First Break* 30.2. DOI: 10.3997/1365-2397.2011039.

Hsu, C.-J. and Sinha, B. K. (1998). "Mandrel effects on the dipole flexural mode in a borehole". In: *The Journal of the Acoustical Society of America* 104.4, pp. 2025–2039. DOI: 10.1121/1.423767.

Hua, Y. and Sarkar, T. K. (1990). "Matrix pencil method for estimating parameters of exponentially damped/undamped sinusoids in noise". In: *IEEE Transactions on Acoustics, Speech, and Signal Processing* 38.5, pp. 814–824. DOI: 10.1109/29.56027.

Igel, H., Mora, P., and Riollet, B. (1995). "Anisotropic wave propagation through finite-difference grids". In: *Geophysics* 60.4, pp. 1203–1216. DOI: 10.1190/1.1443849.

Kimball, C. V. (1998). "Shear slowness measurement by dispersive processing of the borehole flexural mode". In: *Geophysics* 63.2, pp. 337–344. DOI: 10.1190/1.1444333.

Kimball, C. V. and Marzetta, T. L. (1984). "Semblance processing of borehole acoustic array data". In: *Geophysics* 49.3, pp. 274–281. DOI: 10.1190/1.1441659.

Köhn, D., Hellwig, O., De Nil, D., and Rabbel, W. (2015). "Waveform inversion in triclinic anisotropic media—a resolution study". In: *Geophysical Journal International* 201.3, pp. 1642–1656. DOI: 10.1093/gji/ggv097.

Korn, G. A. and Korn, T. M. (1968). *Mathematical handbook for scientists and engineers: definitions, theorems, and formulas for reference and review*. McGraw-Hill. ISBN: 978-0-486-41147-7.

Kurkjian, A. L. and Chang, S.-K. (1986). "Acoustic multipole sources in fluid-filled boreholes". In: *Geophysics* 51.1, pp. 148–163. DOI: 10.1190/1.1442028.

Lax, P. D. and Richtmyer, R. D. (1956). "Survey of the stability of linear finite difference equations". In: *Communications on Pure and Applied Mathematics* 9.2, pp. 267–293.

Lebedev, V. I. (1964). "Difference analogues of orthogonal decompositions, basic differential operators and some boundary problems of mathematical physics. I". In: *USSR Computational Mathematics and Mathematical Physics* 4.3, pp. 69–92. DOI: 10.1016/0041-5553(64)90240-X.

Leslie, H. D. and Randall, C. J. (1990). "Eccentric dipole sources in fluid-filled boreholes: Numerical and experimental results". In: *The Journal of the Acoustical Society of America* 87.6, pp. 2405–2421. DOI: 10.1121/1.399086.

– (1992). “Multipole sources in boreholes penetrating anisotropic formations: Numerical and experimental results”. In: *The Journal of the Acoustical Society of America* 91.1, pp. 12–27. DOI: 10.1121/1.402761.

Lisitsa, V. (2007). “Lebedev schemes for elastic anisotropic problems”. In: *69th EAGE Conference and Exhibition incorporating SPE EUROPEC 2007*. European Association of Geoscientists & Engineers. DOI: 10.3997/2214-4609.201401952.

Lisitsa, V. and Vishnevskiy, D. (2010). “Lebedev scheme for the numerical simulation of wave propagation in 3D anisotropic elasticity”. In: *Geophysical Prospecting* 58.4, pp. 619–635. DOI: 10.1111/j.1365-2478.2009.00862.x.

Liu, Q.-H. and Sinha, B. K. (2000). “Multipole acoustic waveforms in fluid-filled boreholes in biaxially stressed formations: A finite-difference method”. In: *Geophysics* 65.1, pp. 190–201. DOI: 10.1190/1.1444710.

– (2003). “A 3D cylindrical PML/FDTD method for elastic waves in fluid-filled pressurized boreholes in triaxially stressed formations”. In: *Geophysics* 68.5, pp. 1731–1743. DOI: 10.1190/1.1620646.

Market, J. and Bilby, C. (2012). “Introducing the first LWD crossed-dipole sonic imaging service”. In: *Petrophysics* 53.3, pp. 208–221.

McFadden, P. L., Drummond, B. J., and Kravis, S. (1986). “The Nth-root stack: Theory, applications, and examples”. In: *Geophysics* 51.10, pp. 1879–1892. DOI: 10.1190/1.1442045.

Meijer, C. S. (1941). “Eine neue Erweiterung der Laplace Transformation I”. In: vol. 44, pp. 727–737.

Message Passing Interface Forum (2012). *MPI: A Message-Passing Interface Standard Version 3.0*. University of Tennessee.

Mickael, M., Barnett, C., and Diab, M. (2012a). “Azimuthally focused LWD sonic logging for shear wave anisotropy measurement and borehole imaging”. In: *SPE Annual Technical Conference and Exhibition*. Society of Petroleum Engineers. DOI: 10.2118/160133-MS.

– (2012b). “Shear Wave Anisotropy Measurement from Azimuthally Focused LWD Sonic Tool”. In: *SPE Canadian Unconventional Resources Conference*. Society of Petroleum Engineers. DOI: 10.2118/162175-MS.

Moczo, P., Kristek, J., and Halada, L. (2004). *The Finite-Difference Method for Seismologists, An Introduction*. manual. Comenius University Bratislava.

Moczo, P., Kristek, J., Vavryčuk, V., Archuleta, R. J., and Halada, L. (2002). “3D heterogeneous staggered-grid finite-difference modeling of seismic motion with volume harmonic and arithmetic averaging of elastic moduli and densities”. In: *Bulletin of the Seismological Society of America* 92.8, pp. 3042–3066. DOI: 10.1785/0120010167.

Moczo, P., Robertsson, J. O. A., and Eisner, L. (2007). "The finite-difference time-domain method for modeling of seismic wave propagation". In: *Advances in Geophysics* 48, pp. 421–516. DOI: 10.1016/S0065-2687(06)48008-0.

Mueller, M. C., Boyd, A. J., and Esmersoy, C. (1994). "Case studies of the dipole shear anisotropy log". In: *SEG Technical Program Expanded Abstracts 1994*. Society of Exploration Geophysicists, pp. 1143–1146. DOI: 10.1190/1.1822721.

Muller, D. E. (1956). "A method for solving algebraic equations using an automatic computer". In: *Mathematical Tables and Other Aids to Computation* 10.56, pp. 208–215.

Musgrave, M. J. P. (1970). *Crystal acoustics: Introduction to the Study of Elastic Waves and Vibrations in Crystals*. Acoustical Society of America. ISBN: 978-08162-6202-1.

Nayfeh, A. H. (1995). *Wave propagation in layered anisotropic media: With application to composites*. Elsevier. ISBN: 0-444-54214-0.

Nestyagin, A., Al Arfi, S., Mostafa, H., Elkholy, M., Fekry, M., Awad, H., and Mohamed, O. (2017). "Running LWD Azimuthal Sonic and Azimuthal Density in Tandem Confirms the Azimuthal Sonic Technology for Real Time Dip Picking and Geosteering Application. Middle East Case Study". In: *SPE Kingdom of Saudi Arabia Annual Technical Symposium and Exhibition*. Society of Petroleum Engineers. DOI: 10.2118/188024-MS.

Nicoletis, L. M. A., Bamberger, A., Quiblier, J. A., Joly, P., and Kern, M. (1990). "Hole geometry and anisotropic effects on tube-wave propagation: A quasi-static study". In: *Geophysics* 55.2, pp. 167–175. DOI: 10.1190/1.1442823.

Nolte, B., Rao, R., and Huang, X. (1997). *Dispersion analysis of split flexural waves*. Tech. rep. Massachusetts Institute of Technology. Earth Resources Laboratory.

Norris, A. N. (1990). "The speed of a tube wave". In: *The Journal of the Acoustical Society of America* 87.1, pp. 414–417. DOI: 10.1121/1.399262.

Norris, A. N. and Sinha, B. K. (1993). "Weak elastic anisotropy and the tube wave". In: *Geophysics* 58.8, pp. 1091–1098. DOI: 10.1190/1.1443493.

– (1996). "Anisotropy-induced coupling in borehole acoustic modes". In: *Journal of Geophysical Research: Solid Earth* 101.B7, pp. 15945–15952. DOI: 10.1029/96JB01303.

Nwosu, N., Alford, J., Kadir, H., and Byl, J. (2015). "Enhancing Shale Reservoir Completion Design Using Oriented Unipole Logging While Drilling Sonic Measurements in Horizontal Well". In: *SPWLA 56th Annual Logging Symposium*. Society of Petrophysicists and Well-Log Analysts.

Paillet, F. L. and White, J. E. (1982). "Acoustic modes of propagation in the borehole and their relationship to rock properties". In: *Geophysics* 47.8, pp. 1215–1228. DOI: 10.1190/1.1441384.

Pardo, D., Matuszyk, P. J., Torres-Verdin, C., Mora, A., Muga, I., and Calo, V. M. (2013). "Influence of borehole-eccentred tools on wireline and logging-while-drilling sonic logging

measurements". In: *Geophysical Prospecting* 61.s1, pp. 268–283. DOI: 10.1111/1365-2478.12022.

Peterson, E. W. (1974). "Acoustic wave propagation along a fluid-filled cylinder". In: *Journal of Applied Physics* 45.8, pp. 3340–3350. DOI: 10.1063/1.1663783.

Przebindowska, A. and Geerits, T. W. (2019). "Double alternate-polarity multipole measurements in borehole acoustics". In: *SEG Technical Program Expanded Abstracts 2019*. Society of Exploration Geophysicists, pp. 854–858. DOI: 10.1190/segam2019-3214945.1.

Randall, C. J. (1991). "Multipole acoustic waveforms in nonaxisymmetric boreholes and formations". In: *The Journal of the Acoustical Society of America* 90.3, pp. 1620–1631. DOI: 10.1121/1.401903.

Ricker, N. (1943). "Further developments in the wavelet theory of seismogram structure". In: *Bulletin of the Seismological Society of America* 33.3, pp. 197–228.

Roever, W. L., Rosenbaum, J. H., and Vining, T. F. (1974). "Acoustic waves from an impulsive source in a fluid-filled borehole". In: *The Journal of the Acoustical Society of America* 55.6, pp. 1144–1157. DOI: 10.1121/1.1914679.

Rosenbaum, J. H. (1974). "Synthetic microseismograms: Logging in porous formations". In: *Geophysics* 39.1, pp. 14–32. DOI: 10.1190/1.1440407.

Saenger, E. H. and Bohlen, T. (2004). "Finite-difference modeling of viscoelastic and anisotropic wave propagation using the rotated staggered grid". In: *Geophysics* 69.2, pp. 583–591. DOI: 10.1190/1.1707078.

Saenger, E. H., Gold, N., and Shapiro, S. A. (2000). "Modeling the propagation of elastic waves using a modified finite-difference grid". In: *Wave motion* 31.1, pp. 77–92. DOI: 10.1016/S0165-2125(99)00023-2.

Sakiyama, N., Syresin, D., Iritani, R., Yamamoto, H., and Nakajima, H. (2016). "LWD unipole for probing azimuthally heterogeneous formation properties: Characterization through numerical modeling and field data". In: *SEG Technical Program Expanded Abstracts 2016*. Society of Exploration Geophysicists, pp. 612–616. DOI: 10.1190/segam2016-13364233.1.

Schmitt, D. P. (1989). "Acoustic multipole logging in transversely isotropic poroelastic formations". In: *The Journal of the Acoustical Society of America* 86.6, pp. 2397–2421. DOI: 10.1121/1.398448.

Sinha, B. K. and Asvadurov, S (1998). "Higher-order modes in a fluid-filled borehole". In: *1998 IEEE Ultrasonics Symposium*. Vol. 2. IEEE, pp. 1115–1120. DOI: 10.1109/ULTSYM.1998.765032.

Sinha, B. K. and Asvadurov, S. (2004). "Dispersion and radial depth of investigation of borehole modes". In: *Geophysical Prospecting* 52.4, pp. 271–286. DOI: 10.1111/j.1365-2478.2004.00415.x.

Sinha, B. K. and Kostek, S. (1996). "Stress-induced azimuthal anisotropy in borehole flexural waves". In: *Geophysics* 61.6, pp. 1899–1907. DOI: 10.1190/1.1444105.

Sinha, B. K., Norris, A. N., and Chang, S.-K. (1994). "Borehole flexural modes in anisotropic formations". In: *Geophysics* 59.7, pp. 1037–1052. DOI: 10.1190/1.1443660.

Sinha, B. K., Şimşek, E., and Asvadurov, S. (2009). "Influence of a pipe tool on borehole modes". In: *Geophysics* 74.3, E111–E123. DOI: 10.1190/1.3085644.

Sinha, B. K., Şimşek, E., and Liu, Q.-H. (2006). "Elastic-wave propagation in deviated wells in anisotropic formations". In: *Geophysics* 71.6, pp. D191–D202. DOI: 10.1190/1.2358402.

Syresin, D., Sakiyama, N., Yamamoto, H., Iritani, R., and Nakajima, H. (2016). "Characterization of azimuthal slowness sensitivity for LWD unipole tools". In: *SPWLA 57th Annual Logging Symposium*. Society of Petrophysicists and Well-Log Analysts.

Tang, X. (2003). "Determining formation shear-wave transverse isotropy from borehole Stoneley-wave measurements". In: *Geophysics* 68.1, pp. 118–126. DOI: 10.1190/1.1543199.

Tang, X. and Cheng, A. (2004). *Quantitative borehole acoustic methods*. Vol. 24. Elsevier. ISBN: 0-08-044051-7.

Tang, X. and Chunduru, R. K. (1999). "Simultaneous inversion of formation shear-wave anisotropy parameters from cross-dipole acoustic-array waveform data". In: *Geophysics* 64.5, pp. 1502–1511. DOI: 10.1190/1.1444654.

Tang, X., Dubinsky, V., Wang, T., Bolshakov, A., and Patterson, D. (2003). "Shear-velocity measurement in the Logging-While-Drilling environment: Modeling and field evaluations". In: *Petrophysics* 44.2.

Thomsen, L. (1986). "Weak elastic anisotropy". In: *Geophysics* 51.10, pp. 1954–1966. DOI: 10.1190/1.1442051.

Tsang, L. and Rader, D. (1979). "Numerical evaluation of the transient acoustic waveform due to a point source in a fluid-filled borehole". In: *Geophysics* 44.10, pp. 1706–1720. DOI: 10.1190/1.1440932.

Tsvankin, I. (2012). *Seismic signatures and analysis of reflection data in anisotropic media*. 3rd ed. Society of Exploration Geophysicists. ISBN: 978-1-56080-299-0.

Virieux, J. (1984). "SH-wave propagation in heterogeneous media: Velocity-stress finite-difference method". In: *Geophysics* 49.11, pp. 1933–1942. DOI: 10.1190/1.1441605.

– (1986). "P-SV wave propagation in heterogeneous media: Velocity-stress finite-difference method". In: *Geophysics* 51.4, pp. 889–901. DOI: 10.1190/1.1442147.

Voigt, W. (1910). *Lehrbuch der kristallphysik:(mit ausschluss der kristalloptik)*. Vol. 34. BG Teubner.

Walsh, J., Sinha, B. K., and Donald, A. (2006). "Formation anisotropy parameters using borehole sonic data". In: *SPWLA 47th Annual Logging Symposium*. Society of Petrophysicists and Well-Log Analysts.

Wang, P. and Bose, S. (2013). "Broadband dispersion extraction of borehole acoustic modes via sparse Bayesian learning". In: *2013 5th IEEE International Workshop on Computational Advances in Multi-Sensor Adaptive Processing (CAMSAP)*. IEEE, pp. 268–271. DOI: 10.1109/CAMSAP.2013.6714059.

Wang, P., Bose, S., Sinha, B. K., and Blyth, M. (2016). "Dipole shear anisotropy using logging-while-drilling sonic tools". In: *SPWLA 57th Annual Logging Symposium*. Society of Petrophysicists and Well-Log Analysts.

Wang, P., Bose, S., Sinha, B. K., Lei, T., and Blyth, M. (2017). "Logging-while-drilling dipole shear logging in fast formations using higher-order formation flexural mode". In: *SPWLA 58th Annual Logging Symposium*. Society of Petrophysicists and Well-Log Analysts.

Wang, T., Dawber, M., and Boonen, P. (2011). "Theory of unipole acoustic logging tools and their relevance to dipole and quadrupole tools for slow formations". In: *SPE Annual Technical Conference and Exhibition*. Society of Petroleum Engineers. DOI: 10.2118/145515-MS.

Wang, T. and Tang, X. (2003). "Investigation of LWD quadrupole shear measurement in real environments". In: *SPWLA 44th Annual Logging Symposium*. Society of Petrophysicists and Well-Log Analysts.

White, J. E. and Tongtaow, C. (1981). "Cylindrical waves in transversely isotropic media". In: *The Journal of the Acoustical Society of America* 70.4, pp. 1147–1155. DOI: 10.1121/1.386946.

Zemanek, J., Angona, F. A., Williams, D. M., and Caldwell, R. L. (1984). "Continuous acoustic shear wave logging". In: *SPWLA 25th Annual Logging Symposium*. Society of Petrophysicists and Well-Log Analysts.

Zhang, B. and Wang, K. (1996). "Theoretical study of perturbation method for acoustic multipole logging in anisotropic formation". In: *The Journal of the Acoustical Society of America* 99.5, pp. 2674–2685. DOI: 10.1121/1.414855.

Zheng, Y., Huang, X., and Toksöz, M. N. (2004). "A finite element analysis of the effects of tool eccentricity on wave dispersion properties in borehole acoustic logging while drilling". In: *SEG Technical Program Expanded Abstracts 2004*. Society of Exploration Geophysicists, pp. 294–297. DOI: 10.1190/1.1839721.

Zheng, Y., Tang, X., and Patterson, D. J. (2009). "Identifying stress-induced anisotropy and stress direction using cross-dipole acoustic logging". In: *SPWLA 50th Annual Logging Symposium*. Society of Petrophysicists and Well-Log Analysts.

List of Abbreviations and Symbols

Abbreviations

AVO	amplitude-versus-offset
BCI	branch-cut integration
BHA	bottom-hole-assembly
FD	finite-difference
HTI	horizontal transverse isotropy
LWD	logging-while-drilling
MPI	message passing interface
RAI	real-axis integration
SNR	signal-to-noise ratio
SSG	standard staggered grid
STC	slowness time coherency
TI	transverse isotropy
TTI	tilted transverse isotropy
VTI	vertical transverse isotropy
WL	wireline

Symbols

$\mathcal{A}$	matrix
$A(s)$	amplitude spectrum
A_p	area of a surface source
a_0	uniform acceleration of a surface source
$a, a_1, a_2, a_3, \alpha, \alpha_1, \alpha_2, b$	coefficients
$\boldsymbol{\beta} = (\beta_1, \beta_2, \beta_3)^{\mathrm{T}}$ or $(\beta_r, \Theta, \beta_z)^{\mathrm{T}}$	phase slowness vector in Cartesian or cylindrical coordinates
$\beta = \lvert\boldsymbol{\beta}\rvert$	phase slowness (length of phase slowness vector)
C	stiffness tensor
C_{kn}, C_m	effective cylinder functions of the order $kn = m$
$C_{kn}^{q'}, C_m^{q'}$	cylindrical excitation functions of the order $kn = m$
$C_m^{\mathrm{F}}, C_m^{\mathrm{S}}$	fast and slow principal cylinder functions (order m)
$\mathcal{D}$	boundary condition matrix
D_u	finite-difference operator ($u \in \{x, y, z, t\}$)
$\Delta x, \Delta y, \Delta z, \Delta t$	spatial and temporal sampling intervals

$\Delta\theta$	azimuth between X- and Y-multipole source firings
ϵ	strain tensor
ϵ, γ, δ	*Thomsen* parameters
f	arbitrary function
f_c	center frequency of the *Ricker* wavelet
f_{acc}	maximum accurate frequency
$\mathcal{G}_n = \mathrm{diag}\big(C_m^\mathrm{F}, C_m^\mathrm{S}\big)$	diagonal matrix
$\boldsymbol{k}$	wave vector
κ	eigenvalues defining the phase velocities
Λ	matrix to define the eigenvalue problem
λ, μ	*Lamé* parameters
λ_{min}	minimum wavelength
M_T	effective tool modulus
m	azimuthal wavenumber (modal number)
n	source excitation order
ν	order of Bessel functions
$\mathcal{P} = \Big([p_{XX}, p_{YX}]^\mathrm{T}, [p_{XY}, p_{YY}]^\mathrm{T}\Big)$	four-component pressure data matrix
p	acoustic pressure
Φ, $\check{\Psi}^\mathrm{qSV}$, $\check{\Psi}^\mathrm{SH}$	potential functions
ψ_0	inclination angle between the TI symmetry axis and the borehole axis
$\mathcal{Q}$	matrix
$\mathcal{R}, R$	rotation tensor/matrix
$\mathcal{R}^\mathrm{f}$	reflection coefficient
R_H	borehole radius
$R_\mathrm{T}^\mathrm{ID}, R_\mathrm{T}^\mathrm{OD}$	inner and outer LWD tool radius
r, θ, z	cylindrical coordinates: radial coordinate, azimuth, vertical coordinate
$\rho^\mathrm{s}, \rho^\mathrm{f}, \rho^\mathrm{T}$	volumetric mass density of the solid (formation), borehole fluid, logging tool
S	compliance tensor
s	*Laplace* transform parameter (frequency)
$\sigma = \begin{cases} +1 \text{ equal polarity} \\ -1 \text{ alternate polarity} \end{cases}$	multipole source polarity
$\mathcal{T}$	transmission coefficient
t	time
τ	stress tensor
θ^F	azimuth between the formation's fast principal direction and the source excitation direction
θ_0	azimuth between the borehole and tool reference frames

θ^X, θ^Y	azimuths of the X- and Y-multipole source/receiver
U	strain energy density
$\boldsymbol{u} = (u_1, u_2, u_3)^{\mathrm{T}}$ or $(u_r, u_\theta, u_z)^{\mathrm{T}}$	particle displacement vector in Cartesian or cylindrical coordinates
V	eigenvector defining the polarization direction
$\mathcal{V}$	polarization direction multiplied with amplitude
$\boldsymbol{v} = (v_1, v_2, v_3)^{\mathrm{T}}$ or $(v_r, v_\theta, v_z)^{\mathrm{T}}$	particle velocity vector in Cartesian or cylindrical coordinates
$\boldsymbol{v}^{\mathrm{G}}$	group velocity vector
$v_\odot^{(\mathrm{q})\mathrm{P}}, v_\odot^{(\mathrm{q})\mathrm{SV}}, v_\odot^{(\mathrm{q})\mathrm{SH}}, \ \odot \in \{\mathrm{ver}, \mathrm{hor}\}$	vertical/horizontal phase velocity of the (quasi) P-, (quasi) SV-, and (quasi) SH-waves in the formation
v^{f}	phase velocity of the P-wave in the borehole fluid
$v^{\mathrm{St}}(s), v^{\mathrm{tube}} = \lim_{s\to 0} v^{\mathrm{St}}$	phase velocity of the *Stoneley* wave and tube wave in the formation
W_{kn}, W_m	wavefield weighting function
ω	angular frequency
$\boldsymbol{x} = (x_1, x_2, x_3)^{\mathrm{T}}$ or $(r, \theta, z)^{\mathrm{T}}$	position vector in Cartesian or cylindrical coordinates
$\boldsymbol{x}''$	crystallographic reference frame
$\boldsymbol{x}'$	borehole reference frame
$\boldsymbol{x}$	tool reference frame
$\boldsymbol{\zeta} = (\zeta_1, \zeta_2, \zeta_3)^{\mathrm{T}}$	unitary propagation vector

Mathematical symbols and functions

$\delta_{i,j} = \begin{cases} 1 & i = j \\ 0 & i \neq j \end{cases}$	unit tensor of rank two (*Kronecker* delta)
$\Delta^+_{i,j,p,q} = \frac{1}{2}\left(\delta_{i,p}\delta_{j,p} + \delta_{i,q}\delta_{j,p}\right)$	symmetrical unit tensor of rank four
∂_u	partial derivative with respect to u
$\nabla = (\partial_x, \partial_y, \partial_z)^{\mathrm{T}}$	nabla operator
$\nabla\cdot$	divergence operator
$\nabla\times$	curl operator
$\nabla^2 = \Delta = \left(\partial_x^2 + \partial_y^2 + \partial^2\right)^{\mathrm{T}}$ or $(\partial_r^2 + \frac{1}{r}\partial_r + \frac{1}{r^2}\partial_\theta^2 + \partial_z^2)$	*Laplace* operator in Cartesian or cylindrical coordinates
$\delta(\boldsymbol{u})$	*Dirac* delta distribution
$\epsilon_m = \begin{cases} 1 & \text{if } m = 0 \\ 2 & \text{else} \end{cases}$	*Neumann* factor
Br	*Bromwich* integral
$\mathcal{L}, \mathcal{L}^{-1}$	*Laplace* transform and its inverse
$\mathcal{F}, \mathcal{F}^{-1}$	*Fourier* transform and its inverse
$\mathcal{F}_\theta, \mathcal{F}_\theta^{-1}$	azimuthal *Fourier* transform and its inverse

$\mathcal{K}, \mathcal{K}^{-1}$	*Meijer* transform and its inverse
$\check{u}$	*Laplace* transform of u
$\hat{u}$	spatial *Fourier* transform of u
$\tilde{u}_m$	azimuthal *Fourier* transform of u
$\bar{u}$	Meijer transform of u
exp	exponential function
$\sin, \cos, \tan, \cot$	trigonometric functions: sine, cosine, tangent, cotangent
$\arcsin, \arccos, \arctan$	inverse trigonometric functions: arcsine, arccosine, arctangent
I_ν, K_ν	modified *Bessel* functions of the first and second kind of the order ν
lim	limit
min, max	minimum, maximum
I	identity/unit matrix
A^{T}	the transpose of the matrix A
A^{-1}	the inverse of the matrix A
A^{+}	the *Moore-Penrose* inverse of the matrix A
$\det(A)$	determinant of matrix A
sym	symmetric
$\boldsymbol{u}$	vector u
$\boldsymbol{e}_x, \boldsymbol{e}_y, \boldsymbol{e}_z$	unit vectors
$\boldsymbol{u} \cdot \boldsymbol{v}$	scalar product
$\boldsymbol{u} \times \boldsymbol{v}$	cross product
$\lvert Z \rvert$	absolute value of Z
$u * v$	convolution of u and v
$\neq$	inequal
$\propto$	proportional
$\approx$	approximate
$\equiv$	identical to
$\in$	is an element of
$e \approx 2.71828$	*Euler*'s number
$\pi \approx 3.14156$	pi
$\mathrm{i} = \sqrt{-1}$	imaginary unit
$\mathrm{Re}(Z)$, $\mathrm{Im}(Z)$	real and imaginary part of a complex number Z
$\mathbb{C}, \mathbb{N}^*, \mathbb{R}, \mathbb{Z}$	set of complex, natural (without zero), real and integer numbers

List of Figures

List of Tables

A. Integral transforms

A.1. Laplace transform

Integral transforms are standard analysis tools for configurations whose properties are shift-invariant. The one-sided *Laplace* transform is an appropriate integral transform with respect to the time coordinate since causality must be considered. Causality means that a physical quantity cannot be generated before a source is switched on at the instant t_0. The one-side *Laplace* transform pair of some physical quantity $f = f(\boldsymbol{x}, t)$ defined in $t \in \mathcal{T} = \{t \in \mathbb{R}; t > t_0\}$ is given by (e.g., de Hoop, 1995)

$$\mathcal{L}\left(f(\boldsymbol{x}, t)\right) = \check{f}(\boldsymbol{x}, s) = \int_{t=t_0}^{\infty} \exp\left(-st\right) f(\boldsymbol{x}, t) dt, \tag{A.1a}$$

$$\mathcal{L}^{-1}\left(\check{f}(\boldsymbol{x}, s)\right) = f(\boldsymbol{x}, t) = \frac{1}{2\pi \mathrm{i}} \int_{s \in \mathrm{Br}} \exp(st) \check{f}(\boldsymbol{x}, s) \mathrm{d}s, \tag{A.1b}$$

where s is the complex *Laplace* transform parameter (frequency), and $\exp\left(-st\right)$ is referred to as the kernel of the *Laplace* transform. Extending the range of f by $f(\mathbf{x}, t) \equiv 0$ for $t \in \mathcal{T}' = \{t \in \mathbb{R}; t < t_0\}$ enforces causality. Equation A.1a can be considered as an integral equation for a given $\check{f}(\boldsymbol{x}, s)$ with the solution $f(\boldsymbol{x}, t)$ having the value zero for $t \in \mathcal{T}'$ and reproducing the function for $t \in \mathcal{T}$ (de Hoop, 1995). This requirement can be fulfilled by a proper choice of the parameter s. Since all quantities in physics are bounded, it is assumed that the function f is bounded. Therefore, the integral in equation A.1a is convergent if the parameter s is either real and positive $\{s \in \mathbb{R}; s > 0\}$ or complex with a positive real part $\{s \in \mathbb{C}; \mathrm{Re}(s) > 0\}$ (de Hoop, 1995). The limiting case where $s = \mathrm{i}\omega$ and ω is the angular frequency ($\omega \in \mathbb{R}$) yields the temporal *Fourier* transform. The inverse *Laplace* transform is performed by evaluating the integral given in equation A.1b in the complex s plane. The integral is the *Bromwich* integral (Br), where the integration path parallel to the imaginary s–axis lies right-hand of all possible poles of the function $\check{f}$.

The *Laplace* transform of the temporal derivative $\partial_t f(\mathbf{x}, t)$ of a function f can be calculated using partial integration

$$\mathcal{L}\left(\partial_t f(\boldsymbol{x}, t)\right) = \int_{t=t_0}^{\infty} \exp\left(-st\right) \partial_t f(\boldsymbol{x}, t) dt, \tag{A.2a}$$

$$= [\exp(-st) f(\boldsymbol{x}, t)]_{t=t_0}^{\infty} - \int_{t=t_0}^{\infty} (-s) \exp(-st) f(\boldsymbol{x}, t) dt, \tag{A.2b}$$

$$= -\exp(-st_0) \lim_{t \downarrow t_0} f(\boldsymbol{x}, t) + s\check{f}(\boldsymbol{x}, s). \tag{A.2c}$$

The first term of the right-hand side in equation A.2c describes a delta impulse $\delta(t - t_0)$, whose amplitude is defined by the jump of f when passing the instant t_0 (de Hoop, 1995). Note the *Laplace* transform of a delta function is defined as

$$\mathcal{L}\left(\delta(t - t_0)\right) = \exp(-st_0). \tag{A.3}$$

Assuming that the initial condition is given by $f(\boldsymbol{x}, t_0) = 0$ and f is continuous (no jump at t_0), the first term in equation A.2c vanishes and the remaining second term indicates that time differentiation in the time domain is equivalent to multiplication with the parameter s in the *Laplace* transformed or s-domain.

A.2. Spatial Fourier transform

The spatial *Fourier* transform is an integral transform concerning one or more spatial coordinates. Let $f = f(\boldsymbol{x}, t)$ be a scalar function that is defined in the N-dimensional Euclidean space $\mathbb{R}^N$ and let $\check{f} = \check{f}(\boldsymbol{x}, s)$ be its *Laplace* transform with respect to time (Appendix A.1). Then, the spatial *Fourier* transform pair can be defined as (e.g., van der Hijden, 1987)

$$\mathcal{F}\left(\check{f}(\boldsymbol{x}, s)\right) = \hat{f}(\boldsymbol{\beta}, s) = \int_{\boldsymbol{x} \in \mathbb{R}^N} \exp\left(-\mathrm{i} k_q x_q\right) \check{f}(\boldsymbol{x}, s) \mathrm{d}^N \boldsymbol{x} \tag{A.4a}$$

$$\mathcal{F}^{-1}\left(\hat{f}(\boldsymbol{\beta}, s)\right) = \check{f}(\boldsymbol{x}, s) = \left(\frac{s}{2\pi}\right)^N \int_{\boldsymbol{\beta} \in \mathbb{R}^N} \exp\left(\mathrm{i} k_q x_q\right) \hat{f}(\boldsymbol{\beta}, s) \mathrm{d}^N \boldsymbol{\beta}, \tag{A.4b}$$

where $\boldsymbol{k}$ is the transformation parameter referred to as wave vector. If the wave vector is real $\boldsymbol{k} \in \mathbb{R}^N$, the integral is convergent for an absolute integrable function $\check{f}(\boldsymbol{x}, s)$, meaning that for unbounded domains, $\check{f}(\boldsymbol{x}, s)$ goes to zero as $x \to -\infty$ and $x \to \infty$ (de Hoop, 1995). This is sometimes referred to as radiation condition. Analogously to van der Hijden (1987), the wave vector can be expressed by $\mathrm{i}\boldsymbol{k} = s\boldsymbol{\beta}$, where $\boldsymbol{\beta}$ is the phase slowness vector and s the possibly complex *Laplace* transform parameter.

The spatial *Fourier* transform of the derivative of the *Laplace* transformed function $\check{f}$ with respect to the spatial coordinate x_p is defined as

$$\mathcal{F}\left(\partial_p \check{f}(\boldsymbol{x}, s)\right) = \int_{\boldsymbol{x} \in \mathcal{X}} \exp\left(-s\beta_q x_q\right) \partial_p \check{f}(\boldsymbol{x}, s) \mathrm{d}V, \tag{A.5a}$$

$$= \int_{\boldsymbol{x} \in \mathcal{X}} \left[\partial_p \left(\exp(-s\beta_q x_q) \check{f}(\boldsymbol{x}, s)\right) - \left(\partial_p \exp(-s\beta_q x_q)\right) \check{f}(\boldsymbol{x}, s)\right] \mathrm{d}V, \tag{A.5b}$$

$$= \int\limits_{\boldsymbol{x}\in\partial\mathcal{X}} \exp(-s\beta_q x_q)\check{f}(\boldsymbol{x},s)n_p \mathrm{d}A + s\beta_p\hat{f}(\boldsymbol{\beta},s), \tag{A.5c}$$

where partial integration is used, and n_p is the unit vector normal to the surface $\partial\mathcal{X}$ pointing away from $\mathcal{X}$. If the domain $\mathcal{X}$ is extended to $\mathbb{R}^N$ and the function $f(\boldsymbol{x},s)$ goes to zero as $x \to -\infty$ and $x \to \infty$, the surface integral vanishes (de Hoop, 1995). Therefore differentiation with respect to spatial coordinates (∂_p) in $\mathbb{R}^N$ is equivalent to multiplication by the factor $s\beta_p$ in the *Fourier* transformed or spectral domain.

A.3. Azimuthal Fourier transform

A function f defined on a bounded domain in a cylindrical coordinate system depends on the radial coordinate r, the azimuthal coordinate θ, and the vertical coordinate z. While the latter coordinate can be transformed into the spectral domain via the above-described spatial *Fourier* transform, the azimuthal *Fourier* transform is required to transform the azimuth θ. The corresponding transform pair can be defined as (e.g., Geerits et al., 2010)

$$\mathcal{F}_\theta\left(f(\theta)\right) = \tilde{f}_m = \frac{1}{2\pi}\int\limits_{\theta=-\pi}^{\pi} \exp(-\mathrm{i}m\theta)f(\theta)\mathrm{d}\theta, \tag{A.6a}$$

$$\mathcal{F}_\theta^{-1}\left(\tilde{f}_m\right) = f(\theta) = \sum_{m=-\infty}^{\infty} \exp(\mathrm{i}m\theta)\tilde{f}_m. \tag{A.6b}$$

The transform parameter m is the azimuthal wavenumber, sometimes referred to as modal number.

The azimuthal *Fourier* transform of the azimuthal derivative of the function ($\partial_\theta f(\theta)$) is defined as

$$\mathcal{F}_\theta\left(\mathrm{d}_\theta f(\theta)\right) = \frac{1}{2\pi}\Big[\exp(-\mathrm{i}m\theta)f(\theta)\Big]_{-\pi}^{\pi} + \frac{\mathrm{i}m}{2\pi}\int\limits_{\theta=-\pi}^{\pi} \exp(-\mathrm{i}m\theta)f(\theta)\mathrm{d}\theta, \tag{A.7a}$$

$$= \frac{1}{2\pi}\left[(-1)^m(f(\pi) - f(-\pi))\right] + \mathrm{i}m\tilde{f}_m, \tag{A.7b}$$

$$= \mathrm{i}m\tilde{f}_m, \tag{A.7c}$$

where partial integration is applied. Consequently, differentiation with respect to the azimuth θ in the spatial domain is equivalent to multiplication by the factor $\mathrm{i}m$ in the azimuthal *Fourier* transformed domain if the function f is periodic ($f(\pi) = f(-\pi)$). If θ denotes the azimuth of a cylindrical coordinate system, the condition is always fulfilled.

Besides, the azimuthal *Fourier* transforms of the trigonometric cosine and sine functions are derived using *Euler*'s formulas, where δ denotes the *Dirac* delta distribution

$$\begin{aligned}
\mathcal{F}_\theta(\cos(n\theta)) &= \frac{1}{2\pi}\int_{\theta=-\pi}^{\pi} \exp(-\mathrm{i}m\theta)\cos(n\theta)\mathrm{d}\theta, \\
&= \frac{1}{4\pi}\int_{\theta=-\pi}^{\pi} \left(\exp(-\mathrm{i}(m-n)\theta) + \exp(-\mathrm{i}(m+n)\theta)\right)\mathrm{d}\theta, \\
&= \frac{1}{4\pi}\left(\left[\frac{\mathrm{i}}{m-n}\exp(-\mathrm{i}(m-n)\theta)\right]_{\theta=-\pi}^{\pi} + \left[\frac{\mathrm{i}}{m+n}\exp(-\mathrm{i}(m+n)\theta)\right]_{\theta=-\pi}^{\pi}\right), \\
&= \frac{1}{2}\left[\frac{\exp(\mathrm{i}\pi(m-n)) - \exp(-\mathrm{i}\pi(m-n))}{2\mathrm{i}\pi(m-n)} + \frac{\exp(\mathrm{i}\pi(m+n)) - \exp(-\mathrm{i}\pi(m+n))}{2\mathrm{i}\pi(m+n)}\right], \\
&= \frac{1}{2}\left[\frac{\sin(\pi(m-n))}{\pi(m-n)} + \frac{\sin(\pi(m+n))}{\pi(m+n)}\right], \\
&= \frac{1}{2}\left[\delta(m-n) + \delta(m+n)\right], \qquad \text{(A.8a)}
\end{aligned}$$

$$\begin{aligned}
\mathcal{F}_\theta(\sin(n\theta)) &= \frac{1}{2\pi}\int_{\theta=-\pi}^{\pi} \exp(-\mathrm{i}m\theta)\sin(n\theta)\mathrm{d}\theta, \\
&= \frac{1}{4\mathrm{i}\pi}\int_{\theta=-\pi}^{\pi} \left(\exp(-\mathrm{i}(m-n)\theta) - \exp(-\mathrm{i}(m+n)\theta)\right)\mathrm{d}\theta, \\
&= \frac{1}{4\mathrm{i}\pi}\left(\left[\frac{\mathrm{i}}{m-n}\exp(-\mathrm{i}(m-n)\theta)\right]_{\theta=-\pi}^{\pi} - \left[\frac{\mathrm{i}}{m+n}\exp(-\mathrm{i}(m+n)\theta)\right]_{\theta=-\pi}^{\pi}\right), \\
&= \frac{1}{2\mathrm{i}}\left[\frac{\exp(\mathrm{i}\pi(m-n)) - \exp(-\mathrm{i}\pi(m-n))}{2\mathrm{i}\pi(m-n)} - \frac{\exp(\mathrm{i}\pi(m+n)) - \exp(-\mathrm{i}\pi(m+n))}{2\mathrm{i}\pi(m+n)}\right], \\
&= \frac{1}{2\mathrm{i}}\left[\frac{\sin(\pi(m-n))}{\pi(m-n)} - \frac{\sin(\pi(m+n))}{\pi(m+n)}\right], \\
&= \frac{1}{2\mathrm{i}}\left[\delta(m-n) - \delta(m+n)\right]. \qquad \text{(A.8b)}
\end{aligned}$$

The azimuthal *Fourier* transforms of further trigonometric expressions, e.g., the product of the cosine and sine functions or arbitrary powers of them, can be straightforwardly calculated from the above transforms (Eq. A.8a–A.8b) by applying the convolution property

$$\mathcal{F}_\theta\left(f(\theta)g(\theta)\right) = \tilde{f}_m * \tilde{g}_m = \sum_{k=-\infty}^{\infty} \tilde{f}_k \tilde{g}_{m-k}. \qquad \text{(A.9)}$$

Some particular azimuthal *Fourier* transforms are given by

$$\mathcal{F}_\theta\left[\cos^2\theta\right] = \frac{1}{4}\left[\delta(m-2) + 2\delta(m) + \delta(m+2)\right], \qquad \text{(A.10a)}$$

$$\mathcal{F}_\theta\left[\cos^3\theta\right] = \frac{1}{8}\left[\delta(m-3) + 3\delta(m-1) + 3\delta(m+1) + \delta(m+3)\right], \tag{A.10b}$$

$$\mathcal{F}_\theta\left[\cos^4\theta\right] = \frac{1}{16}\left[\delta(m-4) + 4\delta(m-2) + 6\delta(m) + 4\delta(m+2) + \delta(m+4)\right], \tag{A.10c}$$

$$\mathcal{F}_\theta\left[\sin^2\theta\right] = \frac{1}{4}\left[-\delta(m-2) + 2\delta(m) - \delta(m+2)\right], \tag{A.10d}$$

$$\mathcal{F}_\theta\left[\sin^3\theta\right] = \frac{1}{8\mathrm{i}}\left[-\delta(m-3) + 3\delta(m-1) - 3\delta(m+1) + \delta(m+3)\right], \tag{A.10e}$$

$$\mathcal{F}_\theta\left[\sin^4\theta\right] = \frac{1}{16}\left[\delta(m-4) - 4\delta(m-2) + 6\delta(m) - 4\delta(m+2) + \delta(m+4)\right], \tag{A.10f}$$

$$\mathcal{F}_\theta\left[\sin\theta\cos\theta\right] = \frac{1}{4\mathrm{i}}\left[\delta(m-2) - \delta(m+2)\right], \tag{A.10g}$$

$$\mathcal{F}_\theta\left[\sin\theta\cos^2\theta\right] = \frac{1}{8\mathrm{i}}\left[\delta(m-3) + \delta(m-1) - \delta(m+1) - \delta(m+3)\right], \tag{A.10h}$$

$$\mathcal{F}_\theta\left[\sin\theta\cos^3\theta\right] = \frac{1}{16\mathrm{i}}\left[\delta(m-4) + 2\delta(m-2) - 2\delta(m+2) - \delta(m+4)\right], \tag{A.10i}$$

$$\mathcal{F}_\theta\left[\sin^2\theta\cos\theta\right] = \frac{1}{8}\left[-\delta(m-3) + \delta(m-1) + \delta(m+1) - \delta(m+3)\right], \tag{A.10j}$$

$$\mathcal{F}_\theta\left[\sin^3\theta\cos\theta\right] = \frac{1}{16\mathrm{i}}\left[-\delta(m-4) + 2\delta(m-2) - 2\delta(m+2) + \delta(m+4)\right], \tag{A.10k}$$

$$\mathcal{F}_\theta\left[\sin^2\theta\cos^2\theta\right] = \frac{1}{16}\left[-\delta(m-4) + 2\delta(m) - \delta(m+4)\right]. \tag{A.10l}$$

On the other hand, the convolution property has to be also applied for the multiplication of a trigonometric function and an arbitrary function $f(\theta)$ depending on θ

$$\mathcal{F}_\theta\left[\cos\theta f(\theta)\right] = \frac{1}{2}\left[\hat{f}_{m-1} + \hat{f}_{m+1}\right], \tag{A.11a}$$

$$\mathcal{F}_\theta\left[\sin\theta f(\theta)\right] = \frac{1}{2\mathrm{i}}\left[\hat{f}_{m-1} - \hat{f}_{m+1}\right]. \tag{A.11b}$$

A.4. Meijer transform

The *Meijer* transform was originally introduced by Meijer (1941) and is sometimes referred to as (*Meijer*) K-transform or *Meijer-Bessel* transform. The *Meijer* transform of the order ν is defined by (Bateman Manuscript Project, 1954)

$$\mathcal{K}_\nu\left(f(r)\right) = \bar{f}_\nu(k_r) = \int_{r=0}^{\infty} \sqrt{rk_r} K_\nu(rk_r) f(r)\mathrm{d}r, \tag{A.12}$$

where K_ν denotes a modified *Bessel* function of the second kind and the order ν. If the order equals $\nu = \pm\frac{1}{2}$, the *Meijer* transform becomes the *Laplace* transform because of (e.g.,

Gradshteyn and Ryzhik, 2007)

$$K_{\pm\frac{1}{2}}(rk_r) = \sqrt{\frac{\pi}{2rk_r}} \exp\left(-rk_r\right). \tag{A.13}$$

For the transformation of the radial coordinate into the radial wavenumber domain in the *Christoffel* equation, the transforms of various terms (∂_r^2, $\frac{1}{r}\partial_r$, ∂_r, $\frac{1}{r}$, $\frac{1}{r^2}$) have to be considered. Their *Meijer* transforms are given by

$$\mathcal{K}_\nu\left(2\nu\partial_r f(r)\right) = k_r\left[\left(\nu-\frac{1}{2}\right)\bar{f}_{\nu+1}(k_r) + \left(\nu+\frac{1}{2}\right)\bar{f}_{\nu-1}(k_r)\right], \tag{A.14a}$$

$$\begin{aligned}\mathcal{K}_\nu\left(4\nu^2\partial_r^2 f(r)\right) = k_r^2\Bigg[&\left(\nu^2-\nu+\frac{1}{4}\right)\bar{f}_{\nu+2}(k_r) + \left(2\nu^2-\frac{1}{2}\right)\bar{f}_\nu(k_r)\\ &+\left(\nu^2+\nu+\frac{1}{4}\right)\bar{f}_{\nu-2}(k_r)\Bigg],\end{aligned} \tag{A.14b}$$

$$\mathcal{K}_\nu\left(4\nu^2\frac{1}{r}\partial_r f(r)\right) = k_r^2\left[\left(\frac{1}{2}+\nu\right)\bar{f}_{\nu+2}(k_r) - \bar{f}_\nu(k_r) + \left(\frac{1}{2}-\nu\right)\bar{f}_{\nu-2}(k_r)\right], \tag{A.14c}$$

$$\mathcal{K}_\nu\left(2\nu\frac{1}{r}f(r)\right) = k_r\left[\bar{f}_{\nu+1}(k_r) - \bar{f}_{\nu-1}(k_r)\right], \tag{A.14d}$$

$$\mathcal{K}\left(4\nu^2\frac{1}{r^2}f(r)\right) = k_r^2\left[\bar{f}_{\nu+2}(k_r) - 2\bar{f}_\nu(k_r) + \bar{f}_{\nu-2}(k_r)\right]. \tag{A.14e}$$

These equations are derived by using recursion formulas given in Gradshteyn and Ryzhik (2007)

$$\partial_r K_\nu(rk_r) = -\frac{k_r}{2}\big[K_{\nu-1}(rk_r) + K_{\nu+1}(rk_r)\big], \tag{A.15a}$$

$$2\nu K_\nu(rk_r) = rk_r\big[K_{\nu+1}(rk_r) - K_{\nu-1}(rk_r)\big]. \tag{A.15b}$$

B. Stiffness and compliance tensor

B.1. Rotation between reference frames

The symmetries of anisotropic media are applied to define the crystallographic reference frame ($\boldsymbol{x}''$). However, in borehole acoustics, the governing equations are expressed in the borehole reference frame ($\boldsymbol{x}'$). The vertical axis of this reference frame is chosen to be always aligned with the borehole axis (Fig. B.1). Furthermore, a tool reference frame ($\boldsymbol{x}$) can be defined, which vertical axis also coincides with the borehole axis, and the horizontal axes are aligned with a specific defined tool position. Since *Hooke*'s law applies to all orthogonal reference frames, it can be transformed from the crystallographic reference frame into the tool reference frame. Therefore, the stress ($\tau_{i,j}$) and strain ($\epsilon_{k,l}$) tensors are transformed by multiplication with a second-order rotation tensor $\mathcal{R}_{i,j}$

$$\tau_{i,j} = \mathcal{R}_{i,i'}\mathcal{R}_{j,j'}\tau''_{i',j'}, \tag{B.1}$$

$$\epsilon_{k,l} = \mathcal{R}_{k,k'}\mathcal{R}_{l,l'}\epsilon''_{k',l'}. \tag{B.2}$$

The substitution of *Hooke*'s law given in the crystallographic reference frame ($\tau''_{i,j} = C''_{i,j,k,l}\epsilon''_{k,l}$) into equation B.1 yields

$$\tau_{i,j} = \mathcal{R}_{i,i'}\mathcal{R}_{j,j'}C''_{i',j',k',l'}\epsilon''_{k',l'}. \tag{B.3}$$

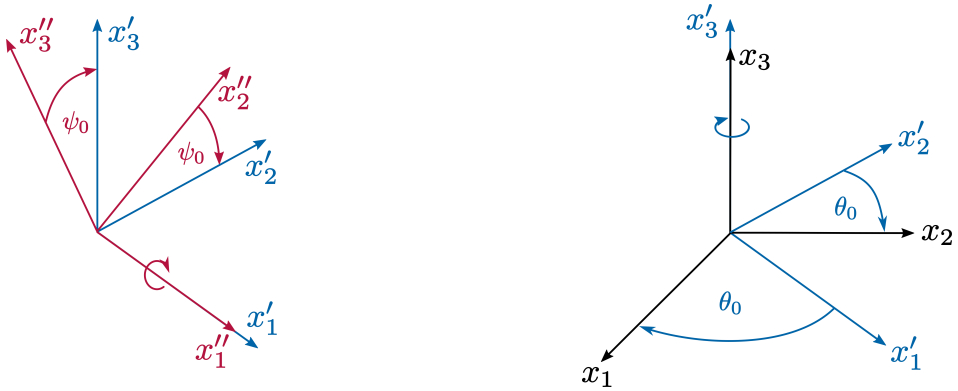

(a) Crystallographic to borehole reference frame

(b) Borehole to tool reference frame

Fig. B.1: Illustration of the transformations from the crystallographic reference frame $\boldsymbol{x}''$ (red) to the borehole reference frame $\boldsymbol{x}'$ (blue) and the tool reference frame $\boldsymbol{x}$ (black).

The inverse of equation B.2 can be easily computed since the rotation tensor is orthogonal ($\mathcal{R}_{i,j}\mathcal{R}_{i,k} = \delta_{j,k}$)

$$\epsilon''_{k',l'} = \mathcal{R}_{k,k'}\mathcal{R}_{l,l'}\epsilon_{k,l}. \tag{B.4}$$

Substitution of the above equation into equation B.3 yields *Hooke*'s law expressed in the tool reference frame

$$\tau_{i,j} = C_{i,j,k,l}\epsilon_{k,l}, \tag{B.5}$$

with

$$C_{i,j,k,l} = \mathcal{R}_{i,i'}\mathcal{R}_{j,j'}\mathcal{R}_{k,k'}\mathcal{R}_{l,l'}C''_{i',j',k',l'}. \tag{B.6}$$

The rotation tensor $\mathcal{R}_{i,j}$ contains two rotations. First, the stiffness tensor is transformed from the crystallographic reference frame $\boldsymbol{x}''$ to the borehole reference frame $\boldsymbol{x}'$ by a rotation around the x''_1–axis by the angle ψ_0 (Fig. B.1a). The elements of the rotation tensor $\mathcal{R}_{i,j}$ are defined by the cosines of the angles between the x'_i and x''_j axes

$$\mathcal{R}^{x''_1}(\psi_0) = \begin{pmatrix} 1 & 0 & 0 \\ 0 & \cos\psi_0 & \sin\psi_0 \\ 0 & -\sin\psi_0 & \cos\psi_0 \end{pmatrix}. \tag{B.7}$$

Second, the stiffness tensor is transformed from the borehole reference frame ($\boldsymbol{x}'$) to the tool reference frame ($\boldsymbol{x}$) by an azimuthal rotation around the x'_3–axis by the angle θ_0 (Fig. B.1b). The corresponding rotation tensor is defined as

$$\mathcal{R}^{x'_3}(\theta_0) = \begin{pmatrix} \cos\theta_0 & \sin\theta_0 & 0 \\ -\sin\theta_0 & \cos\theta_0 & 0 \\ 0 & 0 & 1 \end{pmatrix}. \tag{B.8}$$

Both rotations can be combined by matrix multiplication, and the resulting rotation tensor becomes

$$\mathcal{R}_{i,j}(\psi_0,\theta_0) = \mathcal{R}^{x'_3}_{q,j}(\theta_0)\mathcal{R}^{x''_1}_{i,q}(\psi_0) = \begin{pmatrix} \cos\theta_0 & \cos\psi_0\sin\theta_0 & \sin\psi_0\sin\theta_0 \\ -\sin\theta_0 & \cos\psi_0\cos\theta_0 & \sin\psi_0\cos\theta_0 \\ 0 & -\sin\psi_0 & \cos\psi_0 \end{pmatrix}. \tag{B.9}$$

Since *Hooke*'s law is often expressed in a matrix-vector notation, it is useful to define the rotations also as a matrix-vector multiplication. Straightforward expansion of equation B.1 and the usage of the stress tensor symmetry yields

$$\boldsymbol{\tau} = R\boldsymbol{\tau}'', \qquad \boldsymbol{\tau} = (\tau_{1,1}, \tau_{2,2}, \tau_{3,3}, \tau_{2,3}, \tau_{1,3}, \tau_{1,2})^{\mathrm{T}}, \tag{B.10}$$

with (Auld, 1973)

$$R = \begin{pmatrix} \mathcal{R}_{1,1}^2 & \mathcal{R}_{1,2}^2 & \mathcal{R}_{1,3}^2 \\ \mathcal{R}_{2,1}^2 & \mathcal{R}_{2,2}^2 & \mathcal{R}_{2,3}^2 \\ \mathcal{R}_{3,1}^2 & \mathcal{R}_{3,2}^2 & \mathcal{R}_{3,3}^2 \\ \mathcal{R}_{2,1}\mathcal{R}_{3,1} & \mathcal{R}_{2,2}\mathcal{R}_{3,2} & \mathcal{R}_{2,3}\mathcal{R}_{3,3} \\ \mathcal{R}_{1,1}\mathcal{R}_{3,1} & \mathcal{R}_{1,2}\mathcal{R}_{3,2} & \mathcal{R}_{1,3}\mathcal{R}_{3,3} \\ \mathcal{R}_{1,1}\mathcal{R}_{2,1} & \mathcal{R}_{1,2}\mathcal{R}_{2,2} & \mathcal{R}_{1,3}\mathcal{R}_{2,3} \end{pmatrix}$$

$$\begin{pmatrix} 2\mathcal{R}_{1,3}\mathcal{R}_{1,2} & 2\mathcal{R}_{1,1}\mathcal{R}_{1,3} & 2\mathcal{R}_{1,1}\mathcal{R}_{1,2} \\ 2\mathcal{R}_{2,2}\mathcal{R}_{2,3} & 2\mathcal{R}_{2,1}\mathcal{R}_{2,3} & 2\mathcal{R}_{2,1}\mathcal{R}_{2,2} \\ 2\mathcal{R}_{3,2}\mathcal{R}_{3,3} & 2\mathcal{R}_{3,1}\mathcal{R}_{3,3} & 2\mathcal{R}_{3,1}\mathcal{R}_{3,2} \\ \mathcal{R}_{2,2}\mathcal{R}_{3,3} + \mathcal{R}_{2,3}\mathcal{R}_{3,2} & \mathcal{R}_{2,1}\mathcal{R}_{3,3} + \mathcal{R}_{2,3}\mathcal{R}_{3,1} & \mathcal{R}_{2,1}\mathcal{R}_{3,2} + \mathcal{R}_{2,2}\mathcal{R}_{3,1} \\ \mathcal{R}_{1,2}\mathcal{R}_{3,3} + \mathcal{R}_{1,3}\mathcal{R}_{3,2} & \mathcal{R}_{1,1}\mathcal{R}_{3,3} + \mathcal{R}_{1,3}\mathcal{R}_{3,1} & \mathcal{R}_{1,1}\mathcal{R}_{3,2} + \mathcal{R}_{1,2}\mathcal{R}_{3,1} \\ \mathcal{R}_{1,2}\mathcal{R}_{2,3} + \mathcal{R}_{1,3}\mathcal{R}_{2,2} & \mathcal{R}_{1,1}\mathcal{R}_{2,3} + \mathcal{R}_{1,3}\mathcal{R}_{2,1} & \mathcal{R}_{1,1}\mathcal{R}_{2,2} + \mathcal{R}_{1,2}\mathcal{R}_{2,1} \end{pmatrix}. \tag{B.11}$$

Analogously, equation B.4 can be expanded to obtain

$$\boldsymbol{\epsilon}'' = R^{\mathrm{T}}\boldsymbol{\epsilon}, \qquad \boldsymbol{\epsilon} = (\epsilon_{1,1}, \epsilon_{2,2}, \epsilon_{3,3}, 2\epsilon_{2,3}, 2\epsilon_{1,3}, 2\epsilon_{1,2})^{\mathrm{T}}. \tag{B.12}$$

Important to note is that the rotation matrix is not orthogonal ($RR^{\mathrm{T}} \neq R^{\mathrm{T}}R \neq I$). Nevertheless, the expansion of equation B.4 yields the transpose of the rotation matrix because the strain vector is defined by the normal components and the tangential components multiplied with the factor two. Accordingly, *Hooke*'s law in the tool reference frame and the matrix-vector notation is defined as

$$\boldsymbol{\tau} = C\boldsymbol{\epsilon}, \tag{B.13}$$

with

$$C = RC''R^{\mathrm{T}}. \tag{B.14}$$

Equation B.14 describes the rotation of the stiffness tensor given in *Voigt*'s notation by two matrix-matrix multiplications, and is equivalent to equation B.6.

Substitution of the rotation tensor components defined in equation B.9 into equation B.11 yields the rotation matrix

$$R = \begin{pmatrix} \cos^2\theta_0 & \cos^2\psi_0 \sin^2\theta_0 & \sin^2\psi_0 \sin^2\theta_0 \\ \sin^2\theta_0 & \cos^2\psi_0 \cos^2\theta_0 & \sin^2\psi_0 \cos^2\theta_0 \\ 0 & \sin^2\psi_0 & \cos^2\psi_0 \\ 0 & -\frac{1}{2}\sin(2\psi_0)\cos\theta_0 & \frac{1}{2}\sin(2\psi_0)\cos\theta_0 \\ 0 & -\frac{1}{2}\sin(2\psi_0)\sin\theta_0 & \frac{1}{2}\sin(2\psi_0)\sin\theta_0 \\ -\frac{1}{2}\sin(2\theta_0) & \frac{1}{2}\cos^2\psi_0 \sin(2\theta_0) & \frac{1}{2}\sin^2\psi_0 \sin(2\theta_0) \end{pmatrix}$$

$$\begin{pmatrix} \sin(2\psi_0)\sin^2\theta_0 & \sin\psi_0 \sin(2\theta_0) & \cos\psi_0 \sin(2\theta_0) \\ \sin(2\psi_0)\cos^2\theta_0 & -\sin\psi_0 \sin(2\theta_0) & -\cos\psi_0 \sin(2\theta_0) \\ -\sin(2\psi_0) & 0 & 0 \\ \cos(2\psi_0)\cos\theta_0 & -\cos\psi_0 \sin\theta_0 & \sin\psi_0 \sin\theta_0 \\ \cos(2\psi_0)\sin\theta_0 & \cos\psi_0 \cos\theta_0 & -\sin\psi_0 \cos\theta_0 \\ \frac{1}{2}\sin(2\psi_0)\sin(2\theta_0) & \sin\psi_0 \cos(2\theta_0) & \cos\psi_0 \cos(2\theta_0) \end{pmatrix}. \tag{B.15}$$

The rotation of the stiffness tensor characterizing specific anisotropic symmetries in the crystallographic reference frame to the tool reference frame may cause that these symmetries get lost.

B.2. Cylindrical coordinates

The transformation of the stiffness tensor from Cartesian into cylindrical coordinates is equivalent to a rotation around the x_3–axis. Consequently, equation B.6 or equation B.14 can be used by setting $\psi_0 = 0$ and $\theta_0 \equiv \theta$. The stiffness tensor in cylindrical coordinates is still symmetric, which elements are given by

$$\tilde{C}_{1,1} = C_{1,1}\cos^4\theta + 4C_{1,6}\sin\theta\cos^3\theta + (2C_{1,2} + 4C_{6,6})\sin^2\theta\cos^2\theta + 4C_{2,6}\sin^3\theta\cos\theta + C_{2,2}\sin^4\theta, \tag{B.16a}$$

$$\tilde{C}_{1,2} = C_{1,2}\cos^4\theta + 2(C_{2,6} - C_{1,6})\sin\theta\cos^3\theta + (C_{1,1} + C_{2,2} - 4C_{6,6})\sin^2\theta\cos^2\theta + 2(C_{1,6} - C_{2,6})\sin^3\theta\cos\theta + C_{1,2}\sin^4\theta, \tag{B.16b}$$

$$\tilde{C}_{1,3} = C_{1,3}\cos^2\theta + 2C_{3,6}\cos\theta\sin\theta + C_{2,3}\sin^2\theta, \tag{B.16c}$$

$$\tilde{C}_{1,4} = C_{1,4}\cos^3\theta + (2C_{4,6} - C_{1,5})\sin\theta\cos^2\theta + (C_{2,4} - 2C_{5,6})\sin^2\theta\cos\theta - C_{2,5}\sin^3\theta, \tag{B.16d}$$

(B.16e)

$$\tilde{C}_{1,5} = C_{1,5}\cos^3\theta + (2C_{5,6} + C_{1,4})\sin\theta\cos^2\theta + (C_{2,5} + 2C_{4,6})\sin^2\theta\cos\theta + C_{2,4}\sin^3\theta, \tag{B.16f}$$

$$\tilde{C}_{1,6} = C_{1,6}\cos^4\theta + (C_{1,2} - C_{1,1} + 2C_{6,6})\sin\theta\cos^3\theta + 3\,(C_{2,6} - C_{1,6})\cos^2\theta\sin^2\theta + (C_{2,2} - C_{1,2} - 2C_{6,6})\sin^3\theta\cos\theta - C_{2,6}\sin^4\theta, \tag{B.16g}$$

$$\tilde{C}_{2,2} = C_{2,2}\cos^4\theta - 4C_{2,6}\sin\theta\cos^3\theta + (2C_{1,2} + 4C_{6,6})\sin^2\theta\cos^2\theta - 4C_{1,6}\sin^3\theta\cos\theta + C_{1,1}\sin^4\theta, \tag{B.16h}$$

$$\tilde{C}_{2,3} = C_{1,3}\sin^2\theta + C_{2,3}\cos^2\theta - 2C_{3,6}\sin\theta\cos\theta, \tag{B.16i}$$

$$\tilde{C}_{2,4} = C_{2,4}\cos^3\theta - (C_{2,5} + 2C_{4,6})\sin\theta\cos^2\theta + (C_{1,4} + 2C_{5,6})\sin^2\theta\cos\theta - C_{1,5}\sin^3\theta, \tag{B.16j}$$

$$\tilde{C}_{2,5} = C_{2,5}\cos^3\theta + (C_{2,4} - 2C_{5,6})\sin\theta\cos^2\theta + (C_{1,5} - 2C_{4,6})\sin^2\theta\cos\theta + C_{1,4}\sin^3\theta, \tag{B.16k}$$

$$\tilde{C}_{2,6} = C_{2,6}\cos^4\theta + (C_{2,2} - C_{1,2} - 2C_{6,6})\sin\theta\cos^3\theta + 3\,(C_{1,6} - C_{2,6})\sin^2\theta\cos^2\theta + (C_{1,2} - C_{1,1} + 2C_{6,6})\sin^3\theta\cos\theta - C_{1,6}\sin^4\theta, \tag{B.16l}$$

$$\tilde{C}_{3,3} = C_{3,3}, \tag{B.16m}$$

$$\tilde{C}_{3,4} = C_{3,4}\cos\theta - C_{3,5}\sin\theta, \tag{B.16n}$$

$$\tilde{C}_{3,5} = C_{3,4}\sin\theta + C_{3,5}\cos\theta, \tag{B.16o}$$

$$\tilde{C}_{3,6} = (C_{2,3} - C_{1,3})\sin\theta\cos\theta + C_{3,6}\cos^2\theta - C_{3,6}\sin^2\theta, \tag{B.16p}$$

$$\tilde{C}_{4,4} = C_{4,4}\cos^2\theta - 2C_{4,5}\sin\theta\cos\theta + C_{5,5}\sin^2\theta, \tag{B.16q}$$

$$\tilde{C}_{4,5} = C_{4,5}\cos^2\theta + (C_{4,4} - C_{5,5})\sin\theta\cos\theta - C_{4,5}\sin^2\theta, \tag{B.16r}$$

$$\tilde{C}_{4,6} = C_{4,6}\cos^3\theta + (C_{2,4} - C_{1,4} - C_{5,6})\sin\theta\cos^2\theta + (C_{1,5} - C_{2,5} - C_{4,6})\sin^2\theta\cos\theta + C_{5,6}\sin^3\theta, \tag{B.16s}$$

$$\tilde{C}_{5,5} = C_{5,5}\cos^2\theta + 2C_{4,5}\sin\theta\cos\theta + C_{4,4}\sin^2\theta, \tag{B.16t}$$

$$\tilde{C}_{5,6} = C_{5,6}\cos^3\theta + (C_{4,6} + C_{2,5} - C_{1,5})\sin\theta\cos^2\theta + (C_{2,4} - C_{1,4} - C_{5,6})\sin^2\theta\cos\theta - C_{4,6}\sin^3\theta, \tag{B.16u}$$

$$\tilde{C}_{6,6} = C_{6,6}\cos^4\theta + 2\,(C_{2,6} - C_{1,6})\sin\theta\cos^3\theta + (C_{1,1} + C_{2,2} - 2C_{1,2} - 2C_{6,6})\sin^2\theta\cos^2\theta + 2\,(C_{1,6} - C_{2,6})\sin^3\theta\cos\theta + C_{6,6}\sin^4\theta. \tag{B.16v}$$

C. Christoffel equation

C.1. Cartesian coordinates

The *Christoffel* equation can be derived from equations 2.25 by rearranging the second equation (second row in the matrix) to make it explicit for the temporal derivative of the stress tensor

$$-S_{i,j,p,q}\partial_t\tau_{p,q}(\boldsymbol{x},t)+\Delta^+_{i,j,n,r}\partial_n v_r(\boldsymbol{x},t)=0, \tag{C.1a}$$

$$\underbrace{C_{p',q',i,j}S_{i,j,p,q}}_{=\Delta^+_{p',q',p,q}}\partial_t\tau_{p,q}(\boldsymbol{x},t)=\Delta^+_{i,j,n,r}C_{p',q',i,j}\partial_n v_r(\boldsymbol{x},t), \tag{C.1b}$$

$$\Delta^+_{p',q',p,q}\partial_t\tau_{p,q}(\boldsymbol{x},t)=C_{p',q',n,r}\partial_n v_r(\boldsymbol{x},t), \tag{C.1c}$$

$$\partial_t\tau_{p,q}(\boldsymbol{x},t)=C_{p,q,n,r}\partial_n v_r(\boldsymbol{x},t). \tag{C.1d}$$

Subsequently, equation C.1d is substituted into the equation of motion after temporal differentiation (first row of the matrix in equation 2.25)

$$-\Delta^+_{k,m,p,q}\partial_m\partial_t\tau_{p,q}(\boldsymbol{x},t)+\delta_{k,r}\rho^{\mathrm{s}}\partial_t^2 v_r(\boldsymbol{x},t)=0, \tag{C.2a}$$

$$-\Delta^+_{k,m,p,q}\partial_m C_{p,q,n,r}\partial_n v_r(\boldsymbol{x},t)+\delta_{k,r}\rho^{\mathrm{s}}\partial_t^2 v_r(\boldsymbol{x},t)=0, \tag{C.2b}$$

$$-\partial_m\frac{1}{\rho^{\mathrm{s}}}C_{k,m,n,r}\partial_n v_r(\boldsymbol{x},t)+\delta_{k,r}\partial_t^2 v_r(\boldsymbol{x},t)=0,\qquad \bar{C}_{k,m,n,r}=\frac{1}{\rho^{\mathrm{s}}}C_{k,m,n,r}, \tag{C.2c}$$

$$\left(\partial_m\bar{C}_{k,m,n,r}\partial_n-\delta_{k,r}\partial_t^2\right)v_r(\boldsymbol{x},t)=0. \tag{C.2d}$$

Applying a *Laplace* transform (App. A.1) with respect to the time and spatial *Fourier* transforms (App. A.2) with respect to the spatial coordinates, equation C.2d becomes

$$\left(s\beta_m\bar{C}_{k,m,n,r}s\beta_n-\delta_{k,r}s^2\right)\hat{v}_r(\boldsymbol{\beta},s)=0. \tag{C.3}$$

The equation can be divided by the frequency s^2 ($s\neq 0$), and the phase slowness vector $\boldsymbol{\beta}$ can be separated into its length $|\boldsymbol{\beta}|$ and direction $\boldsymbol{\zeta}$

$$\beta_m=|\boldsymbol{\beta}|\zeta_m, \tag{C.4}$$

to obtain the *Christoffel* equation in the form

$$\left(|\boldsymbol{\beta}|^2\zeta_m\bar{C}_{k,m,n,r}\zeta_n-\delta_{k,r}\right)\hat{v}_r(\boldsymbol{\beta},s)=0. \tag{C.5}$$

Further definitions of $\Lambda_{k,r} = \zeta_m \bar{C}_{k,m,n,r} \zeta_n$ and $\kappa = |\boldsymbol{\beta}|^{(-2)}$ yield the eigenvalue problem

$$(\Lambda_{k,r} - \kappa \delta_{k,r})\, \hat{v}_r(\boldsymbol{\beta}, s) = 0. \tag{C.6}$$

The elements of the symmetric matrix $\Lambda_{k,r}$ (tensor of rank two) can be given in a matrix-vector notation by

$$\begin{pmatrix} \Lambda_{1,1} \\ \Lambda_{1,2} \\ \Lambda_{1,3} \\ \Lambda_{2,2} \\ \Lambda_{2,3} \\ \Lambda_{3,3} \end{pmatrix} = \begin{pmatrix} \bar{C}_{1,1} & \bar{C}_{6,6} & \bar{C}_{5,5} & 2\bar{C}_{1,6} & 2\bar{C}_{1,5} & 2\bar{C}_{5,6} \\ \bar{C}_{1,6} & \bar{C}_{2,6} & \bar{C}_{4,5} & \bar{C}_{1,2} + \bar{C}_{6,6} & \bar{C}_{1,4} + \bar{C}_{5,6} & \bar{C}_{4,6} + \bar{C}_{2,5} \\ \bar{C}_{1,5} & \bar{C}_{4,6} & \bar{C}_{3,5} & \bar{C}_{1,4} + \bar{C}_{5,6} & \bar{C}_{1,3} + \bar{C}_{5,5} & \bar{C}_{3,6} + \bar{C}_{4,5} \\ \bar{C}_{6,6} & \bar{C}_{2,2} & \bar{C}_{4,4} & 2\bar{C}_{2,6} & 2\bar{C}_{4,6} & 2\bar{C}_{2,4} \\ \bar{C}_{5,6} & \bar{C}_{2,4} & \bar{C}_{3,4} & \bar{C}_{4,6} + \bar{C}_{2,5} & \bar{C}_{3,6} + \bar{C}_{4,5} & \bar{C}_{2,3} + \bar{C}_{4,4} \\ \bar{C}_{5,5} & \bar{C}_{4,4} & \bar{C}_{3,3} & 2\bar{C}_{4,5} & 2\bar{C}_{3,5} & 2\bar{C}_{3,4} \end{pmatrix} \begin{pmatrix} \zeta_1^2 \\ \zeta_2^2 \\ \zeta_3^2 \\ \zeta_1\zeta_2 \\ \zeta_1\zeta_3 \\ \zeta_2\zeta_3 \end{pmatrix}, \tag{C.7}$$

where the stiffness tensor elements are expressed in *Voigt*'s notation and are divided by the volumetric mass density ρ^{s}.

Moreover, the *Christoffel* equation (Eq. C.6) can be expressed in matrix-vector form by

$$\begin{pmatrix} \Lambda_{1,1} - \kappa & \Lambda_{1,2} & \Lambda_{1,3} \\ \Lambda_{1,2} & \Lambda_{2,2} - \kappa & \Lambda_{2,3} \\ \Lambda_{1,3} & \Lambda_{2,3} & \Lambda_{3,3} - \kappa \end{pmatrix} \boldsymbol{v} = \boldsymbol{0}. \tag{C.8}$$

Equation C.8 has only non-trivial solutions if the matrix becomes singular. Thus, the values κ are sought for which the determinant of the matrix vanishes. These values are, by definition, the eigenvalues of the matrix Λ and are equivalent to the roots of the characteristic polynomial

$$\det \begin{vmatrix} \Lambda_{1,1} - \kappa & \Lambda_{1,2} & \Lambda_{1,3} \\ \Lambda_{1,2} & \Lambda_{2,2} - \kappa & \Lambda_{2,3} \\ \Lambda_{1,3} & \Lambda_{2,3} & \Lambda_{3,3} - \kappa \end{vmatrix} = 0 \qquad \Leftrightarrow \qquad \kappa^3 + a_1\kappa^2 + a_2\kappa + a_3 = 0, \tag{C.9a}$$

with

$$a_1 = -\Lambda_{1,1} - \Lambda_{2,2} - \Lambda_{3,3}, \tag{C.9b}$$

$$a_2 = \Lambda_{1,1}\Lambda_{2,2} + \Lambda_{1,1}\Lambda_{3,3} + \Lambda_{2,2}\Lambda_{3,3} - \Lambda_{1,3}^2 - \Lambda_{2,3}^2 - \Lambda_{1,2}^2, \tag{C.9c}$$

$$a_3 = \Lambda_{2,3}^2\Lambda_{1,1} + \Lambda_{1,3}^2\Lambda_{2,2} + \Lambda_{1,2}^2\Lambda_{3,3} - \Lambda_{1,1}\Lambda_{2,2}\Lambda_{3,3} - 2\Lambda_{1,2}\Lambda_{2,3}\Lambda_{1,3}. \tag{C.9d}$$

The roots of the cubic characteristic polynomial can be solved by first substituting $\kappa = \gamma - \frac{a_1}{3}$ to eliminate the quadratic term (Korn and Korn, 1968)

$$\left(\gamma - \frac{a_1}{3}\right)^3 + a_1\left(\gamma - \frac{a_1}{3}\right)^2 + b\left(\gamma - \frac{a_1}{3}\right) + a_3 = 0, \tag{C.10a}$$

$$\gamma^3 + \left(-\frac{a_1^2}{3} + a_2\right)\gamma + \frac{2a_1^3}{27} - \frac{a_1 a_2}{3} + a_3 = 0, \tag{C.10b}$$

$$\gamma^3 + d\gamma + q = 0, \tag{C.10c}$$

with

$$d = -\frac{a_1^2}{3} + a_2, \qquad q = \frac{2a_1^3}{27} - \frac{a_1 a_2}{3} + a_3. \tag{C.10d}$$

Because the matrix Λ is symmetric, it can be shown that the coefficient d is negative

$$d = -\frac{a_1^2}{3} + a_2 < 0, \tag{C.11a}$$

$$-a_1^2 + 3a_2 < 0. \tag{C.11b}$$

Substitution of equations C.9b and C.9c into equation C.11b yields

$$(\Lambda_{1,1} - \Lambda_{2,2})^2 + (\Lambda_{1,1} - \Lambda_{3,3})^2 + (\Lambda_{2,2} - \Lambda_{3,3})^2 + 6\left(\Lambda_{2,3}^2 + \Lambda_{1,3}^2 + \Lambda_{1,2}^2\right) \geq 0. \tag{C.12}$$

Obviously, equation C.12 is satisfied for arbitrary elements of Λ. Accordingly, the roots of the cubic characteristic polynomial are real if the following relation is non-positive (Tsvankin, 2012)

$$Q = \frac{d^3}{27} + \frac{q^2}{4} \leq 0. \tag{C.13}$$

Because the characteristic polynomial is of degree three, there exists three roots which can be computed by (Korn and Korn, 1968)

$$\gamma_{1,2,3} = 2\sqrt{\frac{-d}{3}}\cos\left(\frac{\beta}{3} + k\frac{2\pi}{3}\right), \qquad k = 0, 1, 2, \tag{C.14}$$

with

$$\beta = \arccos\left(-\frac{q}{2\sqrt{\left(\frac{-d}{3}\right)^3}}\right), \qquad 0 \leq \beta \leq \pi. \tag{C.15}$$

Finally, the substitution is reversed, and the three roots of the characteristic polynomial are computed using

$$\kappa_{1,2,3} = \gamma_{1,2,3} - \frac{a_1}{3}. \tag{C.16}$$

The root with the largest absolute value corresponds to the qP-wave, whereas the other two roots correspond to the qSV- and SH-wave. The latter two roots are equal if $Q = 0$ (Eq. C.13), e.g., for isotropic media or pure modes in anisotropic media, and are distinct if $Q < 0$ (Tsvankin, 2012).

C.2. Cylindrical coordinates

The *Christoffel* equation in cylindrical coordinates can be expressed in the *Laplace*-space-domain (r, θ, z, s) according to equation 2.55 as

$$\left(\Lambda - \rho^s s^2 I\right) \begin{pmatrix} \check{v}_r \\ \check{v}_\theta \\ \check{v}_z \end{pmatrix} (r, \theta, z, s) = \mathbf{0}. \tag{C.17}$$

The components of the non-symmetric matrix Λ are defined by

$$\begin{aligned}
\Lambda_{1,1} = {} & \tilde{C}_{1,1}\partial_r^2 + \left[\tilde{C}_{1,1} + \left(\partial_\theta \tilde{C}_{1,6}\right)\right]\frac{1}{r}\partial_r + \left[\left(\partial_\theta \tilde{C}_{2,6}\right) - \tilde{C}_{2,2}\right]\frac{1}{r^2} + \tilde{C}_{6,6}\frac{1}{r^2}\partial_\theta^2 \\
& + \left(\partial_\theta \tilde{C}_{6,6}\right)\frac{1}{r^2}\partial_\theta + \tilde{C}_{5,5}\partial_z^2 + \left[\tilde{C}_{1,5} + \left(\partial_\theta \tilde{C}_{5,6}\right)\right]\frac{1}{r}\partial_z \\
& + 2\left[\tilde{C}_{1,6}\frac{1}{r}\partial_r\partial_\theta + \tilde{C}_{1,5}\partial_r\partial_z + \tilde{C}_{5,6}\frac{1}{r}\partial_\theta\partial_z\right],
\end{aligned} \tag{C.18a}$$

$$\begin{aligned}
\Lambda_{1,2} = {} & \tilde{C}_{1,6}\partial_r^2 + \left[\left(\partial_\theta \tilde{C}_{6,6}\right) - \tilde{C}_{2,6}\right]\frac{1}{r}\partial_r + \left[\tilde{C}_{2,6} - \left(\partial_\theta \tilde{C}_{6,6}\right)\right]\frac{1}{r^2} + \tilde{C}_{2,6}\frac{1}{r^2}\partial_\theta^2 \\
& + \left[\left(\partial_\theta \tilde{C}_{2,6}\right) - \tilde{C}_{2,2} - \tilde{C}_{6,6}\right]\frac{1}{r^2}\partial_\theta + \tilde{C}_{4,5}\partial_z^2 + \left[\tilde{C}_{1,4} - \tilde{C}_{2,4} - \tilde{C}_{5,6} + \left(\partial_\theta \tilde{C}_{4,6}\right)\right]\frac{1}{r}\partial_z \\
& + \left[\tilde{C}_{1,2} + \tilde{C}_{6,6}\right]\frac{1}{r}\partial_r\partial_\theta + \left[\tilde{C}_{1,4} + \tilde{C}_{5,6}\right]\partial_r\partial_z + \left[\tilde{C}_{2,5} + \tilde{C}_{4,6}\right]\frac{1}{r}\partial_\theta\partial_z,
\end{aligned} \tag{C.18b}$$

$$\begin{aligned}
\Lambda_{1,3} = {} & \tilde{C}_{1,5}\partial_r^2 + \left[\left(\partial_\theta \tilde{C}_{5,6}\right) + \tilde{C}_{1,5} - \tilde{C}_{2,5}\right]\frac{1}{r}\partial_r + \tilde{C}_{4,6}\frac{1}{r^2}\partial_\theta^2 \\
& + \left[\left(\partial_\theta \tilde{C}_{4,6}\right) - \tilde{C}_{2,4}\right]\frac{1}{r^2}\partial_\theta + \tilde{C}_{3,5}\partial_z^2 + \left[\tilde{C}_{1,3} - \tilde{C}_{2,3} + \left(\partial_\theta \tilde{C}_{3,6}\right)\right]\frac{1}{r}\partial_z \\
& + \left[\tilde{C}_{1,4} + \tilde{C}_{5,6}\right]\frac{1}{r}\partial_r\partial_\theta + \left[\tilde{C}_{1,3} + \tilde{C}_{5,5}\right]\partial_r\partial_z + \left[\tilde{C}_{3,6} + \tilde{C}_{4,5}\right]\frac{1}{r}\partial_\theta\partial_z,
\end{aligned} \tag{C.18c}$$

$$\begin{aligned}
\Lambda_{2,1} = {} & \tilde{C}_{1,6}\partial_r^2 + \left[\left(\partial_\theta \tilde{C}_{1,2}\right) + \tilde{C}_{2,6} + 2\tilde{C}_{1,6}\right]\frac{1}{r}\partial_r + \left[\left(\partial_\theta \tilde{C}_{2,2}\right) + \tilde{C}_{2,6}\right]\frac{1}{r^2} + \tilde{C}_{2,6}\frac{1}{r^2}\partial_\theta^2 \\
& + \left[\left(\partial_\theta \tilde{C}_{2,6}\right) + \tilde{C}_{2,2} + \tilde{C}_{6,6}\right]\frac{1}{r^2}\partial_\theta + \tilde{C}_{4,5}\partial_z^2 + \left[\left(\partial_\theta \tilde{C}_{2,5}\right) + \tilde{C}_{2,4} + 2\tilde{C}_{5,6}\right]\frac{1}{r}\partial_z \\
& + \left[\tilde{C}_{1,2} + \tilde{C}_{6,6}\right]\frac{1}{r}\partial_r\partial_\theta + \left[\tilde{C}_{1,4} + \tilde{C}_{5,6}\right]\partial_r\partial_z + \left[\tilde{C}_{2,5} + \tilde{C}_{4,6}\right]\frac{1}{r}\partial_\theta\partial_z,
\end{aligned} \tag{C.18d}$$

(C.18e)

$$\Lambda_{2,2} = \tilde{C}_{6,6}\partial_r^2 + \left[\tilde{C}_{6,6} + \left(\partial_\theta \tilde{C}_{2,6}\right)\right]\frac{1}{r}\partial_r + \left[-\left(\partial_\theta \tilde{C}_{2,6}\right) - \tilde{C}_{6,6}\right]\frac{1}{r^2} + \tilde{C}_{2,2}\frac{1}{r^2}\partial_\theta^2 + \left(\partial_\theta \tilde{C}_{2,2}\right)\frac{1}{r^2}\partial_\theta + \tilde{C}_{4,4}\partial_z^2 + \left[\tilde{C}_{4,6} + \left(\partial_\theta \tilde{C}_{2,4}\right)\right]\frac{1}{r}\partial_z + 2\left[\tilde{C}_{2,6}\frac{1}{r}\partial_r\partial_\theta + \tilde{C}_{4,6}\partial_r\partial_z + \tilde{C}_{2,4}\frac{1}{r}\partial_\theta\partial_z\right], \tag{C.18f}$$

$$\Lambda_{2,3} = \tilde{C}_{5,6}\partial_r^2 + \left[\left(\partial_\theta \tilde{C}_{2,5}\right) + 2\tilde{C}_{5,6}\right]\frac{1}{r}\partial_r + \tilde{C}_{2,4}\frac{1}{r^2}\partial_\theta^2 + \left[\left(\partial_\theta \tilde{C}_{2,4}\right) + \tilde{C}_{4,6}\right]\frac{1}{r^2}\partial_\theta + \tilde{C}_{3,4}\partial_z^2 + \left[2\tilde{C}_{3,6} + \left(\partial_\theta \tilde{C}_{2,3}\right)\right]\frac{1}{r}\partial_z + \left[\tilde{C}_{2,5} + \tilde{C}_{4,6}\right]\frac{1}{r}\partial_r\partial_\theta + \left[\tilde{C}_{3,6} + \tilde{C}_{4,5}\right]\partial_r\partial_z + \left[\tilde{C}_{2,3} + \tilde{C}_{4,4}\right]\frac{1}{r}\partial_\theta\partial_z, \tag{C.18g}$$

$$\Lambda_{3,1} = \tilde{C}_{1,5}\partial_r^2 + \left[\left(\partial_\theta \tilde{C}_{1,4}\right) + \tilde{C}_{1,5} + \tilde{C}_{2,5}\right]\frac{1}{r}\partial_r + \left(\partial_\theta \tilde{C}_{2,4}\right)\frac{1}{r^2} + \tilde{C}_{4,6}\frac{1}{r^2}\partial_\theta^2 + \left[\left(\partial_\theta \tilde{C}_{4,6}\right) + \tilde{C}_{2,4}\right]\frac{1}{r^2}\partial_\theta + \tilde{C}_{3,5}\partial_z^2 + \left[\tilde{C}_{2,3} + \tilde{C}_{5,5} + \left(\partial_\theta \tilde{C}_{4,5}\right)\right]\frac{1}{r}\partial_z + \left[\tilde{C}_{1,4} + \tilde{C}_{5,6}\right]\frac{1}{r}\partial_r\partial_\theta + \left[\tilde{C}_{1,3} + \tilde{C}_{5,5}\right]\partial_r\partial_z + \left[\tilde{C}_{3,6} + \tilde{C}_{4,5}\right]\frac{1}{r}\partial_\theta\partial_z, \tag{C.18h}$$

$$\Lambda_{3,2} = \tilde{C}_{5,6}\partial_r^2 + \left(\partial_\theta \tilde{C}_{4,6}\right)\frac{1}{r}\partial_r - \left(\partial_\theta \tilde{C}_{4,6}\right)\frac{1}{r^2} + \tilde{C}_{2,4}\frac{1}{r^2}\partial_\theta^2 + \left[\left(\partial_\theta \tilde{C}_{2,4}\right) - \tilde{C}_{4,6}\right]\frac{1}{r^2}\partial_\theta + \tilde{C}_{3,4}\partial_z^2 + \left[\tilde{C}_{4,5} - \tilde{C}_{3,6} + \left(\partial_\theta \tilde{C}_{4,4}\right)\right]\frac{1}{r}\partial_z + \left[\tilde{C}_{2,5} + \tilde{C}_{4,6}\right]\frac{1}{r}\partial_r\partial_\theta + \left[\tilde{C}_{3,6} + \tilde{C}_{4,5}\right]\partial_r\partial_z + \left[\tilde{C}_{2,3} + \tilde{C}_{4,4}\right]\frac{1}{r}\partial_\theta\partial_z, \tag{C.18i}$$

$$\Lambda_{3,3} = \tilde{C}_{5,5}\partial_r^2 + \left[\tilde{C}_{5,5} + \left(\partial_\theta \tilde{C}_{4,5}\right)\right]\frac{1}{r}\partial_r + \tilde{C}_{4,4}\frac{1}{r^2}\partial_\theta^2 + \left(\partial_\theta \tilde{C}_{4,4}\right)\frac{1}{r^2}\partial_\theta + \tilde{C}_{3,3}\partial_z^2 + \left[\tilde{C}_{3,5} + \left(\partial_\theta \tilde{C}_{3,4}\right)\right]\frac{1}{r}\partial_z + 2\left[\tilde{C}_{4,5}\frac{1}{r}\partial_r\partial_\theta + \tilde{C}_{3,5}\partial_r\partial_z + \tilde{C}_{3,4}\frac{1}{r}\partial_\theta\partial_z\right]. \tag{C.18j}$$

The stiffness tensor elements in cylindrical coordinates are defined in Appendix B.2.

Special Case: VTI

Since the stiffness tensor characterizing an anisotropic medium exhibiting VTI symmetry is azimuthal invariant ($\tilde{C}(\theta) = C$), the components of the matrix Λ in cylindrical coordinates reduces to

$$\Lambda_{1,1} = C_{1,1}\left(\partial_r^2 + \frac{1}{r}\partial_r - \frac{1}{r^2}\right) + C_{6,6}\frac{1}{r^2}\partial_\theta^2 + C_{4,4}\partial_z^2, \tag{C.19a}$$

$$\Lambda_{1,2} = \left(C_{1,1} - C_{6,6}\right)\frac{1}{r}\partial_r\partial_\theta - \left(C_{1,1} + C_{6,6}\right)\frac{1}{r^2}\partial_\theta, \tag{C.19b}$$

$$\Lambda_{1,3} = (C_{1,3} + C_{4,4})\,\partial_r\partial_z, \tag{C.19c}$$

$$\Lambda_{2,1} = (C_{1,1} - C_{6,6})\,\frac{1}{r}\partial_r\partial_\theta + (C_{1,1} + C_{6,6})\,\frac{1}{r^2}\partial_\theta, \tag{C.19d}$$

$$\Lambda_{2,2} = C_{6,6}\left(\partial_r^2 + \frac{1}{r}\partial_r - \frac{1}{r^2}\right) + C_{1,1}\frac{1}{r^2}\partial_\theta^2 + C_{4,4}\partial_z^2, \tag{C.19e}$$

$$\Lambda_{2,3} = (C_{1,3} + C_{4,4})\,\frac{1}{r}\partial_\theta\partial_z, \tag{C.19f}$$

$$\Lambda_{3,1} = (C_{1,3} + C_{4,4})\left(\partial_r\partial_z + \frac{1}{r}\partial_z\right), \tag{C.19g}$$

$$\Lambda_{3,2} = (C_{1,3} + C_{4,4})\,\frac{1}{r}\partial_\theta\partial_z, \tag{C.19h}$$

$$\Lambda_{3,3} = C_{4,4}\left(\partial_r^2 + \frac{1}{r}\partial_r + \frac{1}{r^2}\partial_\theta^2\right) + C_{3,3}\partial_z^2. \tag{C.19i}$$

General triclinic case

In contrast, for anisotropic media exhibiting symmetries lower than VTI, the stiffness tensor elements are not azimuthal invariant and depend on θ. Hence, these components in cylindrical coordinates (Eq. B.2) have to be substituted into equation C.18 involving azimuthal differentiation. The elements of the *Christoffel* equation for the most general triclinic symmetry are defined as

$$\begin{aligned}
\Lambda_{1,1} = \cos^4\theta\Bigg[&C_{1,1}\partial_r^2 + (2C_{1,6}\partial_\theta + C_{1,2} + 2C_{6,6})\frac{1}{r}\partial_r \\
&+ \left(C_{6,6}\partial_\theta^2 - 2(C_{1,6} - C_{2,6})\partial_\theta - (C_{1,2} + 2C_{6,6})\right)\frac{1}{r^2}\Bigg] \\
+ \sin\theta\cos^3\theta\Bigg[&4C_{1,6}\partial_r^2 - ((2C_{1,1} - 2C_{1,2} - 4C_{6,6})\partial_\theta + 6(C_{1,6} - C_{2,6}))\frac{1}{r}\partial_r \\
&+ \left(-2(C_{1,6} - C_{2,6})\partial_\theta^2 + (2C_{1,1} + 2C_{2,2} - 4C_{1,2} - 8C_{6,6})\partial_\theta + 6(C_{1,6} - C_{2,6})\right)\frac{1}{r^2}\Bigg] \\
+ \sin^2\theta\cos^2\theta\Bigg[&(2C_{1,2} + 4C_{6,6})\partial_r^2 \\
&+ (-6(C_{1,6} - C_{2,6})\partial_\theta + 3C_{1,1} + 3C_{2,2} - 4C_{1,2} - 8C_{6,6})\frac{1}{r}\partial_r \\
&+ \big((C_{1,1} + C_{2,2} - 2C_{1,2} - 2C_{6,6})\partial_\theta^2 + 12(C_{1,6} - C_{2,6})\partial_\theta \\
&-(3C_{1,1} + 3C_{2,2} - 4C_{1,2} - 8C_{6,6})\big)\frac{1}{r^2}\Bigg] \\
+ \sin^3\theta\cos\theta\Bigg[&4C_{2,6}\partial_r^2 + ((2C_{2,2} - 2C_{1,2} - 4C_{6,6})\partial_\theta + 6(C_{1,6} - C_{2,6}))\frac{1}{r}\partial_r \\
&+ \left(2(C_{1,6} - C_{2,6})\partial_\theta^2 - (2C_{1,1} + 2C_{2,2} - 4C_{1,2} - 8C_{6,6})\partial_\theta - 6(C_{1,6} - C_{2,6})\right)\frac{1}{r^2}\Bigg] \\
+ \sin^4\theta\Bigg[&C_{2,2}\partial_r^2 + (-2C_{2,6}\partial_\theta + C_{1,2} + 2C_{6,6})\frac{1}{r}\partial_r \\
&+ \left(C_{6,6}\partial_\theta^2 - 2(C_{1,6} - C_{2,6})\partial_\theta - (C_{1,2} + 2C_{6,6})\right)\frac{1}{r^2}\Bigg]
\end{aligned}$$

$$
\begin{aligned}
&+\cos^3\theta\left[2C_{1,5}\partial_r\partial_z+(2C_{5,6}\partial_\theta+C_{4,6}+C_{2,5})\,\frac{1}{r}\partial_z\right]\\
&+\sin\theta\cos^2\theta\Bigg[(2C_{1,4}+4C_{5,6})\partial_r\partial_z\\
&\qquad-((2C_{1,5}-2C_{2,5}-2C_{4,6})\partial_\theta+(C_{1,4}-2C_{2,4}+3C_{5,6}))\,\frac{1}{r}\partial_z\Bigg]\\
&+\sin^2\theta\cos\theta\Bigg[(2C_{2,5}+4C_{4,6})\partial_r\partial_z\\
&\qquad-((2C_{1,4}-2C_{2,4}+2C_{5,6})\partial_\theta-(2C_{1,5}-C_{2,5}-3C_{4,6}))\,\frac{1}{r}\partial_z\Bigg]\\
&+\sin^3\theta\left[2C_{2,4}\partial_r\partial_z+(-2C_{4,6}\partial_\theta+(C_{1,4}+C_{5,6}))\,\frac{1}{r}\partial_z\right]\\
&+C_{5,5}\partial_z^2\cos^2\theta+2C_{4,5}\partial_z^2\sin\theta\cos\theta+C_{4,4}\partial_z^2\sin^2\theta,
\end{aligned}
\tag{C.20a}
$$

$$
\begin{aligned}
\Lambda_{1,2}=&\cos^4\theta\Bigg[C_{1,6}\partial_r^2+((C_{1,2}+C_{6,6})\partial_\theta-(2C_{1,6}-C_{2,6}))\,\frac{1}{r}\partial_r\\
&\qquad+\left(C_{2,6}\partial_\theta^2-(C_{1,2}+3C_{6,6})\partial_\theta+(2C_{1,6}-C_{2,6})\right)\frac{1}{r^2}\Bigg]\\
&+\cos^3\theta\sin\theta\Bigg[-(C_{1,1}-C_{1,2}-2C_{6,6})\partial_r^2\\
&\qquad+(-4(C_{1,6}-C_{2,6})\partial_\theta+(2C_{1,1}+C_{2,2}-3C_{1,2}-6C_{6,6}))\,\frac{1}{r}\partial_r\\
&\qquad+\left((C_{2,2}-C_{1,2}-2C_{6,6})\partial_\theta^2+8(C_{1,6}-C_{2,6})\partial_\theta-(2C_{1,1}+C_{2,2}-3C_{1,2}-6C_{6,6})\right)\frac{1}{r^2}\Bigg]\\
&+\cos^2\theta\sin^2\theta\Bigg[-3(C_{1,6}-C_{2,6})\partial_r^2\\
&\qquad+((2C_{1,1}+2C_{2,2}-2C_{1,2}-6C_{6,6})\partial_\theta+9(C_{1,6}-C_{2,6}))\,\frac{1}{r}\partial_r\\
&\qquad+\left(3(C_{1,6}-C_{2,6})\partial_\theta^2-(4C_{1,1}+4C_{2,2}-6C_{1,2}-10C_{6,6})\partial_\theta-9(C_{1,6}-C_{2,6})\right)\frac{1}{r^2}\Bigg]\\
&+\sin^3\theta\cos\theta\Bigg[(C_{2,2}-C_{1,2}-2C_{6,6})\partial_r^2\\
&\qquad+(4(C_{1,6}-C_{2,6})\partial_\theta-(C_{1,1}+2C_{2,2}-3C_{1,2}-6C_{6,6}))\,\frac{1}{r}\partial_r\\
&\qquad+\left(-(C_{1,1}-C_{1,2}-2C_{6,6})\partial_\theta^2-8(C_{1,6}-C_{2,6})\partial_\theta\right.\\
&\qquad\left.+(C_{1,1}+2C_{2,2}-3C_{1,2}-6C_{6,6})\right)\frac{1}{r^2}\Bigg]\\
&+\sin^4\theta\Bigg[-C_{2,6}\partial_r^2+((C_{1,2}+C_{6,6})\partial_\theta-(C_{1,6}-2C_{2,6}))\,\frac{1}{r}\partial_r\\
&\qquad+\left(-C_{1,6}\partial_\theta^2-(C_{1,2}+3C_{6,6})\partial_\theta+(C_{1,6}-2C_{2,6})\right)\frac{1}{r^2}\Bigg]\\
&+\cos^3\theta\left[(C_{1,4}+C_{5,6})\partial_r\partial_z+((C_{2,5}+C_{4,6})\partial_\theta-2C_{5,6})\,\frac{1}{r}\partial_z\right]\\
&+\sin\theta\cos^2\theta\Bigg[(C_{2,5}-2C_{1,5}+3C_{4,6})\partial_r\partial_z
\end{aligned}
$$

$$
\begin{aligned}
&\quad + ((2C_{2,4} - C_{1,4} - 3C_{5,6})\partial_\theta + (2C_{1,5} - 2C_{2,5} - 2C_{4,6}))\,\frac{1}{r}\partial_z\Big] \\
&+ \sin^2\theta\cos\theta\Big[(2C_{2,4} - C_{1,4} - 3C_{5,6})\partial_r\partial_z \\
&\quad + ((2C_{1,5} - C_{2,5} - 3C_{4,6})\partial_\theta + (2C_{1,4} - 2C_{2,4} + 2C_{5,6}))\,\frac{1}{r}\partial_z\Big] \\
&+ \sin^3\theta\Big[- (C_{2,5} + C_{4,6})\partial_r\partial_z + ((C_{1,4} + C_{5,6})\partial_\theta + 2C_{4,6})\,\frac{1}{r}\partial_z\Big] \\
&+ C_{4,5}\partial_z^2\cos^2\theta + (C_{4,4} - C_{5,5})\partial_z^2\sin\theta\cos\theta - C_{4,5}\partial_z^2\sin^2\theta,
\end{aligned}
\tag{C.20b}
$$

$$
\begin{aligned}
\Lambda_{1,3} &= \cos^3\theta\Big[C_{1,5}\partial_r^2 + ((C_{1,4} + C_{5,6})\partial_\theta + C_{4,6})\,\frac{1}{r}\partial_r + \big(C_{4,6}\partial_\theta^2 - (C_{1,4} + C_{5,6})\partial_\theta\big)\,\frac{1}{r^2}\Big] \\
&\quad + \sin\theta\cos^2\theta\Big[(C_{1,4} + 2C_{5,6})\partial_r^2 - ((2C_{1,5} - C_{2,5} - 3C_{4,6})\partial_\theta + (C_{1,4} - C_{2,4} + C_{5,6}))\,\frac{1}{r}\partial_r \\
&\qquad + \big(-(C_{1,4} - C_{2,4} + C_{5,6})\partial_\theta^2 + (2C_{1,5} - C_{2,5} - 3C_{4,6})\partial_\theta\big)\,\frac{1}{r^2}\Big] \\
&\quad + \sin^2\theta\cos\theta\Big[(C_{2,5} + 2C_{4,6})\partial_r^2 - ((C_{1,4} - 2C_{2,4} + 3C_{5,6})\partial_\theta - (C_{1,5} - C_{2,5} - C_{4,6}))\,\frac{1}{r}\partial_r \\
&\qquad + \big((C_{1,5} - C_{2,5} - C_{4,6})\partial_\theta^2 + (C_{1,4} - 2C_{2,4} + 3C_{5,6})\partial_\theta\big)\,\frac{1}{r^2}\Big] \\
&\quad + \sin^3\theta\Big[C_{2,4}\partial_r^2 - ((C_{2,5} + C_{4,6})\partial_\theta - C_{5,6})\,\frac{1}{r}\partial_r + \big(C_{5,6}\partial_\theta^2 + (C_{2,5} + C_{4,6})\partial_\theta\big)\,\frac{1}{r^2}\Big] \\
&\quad + \cos^2\theta\Big[(C_{1,3} + C_{5,5})\partial_r\partial_z + (C_{3,6} + C_{4,5})\frac{1}{r}\partial_\theta\partial_z\Big] \\
&\quad + \sin\theta\cos\theta\Big[2(C_{3,6} + C_{4,5})\partial_r\partial_z - (C_{1,3} - C_{2,3} - C_{4,4} + C_{5,5})\frac{1}{r}\partial_\theta\partial_z\Big] \\
&\quad + \sin^2\theta\Big[(C_{2,3} + C_{4,4})\partial_r\partial_z - (C_{3,6} + C_{4,5})\frac{1}{r}\partial_\theta\partial_z\Big] \\
&\quad + C_{3,5}\partial_z^2\cos\theta + C_{3,4}\partial_z^2\sin\theta,
\end{aligned}
\tag{C.20c}
$$

$$
\begin{aligned}
\Lambda_{2,1} &= \cos^4\theta\Big[C_{1,6}\partial_r^2 + ((C_{1,2} + C_{6,6})\partial_\theta + 3C_{2,6})\,\frac{1}{r}\partial_r \\
&\qquad + \big(C_{2,6}\partial_\theta^2 + (2C_{2,2} - C_{1,2} - C_{6,6})\partial_\theta - 3C_{2,6}\big)\,\frac{1}{r^2}\Big] \\
&\quad + \sin\theta\cos^3\theta\Big[- (C_{1,1} - C_{1,2} - 2C_{6,6})\partial_r^2 \\
&\qquad + (-4(C_{1,6} - C_{2,6})\partial_\theta + (3C_{2,2} - 3C_{1,2} - 6C_{6,6}))\,\frac{1}{r}\partial_r \\
&\qquad + \big((C_{2,2} - C_{1,2} - 2C_{6,6})\partial_\theta^2 + (4C_{1,6} - 12C_{2,6})\partial_\theta - (3C_{2,2} - 3C_{1,2} - 6C_{6,6})\big)\,\frac{1}{r^2}\Big] \\
&\quad + \sin^2\theta\cos^2\theta\Big[- 3(C_{1,6} - C_{2,6})\partial_r^2
\end{aligned}
$$

$$
\begin{aligned}
&\quad + \left((2C_{1,1} + 2C_{2,2} - 2C_{1,2} - 6C_{6,6})\partial_\theta + 9(C_{1,6} - C_{2,6})\right)\frac{1}{r}\partial_r \\
&\quad + \left(3(C_{1,6} - C_{2,6})\partial_\theta^2 - (2C_{1,1} + 2C_{2,2} - 6C_{1,2} - 14C_{6,6})\partial_\theta - 9(C_{1,6} - C_{2,6})\right)\frac{1}{r^2}\Big] \\
&+ \sin^3\theta\cos\theta\Big[(C_{2,2} - C_{1,2} - 2C_{6,6})\partial_r^2 \\
&\quad + \left(4(C_{1,6} - C_{2,6})\partial_\theta - (3C_{1,1} - 3C_{1,2} - 6C_{6,6})\right)\frac{1}{r}\partial_r \\
&\quad + \left(-(C_{1,1} - C_{1,2} - 2C_{6,6})\partial_\theta^2 - (12C_{1,6} - 4C_{2,6})\partial_\theta + (3C_{1,1} - 3C_{1,2} - 6C_{6,6})\right)\frac{1}{r^2}\Big] \\
&+ \sin^4\theta\Big[- C_{2,6}\partial_r^2 + \left((C_{1,2} + C_{6,6})\partial_\theta - 3C_{1,6}\right)\frac{1}{r}\partial_r \\
&\quad + \left(-C_{1,6}\partial_\theta^2 + (2C_{1,1} - C_{1,2} - C_{6,6})\partial_\theta + 3C_{1,6}\right)\frac{1}{r^2}\Big] \\
&+ \cos^3\theta\Big[(C_{1,4} + C_{5,6})\partial_r\partial_z + \left((C_{2,5} + C_{4,6})\partial_\theta + 2C_{2,4}\right)\frac{1}{r}\partial_z\Big] \\
&+ \sin\theta\cos^2\theta\Big[(C_{2,5} - 2C_{1,5} + 3C_{4,6})\partial_r\partial_z \\
&\quad + \left((2C_{2,4} - C_{1,4} - 3C_{5,6})\partial_\theta - (2C_{2,5} + 4C_{4,6})\right)\frac{1}{r}\partial_z\Big] \\
&+ \sin^2\theta\cos\theta\Big[(2C_{2,4} - C_{1,4} - 3C_{5,6})\partial_r\partial_z \\
&\quad + \left((2C_{1,5} - C_{2,5} - 3C_{4,6})\partial_\theta + (2C_{1,4} + 4C_{5,6})\right)\frac{1}{r}\partial_z\Big] \\
&+ \sin^3\theta\Big[- (C_{2,5} + C_{4,6})\partial_r\partial_z + \left((C_{1,4} + C_{5,6})\partial_\theta - 2C_{1,5}\right)\frac{1}{r}\partial_z\Big] \\
&+ C_{4,5}\partial_z^2\cos^2\theta + (C_{4,4} - C_{5,5})\partial_z^2\sin\theta\cos\theta - C_{4,5}\partial_z^2\sin^2\theta, \qquad \text{(C.20d)}
\end{aligned}
$$

$$
\begin{aligned}
\Lambda_{2,2} = &\cos^4\theta\Big[C_{6,6}\partial_r^2 + \left(2C_{2,6}\partial_\theta + (C_{2,2} - C_{1,2} - C_{6,6})\right)\frac{1}{r}\partial_r \\
&\quad + \left(C_{2,2}\partial_\theta^2 - 4C_{2,6}\partial_\theta - (C_{2,2} - C_{1,2} - C_{6,6})\right)\frac{1}{r^2}\Big] \\
&+ \sin\theta\cos^3\theta\Big[2(C_{2,6} - C_{1,6})\partial_r^2 + \left((2C_{2,2} - 2C_{1,2} - 4C_{6,6})\partial_\theta + (4C_{1,6} - 8C_{2,6})\right)\frac{1}{r}\partial_r \\
&\quad + \left(-4C_{2,6}\partial_\theta^2 - (4C_{2,2} - 4C_{1,2} - 8C_{6,6})\partial_\theta - (4C_{1,6} - 8C_{2,6})\right)\frac{1}{r^2}\Big] \\
&+ \sin^2\theta\cos^2\theta\Big[(C_{1,1} + C_{2,2} - 2C_{1,2} - 2C_{6,6})\partial_r^2 \\
&\quad + \left(6(C_{1,6} - C_{2,6})\partial_\theta - (2C_{1,1} + 2C_{2,2} - 4C_{1,2} - 10C_{6,6})\right)\frac{1}{r}\partial_r \\
&\quad + \left((2C_{1,2} + 4C_{6,6})\partial_\theta^2 - 12(C_{1,6} - C_{2,6})\partial_\theta + (2C_{1,1} + 2C_{2,2} - 4C_{1,2} - 10C_{6,6})\right)\frac{1}{r^2}\Big] \\
&+ \sin^3\theta\cos\theta\Big[2(C_{1,6} - C_{2,6})\partial_r^2 - \left((2C_{1,1} - 2C_{1,2} - 4C_{6,6})\partial_\theta + (8C_{1,6} - 4C_{2,6})\right)\frac{1}{r}\partial_r
\end{aligned}
$$

$$
\begin{aligned}
&\quad + \left(-4C_{1,6}\partial_\theta^2 + (4C_{1,1} - 4C_{1,2} - 8C_{6,6})\partial_\theta + (8C_{1,6} - 4C_{2,6})\right)\frac{1}{r^2}\Bigg] \\
&+ \sin^4\theta\Bigg[C_{6,6}\partial_r^2 + (-2C_{1,6}\partial_\theta + C_{1,1} - C_{1,2} - C_{6,6})\frac{1}{r}\partial_r \\
&\quad + \left(C_{1,1}\partial_\theta^2 + 4C_{1,6}\partial_\theta - (C_{1,1} - C_{1,2} - C_{6,6})\right)\frac{1}{r^2}\Bigg] \\
&+ \cos^3\theta\left[2C_{4,6}\partial_r\partial_z + (2C_{2,4}\partial_\theta - (C_{2,5} + C_{4,6}))\frac{1}{r}\partial_z\right] \\
&+ \sin\theta\cos^2\theta\Bigg[(2C_{2,4} - 2C_{1,4} - 2C_{5,6})\partial_r\partial_z \\
&\quad + (-(2C_{2,5} + 4C_{4,6})\partial_\theta + (C_{1,4} - 2C_{2,4} + 3C_{5,6}))\frac{1}{r}\partial_z\Bigg] \\
&+ \sin^2\theta\cos\theta\Bigg[(2C_{1,5} - 2C_{2,5} - 2C_{4,6})\partial_r\partial_z \\
&\quad + ((2C_{1,4} + 4C_{5,6})\partial_\theta + (C_{2,5} - 2C_{1,5} + 3C_{4,6}))\frac{1}{r}\partial_z\Bigg] \\
&+ \sin^3\theta\left[2C_{5,6}\partial_r\partial_z + (-2C_{1,5}\partial_\theta - (C_{1,4} + C_{5,6}))\frac{1}{r}\partial_z\right] \\
&+ C_{4,4}\partial_z^2\cos^2\theta - 2C_{4,5}\partial_z^2\sin\theta\cos\theta + C_{5,5}\partial_z^2\sin^2\theta, \qquad \text{(C.20e)}
\end{aligned}
$$

$$
\begin{aligned}
\Lambda_{2,3} &= \cos^3\theta\left[C_{5,6}\partial_r^2 + ((C_{2,5} + C_{4,6})\partial_\theta + C_{2,4})\frac{1}{r}\partial_r + \left(C_{2,4}\partial_\theta^2 - (C_{2,5} + C_{4,6})\partial_\theta\right)\frac{1}{r^2}\right] \\
&+ \sin\theta\cos^2\theta\Bigg[- (C_{1,5} - C_{2,5} - C_{4,6})\partial_r^2 - ((C_{1,4} - 2C_{2,4} + 3C_{5,6})\partial_\theta + (C_{2,5} + 2C_{4,6}))\frac{1}{r}\partial_r \\
&\quad + \left(-(C_{2,5} + 2C_{4,6})\partial_\theta^2 + (C_{1,4} - 2C_{2,4} + 3C_{5,6})\partial_\theta\right)\frac{1}{r^2}\Bigg] \\
&+ \sin^2\theta\cos\theta\Bigg[- (C_{1,4} - C_{2,4} + C_{5,6})\partial_r^2 + ((2C_{1,5} - C_{2,5} - 3C_{4,6})\partial_\theta + (C_{1,4} + 2C_{5,6}))\frac{1}{r}\partial_r \\
&\quad + \left((C_{1,4} + 2C_{5,6})\partial_\theta^2 - (2C_{1,5} - C_{2,5} - 3C_{4,6})\partial_\theta\right)\frac{1}{r^2}\Bigg] \\
&+ \sin^3\theta\Bigg[- C_{4,6}\partial_r^2 + ((C_{1,4} + C_{5,6})\partial_\theta - C_{1,5})\frac{1}{r}\partial_r - \left(C_{1,5}\partial_\theta^2 + (C_{1,4} + C_{5,6})\partial_\theta\right)\frac{1}{r^2}\Bigg] \\
&+ \cos^2\theta\left[(C_{3,6} + C_{4,5})\partial_r\partial_z + (C_{2,3} + C_{4,4})\frac{1}{r}\partial_\theta\partial_z\right] \\
&+ \sin\theta\cos\theta\Bigg[- (C_{1,3} - C_{2,3} - C_{4,4} + C_{5,5})\partial_r\partial_z - 2(C_{3,6} + C_{4,5})\frac{1}{r}\partial_\theta\partial_z\Bigg] \\
&+ \sin^2\theta\Bigg[- (C_{3,6} + C_{4,5})\partial_r\partial_z + (C_{1,3} + C_{5,5})\frac{1}{r}\partial_\theta\partial_z\Bigg] \\
&+ C_{3,4}\partial_z^2\cos\theta - C_{3,5}\partial_z^2\sin\theta, \qquad \text{(C.20f)}
\end{aligned}
$$

$$
\begin{aligned}
\Lambda_{3,1} = \cos^3\theta \Big[& C_{1,5}\partial_r^2 + \left((C_{1,4}+C_{5,6})\partial_\theta + (C_{2,5}+2C_{4,6})\right)\frac{1}{r}\partial_r \\
& + \left(C_{4,6}\partial_\theta^2 - (C_{1,4}-2C_{2,4}+C_{5,6})\partial_\theta - (C_{2,5}+2C_{4,6})\right)\frac{1}{r^2}\Big] \\
& + \sin\theta\cos^2\theta \Big[(C_{1,4}+2C_{5,6})\partial_r^2 - \left((2C_{1,5}-C_{2,5}-3C_{4,6})\partial_\theta + (2C_{1,4}-3C_{2,4}+4C_{5,6})\right)\frac{1}{r}\partial_r \\
& + \left(-(C_{1,4}-C_{2,4}+C_{5,6})\partial_\theta^2 + (2C_{1,5}-3C_{2,5}-7C_{4,6})\partial_\theta + (2C_{1,4}-3C_{2,4}+4C_{5,6})\right)\frac{1}{r^2}\Big] \\
& + \sin^2\theta\cos\theta \Big[(C_{2,5}+2C_{4,6})\partial_r^2 - \left((C_{1,4}-2C_{2,4}+3C_{5,6})\partial_\theta - (3C_{1,5}-2C_{2,5}-4C_{4,6})\right)\frac{1}{r}\partial_r \\
& + \left((C_{1,5}-C_{2,5}-C_{4,6})\partial_\theta^2 + (3C_{1,4}-2C_{2,4}+7C_{5,6})\partial_\theta - (3C_{1,5}-2C_{2,5}-4C_{4,6})\right)\frac{1}{r^2}\Big] \\
& + \sin^3\theta \Big[C_{2,4}\partial_r^2 - \left((C_{2,5}+C_{4,6})\partial_\theta - (C_{1,4}+2C_{5,6})\right)\frac{1}{r}\partial_r \\
& + \left(C_{5,6}\partial_\theta^2 - (2C_{1,5}-C_{2,5}-C_{4,6})\partial_\theta - (C_{1,4}+2C_{5,6})\right)\frac{1}{r^2}\Big] \\
& + \cos^2\theta \Big[(C_{1,3}+C_{5,5})\partial_r\partial_z + \left((C_{3,6}+C_{4,5})\partial_\theta + (C_{2,3}+C_{4,4})\right)\frac{1}{r}\partial_z\Big] \\
& + \sin\theta\cos\theta \Big[2(C_{3,6}+C_{4,5})\partial_r\partial_z - \left((C_{1,3}-C_{2,3}-C_{4,4}+C_{5,5})\partial_\theta + 2(C_{3,6}+C_{4,5})\right)\frac{1}{r}\partial_z\Big] \\
& + \sin^2\theta \Big[(C_{2,3}+C_{4,4})\partial_r\partial_z + \left(-(C_{3,6}+C_{4,5})\partial_\theta + (C_{1,3}+C_{5,5})\right)\frac{1}{r}\partial_z\Big] \\
& + C_{3,5}\partial_z^2\cos\theta + C_{3,4}\partial_z^2\sin\theta, \qquad \text{(C.20g)}
\end{aligned}
$$

$$
\begin{aligned}
\Lambda_{3,2} = \cos^3\theta \Big[& C_{5,6}\partial_r^2 + \left((C_{2,5}+C_{4,6})\partial_\theta - (C_{1,4}-C_{2,4}+C_{5,6})\right)\frac{1}{r}\partial_r \\
& + \left(C_{2,4}\partial_\theta^2 - (C_{2,5}+3C_{4,6})\partial_\theta + (C_{1,4}-C_{2,4}+C_{5,6})\right)\frac{1}{r^2}\Big] \\
& + \sin\theta\cos^2\theta \Big[- (C_{1,5}-C_{2,5}-C_{4,6})\partial_r^2 \\
& - \left((C_{1,4}-2C_{2,4}+3C_{5,6})\partial_\theta - (2C_{1,5}-2C_{2,5}-5C_{4,6})\right)\frac{1}{r}\partial_r \\
& + \left(-(C_{2,5}+2C_{4,6})\partial_\theta^2 + (3C_{1,4}-4C_{2,4}+5C_{5,6})\partial_\theta - (2C_{1,5}-2C_{2,5}-5C_{4,6})\right)\frac{1}{r^2}\Big] \\
& + \sin^2\theta\cos\theta \Big[- (C_{1,4}-C_{2,4}+C_{5,6})\partial_r^2 \\
& + \left((2C_{1,5}-C_{2,5}-3C_{4,6})\partial_\theta + (2C_{1,4}-2C_{2,4}+5C_{5,6})\right)\frac{1}{r}\partial_r \\
& + \left((C_{1,4}+2C_{5,6})\partial_\theta^2 - (4C_{1,5}-3C_{2,5}-5C_{4,6})\partial_\theta - (2C_{1,4}-2C_{2,4}+5C_{5,6})\right)\frac{1}{r^2}\Big] \\
& + \sin^3\theta \Big[- C_{4,6}\partial_r^2 + \left((C_{1,4}+C_{5,6})\partial_\theta - (C_{1,5}-C_{2,5}-C_{4,6})\right)\frac{1}{r}\partial_r
\end{aligned}
$$

$$
\begin{aligned}
&\quad - \left(C_{1,5}\partial_\theta^2 + (C_{1,4} + 3C_{5,6})\partial_\theta - (C_{1,5} - C_{2,5} - C_{4,6})\right)\frac{1}{r^2}\Bigg] \\
&+ \cos^2\theta\Bigg[(C_{3,6} + C_{4,5})\partial_r\partial_z + ((C_{2,3} + C_{4,4})\partial_\theta - (C_{3,6} + C_{4,5}))\,\frac{1}{r}\partial_z\Bigg] \\
&+ \sin\theta\cos\theta\Bigg[- (C_{1,3} - C_{2,3} - C_{4,4} + C_{5,5})\partial_r\partial_z \\
&\quad + (-2(C_{3,6} + C_{4,5})\partial_\theta + (C_{1,3} - C_{2,3} - C_{4,4} + C_{5,5}))\,\frac{1}{r}\partial_z\Bigg] \\
&+ \sin^2\theta\Bigg[- (C_{3,6} + C_{4,5})\partial_r\partial_z + ((C_{1,3} + C_{5,5})\partial_\theta + (C_{3,6} + C_{4,5}))\,\frac{1}{r}\partial_z\Bigg] \\
&+ C_{3,4}\partial_z^2\cos\theta - C_{3,5}\partial_z^2\sin\theta,
\end{aligned}
\tag{C.20h}
$$

$$
\begin{aligned}
\Lambda_{3,3} = {}& \cos^2\theta\left[C_{5,5}\partial_r^2 + (2C_{4,5}\partial_\theta + C_{4,4})\,\frac{1}{r}\partial_r + \left(C_{4,4}\partial_\theta^2 - 2C_{4,5}\partial_\theta\right)\frac{1}{r^2}\right] \\
&+ \sin\theta\cos\theta\Bigg[2C_{4,5}\partial_r^2 + (2(C_{4,4} - C_{5,5})\partial_\theta - 2C_{4,5})\,\frac{1}{r}\partial_r \\
&\quad + \left(-2C_{4,5}\partial_\theta^2 - 2(C_{4,4} - C_{5,5})\partial_\theta\right)\frac{1}{r^2}\Bigg] \\
&+ \sin^2\theta\left[C_{4,4}\partial_r^2 - (2C_{4,5}\partial_\theta - C_{5,5})\,\frac{1}{r}\partial_r + \left(C_{5,5}\partial_\theta^2 + 2C_{4,5}\partial_\theta\right)\frac{1}{r^2}\right] \\
&+ \cos\theta\left[2C_{3,5}\partial_r\partial_z + 2C_{3,4}\frac{1}{r}\partial_\theta\partial_z\right] \\
&+ \sin\theta\left[2C_{3,4}\partial_r\partial_z - 2C_{3,5}\frac{1}{r}\partial_\theta\partial_z\right] \\
&+ C_{3,3}\partial_z^2.
\end{aligned}
\tag{C.20i}
$$

Application of an azimuthal *Fourier* transform with respect to the azimuthal coordinate θ and a spatial *Fourier* transform with respect to the vertical z–coordinate yields the *Christoffel* equation in the (r, m, β_z, s)–domain

$$
\tilde{\Lambda}(r, m, \beta_z, s) = \mathbf{0}, \tag{C.21a}
$$

where the elements of the matrix $\tilde{\Lambda}$ are given in the following equations C.21b–C.21j. For clarity reasons, the $\pm$ sign is meant to sum over both signs, e.g., $\Lambda_{1,1} = \sum_{l=m-4}^{m+4}(...)\tilde{v}_r^l(r, \beta_z, s)$.

$$
\begin{aligned}
16\tilde{\Lambda}_{1,1} = {}& \left[C_{1,1} + C_{2,2} - 2C_{1,2} - 4C_{6,6} \pm 4\mathrm{i}\,(C_{1,6} - C_{2,6})\right] \\
&\quad \cdot \left[\partial_r^2 + (\pm 2m + 5)\frac{1}{r}\partial_r + (m^2 \pm 4m + 3)\frac{1}{r^2}\right]\tilde{v}_r^{m\pm 4} \\
&+ 4s\beta_z\left[(C_{1,5} - C_{2,5} - 2C_{4,6}) \pm \mathrm{i}\,(C_{1,4} - C_{2,4} + 2C_{5,6})\right]\left[\partial_r + (\pm m + 2)\frac{1}{r}\right]\tilde{v}_r^{m\mp 3} \\
&+ \Bigg(4\left[C_{1,1} - C_{2,2} \pm 2\mathrm{i}\,(C_{1,6} + C_{2,6})\right]\left[\partial_r^2 + (\pm m + 2)\frac{1}{r}\partial_r\right]
\end{aligned}
$$

$$
\begin{aligned}
&\quad + 4s^2\beta_z^2\left[C_{5,5} - C_{4,4} \pm 2\mathrm{i}C_{4,5}\right]\Big)\tilde{v}_r^{m\pm2} \\
&+ s\beta_z\Big(\Big[8\left[(C_{1,5}+C_{4,6}) \pm \mathrm{i}\left(C_{2,4}+C_{5,6}\right)\right] \\
&\quad \pm 4m\left[(C_{1,5}-C_{2,5}+2C_{4,6}) \pm \mathrm{i}\left(C_{1,4}-C_{2,4}-2C_{5,6}\right)\right]\Big]\frac{1}{r} \\
&\quad + 4\left[(3C_{1,5}+C_{2,5}+2C_{4,6}) \pm \mathrm{i}\left(C_{1,4}+3C_{2,4}+2C_{5,6}\right)\right]\partial_r\Big)\tilde{v}_r^{m\pm1} \\
&+ \Big(\left[6C_{1,1}+6C_{2,2}+4C_{1,2}+8C_{6,6}\right]\left[\partial_r^2 + \frac{1}{r}\partial_r - \frac{1}{r^2}\right] \\
&\quad - 2m^2\left[C_{1,1}+C_{2,2}-2C_{1,2}+4C_{6,6}\right]\frac{1}{r^2} + 8s^2\beta_z^2\left[C_{4,4}+C_{5,5}\right] - 16\rho^{\mathrm{s}}s^2\Big)\tilde{v}_r^m,
\end{aligned}
\tag{C.21b}
$$

$$
\begin{aligned}
16\tilde{\Lambda}_{1,2} &= \left[4\left(C_{1,6}-C_{2,6}\right) \mp \mathrm{i}\left(C_{1,1}+C_{2,2}-2C_{1,2}-4C_{6,6}\right)\right] \\
&\quad \cdot \left[\partial_r^2 + (\pm2m+5)\frac{1}{r}\partial_r + (m^2 \pm 4m + 3)\frac{1}{r^2}\right]\tilde{v}_\theta^{m\pm4} \\
&+ 4s\beta_z\left[(C_{1,4}-C_{2,4}+2C_{5,6}) \mp \mathrm{i}\left(C_{1,5}-C_{2,5}-2C_{4,6}\right)\right]\left[\partial_r + (\pm m+2)\frac{1}{r}\right]\tilde{v}_\theta^{m\pm3} \\
&+ \Big(\left[4\left(C_{1,6}+C_{2,6}\right) \mp 2\mathrm{i}\left(C_{1,1}-C_{2,2}\right)\right]\left[\partial_r^2 - \frac{1}{r}\partial_r - (m^2 \pm 4m + 3)\frac{1}{r^2}\right] \\
&\quad + 4s^2\beta_z^2\left[2C_{4,5} \pm \mathrm{i}\left(C_{4,4}-C_{5,5}\right)\right]\Big)\tilde{v}_\theta^{m\pm2} \\
&+ s\beta_z\Big(8\left[-(C_{2,4}+C_{5,6}) \pm \mathrm{i}\left(C_{1,5}+C_{4,6}\right)\right]\frac{1}{r} \\
&\quad + 4\left[(C_{1,4}+C_{2,4}) \mp \mathrm{i}\left(C_{1,5}+C_{2,5}\right)\right]\left[\partial_r \mp \frac{m}{r}\right]\Big)\tilde{v}_\theta^{m\pm1} \\
&+ 4\mathrm{i}m\left[\left(C_{1,1}+C_{2,2}+2C_{1,2}\right)\frac{1}{r}\partial_r - \left(2C_{1,1}+2C_{2,2}+4C_{6,6}\right)\frac{1}{r^2}\right]\tilde{v}_\theta^m,
\end{aligned}
\tag{C.21c}
$$

$$
\begin{aligned}
8\tilde{\Lambda}_{1,3} &= \left[C_{1,5}-C_{2,5}-2C_{4,6} \pm \mathrm{i}\left(C_{1,4}-C_{2,4}+2C_{5,6}\right)\right] \\
&\quad \cdot \left[\partial_r^2 + (\pm2m+5)\frac{1}{r}\partial_r + (m^2 \pm 4m + 3)\frac{1}{r^2}\right]\tilde{v}_z^{m\pm3} \\
&+ 2s\beta_z\left[(C_{1,3}-C_{2,3}-C_{4,4}+C_{5,5}) \pm 2\mathrm{i}\left(C_{3,6}+C_{4,5}\right)\right]\left[\partial_r + (\pm m+2)\frac{1}{r}\right]\tilde{v}_z^{m\pm2} \\
&+ \Big(\left[3C_{1,5}+C_{2,5}+2C_{4,6} \pm \mathrm{i}\left(C_{1,4}+3C_{2,4}+2C_{5,6}\right)\right]\left[\partial_r^2 + \frac{1}{r}\partial_r - \frac{1}{r^2}\right] \\
&\quad - m^2\left[C_{1,5}-C_{2,5}+2C_{4,6} \mp \mathrm{i}\left(C_{1,4}-C_{2,4}-2C_{5,6}\right)\right]\frac{1}{r^2}
\end{aligned}
$$

$$\pm 2m\left[C_{1,5}+C_{2,5}\pm \mathrm{i}\left(C_{1,4}+C_{2,4}\right)\right]\left[\frac{1}{r}\partial_r-\frac{2}{r^2}\right]+4s^2\beta_z^2\left[C_{3,5}\pm \mathrm{i}C_{3,4}\right]\Big)\tilde{v}_z^{m\pm1}$$
$$+4s\beta_z\left[C_{1,3}+C_{2,3}+C_{4,4}+C_{5,5}\right]\partial_r\tilde{v}_z^m, \tag{C.21d}$$

$$16\tilde{\Lambda}_{2,1}=\Big[4\left(C_{1,6}-C_{2,6}\right)\mp \mathrm{i}\left(C_{1,1}+C_{2,2}-2C_{1,2}-4C_{6,6}\right)\Big]$$
$$\cdot\left[\partial_r^2+(\pm2m+5)\frac{1}{r}\partial_r+(m^2\pm4m+3)\frac{1}{r^2}\right]\tilde{v}_r^{m\pm4}$$
$$+4s\beta_z\left[\left(C_{1,4}-C_{2,4}+2C_{5,6}\right)\mp \mathrm{i}\left(C_{1,5}-C_{2,5}-2C_{4,6}\right)\right]\left[\partial_r+(\pm m+2)\frac{1}{r}\right]\tilde{v}_r^{m\pm3}$$
$$+\Big(\left[4\left(C_{1,6}+C_{2,6}\right)\mp 2\mathrm{i}\left(C_{1,1}-C_{2,2}\right)\right]\left[\partial_r^2+\frac{3}{r}\partial_r+(-m^2+1)\frac{1}{r^2}\right]$$
$$+4s^2\beta_z^2\left[2C_{4,5}\pm \mathrm{i}\left(C_{4,4}-C_{5,5}\right)\right]\Big)\tilde{v}_r^{m\pm2}$$
$$+s\beta_z\Big(8\left[\left(C_{2,4}+C_{5,6}\right)\mp \mathrm{i}\left(C_{1,5}+C_{4,6}\right)\right]\frac{1}{r}$$
$$+4\left[\left(C_{1,4}+C_{2,4}\right)\mp \mathrm{i}\left(C_{1,5}+C_{2,5}\right)\right]\left[\partial_r\mp\frac{m}{r}\right]\Big)\tilde{v}_r^{m\pm1}$$
$$+4\mathrm{i}m\left[\left(C_{1,1}+C_{2,2}+2C_{1,2}\right)\frac{1}{r}\partial_r+\left(2C_{1,1}+2C_{2,2}+4C_{6,6}\right)\frac{1}{r^2}\right]\tilde{v}_r^m, \tag{C.21e}$$

$$16\tilde{\Lambda}_{2,2}=-\Big[C_{1,1}+C_{2,2}-2C_{1,2}-4C_{6,6}\pm 4\mathrm{i}\left(C_{1,6}-C_{2,6}\right)\Big]$$
$$\cdot\left[\partial_r^2+(\pm2m+5)\frac{1}{r}\partial_r+(m^2\pm4m+3)\frac{1}{r^2}\right]\tilde{v}_r^{m\pm4}$$
$$-4\big[\mathrm{i}(C_{1,5}-C_{2,5}-2C_{4,6})\mp\left(C_{1,4}-C_{2,4}+2C_{5,6}\right)\big]\left[\partial_r+(\pm m+2)\frac{1}{r}\right]\tilde{v}_r^{m\pm3}$$
$$+\big(4\left[C_{1,1}-C_{2,2}\pm 2\mathrm{i}\left(C_{1,6}+C_{2,6}\right)\right]\left[(\pm m+1)\frac{1}{r}\partial_r+(m^2\pm2m+1)\frac{1}{r^2}\right]$$
$$+4s^2\beta_z^2\left[C_{4,4}-C_{5,5}\mp 2\mathrm{i}C_{4,5}\right]\big)\tilde{v}_r^{m\pm2}$$
$$+s\beta_z\Big(4\left[\left(C_{1,5}-C_{2,5}+2C_{4,6}\right)\mp \mathrm{i}\left(C_{1,4}-C_{2,4}-2C_{5,6}\right)\right]\partial_r$$
$$+\big[\pm4m\left[\left(3C_{1,5}+C_{2,5}+2C_{4,6}\right)\pm\mathrm{i}(C_{1,4}+3C_{2,4}+2C_{5,6})\right]$$
$$+8\left[\left(C_{1,5}+C_{4,6}\right)\pm\mathrm{i}(C_{2,4}+C_{5,6})\right]\big]\frac{1}{r}\Big)\tilde{v}_r^{m\pm1}$$
$$+\Big(\left[2C_{1,1}+2C_{2,2}-4C_{1,2}+8C_{6,6}\right]\left[\partial_r^2+\frac{1}{r}\partial_r-\frac{1}{r^2}\right]$$
$$-m^2\left[6C_{1,1}+6C_{2,2}+4C_{1,2}+8C_{6,6}\right]\frac{1}{r^2}+8s^2\beta_z^2\left[C_{4,4}+C_{5,5}\right]-16\rho^{\mathrm{s}}s^2\Big)\tilde{v}_r^m, \tag{C.21f}$$

$$
\begin{aligned}
8\tilde{\Lambda}_{2,3} = &\left[C_{1,4} - C_{2,4} + 2C_{5,6} \mp \mathrm{i}\,(C_{1,5} - C_{2,5} - 2C_{4,6})\,\right] \\
&\quad \cdot \left[\partial_r^2 + (\pm 2m + 5)\frac{1}{r}\partial_r + (m^2 \pm 4m + 3)\frac{1}{r^2}\right] \tilde{v}_z^{m\pm 3} \\
&+ s\beta_z\left[4\,(C_{3,6} + C_{4,5}) \mp 2\mathrm{i}\,(C_{1,3} - C_{2,3} - C_{4,4} + C_{5,5})\,\right] \left[\partial_r + (\pm m + 2)\frac{1}{r}\right] \tilde{v}_z^{m\pm 2} \\
&+ \Bigg(- \left[C_{1,4} - C_{2,4} - 2C_{5,6} \pm \mathrm{i}\,(C_{1,5} - C_{2,5} + 2C_{4,6})\right] \left[\partial_r^2 + \frac{1}{r}\partial_r - \frac{1}{r^2}\right] \\
&\quad - m^2\left[C_{1,4} + 3C_{2,4} + 2C_{5,6} \mp \mathrm{i}\,(3C_{1,5} + C_{2,5} + 2C_{4,6})\right]\frac{1}{r^2} \\
&\quad \mp 2m\left[\left[C_{1,4} + C_{2,4} \mp \mathrm{i}\,(C_{1,5} + C_{2,5})\right]\frac{1}{r}\partial_r + 2\left[C_{2,4} + C_{5,6} \mp \mathrm{i}(C_{1,5} + C_{4,6})\right]\frac{1}{r^2}\right] \\
&\quad + 4s^2\beta_z^2\left[C_{3,4} \mp \mathrm{i}C_{3,5}\right]\Bigg)\tilde{v}_z^{m\pm 1} \\
&+ 4\mathrm{i}s\beta_z m\left[C_{1,3} + C_{2,3} + C_{4,4} + C_{5,5}\right]\frac{1}{r}\tilde{v}_z^m,
\end{aligned}
\tag{C.21g}
$$

$$
\begin{aligned}
8\tilde{\Lambda}_{3,1} = &\left[C_{1,5} - C_{2,5} - 2C_{4,6} \pm \mathrm{i}\,(C_{1,4} - C_{2,4} + 2C_{5,6})\,\right] \\
&\quad \cdot \left[\partial_r^2 + (\pm 2m + 3)\frac{1}{r}\partial_r + (m^2 \pm 2m)\frac{1}{r^2}\right] \tilde{v}_r^{m\pm 3} \\
&+ 2s\beta_z\left[C_{1,3} - C_{2,3} - C_{4,4} + C_{5,5} \pm 2\mathrm{i}\,(C_{3,6} + C_{4,5})\,\right] \left[\partial_r + (\pm m + 1)\frac{1}{r}\right] \tilde{v}_r^{m\pm 2} \\
&+ \Bigg(\left[3C_{1,5} + C_{2,5} + 2C_{4,6} \pm \mathrm{i}\,(C_{1,4} + 3C_{2,4} + 2C_{5,6})\right]\partial_r^2 \\
&\quad + \left[5C_{1,5} + 3C_{2,5} + 2C_{4,6} \pm \mathrm{i}\,(3C_{1,4} + 5C_{2,4} + 2C_{5,6})\right]\frac{1}{r}\partial_r \\
&\quad \pm 2m\left[C_{1,5} + C_{2,5} \pm \mathrm{i}\,(C_{1,4} + C_{2,4})\right]\left[\frac{1}{r}\partial_r + \frac{1}{r^2}\right] \\
&\quad - m^2\left[C_{1,5} - C_{2,5} + 2C_{4,6} \mp \mathrm{i}\,(C_{1,4} - C_{2,4} - 2C_{5,6})\right]\frac{1}{r^2} + 4s^2\beta_z^2\left[C_{3,5} \pm \mathrm{i}C_{3,4}\right]\Bigg)\tilde{v}_r^{m\pm 1} \\
&+ 4s\beta_z\left[C_{1,3} + C_{2,3} + C_{4,4} + C_{5,5}\right]\left[\partial_r + \frac{1}{r}\right]\tilde{v}_r^m,
\end{aligned}
\tag{C.21h}
$$

$$
\begin{aligned}
8\tilde{\Lambda}_{3,2} = &\left[C_{1,4} - C_{2,4} + 2C_{5,6} \mp \mathrm{i}\,(C_{1,5} - C_{2,5} - 2C_{4,6})\,\right] \\
&\quad \cdot \left[\partial_r^2 + (\pm 2m + 3)\frac{1}{r}\partial_r + (m^2 \pm 2m)\frac{1}{r^2}\right] \tilde{v}_\theta^{m\pm 3} \\
&+ s\beta_z\left[4\,(C_{3,6} + C_{4,5}) \mp 2\mathrm{i}\,(C_{1,3} - C_{2,3} - C_{4,4} + C_{5,5})\,\right] \left[\partial_r + (\pm m + 1)\frac{1}{r}\right] \tilde{v}_\theta^{m\pm 2} \\
&+ \Bigg(- \left[C_{1,4} - C_{2,4} - 2C_{5,6} \pm \mathrm{i}\,(C_{1,5} - C_{2,5} + 2C_{4,6})\right]\partial_r^2
\end{aligned}
$$

$$
\begin{aligned}
&- \left[3C_{1,4} + C_{2,4} - 2C_{5,6} \mp \mathrm{i}\left(C_{1,5} + 3C_{2,5} - 2C_{4,6}\right)\right] \frac{1}{r}\partial_r \\
&\mp 2m \left[C_{1,4} + C_{2,4} \mp \mathrm{i}\left(C_{1,5} + C_{2,5}\right)\right] \left[\frac{1}{r}\partial_r + \frac{1}{r^2}\right] \\
&- m^2 \left[C_{1,4} + 3C_{2,4} + 2C_{5,6} \mp \mathrm{i}\left(3C_{1,5} + C_{2,5} + 2C_{4,6}\right)\right] \frac{1}{r^2} \\
&+ 4s^2\beta_z^2 \left[C_{3,4} \mp \mathrm{i}C_{3,5}\right] \Bigg) \tilde{v}_\theta^{m\pm1} \\
&+ 4\mathrm{i}s\beta_z m \left[C_{1,3} + C_{2,3} + C_{4,4} + C_{5,5}\right] \frac{1}{r}\tilde{v}_\theta^m,
\end{aligned}
\tag{C.21i}
$$

$$
\begin{aligned}
4\tilde{\Lambda}_{3,3} = &\left[C_{5,5} - C_{4,4} \pm 2\mathrm{i}C_{4,5}\right] \left[\partial_r^2 + (\pm 2m + 3)\frac{1}{r}\partial_r + (m^2 \pm 2m)\frac{1}{r^2}\right] \tilde{v}_z^{m\pm2} \\
&+ 4s\beta_z \left[C_{3,5} \pm \mathrm{i}C_{3,4}\right] \left[\partial_r + (\pm m + 1)\frac{1}{r}\right] \tilde{v}_z^{m\pm1} \\
&+ 2\left(\left[C_{4,4} + C_{5,5}\right] \left[\partial_r^2 + \frac{1}{r}\partial_r - \frac{m^2}{r^2}\right] + 2s^2\beta_z^2 C_{3,3} - 4\rho^{\mathrm{s}} s^2\right) \tilde{v}_z^m.
\end{aligned}
\tag{C.21j}
$$

D. Processing of borehole acoustic waveform array data

Section 1.1 presents that borehole acoustic tools contain an array of receivers that are axially offset from each other by a constant distance. The wavefield emitted by the transmitter is measured at each receiver yielding a waveform array. The main objective is to extract the wave velocity or slowness of different wave modes from the waveform array data. For this purpose, several methods were developed in the past, which can be classified into time-domain and frequency-domain methods. Some of these methods are briefly explained in the following sections, and examples in isotropic formations are presented.

D.1. Time-domain methods

The most widespread slowness time coherence (STC) method is semblance processing developed by Kimball and Marzetta (1984). This method determines the first arrival time (T) and the slowness value (β) that maximize the coherence of stacked waveform data. The coherence or semblance (ρ) is defined as (Kimball and Marzetta, 1984)

$$\rho(\beta, T, T_w) = \frac{1}{N} \frac{\int_{t=T}^{T+T_w} \left| \sum_{k=1}^{N} w_k \left(t + \beta(k-1)\Delta z\right) \right|^2 \mathrm{d}t}{\sum_{k=1}^{N} \int_{t=T}^{T+T_w} \left| w_k \left(t + \beta(k-1)\Delta z\right) \right|^2 \mathrm{d}t}. \tag{D.1}$$

The variable w_k denotes the measured time-domain waveform at the kth receiver in the receiver array. The array contains N receivers that are axially offset by the equidistant spacing Δz. As an example, the upper plot of figure D.1 displays the FD modeled waveform array data of the wavefield emitted by an LWD monopole source in a fluid-filled borehole that is surrounded by a fast isotropic formation. Equation D.1 expresses that the waveform at the kth receiver is propagated to the first receiver position by applying a time shift $\beta(k-1)\Delta z$ (Tang and Cheng, 2004). This time shift is illustrated in figure D.1 by the orange lines and depends on the chosen slowness value β. For calculating the nominator of equation D.1, the waveform data of the first receiver and all other $(N-1)$ time-shifted waveforms are summed. Then, the absolute values of the summed waveforms are squared and integrated over a time window. The start of the time window depends on the first arrival time (T), and its length is defined by the chosen time window length T_w (Fig. D.1). The denominator of equation D.1 looks similar, but the absolute values of the time-shifted waveforms are squared and integrated over the time window before they are summed. Hence, the denominator represents the

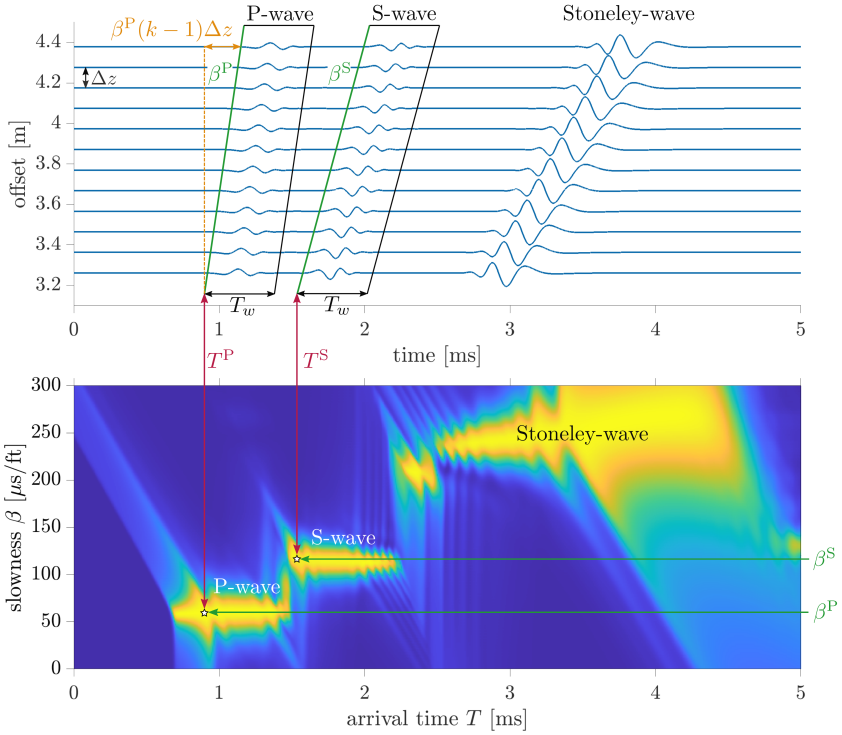

Fig. D.1: The upper figure shows the time-domain waveform array data of the wavefield emitted by an LWD monopole source ($f_c = 4\,\mathrm{kHz}$) in a fluid-filled borehole surrounded by a fast isotropic formation. The wave modes are differently amplified for better visualization. The bottom figure displays the semblance function in relation to the slowness β and the arrival time T at the first receiver. The maxima of the semblance function correspond to the refracted P-, refracted S-, and *Stoneley* waves.

stacked coherent power contained in a time windowed portion of each waveform. In contrast, the physically meaning of the nominator is the power contained in the time windowed portion of the stacked waveform. Consequently, the nominator is always smaller or equal to the denominator, and the semblance ρ attains values between zero and one ($0 \leq \rho \leq 1$). The value one is obtained if all time-shifted waveforms are identical. This can only be obtained if the slowness value used in the time shift coincides with the true slowness value at which the wave propagates. Additionally, the waveforms of a particular wave must be contained in the time window $T \leq t \leq T + T_w$. Thus, the scalar semblance value depends on the slowness β, the first arrival time T, and the time window length T_w. The latter is usually set to contain two or three wave cycles (Tang and Cheng, 2004). Then, the first arrival time and the slowness value are numerically varied in the range of interest, and for each (β,T)–pair, the semblance value is computed. This results in a two-dimensional semblance function, as displayed at the bottom of Fig. D.1. It can be observed that the semblance function contains several local maxima corresponding to different wave modes. The first maximum located at the earliest first arrival time corresponds to the refracted P-wave propagating vertically along the borehole. The location of the respective maximum semblance value indicated by the star corresponds to the first arrival time of the refracted P-wave (T^{P}) at the first receiver, as illustrated by the red line in figure D.1. Moreover, the slowness value that makes the semblance value maximum coincide with the slowness of the refracted P-wave (β^{P}), corresponding to the slope of the green line plotted on top of the first arrivals in the upper plot of Fig. D.1. Analogously, the location

of the second maximum defines the first arrival time (T^{S}) and slowness (β^{S}) of the refracted shear wave. The third maximum corresponds to the borehole-guided *Stoneley* wave, which is dispersive, i.e., the wave propagates with different slowness at different frequencies. The problem is that the waveforms are time-shifted in the semblance method using a constant slowness value. Consequently, the semblance method cannot process dispersive waves correctly, and frequency-domain methods are required instead. Geerits and Tang (2003) have shown that semblance processing of dispersive borehole waves yields a weighted spectral average of the dispersion curve over the frequency range of the wave spectrum.

Although the semblance method is the most common slowness time coherence (STC) technique, McFadden et al. (1986) proposed the Nth root stacking method as an alternative based on the same physics, whereas the mathematical formulation is slightly different.

D.2. Frequency-domain methods

D.2.1. Weighted spectral semblance method

Nolte et al. (1997) proposed a weighted spectral semblance method that processes the waveform array data in the frequency domain. For this reason, the N waveforms of the array are *Laplace* transformed (App. A.1) from the time domain ($w(t)$) to the frequency domain ($\breve{w}(s)$) first. The upper plot in figure D.2 displays an example for the frequency-domain waveform array of the wavefield emitted by an LWD monopole source in a fluid-filled borehole surrounded by a fast isotropic formation.

In the next step of the method, the spectral semblance is computed defined as (e.g., Tang and Cheng, 2004)

$$\rho(\beta, s) = \frac{\left| \sum_{k=1}^{N} \breve{w}_k^*(s) \exp(-s\beta(k-1)\Delta z) \right|^2}{\sqrt{N \sum_{k=1}^{N} \breve{w}_k(s)^* \breve{w}_k(s)}}, \tag{D.2}$$

where $\breve{w}_k^*$ denotes the complex conjugate of $\breve{w}_k(s)$. Equation D.2 describes a coherence stacking of the waveform array data in the frequency domain. If the slowness value β coincides with the slowness of a wave mode contained in the waveform array at a particular frequency ($s = \mathrm{i}\omega$), the phase of the nominator in equation D.2 vanishes, and the semblance is maximized approaching the value one for noise-free data (Tang and Cheng, 2004). In the next step, the computed semblance values are weighted over neighboring frequency points to enhance the data information and reduce noise, as explained by Nolte et al. (1997) and Tang and Cheng (2004). The weighted semblance values are calculated for different slowness values and frequencies in the range of interest to obtain a two-dimensional semblance function, as displayed in the bottom plot of figure D.2. The location of the maximum semblance value for each frequency defines the slowness dispersion curves of the corresponding wave mode contained

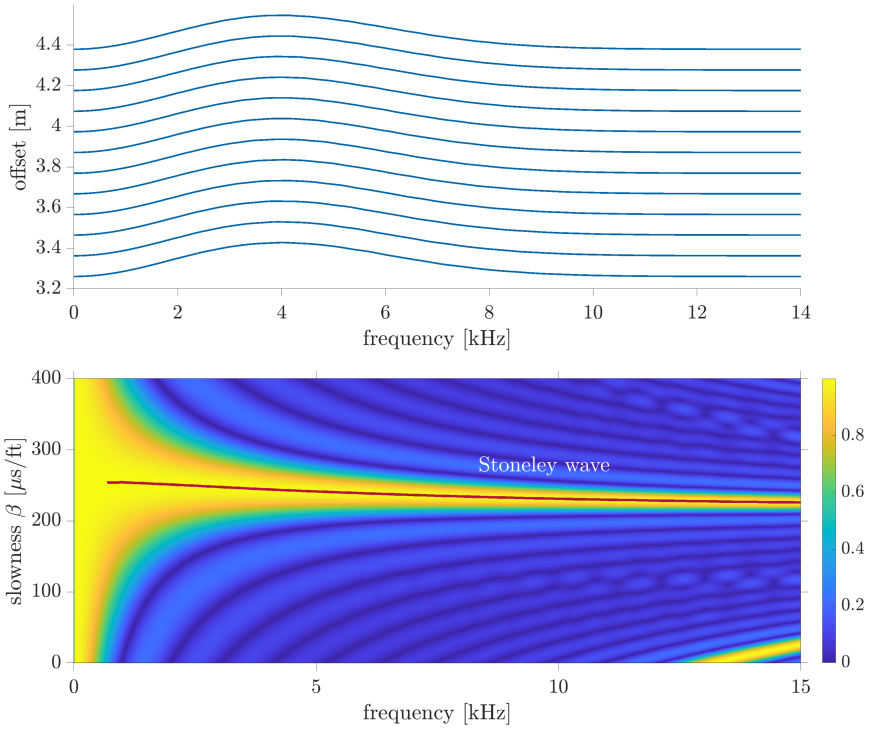

Fig. D.2: The upper figure shows the frequency-domain waveform array data (absolute values) of the wavefield emitted by an LWD monopole source ($f_c = 4\,\mathrm{kHz}$) in a fluid-filled borehole surrounded by a fast isotropic formation. The bottom figure displays the semblance function in relation to the slowness and frequency. The maximum of the semblance for each frequency defines the slowness dispersion curve of the *Stoneley* wave illustrated by the red line.

in the waveform array data. In figure D.2, the maximum semblance values in dependence with the frequency define the dispersion curve of the *Stoneley* wave. Since the waveform array contains only weak signals at low frequencies, the semblance possesses a wide maximum below 1 kHz.

D.2.2. Modified matrix pencil method

Ekstrom (1996) has developed a modified matrix pencil method that is a multi-mode dispersion extraction method to extract several borehole modes from the waveform array data. This method is a frequency-domain method, and the received waveforms at the N receivers of the array are *Laplace* transformed (App. A.1) from the time domain ($w(t)$) to the frequency domain ($\check{w}(s)$) first. Next, the slowness values β are estimated at a particular temporal frequency s. The complex sequence $\check{w}_k(s)$ ($k = 1, ..., N$) at a particular frequency has the length N and can be approximated as a set of p complex exponentials (Ekstrom, 1996)

$$\check{w}_k(s) \approx \sum_{j=1}^{p} a_j \exp(-s\beta^{[j]} z_k), \tag{D.3}$$

where z_k represents the axial offset between the transmitter and kth receiver. The objective is to find the p exponentials (poles) that fit the waveform data best. Since the waveforms contain the signal and noise in real measurements, Ekstrom (1996) explained that the estimation of

the signal poles improves if the noise poles are also fit. Thus, he proposed to choose a larger number for p than the number of expected signal modes q. For the estimation of the exponentials, a forward and backward pencil is used. For this purpose, two matrices are defined as (Ekstrom, 1996)

$$\mathcal{W}_0(s) = \begin{pmatrix} \breve{w}_2(s) & \breve{w}_3(s) & \dots & \breve{w}_{p+1}(s) \\ \breve{w}_3(s) & \breve{w}_4(s) & \dots & \breve{w}_{p+2}(s) \\ \vdots & \vdots & \ddots & \vdots \\ \breve{w}_{N-p+1}(s) & \breve{w}_{N-p+2}(s) & \cdots & \breve{w}_N(s) \end{pmatrix}, \tag{D.4}$$

and

$$\mathcal{W}_1(s) = \begin{pmatrix} \breve{w}_1(s) & \breve{w}_2(s) & \dots & \breve{w}_p(s) \\ \breve{w}_2(s) & \breve{w}_3(s) & \dots & \breve{w}_{p+1}(s) \\ \vdots & \vdots & \ddots & \vdots \\ \breve{w}_{N-p}(s) & \breve{w}_{N-p+1}(s) & \cdots & \breve{w}_{N-1}(s) \end{pmatrix}. \tag{D.5}$$

Hua and Sarkar (1990) proved that the poles are the generalized eigenvalues of the matrix pair ($\mathcal{W}_0$ and $\mathcal{W}_1$). Thus, the pole estimates can be computed by solving the standard eigenvalue problems (Ekstrom, 1996)

$$\left(\mathcal{W}_1^{+}\mathcal{W}_0 - \lambda_0 I\right) \boldsymbol{e}^0 = 0, \tag{D.6}$$

and

$$\left(\mathcal{W}_0^{+}\mathcal{W}_1 - \lambda_1 I\right) \boldsymbol{e}^1 = 0, \tag{D.7}$$

where the $\mathcal{W}^{+}$ denotes the *Moore-Penrose* inverse of $\mathcal{W}$. The pole estimates obtained from equation D.6 are referred to as backward estimates, whereas the eigenvalues of equation D.7 yield the forward estimates for the exponentials. Ekstrom (1996) proposed a simple variation of the pencil formulation that is more robust and also applicable for attenuative signals. For this reason, the forward and backward pole estimates are computed separately. Subsequently, the forward and backward sets of the pole estimates are matched by finding the corresponding poles of each set that are closest together in magnitude. If the difference between two poles is within a chosen tolerance, the two poles are arithmetically averaged to yield a final estimate. Otherwise, the estimated pole pair is discarded (Ekstrom, 1996). In the above-described way, the estimates of the poles are obtained in the form of averaged complex eigenvalues ($\bar{\lambda}$) characterized by its length $|\lambda|$ and argument (phase) φ

$$\bar{\lambda}^{[j]}(s) = |\lambda^{[j]}| \exp(\mathrm{i}\varphi^{[j]}), \quad j = 1, ..., p. \tag{D.8}$$

While the length of the complex eigenvalues represents the attenuation of the corresponding wave modes, their argument can be used to obtain the slowness of the extracted modes at the particular frequency s $(= \mathrm{i}\omega)$

$$\beta^{[j]}(s) = \frac{\varphi^{[j]}(s)}{\mathrm{i}s\Delta z}, \qquad j = 1, ..., p. \tag{D.9}$$

The modified matrix pencil method can be applied to all frequency samples in the frequency range of interest to obtain the slowness dispersion curves of the wave modes contained in the waveform array data. The upper plot of figure D.3 shows an example for waveform array data in the frequency domain. The figure displays the absolute value of the frequency-domain waveforms of the wavefield emitted by an LWD dipole source in a fluid-filled borehole surrounded by a fast isotropic formation. The bottom of figure D.3 displays the slowness dispersion curves of the excited wave modes, which are extracted from the frequency-domain waveform array data using the modified matrix pencil method. This method can extract both dispersive waves, e.g., the tool flexural or formation flexural waves, and non-dispersive waves, e.g., the refracted S-wave, as displayed in the figure.

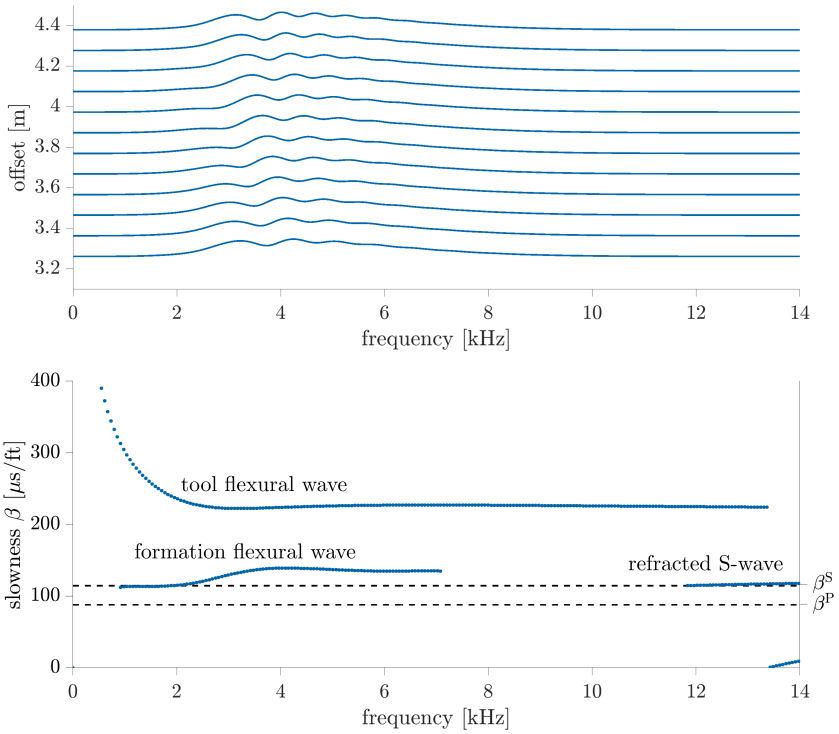

Fig. D.3: The upper figure shows the frequency-domain waveform array data (absolute values) of the wavefield emitted by an LWD dipole source ($f_c = 4\,\mathrm{kHz}$) in a fluid-filled borehole surrounded by a fast isotropic formation. The bottom figure displays the slowness dispersion curves of the tool flexural, formation flexural, and refracted S-waves extracted via the matrix pencil method ($p = 3$). The dashed black lines illustrate the slowness values of the P- and S-wave in the formation.

Addendum: Inaccuracy in the sensitivity analysis

This thesis contains a number of sensitivity calculations shown in the corresponding sensitivity plots (Fig. 4.2e–4.2f, 4.3c–4.3d, 4.4c–4.4d, 4.5c–4.5d, 4.6c–4.6d, 4.7c–4.7d, 4.9d, 4.10b, 4.16c–4.16f, 4.18c–4.18f, and 4.21c–4.21f), which are potentially inaccurate. The inaccuracy of these plots can be caused by different aspects. First, the FD modeled waveforms contain an inaccuracy because of the FD method. As explained in section 3.4, grid dispersion can introduce errors depending on the spacing of the FD grid. Since decreasing the spacing of the FD grid increases the computational effort, a balance for the spacing was chosen so that the simulations are still manageable on a high-performance cluster and the grid dispersion errors are at an acceptable level.

Nevertheless, this error can also be partially contained in the phase slowness dispersion curves of the borehole waves since they are directly extracted from the FD modeled waveform array data using the modified matrix pencil method (Sec. D.2.2). Figure 1 shows a comparison of the phase slowness dispersion curves of the tool flexural (Fig. 1a) and formation quadrupole (Fig. 1b) waves in an isotropic environment. While the blue dots illustrate the phase slowness dispersion curves obtained from the FD modeled waveforms, the dispersion curves displayed by the solid red lines are computed using an analytical solution (Geerits et al., 2010). The comparison shows that both modeled phase slowness dispersion curves are very similar, where the difference for the tool flexural wave is less than 3.4 %. Similarly, the modeled phase slowness dispersion curves of the formation quadrupole wave show a good agreement and differ

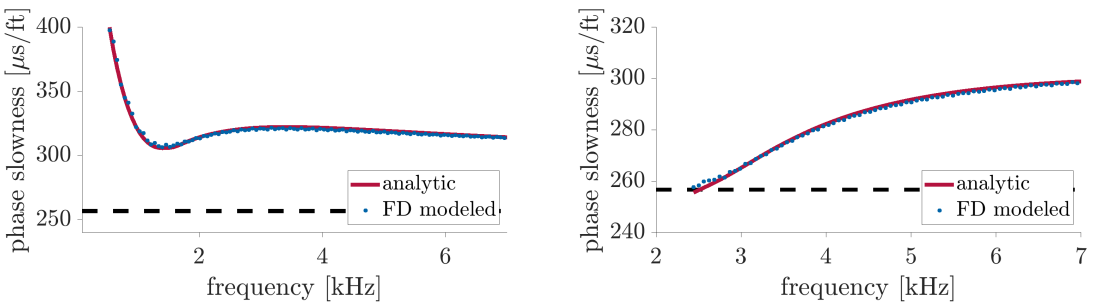

(a) Phase slowness dispersion (tool flexural)

(b) Phase slowness dispersion (formation quadrupole)

Fig. 1: Phase slowness dispersion curves of the tool flexural (a) and formation quadrupole (b) waves excited by a dipole/quadrupole source in a fluid-filled borehole surrounded by an isotropic formation ($v^{\mathrm{P}} = 3162.3\,\mathrm{m\,s^{-1}}$, $v^{\mathrm{S}} = 1187.1\,\mathrm{m\,s^{-1}}$, $\rho^{\mathrm{s}} = 2200\,\mathrm{kg\,m^{-3}}$) in the presence of an LWD tool. The blue dots illustrate the phase slowness dispersion curves extracted from FD modeled waveform array data, whereas the solid red lines display the dispersion curves computed using an analytical solution.

only slightly in the low-frequency limit with a maximum error of 2.1 %. Consequently, these comparisons of FD and analytic modeled phase slowness dispersion curves show that the FD modeled data agree well with the analytic modeling in isotropic environments and the FD error is relatively small. Therefore, it is assumed that the FD modeling also works well in TI environments. Unfortunately, the FD results in HTI or TTI formations cannot be benchmarked against an analytical solution because it is not available, as discussed in section 2.4.2.

While the above discussion shows that there is only slight inaccuracy introduced in the FD modeling of the phase slowness dispersion curves, the sensitivity calculation itself causes further inaccuracies. The formula for the sensitivity (Eq. 4.2) involves the partial derivative of the phase slowness with respect to the considered parameter. This partial derivative itself must be calculated using a finite-difference since there are no explicit formulas for the phase slowness in TI formation. In the sensitivity analysis of this work, the partial difference is modeled by a forward difference

$$\frac{\partial \beta(s)}{\partial \text{parameter}} \approx \frac{\beta(\text{parameter} + \Delta\text{parameter}, s) - \beta(\text{parameter}, s)}{\Delta\text{parameter}}. \tag{1}$$

This approximation of the partial derivation in the calculation of the sensitivity introduces further errors, which highly depend on the perturbation of the parameter (Δparameter). The smaller the perturbation of the considered parameter is chosen, the less the discretization error becomes. On the other hand, a small perturbation can strongly increase errors in the phase slowness dispersion curves. Since the phase slowness values involved in the nominator of the forward difference (Eq. 1) contain errors caused by the FD modeling, these errors would be strongly amplified by a small value of the perturbation parameter in the denominator. Consequently, when weighting the computational costs of highly accurate sensitivity coefficients against the practical goal to demonstrate general trends in the sensitivity analysis with respect to various parameters, e.g., stiffness tensor elements, it appears reasonable to refrain from the former.

Danksagung

An dieser Stelle möchte ich mich bei allen beteiligten Personen bedanken, die mich während der letzten drei Jahre bei der Anfertigung meiner Dissertation unterstützt haben.

Mein besonderer Dank gilt meinem Betreuer Tim Geerits, für die intensive und kompetente Betreuung sowie den stundenlangen Diskussionen am Telefon. Auch möchte ich mich für die Einführung in die spannende Welt der Bohrlochakustik und den großen Einsatz bedanken, dass meine Doktorandenstelle ermöglicht wurde.

Weiterhin möchte ich mich bei meinem Betreuer Stefan Buske für die eingeräumten Freiheiten und die Unterstützung in allen Anliegen bedanken.

Außerdem möchte ich mich bei meinen Freiberger Kollegen und Freunden für die angenehme Arbeitsatmosphäre und gemeinsamen Erlebnisse bedanken. Insbesondere möchte ich Olaf Hellwig hervorheben, der den Kontakt mit meinem Betreuer Tim Geerits hergestellt hat und mir somit meine Promotion ermöglicht hat. Des Weiteren möchte ich mich für die tiefgehenden Einblicke in die Finite-Differenzen Methode bedanken und dass ich den vorhandenen Code verwenden und weiterentwickeln konnte. Bei meinem Bürokollegen Maik Linke bedanke ich mich für das freundschaftliche Verhältnis und die hilfreichen Diskussionen im Bereich der Bohrlochakustik und Themen die weit darüber hinaus gehen. Für das sprachliche Korrekturlesen meiner Doktorarbeit und den Diskussionen über verschiedene Eigenheiten der englischen Sprache möchte ich mich herzlich bei meiner Bürokollegin Catrina Alexandrakis-Zieger bedanken. Felix Hloušek danke ich für die technischen Hinweise und Tipps bezüglich des Rechenclusters und verschiedener verwendeter Software.

Bei dieser Gelegenheit bedanke ich mich für die zur Verfügung gestellte Rechenzeit auf dem Rechencluster der Fakultät für Mathematik und Informatik der TU Bergakademie Freiberg, welches vom Universitätsrechenzentrum (URZ) betrieben wird und von der Deutsche Forschungsgemeinschaft (DFG) finanziert wurde (Nummer: 397252409).

Für die Finanzierung meiner Doktorandenstelle, sowie die gute Zusammenarbeit mit der TU Bergakademie Freiberg möchte ich mich bei dem Erdöl-Service Konzern Baker Hughes bedanken.

Des Weiteren bedanke ich mich bei Johan Robertsson und Erik Koene für die Hinweise das richtige Gitter für die Finite-Differenzen Methode für anisotrope Medien zu verwenden und

Diskussionen über die beste Implementierung.

Der Graduierten- und Forschungsakademie möchte ich meinen Dank für die schnelle und kompetente Unterstützung bei allen formellen Anliegen aussprechen.

Nicht zuletzt will ich mich bei meinen Eltern Birgit und Volker, sowie meiner gesamten Familie bedanken, die mich bei meinen Vorhaben unterstützt haben. Mein großer Dank gilt meiner Frau Vera, die mich in der gesamten Zeit so gut wie möglich unterstützt hat, immer für mich da war und mich auch durch schwierige Phasen der Promotion begleitet hat.

Versicherung

Hiermit versichere ich, dass ich die vorliegende Arbeit ohne unzulässige Hilfe Dritter und ohne Benutzung anderer als der angegebenen Hilfsmittel angefertigt habe; die aus fremden Quellen direkt oder indirekt übernommenen Gedanken sind als solche kenntlich gemacht.
Bei der Auswahl und Auswertung des Materials sowie bei der Herstellung des Manuskripts habe ich Unterstützungsleistungen von folgenden Personen erhalten:

- Dr. Catherine Alexandrakis-Zieger bei der Korrektur von Rechtschreibung und Grammatik

Weitere Personen waren an der Abfassung der vorliegenden Arbeit nicht beteiligt.
Die Hilfe eines Promotionsberaters habe ich nicht in Anspruch genommen. Weitere Personen haben von mir keine geldwerten Leistungen für Arbeiten erhalten, die nicht als solche kenntlich gemacht worden sind. Die Arbeit wurde bisher weder im Inland noch im Ausland in gleicher oder ähnlicher Form einer anderen Prüfungsbehörde vorgelegt.

25. Oktober 2021 M. Sc., Christoph, Demmler